

Energy failure following traumatic brain injury: Potential mechanisms and impact of normobaric hyperoxia

Tonny V Veenith

Wolfson College



University of Cambridge



June 2019

This dissertation is submitted for the degree of Doctor of Philosophy

This dissertation is the result of my own work and includes nothing which is the outcome of work done in collaboration except as declared in the preface and specified in the text.

It is not substantially the same as any that I have submitted, or, is being concurrently submitted for a degree or diploma or other qualification at the University of Cambridge or any other University or similar institution except as declared in the Preface and specified in the text.

This thesis does not exceed 60,000 word limit.

Contents

CONTENTS	3
LIST OF FIGURES	7
LIST OF TABLES	9
ACKNOWLEDGEMENTS	11
ABSTRACT	12
PUBLICATIONS AND BOOK CHAPTERS RESULTING FROM THIS WORK	13
LIST OF ABBREVIATIONS	14
CHAPTER 1 REVIEW OF THE LITERATURE	17
INTRODUCTION	17
MANAGEMENT OF TRAUMATIC BRAIN INJURY	17
<i>Intracranial pressure</i>	17
<i>Cerebral perfusion pressure and control of intracranial pressure</i>	18
<i>Ischaemia</i>	19
<i>Excitotoxicity and Neuroinflammation</i>	21
<i>Second tier therapies for the management of raised intracranial pressure</i>	22
LONG TERM NEURONAL LOSS – APOPTOSIS, SELECTIVE NEURONAL LOSS, MITOCHONDRIAL AND AUTOREGULATORY FAILURE AFTER TRAUMATIC BRAIN INJURY	24
<i>Mitochondrial dysfunction after traumatic brain injury</i>	24
<i>Autoregulation after traumatic brain injury</i>	25
CHAPTER 2 GENERIC MATERIALS AND METHODS	26
DIFFUSION TENSOR IMAGING	26
<i>Physical principles of diffusion weighted imaging</i>	26
<i>Anisotropic diffusion and the biological basis of anisotropy</i>	28
<i>Fractional anisotropy</i>	28
<i>Mean diffusivity or “trace water”</i>	29
<i>Apparent Diffusion Coefficient</i>	29
<i>Translating diffusion tensor imaging physics to pathophysiology in head injury and its limitations</i>	30
MAGNETIC RESONANCE SPECTROSCOPY	31
<i>Chemical shift and signal intensity</i>	32
<i>Water and fat suppression:</i>	32
<i>Spin-spin coupling</i>	33
<i>Localising MRS signals</i>	33
<i>Single voxel, two dimensional and three dimensional MR spectroscopic imaging (MRSI)</i>	33
<i>Whole brain spectroscopy using Metabolite Imaging and Data Analysis System</i>	33
<i>Quantitation of proton magnetic resonance spectra</i>	34
<i>Peak ratios and absolute quantification</i>	34

<i>Absolute quantitation versus metabolic ratios in proton spectroscopy</i>	35
POSITRON EMISSION TOMOGRAPHY	37
<i>Physical principles</i>	37
¹⁵ Oxygen positron emission tomography.....	37
¹⁸ F-fluoromisonidazole positron emission tomography	41
CHAPTER 3 AIMS AND HYPOTHESIS	43
AIMS AND HYPOTHESES	44
<i>Methodological Aims</i>	44
<i>Experimental Hypotheses</i>	45
CHAPTER 4 INTER-SUBJECT VARIABILITY AND REPRODUCIBILITY OF DIFFUSION TENSOR IMAGING WITHIN AND BETWEEN DIFFERENT IMAGING SESSIONS	46
INTRODUCTION	46
MATERIALS AND METHODS.....	47
<i>Ethics statement</i>	47
<i>Imaging data acquisition</i>	47
<i>Image processing</i>	47
<i>Analysis Strategy</i>	49
RESULTS	49
<i>Intersubject variability of diffusion tensor imaging metrics</i>	49
<i>Within-session and between-session reproducibility of diffusion tensor imaging</i>	53
<i>Calculation of 95% prediction interval for zero change</i>	58
DISCUSSION	59
<i>Methodological limitations</i>	61
CONCLUSIONS	62
CHAPTER 5 COMPARISON OF INTER SUBJECT VARIABILITY AND REPRODUCIBILITY OF WHOLE BRAIN PROTON SPECTROSCOPY.....	63
INTRODUCTION	63
MATERIALS AND METHODS.....	64
<i>Ethics statement</i>	64
<i>Imaging data acquisition</i>	64
<i>Spectroscopic data processing</i>	65
<i>Analysis Strategy</i>	66
<i>Statistical analysis</i>	67
RESULTS	68
<i>Intersubject variability for whole brain proton spectroscopic imaging</i>	68
CONCLUSIONS	84
CHAPTER 6 PATHOPHYSIOLOGICAL MECHANISMS OF CEREBRAL ISCHAEMIA AND DIFFUSION HYPOXIA IN TRAUMATIC BRAIN INJURY	85

INTRODUCTION	85
MATERIALS AND METHODS.....	85
<i>Subjects</i>	86
<i>Imaging</i>	88
<i>Region of interest analysis</i>	89
<i>Ischaemic brain volume</i>	89
<i>Hypoxic brain volume</i>	90
RESULTS	91
<i>Regional physiology</i>	91
<i>Ischaemic brain volume</i>	92
<i>Hypoxic Brain Volume</i>	93
<i>Comparison with tissue pO₂ measurements</i>	94
DISCUSSION	95
CHAPTER 7 USE OF DIFFUSION TENSOR IMAGING TO ASSESS THE IMPACT OF NORMOBARIC HYPEROXIA WITHIN AT-RISK PERICONTUSIONAL TISSUE FOLLOWING TRAUMATIC BRAIN INJURY.....	99
INTRODUCTION	99
MATERIALS AND METHODS.....	99
<i>Subjects</i>	100
<i>Imaging</i>	102
<i>Region of interest analysis</i>	103
RESULTS	106
<i>Impact of oxygen therapy on diffusion tensor imaging in healthy volunteers</i>	106
<i>Injured brain regions</i>	106
DISCUSSION	108
CONCLUSIONS	112
CHAPTER 8 NORMOBARIC HYPEROXIA DOES NOT IMPROVE DERANGEMENTS IN DIFFUSION TENSOR IMAGING FOUND DISTANT FROM VISIBLE CONTUSIONS FOLLOWING ACUTE TRAUMATIC BRAIN INJURY ..	113
INTRODUCTION	113
MATERIALS AND METHODS.....	114
<i>Subjects</i>	114
<i>Controls</i>	116
<i>Region of interest analysis</i>	117
<i>Impact of hyperoxia</i>	118
RESULTS	119
<i>Effect of graduated oxygen therapy on diffusion tensor imaging in healthy volunteers</i>	119
<i>Diffusion tensor imaging in patients and healthy volunteers</i>	122
<i>Impact of hyperoxia in patients</i>	125
DISCUSSION	136

CHAPTER 9 IMPACT OF NORMOBARIC HYPEROXIA ON THE METABOLIC DERANGEMENTS IDENTIFIED BY WHOLE-BRAIN PROTON SPECTROSCOPY FOLLOWING SEVERE TRAUMATIC BRAIN INJURY	141
INTRODUCTION	141
MATERIAL AND METHODS	142
<i>Subjects</i>	142
<i>Controls</i>	142
<i>Image processing</i>	145
RESULTS	146
<i>Impact of oxygen therapy on whole brain proton spectroscopy in healthy volunteers</i>	146
<i>Baseline metabolite concentration in at-risk regions after TBI</i>	148
<i>Baseline metabolite concentration in injured brain</i>	151
<i>Impact of normobaric hyperoxia on metabolite concentration in patients</i>	151
DISCUSSION	155
CHAPTER 10 SUMMARY AND CONCLUSIONS	157
METHODOLOGICAL AIMS	157
EXPERIMENTAL HYPOTHESES	158
CONCLUSIONS	160
CHAPTER 11 THE DIRECTION OF FUTURE RESEARCH	161
EXTENSION OF PRESENT STUDIES	161
DATA ANALYSIS TECHNIQUES	161
SEQUENTIAL IMAGING STUDIES AND NEUROCOGNITIVE OUTCOME ASSESSMENT	162
IMAGING OF NEURONAL LOSS	162
CLINICAL IMPLICATIONS AND THE EFFECTS OF THERAPY.....	163
REFERENCES.....	164

List of figures

Figure 1-1 Interdependence of cerebral blood volume and intracranial pressure and the rationale for maintaining the cerebral perfusion pressure	19
Figure 1-2 Spectrum of cerebral blood flow patterns following severe head injury	19
Figure 1-3 Electrophysiological and metabolic consequences of graded reductions in cerebral blood flow	20
Figure 1-4 Relationship of cerebral blood flow to the presence of ischaemia under conditions of varying metabolism	21
Figure 1-5 Head injury protocol in the Neurosciences Critical Care Unit, Addenbrooke's Hospital, Cambridge...	23
Figure 2-1 Diffusion in a neuron and white matter tracts of brain	27
Figure 2-2 Fractional Anisotropy and Apparent Diffusion Coefficient maps in a volunteer.....	29
Figure 2-3 Temporal profile of cytotoxic and vasogenic oedema after traumatic brain injury	30
Figure 2-4 ¹ H MRS Spectrum with water suppression acquired during whole brain proton spectroscopy.....	31
Figure 2-5 Unsuppressed water spectrum acquired during whole-brain proton spectroscopy	32
Figure 2-6 Array of detectors in positron emission tomography scanner used in this thesis.....	38
Figure 2-7 Acquisition and visualisation of the positron emission tomography image using an integrated approach.....	38
Figure 2-8 Steady-state H ₂ ¹⁵ O and ¹⁵ O ₂ used in PET studies.	40
Figure 2-9 Bolus C ¹⁵ O used in PET studies.....	40
Figure 4-1 Region of interest template in MNI152 space used for intersubject, within and between session variability of diffusion tensor imaging.....	48
Figure 4-2 Variability in fractional anisotropy measurements	50
Figure 5-1 Region of interest template with a representative spectra from right thalamus used for calculating metabolite ratios for whole brain proton spectroscopy	66
Figure 5-2 Region of interest template with a representative spectra from right thalamus.....	71
Figure 5-3 Variability in N Acetyl Aspartate / Creatine ratio measurements	72
Figure 5-4 Variability in N Acetyl Aspartate concentration	73
Figure 6-1 Regional physiology.....	91
Figure 6-2 ¹⁵ O Evidence of cerebral ischaemia using ¹⁵ O positron emission tomography following head injury .	92
Figure 6-3 Comparison of physiology within the ischaemic brain volume and hypoxic brain volume.....	93
Figure 6-4 Evidence of tissue hypoxia using ¹⁸ Fluoromisonidazole positron emission tomography.....	94
Figure 6-5 Relationship between PET parameters.....	97
Figure 7-1 Lesion regions of Interest drawn using Fluid attenuated inversion recovery (FLAIR) and apparent diffusion coefficient (ADC) images.....	104
Figure 7-2 Impact of hyperoxia on traumatic penumbra in apparent diffusion coefficient (ADC) image	105
Figure 7-3 Lesion based analysis.....	107
Figure 7-4 Impact of hyperoxia within traumatic penumbra.....	107
Figure 8-1 Lesion regions of Interest.....	117
Figure 8-2 Individualised template regions of interest	118

<i>Figure 8-3 Impact of hyperoxia in patients.....</i>	<i>128</i>
<i>Figure 9-1 Lesion based regions of interest</i>	<i>146</i>
<i>Figure 9-2 Metabolite concentration in healthy volunteers at room air, sixty and hundred percentage of oxygen</i>	<i>147</i>
<i>Figure 9-3 Parametric maps of metabolites in a patient with traumatic brain injury</i>	<i>148</i>
<i>Figure 9-4 Baseline regional physiology</i>	<i>150</i>
<i>Figure 9-5 Region of interest analysis within deep grey matter regions</i>	<i>152</i>
<i>Figure 9-6 Region of interest analysis within mixed cortical regions of interest</i>	<i>153</i>
<i>Figure 9-7 Region of interest analysis within white matter regions of interest</i>	<i>154</i>

List of tables

<i>Table 2-1 Normal whole brain concentrations in millimoles of metabolites quantified by in vivo proton spectroscopy in brain</i>	35
<i>Table 2-2 Metrics used in this thesis for diffusion tensor imaging and proton spectroscopy of the brain</i>	36
<i>Table 3-1 Mechanisms of energy failure following head injury</i>	44
<i>Table 4-1A and 1B Intersubject variability for diffusion tensor imaging measurements</i>	52
<i>Table 4-2 Within and between session variability of diffusion tensor imaging region of interest measurements</i>	57
<i>Table 4-3 Analysis of variance table for diffusion tensor imaging parameters</i>	58
<i>Table 5-1 Intersubject variability of metabolite ratios for whole brain proton spectroscopy</i>	69
<i>Table 5-2 Intersubject variability of metabolite concentrations for whole brain proton spectroscopy</i>	70
<i>Table 5-3 Within session and between session variability of metabolites for whole brain proton spectroscopy</i> .	78
<i>Table 5-4 Within session and between session intraclass correlation coefficient for metabolites</i>	79
<i>Table 5-5 Analysis of variance table for whole brain proton magnetic resonance spectroscopy</i>	80
<i>Table 6-1 Patient Characteristics</i>	87
<i>Table 7-1 Patient characteristics</i>	101
<i>Table 8-1 Patient characteristics</i>	115
<i>Table 8-2 Impact of oxygen therapy on diffusion tensor imaging parameters in healthy volunteers within white matter regions</i>	120
<i>Table 8-3 Impact of oxygen therapy on diffusion tensor imaging parameters in healthy volunteers within mixed cortical and deep grey matter regions</i>	121
<i>Table 8-4 Region of interest data within white matter regions in healthy volunteers and normoxic patients</i> ..	123
<i>Table 8-5 Region of interest data within mixed cortical and deep grey matter regions in healthy volunteers and normoxic patients</i>	124
<i>Table 8-6 Region of interest data within white matter regions in normoxic and hyperoxic patients</i>	126
<i>Table 8-7 Region of interest data within mixed cortical and deep grey matter regions in normoxic and hyperoxic patients</i>	127
<i>Table 8-8 Patient white matter regions demonstrating a change following hyperoxia using the population 99% prediction interval</i>	130
<i>Table 8-9 Patient mixed cortical and deep grey matter regions demonstrating a change following hyperoxia using the population 99% prediction interval</i>	131
<i>Table 8-10 Healthy volunteer white matter regions demonstrating a change following hyperoxia using the population 99% prediction interval</i>	132
<i>Table 8-11 Healthy volunteer mixed cortical and deep grey matter regions demonstrating a change following hyperoxia using the population 99% prediction interval</i>	132
<i>Table 8-12 Patient white matter regions demonstrating a change following hyperoxia using the regional 99% prediction interval</i>	133

<i>Table 8-13 Patient mixed cortical and deep grey matter regions demonstrating a change following hyperoxia using the regional 99% prediction interval</i>	<i>134</i>
<i>Table 8-14 Healthy volunteer white matter regions demonstrating a change following hyperoxia using the regional 99% prediction interval.....</i>	<i>135</i>
<i>Table 8-15 Healthy volunteer mixed cortical and deep grey matter regions demonstrating a change following hyperoxia using the regional 99% prediction interval</i>	<i>135</i>
<i>Table 9-1 Patient characteristics</i>	<i>144</i>
<i>Table 9-2 Impact of oxygen therapy on whole brain proton spectroscopy metabolite concentrations in healthy volunteers</i>	<i>146</i>
<i>Table 9-3 Impact of oxygen therapy on injured brain measured with whole brain proton spectroscopy in patients with severe traumatic brain injury.....</i>	<i>149</i>

Acknowledgements

Special praise must also go to my supervisors, Dr Jon Coles and Professor David Menon, whose knowledge and endless enthusiasm, intelligence and patience have guided me through these studies. Jon has always been an inspiration to me, it is only through my admiration for his research and people skills that I have been able to complete this work, and I much appreciate all that he has done for me. Finally, a special thanks must go to my children Niah and Aaron whose love and sense of fun have helped me finish this thesis.

Abstract

Cerebral ischaemia is a frequent finding in post mortem studies following traumatic brain injury (TBI), but clinical studies using ^{15}O oxygen positron emission tomography (^{15}O PET) suggest that classical ischaemia is uncommon beyond the first 24 hours after injury. Evidence of metabolic failure in the absence of classical ischaemia may represent ongoing neuronal dysfunction and progressive neuronal loss. Any therapeutic intervention that mitigates such metabolic derangements before they result in irreversible neuronal injury may improve tissue fate and improve the functional outcome for patients.

Energy failure was spatially defined, characterised, and mapped using ^{15}O and ^{18}F Fluoromisinidazole ([^{18}F] FMISO) positron emission tomography. This enabled differentiation of classical ischaemia, diffusion hypoxia, and established infarction, and provided data on the dominant local mechanism at any given time after TBI. My thesis also aimed to examine the utility of diffusion tensor imaging and whole-brain proton MR spectroscopy (WB ^1H MRS) as imaging biomarkers to investigate normobaric hyperoxia as a therapeutic option following traumatic brain injury (TBI).

Using ([^{18}F] FMISO) PET evidence of tissue hypoxia consistent with microvascular ischaemia was found across the injured brain. The impact of normobaric hyperoxia (NBH) was examined in a clinical TBI cohort using diffusion tensor imaging and WB ^1H MRS. Some evidence of benefit was found within the perilesional brain, but further studies should examine the value of a longer period of exposure to NBH and whether this has implications for functional outcome.

Publications and book chapters resulting from this work

Reviews and Book chapters – Introduction

1. Veenith T et al. Anaesthesia for MRI and PET. Current opinion in anaesthesiology Curr Opin Anaesthesiol. 2011 Aug;24(4):451-8. (Chapter 1 and 2)
1. Veenith T et al. Molecular mechanisms of traumatic brain injury: the missing link in management. World J Emerg Surg. 2009 Feb 2; 4:7 (Chapter 1)
2. Veenith T et al. Cerebral Physiology for the textbook of neuroanaesthesia and neurocritical care edited by Menon, Matta, Smith (Chapter 1)

Original articles – Methodology

1. Veenith TV et al. Comparison of intersubject variability and reproducibility of whole brain proton spectroscopy. PLoS One. 2014 Dec 17;9(12):e115304 (Chapter 4)
2. Veenith TV et al. Inter subject variability and reproducibility of diffusion tensor imaging within and between different imaging sessions. PLoS One. 2013 Jun 28;8(6):e65941 (Chapter 5)

Original articles - Results

1. Veenith TV et al. Pathophysiologic Mechanisms of Cerebral Ischemia and Diffusion Hypoxia in Traumatic Brain Injury. JAMA Neurol. 2016 May 1;73(5):542-50 (Chapter 6)
 2. Veenith TV et al. Use of diffusion tensor imaging to assess the impact of normobaric hyperoxia within at-risk pericontusional tissue after traumatic brain injury. J Cereb Blood Flow Metab. 2014 Oct;34(10):1622-7 (Chapter 7)
- Veenith TV et al. Normobaric hyperoxia does not improve derangements in diffusion tensor imaging found distant from visible contusions following acute traumatic brain injury. Sci Rep. 2017 Sep 29;7(1):12419 (Chapter 8)

List of abbreviations

ACA	Anterior cerebral artery
ASL	Arterial spin labelling
BSR	Burst suppression ratio
CBF	Cerebral blood flow
rCBF	Regional cerebral blood flow
CBV	Cerebral blood volume
CEO	Cerebral extraction of oxygen
Cho	Choline
CI	Confidence interval
CMRO ₂	Cerebral metabolic rate for oxygen
CoV	Coefficient of variation
CPP	Cerebral perfusion pressure
Cr	Creatine
CSF	Cerebrospinal fluid
CvO ₂	Cerebral venous oxygen content
CVR	Cerebrovascular resistance
CjvO ₂	Jugular venous oxygen content
CRASH	Corticosteroid randomisation after significant head Injury trial
DAI	Diffuse axonal injury
DTI	Diffusion tensor imaging
DWI	Diffusion-weighted imaging
EEG	Electroencephalogram
¹⁸ FDG	18-Fluorodeoxyglucose
FLAIR	Fluid attenuation inversion recovery
FV	Flow velocity

FOV	Field of view
GABA	γ -aminobutyric acid
GCS	Glasgow Coma Score
GOS	Glasgow Outcome Scale
^1H MRS	Proton spectroscopy
Hb	Haemoglobin
IBV	Ischaemic brain volume
ICP	Intracranial pressure
LASER	localized adiabatic selective refocusing
MRI	magnetic resonance imaging
MAP	Mean arterial pressure
MCA	Middle cerebral artery
MRI	Magnetic resonance imaging
MRS	Magnetic resonance spectroscopy
MRSI	Magnetic resonance spectroscopic imaging
MIDAS	Metabolic imaging and data analysis system
NO	Nitric oxide
N_2O	Nitrous oxide
NAA	N-acetyl aspartate
NCCU	Neurosciences Critical Care Unit
NMR	Nuclear magnetic resonance
OEF	Oxygen extraction fraction
^{15}O PET	^{15}O Oxygen positron emission tomography
PaCO_2	Arterial partial pressure of carbon dioxide
PaO_2	Arterial partial pressure of oxygen
PCA	Posterior cerebral artery
PCr	Phosphocreatine

PI	Prediction interval
PvO ₂	Cerebral venous partial pressure of oxygen
PtO ₂	Brain tissue partial pressure of oxygen
PRESS	Point resolved spectroscopy
ROI	Region of interest
RF	Radiofrequency energy
SaO ₂	Arterial oxygen saturation
SD	Standard deviation
SjO ₂	Jugular bulb oxygen saturation
SVS	Single voxel spectroscopy
STEAM	Stimulated Echo Acquisition Mode
TBI	Traumatic brain injury
TCD	Transcranial Doppler
VOI	Volume of interest
WBIC	Wolfson Brain Imaging Centre

Chapter 1 Review of the literature

Introduction

Traumatic brain injury (TBI) is a neurological disorder, with enormous impact on the nation's health. Head injury accounts for less than 1 % of all deaths; but in the age group of 15 to 24 years, it can be attributed for up to 15% of deaths.¹ Head injury caused 156,000 national health service (NHS) hospital admissions in 2015-16, requiring over 0.5 million acute hospital bed-days, and over 50,000 intensive care unit bed-days annually.² It is the leading cause of disability in people under 40, and it severely disables 150 – 200 people per million annually in the United Kingdom (UK). In North America, TBI affects 1.4 million people, at an estimated annual cost of \$56 billion.^{1,3-7}

Management of traumatic brain injury

Prevention of secondary brain damage lies at the heart of intensive care management following TBI. The common factors associated with worsening secondary brain damage following trauma are ischaemia, hypoxemia, hyper and hypocarbia and intracranial hypertension.⁸ Hypoxemia occurred in 22.4% of severe TBI patients and was significantly associated with increased morbidity and mortality.⁹ A single pre-hospital observation of hypotension (systolic blood pressure < 90 mmHg) was amongst the five most potent predictors of poor outcome after TBI and was independent of other significant predictors including age, admission motor Glasgow Coma Scale (GCS) score, intracranial diagnosis, and pupillary status.⁸

Intracranial pressure

The intracranial blood volume of approximately 200 ml is contained in the venous sinuses and pial veins, which constitute the capacitance vessels of the cerebral circulation.¹⁰ A reduction in this volume can buffer rises in the volume of other intracranial contents such as the brain and cerebrospinal fluid (CSF). When these compensatory mechanisms to control intracranial pressure (ICP) have been exhausted, even small increases in CBV can result in steep rises of ICP.¹¹ The position of the system on this curve can be expressed in terms of the pressure-volume index, which is defined as the change in intracranial volume that produces a ten-fold increase in ICP. This usually is about 26 ml, but may be markedly lower in patients with pre-existing intracranial hypertension, who are on the steep part of the intracranial pressure-volume curve. Except for oedema reduction by mannitol and hypertonic saline, the only intracranial constituent whose volume can be readily modified by physiological or pharmacological interventions is the parenchymal CBV, whose capacity is set by intrinsic vasomotor tone.¹² Although the total size of CBV is only a small part of the intracranial volume, and interventions to modify it only produce small absolute changes (typically ~ 10 ml or less), they may result in marked reductions in intracranial pressure in the presence of intracranial hypertension.¹³

Conversely, inappropriate clinical management may cause the CBV to increase. Although the absolute magnitude of such an increase in CBV may be small, it may result in steep rises in ICP in the presence of intracranial hypertension. Interventions aimed at reducing CBV in patients with intracranial hypertension such as hyperventilation may have noticeable effects on CBF and result in cerebral ischaemia. The drugs that produce different effects on CBF may have similar effects on CBV and using CBF measurement to infer the impact on CBV and ICP may result in erroneous conclusions. While normal ICP is less than 10mmHg, different authors have used threshold values from 15 - 25 mmHg as a limit beyond which treatment is initiated, although most centres treat a persistent increase in ICP > 20 mmHg.¹⁴⁻¹⁷

Cerebral perfusion pressure and control of intracranial pressure

The driving pressure in most organs is the difference between arterial and venous pressure. However, in the brain, the downstream pressure is not the jugular venous pressure, but the intracranial pressure. This is because the brain lies in a closed cavity, and when ICP is elevated, it results in the collapse of the bridging pial veins and venous sinuses, which act as Starling resistors. Consequently, the CPP is defined as the difference between mean arterial pressures (MAP) and mean ICP:

$$\text{CPP} = \text{MAP} - \text{ICP}$$

Management of patients within specialist neuro-intensive care units using protocol-driven therapy aimed at preserving CPP, and minimising elevations in ICP has resulted in improved outcome. While the Traumatic Coma Data Bank suggests that an ICP > 20 mmHg provides the most accurate predictor of outcome, there are no prospective multi-centre studies demonstrating the effectiveness of ICP monitoring. Cerebral perfusion pressure is of importance in traumatic brain injury since elevations in ICP result in reductions in CPP and cerebral ischaemia, which leads to secondary brain injury. There is strong evidence that maintenance of a CPP above 60 mmHg improves outcome in patients with head injury with rises in ICP. The effect of cerebral perfusion pressure is summarised in Figure 1-1 Interdependence of cerebral blood volume and intracranial pressure and the rationale for maintaining the cerebral perfusion pressure. Even though hypotension is harmful, there is no convincing evidence for the effectiveness of supernormal CPP.¹⁸

Acute TBI is characterised by a primary (ictus) and secondary injury phases. The aim of acute TBI management in the critical care unit is to limit the on-going insults resulting in secondary injury. Secondary brain injury is often caused by a dynamic interplay between ischaemic, metabolic, inflammatory and cytotoxic processes.^{19,20} The primary insult also results in an immediate disturbance

of the cerebral circulation, resulting in cerebral ischaemia that contributes significantly to about 90% of deaths after closed head injury.²¹

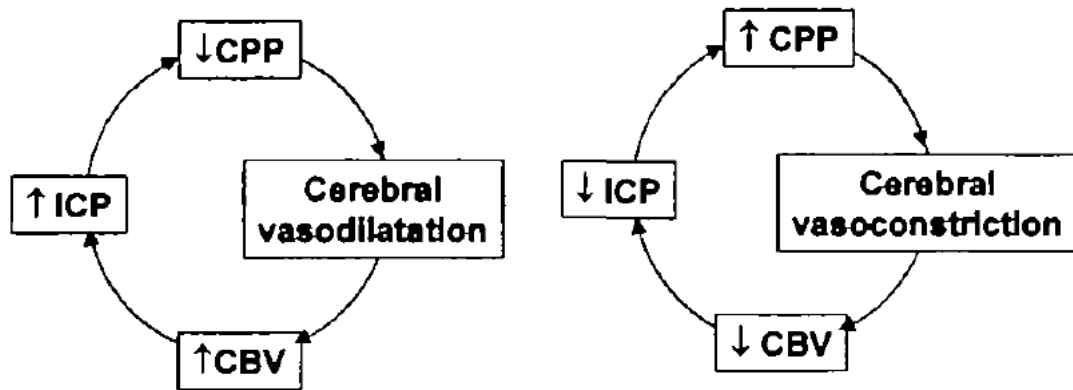


Figure 1-1 Interdependence of cerebral blood volume and intracranial pressure and the rationale for maintaining the cerebral perfusion pressure
There is a vicious cycle with an increase in the intracranial pressure; it reduces the cerebral perfusion pressure (CPP), resulting in vasodilation and an increase in cerebral blood volume (CBV), and finally a rise in intracranial pressure (ICP). (Redrawn from Menon DK et al.)

Ischaemia

Severe head injury is associated with direct and indirect effects on CBF and metabolism, which show temporal and spatial variations.²² Cerebral blood flow can be high, normal or low after ictus, but is typically reduced. Thirty percent of patients undergoing CBF studies within 6 - 8 hours of a head injury have significant cerebral ischaemia.²³⁻²⁷ Global hypoperfusion in these studies was associated with 100% mortality at 48 hours, and regional ischaemia with significant neurocognitive deficits. Initial CBF reductions are replaced, especially in patients who achieve good outcome, by a period of a relative increase in CBF, which towards the end of the first-week after ictus, may be replaced by a reduction in CBF due to arterial vasospasm associated with traumatic subarachnoid haemorrhage (Figure 1-2).¹⁰ Cerebral blood flow changes are non-uniform in the injured brain. Blood flow tends to be reduced near intracranial contusions and does not respond to augmentation of cerebral perfusion pressure.^{28,29}

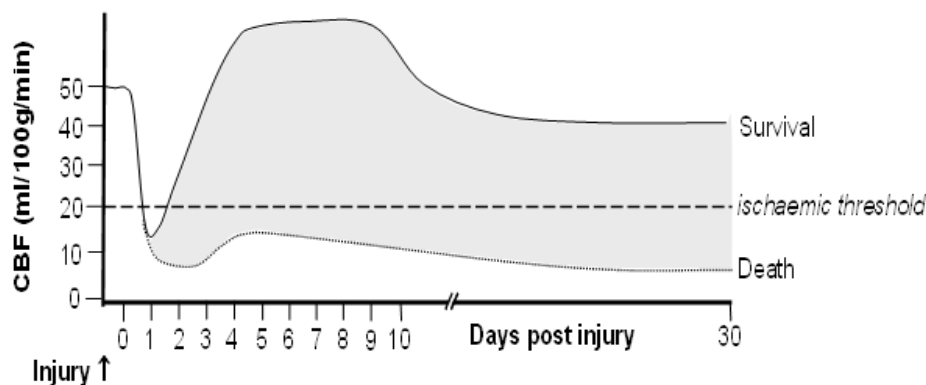


Figure 1-2 Spectrum of cerebral blood flow patterns following severe head injury

After an initial period of ischaemia lasting < 24 hours, cerebral blood flow (CBF) rises and may exceed average values on the second to fourth day. Later, CBF may fall to subnormal levels, due to vasospasm secondary to traumatic subarachnoid haemorrhage. In some patients CBF may never rise and is associated with poor outcome. [Redrawn from the textbook of neuroanaesthesia and neurointensive care edited by Menon et al.]

Ischaemic brain damage is perpetuated by factors such as hypotension, hypoxia, raised intracranial pressure, oedema, focal tissue compression, microvascular injury, and in the late phase, arterial vasospasm. Graded reductions in CBF are associated with specific electrophysiological and metabolic consequences, all of which are triggered at particular levels of CBF (Figure 1-3).¹⁰ Some of these thresholds for metabolic events are well recognised, but others, such as the development of acidosis, cessation of protein synthesis and the failure of osmotic regulation have only recently received attention.³⁰⁻³³ Ischaemia is thus a continuum between normal cellular function and cell death. Cell death is dependent on the duration of ischaemia and other circumstances that can modify the effects of tissue hypoxia. The effects of ischaemia may be ameliorated by metabolic depression produced by hypothermia or drugs and exacerbated by increased metabolic demand associated with excitatory neurotransmitter release or compounded by other mechanisms of secondary injury (such as cellular calcium overload or reperfusion injury).

CBF	Electrophysiological and metabolic consequences
> 50 ml.100g ⁻¹ .min ⁻¹	<i>Normal neuronal function</i>
?	<i>Immediate early gene activation</i>
?	<i>Cessation of protein synthesis</i>
?	<i>Cellular acidosis</i>
20-23 ml.100g ⁻¹ .min ⁻¹	<i>Reduction in electrical activity</i>
12-18 ml.100g ⁻¹ .min ⁻¹	<i>Cessation of electrical activity</i>
8-10 ml.100g ⁻¹ .min ⁻¹	<i>ATP rundown, loss of ionic homeostasis</i>
<8 ml.100g ⁻¹ .min ⁻¹	<i>Cell death (also depends on other modifiers: duration, CMR etc)</i>

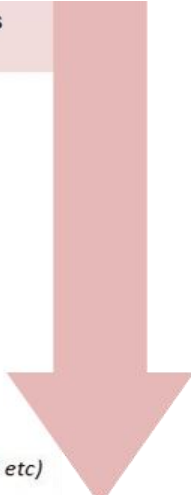


Figure 1-3 Electrophysiological and metabolic consequences of graded reductions in cerebral blood flow

There are physiological and metabolic consequences around contusions, which can be explained by a graded decrease in cerebral blood flow (CBF).

It is essential to recognise that reductions in CBF do not always equate to ischaemia; a diagnosis of ischaemia requires showing that CBF is inadequate to meet oxygen demand. For example, reductions in CBF associated with coupled reductions in the cerebral metabolic requirement of oxygen (e.g. following sedation) represent appropriate hypoperfusion.¹⁰ Increases in CBF that do not meet increased metabolic demand (e.g. with seizures in the context of intracranial hypertension) can be interpreted as hyperperfusion, but in reality, represent ischaemia (Figure 1-4).

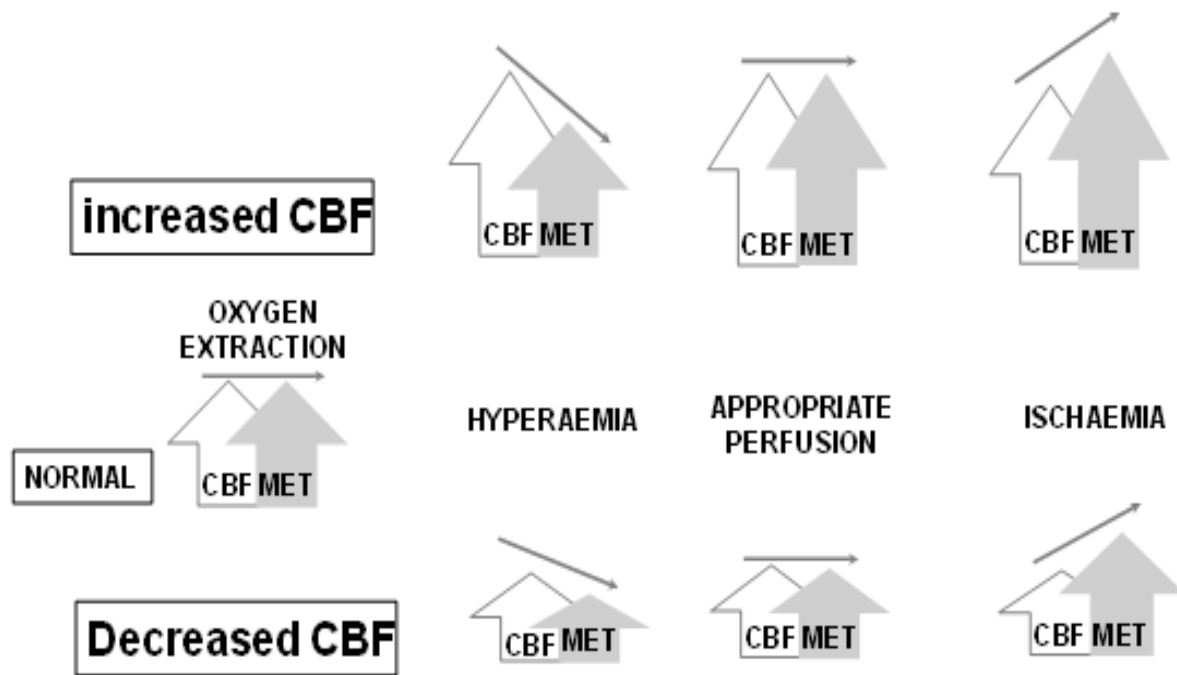


Figure 1-4 Relationship of cerebral blood flow to the presence of ischaemia under conditions of varying metabolism
 Changes in cerebral blood flow (CBF) levels may be misleading since a diagnosis of ischaemia or hyperaemia demands that CBF levels be assessed in the context of metabolic requirements (MET). (Redrawn from the textbook of neuroanaesthesia and neurointensive care edited by Menon et al.)

Excitotoxicity and Neuroinflammation

Studies with microdialysis techniques have shown that one of the most significant factors causing secondary brain injury is the excessive release of excitotoxins such as glutamate and aspartate at the time of primary brain injury. There is also a complex cascade of the cellular inflammatory response which propagates secondary brain damage.^{34,35} This inflammatory process lasts from hours to days contributing continuously to the cause of secondary brain damage.³⁶ The inflammatory response resulting from an acute TBI is not limited to the brain, and multiple organ dysfunction syndromes are commonly seen. The principal molecules in the brain involved in this cascade are growth factors, catecholamines, neurokinins, cytokines and chemokines. The Interleukins (IL) are a group of pro and anti-inflammatory cytokines, and increased levels following intracerebral haemorrhage correlate with the magnitude of perilesional oedema and mortality.³⁷⁻⁴⁰ Inflammatory cytokines facilitate neurotoxicity by encouraging excitotoxicity and the inflammatory response, but simultaneously, they

promote neurotropic mechanisms and induction of cell growth factors that are neuroprotective.⁴¹ Unfortunately, there is no convincing evidence of benefit from using these targets as a therapeutic option in TBI.^{42,43}

Second tier therapies for the management of raised intracranial pressure

In the presence of refractory intracranial hypertension 'second tier' therapies are required in addition to conventional standard treatment. These include barbiturate coma, hypothermia and surgical treatment (diversion of cerebrospinal fluid via the lumbar or ventricular drain and decompressive craniectomy). Data suggest that surgical decompression results in a reduction in ICP with an increase in the number of survivors, with some having poor neurocognitive outcomes. The management protocol for patients treated within the Neurosciences Critical Care Unit (NCCU) at Addenbrooke's Hospital,⁴⁴ Cambridge, is detailed in Figure 1-5.

Traumatic Brain Injury ICP/ CPP Algorithm

Patients with traumatic brain injury admitted to NCCU are managed according to this protocol. Each step of the protocol must be preceded by thorough check of the position and accuracy of all intracranial monitoring. Surgical referral for evacuation of significant space occupying lesions (SOL) is mandatory before escalating medical treatment. Consider EVD insertion before escalating medical treatment. All patients must have the following within 4h of admission to NCCU:

- 1) Invasive arterial (transducer at tragus) and central venous catheter
- 2) ICP monitoring
- 3) Cerebral microdialysis catheter and PbO_2 probe
- 4) ICM+

Initial target CPP of 65mmHg (CPP > 55mmHg may be acceptable). Autoregulation parameters and brain biochemistry are used to individualise targets.

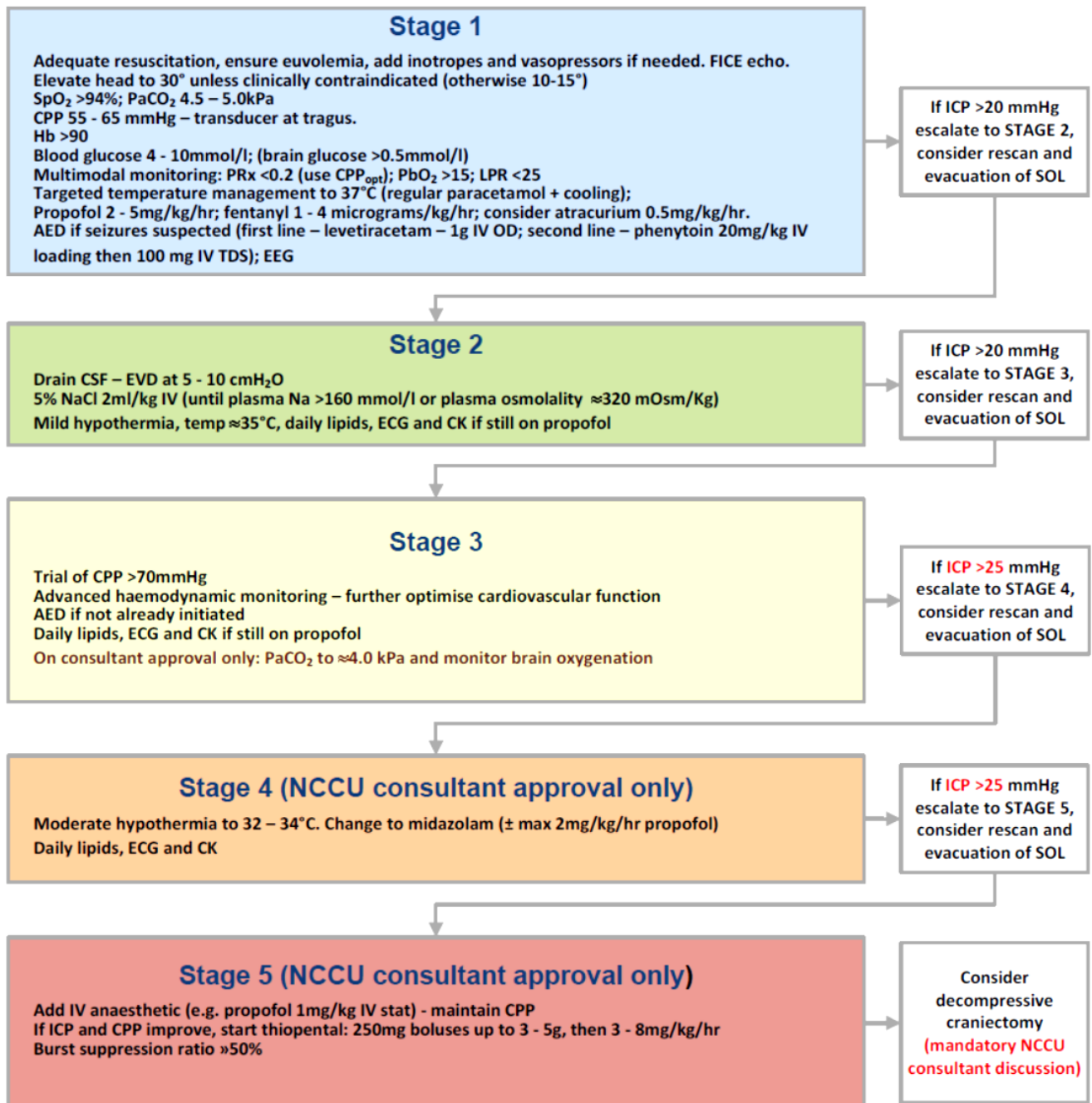


Figure 1-5 Head injury protocol in the Neurosciences Critical Care Unit, Addenbrooke's Hospital, Cambridge

(Abbreviations : Neurosciences Critical Care Unit (NCCU), Central Venous Pressure (CVP), intracranial pressure (ICP), jugular bulb venous saturation (SjVO2), Magnetic resonance imaging (MRI), cerebral perfusion pressure (CPP), space occupying lesion (SOL), Pressure reactivity index (PRI), brain tissue oxygenation (BtPO2) form licox, arterial oxygen saturation (SpO2), Proton pump inhibitors (PPI), electrocardiogram (ECG), electroencephalogram (EEG), bispectral index (BSI), creatine kinase (CK), arterial partial pressure of carbon dioxide (PaCO2), computed tomography (CT).

Long term neuronal loss – Apoptosis, Selective neuronal loss, mitochondrial and autoregulatory failure after traumatic brain injury

Apoptosis refers to the distinct morphological changes after programmed cell death, developing after the elimination of cells during development. Apoptosis is now recognised as an essential factor in secondary brain injury.⁴⁵ Cells undergoing apoptosis die without membrane rupture and therefore, elicit a reduced inflammatory response in contrast to cells undergoing necrosis. There is, therefore, a suggestion that neuronal apoptosis after TBI may be a protective response by the brain to remove injured tissue cells without affecting the healthy brain.⁴⁵ Apoptotic cells have been identified within contusions in the acute post-traumatic period, and in regions remote from the site of injury days and weeks after trauma.⁴⁶

Evidence for selective neuronal loss within normal appearing brain following head injury

The rotational acceleration-deceleration after head injury also causes shear strain and deformation resulting in diffuse axonal injury (DAI or traumatic axonal injury) typically in the deep white matter and grey-white interface.^{47,48} In experimental models and humans, the initial hyperacute neurological damage is followed by slow progressive neuronal loss lasting for years. This ongoing loss of neurons may provide the neuroanatomical substrate for neurocognitive decline following neurotrauma.⁴⁹⁻⁵¹ This selective neuronal loss (SNL) can result in cortical thinning, white matter atrophy, hippocampal volume loss, temporal lobe atrophy and increase in total ventricular volume. Experimental studies have revealed evidence of selective neuronal loss within the hippocampus, amygdala, entorhinal and piriform cortices, thalamus, hypothalamus, and perilesional cortex.⁵²⁻⁵⁸ Since conventional MRI does not pick up SNL, we need alternative techniques such as DTI and WB ¹H MRS.⁵⁹⁻⁶⁴ Understanding the mechanisms, temporal profile and extent of such neuronal injury may result in the design of novel neuroprotective agents or improved management strategies that result in a better outcome for patients.

Mitochondrial dysfunction after traumatic brain injury

Mitochondria play an essential role in the recovery after an acute TBI. It is required for the maintenance of neuronal energetics to preserve the ionic equilibrium and repair after ictus.⁶⁵ It also plays a role in the creation, clearance of free radicals (when unchecked would damage the brain) and modulation of apoptosis of vulnerable neurons resulting in selective neuronal loss.⁶⁶ In acute traumatic brain injury, the presence of hypoxia due to microvascular collapse may lead to in regions of low oxygen tension leading to nitric oxide release competitively inhibiting cytochrome oxidase thereby rendering mitochondrial respiration dependent on the level of cellular oxygen.⁶⁷ Protecting the mitochondria by hyperoxia can be a readily available neurotherapeutic option in severe

traumatic brain injury. In this thesis I will explore normobaric hyperoxia as a therapeutic option to mitigate the diffusion barrier resulting in mitochondrial failure after TBI.

Autoregulation after traumatic brain injury

Autoregulation refers to the ability of the cerebral circulation to maintain cerebral blood flow at a relatively constant level during despite changes in cerebral perfusion pressure, by altering cerebrovascular resistance. In critically ill patients with TBI, there is significant intersubject and within-subject temporal variation of cerebral autoregulation during the first 4–5 days after injury.^{68,69} Young patients who had autoregulation guided therapy after an acute traumatic brain injury had better outcomes compared to patients without.^{68,70}

Chapter 2 Generic materials and methods

This chapter describes the basic physical principles of the imaging techniques used in this thesis. This summary is not meant to represent an exhaustive review of these topics but provides a framework for the methodology used in subsequent chapters of this thesis. This discussion is organised into three major sections diffusion tensor imaging, spectroscopy and positron emission tomography with the principles of image processing described for each.

Diffusion tensor imaging

Diffusion imaging is used non-invasively to examine the microstructure and microenvironment of the brain. This modality is based on the diffusion of free water within brain tissue. These advances have been used to probe and predict the outcomes following microstructural derangements in TBI.^{59,71-74}

Physical principles of diffusion weighted imaging

Diffusion-weighted imaging (DWI) provides tissue contrast based on differences in the diffusion of water molecules within the brain.⁷⁵⁻⁸⁰ Diffusion within the brain is determined by the microarchitecture and environment of tissue in which the diffusion takes place.⁸⁰ Diffusion of water molecules within the cerebrospinal fluid (CSF) is less limited than the diffusion of molecules within the extracellular and intracellular spaces.⁸⁰ Einstein's equation governs diffusion, and the distance travelled by the molecule is given by the formula

$$r^2 = 2Dt$$

(Where " r^2 " is an average value for the square of the distance travelled and " D " is the diffusion coefficient and " t " is time)

The diffusion coefficient can be calculated by the following formula

$$D = RT / 6\pi Nvr$$

Where R is the ideal gas constant (in SI units), π is 3.14, N = Avogadro constant 6×10^{23} , T is the absolute temperature, ν is the viscosity of the solvent (0.001 for water in SI units), r is the radius of the particle or molecule. The diffusion coefficient of water at 20°C is $2.0 \times 10^{-3} \text{mm}^2/\text{s}$.

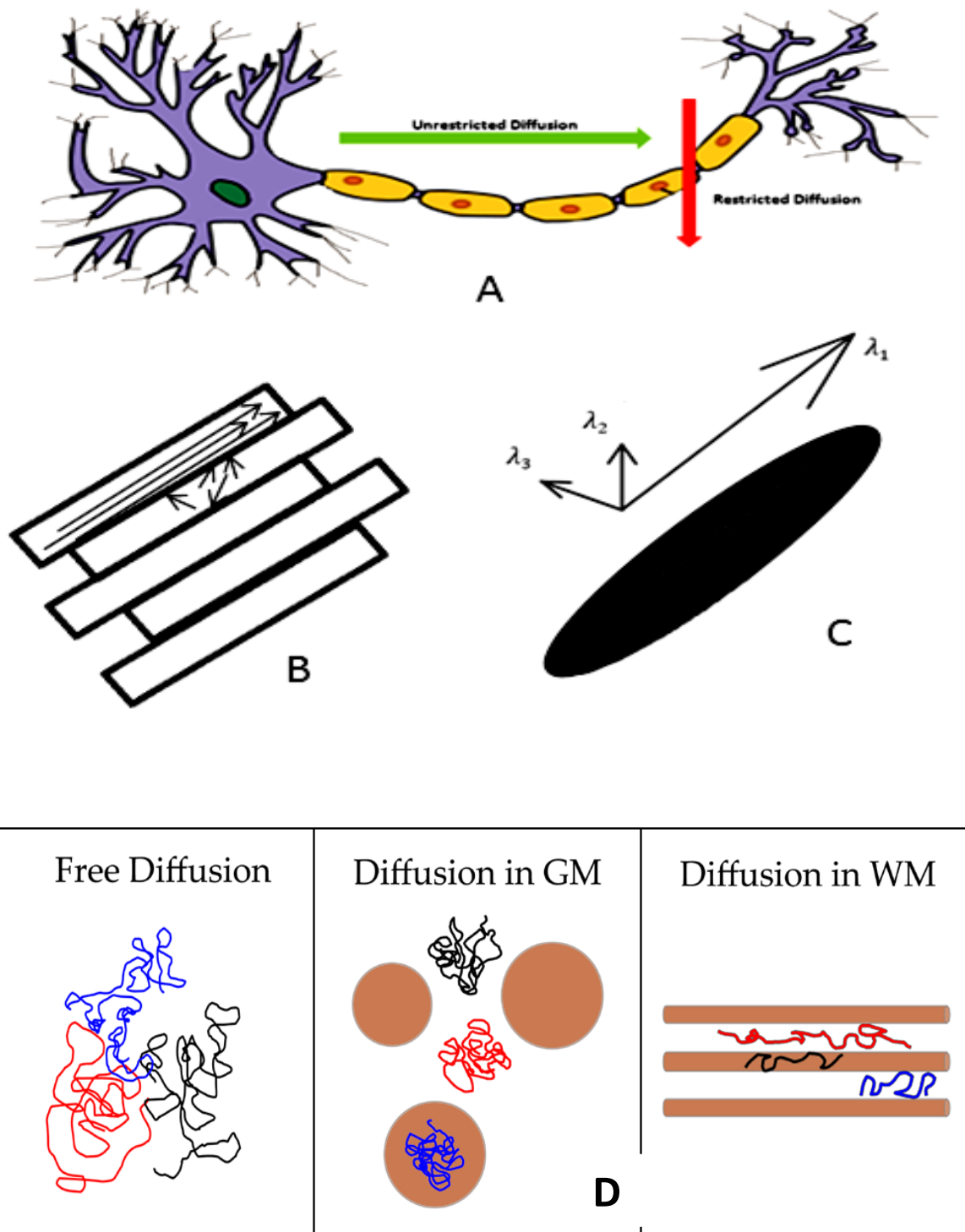


Figure 2-1 Diffusion in a neuron and white matter tracts of brain

[A] Myelinated axons within white matter restrict the diffusion of water perpendicular to their course

[B] The direction of diffusion within a block of white matter tracts is predominantly parallel to the orientation of the tract

[C] The direction of movement within a region is defined using Eigen vectors in three orthogonal axes (λ_1 represents the axial, and λ_2 and λ_3 represent the two perpendicular radial axes)

[D] Diffusion within various compartments within the brain. Diffusion is unrestricted within the cerebrospinal fluid (CSF), is isotropic within grey matter (GM) and anisotropic within white matter (WM).

Diffusion of water within the brain is not isotropic, as there are tissue membranes and barriers to diffusion (e.g. myelin sheath). This anisotropic nature caused by neuronal membranes results in preferential diffusion of water along the long axis of white matter tracts than radially in fibres (Figure 2-1). This “anisotropic” property of water diffusion could be used to probe the orientation of neurons and white tracts at a microscopic level (a measure of the functional connectivity in the brain).^{80,81} At the typical resolution of diffusion tensor imaging (DTI) (2 – 3mm) diffusion in CSF and grey matter is isotropic while the white matter has anisotropic diffusion. This information may also be helpful to define, quantify, and differentiate extra and intraneuronal swelling in acute traumatic brain injury.⁸²

Anisotropic diffusion and the biological basis of anisotropy

Basser described the anisotropic behaviour of water during image acquisition using a diffusion tensor model, which is a matrix in three directions. The diffusion tensor is obtained by acquiring multiple images, each sensitive to diffusion at a different orientation, and fitting these data to create a diffusion tensor. This tensor helps us to quantify the mean diffusivity of the water molecule and the fractional anisotropy of the tissue.

Fractional anisotropy

A variety of summary statistics have been used to compute and express the extent of anisotropy, and the mean diffusivity in tissue. Fractional anisotropy (FA) is one such metric used, and it is calculated by the following formula. If diffusion is unconstrained (i.e., isotropic), FA is close to zero. If diffusion has one primary orientation (i.e., is anisotropic), FA can approach 1.

$$FA = \sqrt{\frac{3}{2}} \sqrt{\frac{(\lambda_1 - \bar{\lambda})^2 + (\lambda_2 - \bar{\lambda})^2 + (\lambda_3 - \bar{\lambda})^2}{\lambda_1^2 + \lambda_2^2 + \lambda_3^2}}$$

Where $\bar{\lambda}$ is mean diffusivity or MD

$$\bar{\lambda} = \frac{\lambda_1 + \lambda_2 + \lambda_3}{3}$$

Following traumatic brain injury, fractional anisotropy in white matter is mostly decreased and is indicative of traumatic axonal degeneration and demyelination with resultant disruption of white matter microstructure.⁸³

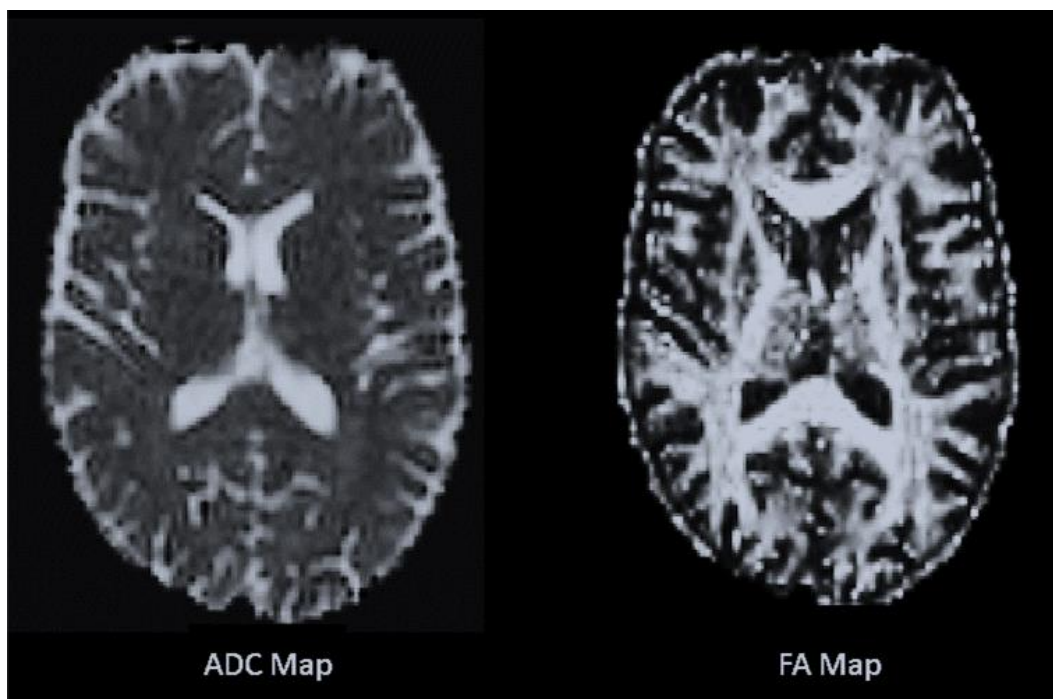


Figure 2-2 Fractional Anisotropy and Apparent Diffusion Coefficient maps in a volunteer

Fractional anisotropy (FA) maps have a value between zero and one explained by the anisotropy of underlying tissues (cerebrospinal fluid (CSF), white matter and grey matter). The apparent diffusion coefficient (ADC) map is obtained by quantifying the movement of the water molecule, note that the CSF is bright due to unrestricted water movement.

Mean diffusivity or “trace water”

The diffusivity along the principal axis or the principal diffusion vector is also called axial diffusivity. The smaller diffusivities orthogonal to the principal diffusion coefficient are averaged to produce the radial diffusivity or perpendicular diffusivity $[(\lambda_2 + \lambda_3)/2]$. A useful metric for summarising the total diffusivity of a particular tensor is mean diffusivity, which is the average of the sum of three eigenvalues.

Apparent Diffusion Coefficient

The apparent diffusion coefficient (ADC) describes the magnitude of water diffusion and produces characteristic changes in cytotoxic and vasogenic brain oedema (Figure 2-2). It is obtained by dividing the magnitude of molecular movement by overall diffusivity in each voxel calculated from all the diffusion weighted images acquired.⁸⁰ Hahn identified a reduction in signal in response to spin echo, due to the effects of diffusion, using different diffusion-sensitising factors (b values). The reduction in the signal is explained by translational diffusion, and calculations are used to generate the diffusion maps by using two different b values, b_0 and $b > 0$. A parametric image containing these data is called a diffusion map or apparent diffusion map (ADC).⁸⁰

Translating diffusion tensor imaging physics to pathophysiology in head injury and its limitations

Diffusion tensor imaging can be used to image and predict prognosis after TBI in children and adults. DTI is unique in its ability to probe tissue microstructure non-invasively following head injury and can reveal numerous abnormalities which are not visible using conventional imaging techniques. Lesions such as cytotoxic and vasogenic oedema (Figure 3-3) help to define the “at risk regions” of the brain after a TBI. Such data provide improved prediction of neurocognitive outcomes following TBI.^{73,84-89} Intersecting fibres limit the sensitivity of diffusion images as it is unable to resolve the diffusion maxima in these regions. Subject movement can cause signal dropouts and artefacts in DTI.^{80,84,89} A summary of expected changes of various DTI metrics in traumatic brain injury are given in Table 2-2.

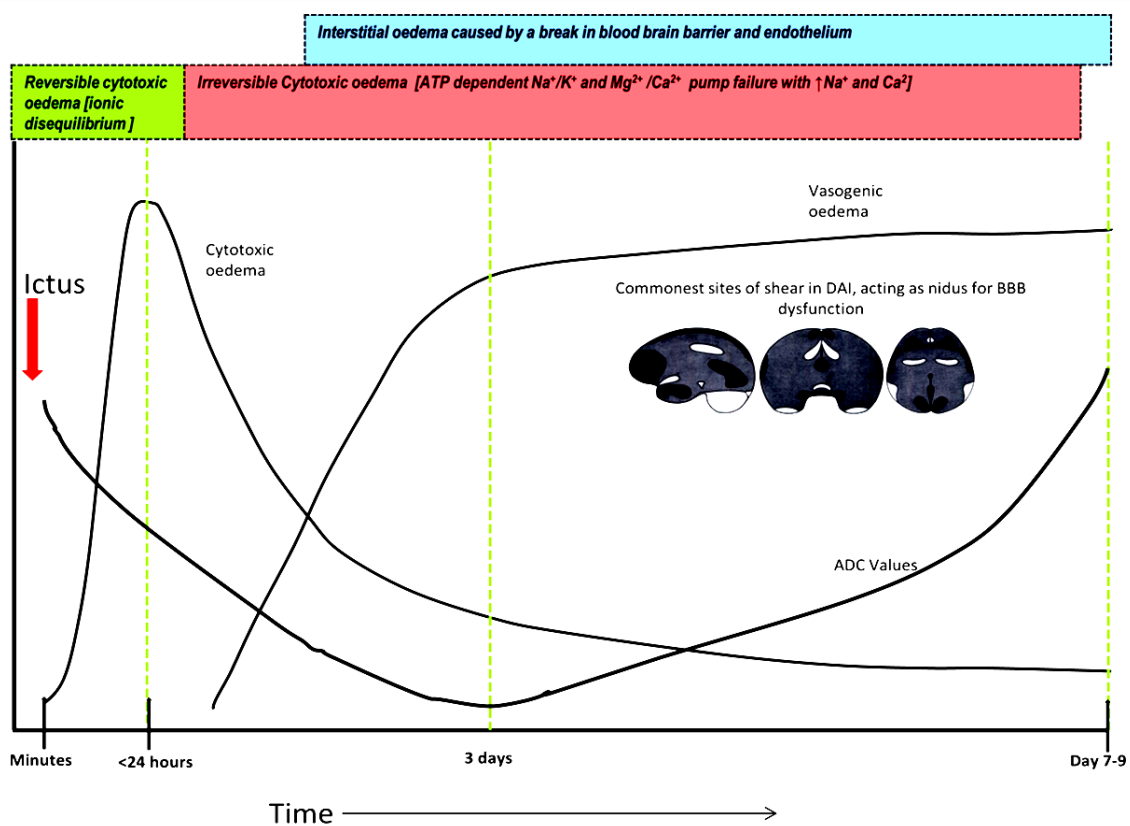


Figure 2-3 Temporal profile of cytotoxic and vasogenic oedema after traumatic brain injury

Cytotoxic oedema is a feature of early traumatic brain injury, where the at-risk region of the brain can be identified and subjected to neurotherapeutic options. Vasogenic oedema appears late after traumatic brain injury.

Magnetic resonance spectroscopy

Magnetic resonance spectroscopy (MRS) of the brain provides a quantitative readout for chemicals in vivo after traumatic brain injury (e.g. N - Acetylaspartate, glucose, lactate, choline and creatine).⁹⁰ When tissue is placed in an external magnetic field, hydrogen nuclei in the tissue resonate at their Larmor frequency. Interactions of the electronic shell of these protons with the surrounding molecules result in local alterations of the magnetic field, changing the spin frequency of the atom (chemical shift, described below).⁹¹ This shift in the resonant frequency of the spins gives information about the molecule containing the ^1H atom and is expressed as parts per million of Radiofrequency (RF) of the B_0 field. Some metabolites such as lactate (due to the presence of multiple methylene and methyl groups) generate splitting of the resonances (see spin to spin coupling below).⁹² The area under the metabolite peak is directly proportional to the number of nuclei that contribute to it and hence to the concentration of the chemical species being studied (Figure 2-4).

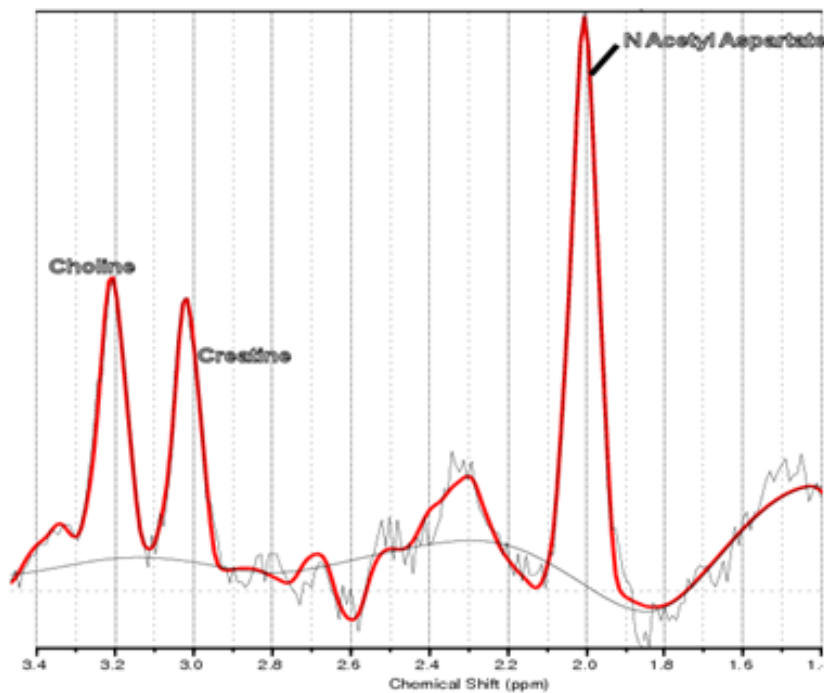


Figure 2-4 ^1H MRS Spectrum with water suppression acquired during whole brain proton spectroscopy. Note that the metabolic resonances are marked

Proton magnetic resonance spectroscopy acquisition requires an anatomical image, on which a volume of interest (VOI) can be specified for acquisition of spectral data. Different techniques may be used to acquire the spectrum (single voxel, multi-voxel and echo-planar spectroscopic imaging (EPSI)) imaging using both long and short echo times (TE). Proton magnetic resonance spectroscopy is challenging because of millimolar concentrations of metabolites, which can be overwhelmed by water (Figure 2-5), macromolecules (e.g. scalp lipids and pericontusional mobile lipids). Magnetic field

inhomogeneity induced by local tissue anatomy (e.g. paranasal sinuses) or pathology (e.g. blood) can also reduce the spectral resolution.⁹³

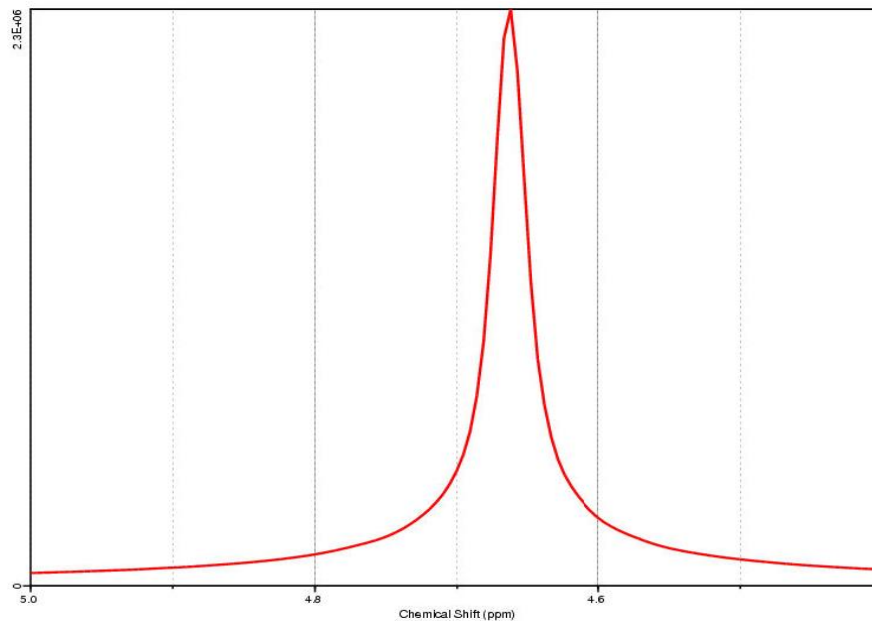


Figure 2-5 Unsuppressed water spectrum acquired during whole-brain proton spectroscopy
Note the concentration of water in unsuppressed spectra is 2.3×10^6 (Chemical shift is shown on the x-axis)

Chemical shift and signal intensity

The magnetic field surrounding a given nucleus is modified by the electron shell surrounding the nucleus, with a subtle change in the local resonant frequency, which gives rise to chemical shift.^{91,94} The chemical shift gives direct information about the nuclei, thereby aiding in the identification of compounds. The chemical shift is referenced to a spectral peak of known chemical shift, which is ideally a singlet resonance. In ^1H spectra acquired in vitro, tetramethylsilane (abbreviated as TMS, formula $\text{Si}(\text{CH}_3)_4$) is commonly used for this purpose. In the case of in vivo ^1H MRS of the brain, N acetylaspartate is used as a reference compound which has a chemical shift of 2.02ppm.

Water and fat suppression:

The high concentration of tissue water can swamp (Figure 2-5) the metabolite peaks (Figure 2-4). Water suppression is achieved by a frequency selective excitation that picks out the water resonance and then destroying the resultant XY magnetisation from water using large gradients. The spectral excitation pulse immediately follows this, when there has been no T1 recovery for the water spins, and they contribute substantially attenuated signal to the spectrum.^{95,96} A similar approach cannot be used for fat suppression since the chemical shift of fat resonances overlies the metabolites of interest,

hence spatially selective saturation pulses are used, so the fat spins contribute less to metabolic imaging.⁹⁷

Spin-spin coupling

The resonance from some molecules, such as lactate, can be split into multiplets (in the case of lactate, a doublet resonating at 1.3 ppm).^{93,95} The magnetic moment of protons in the methyl resonance of the lactate molecule interact with the neighbouring nuclei and adjacent electrons, resulting in spin-spin splitting referred to as J coupling. The J coupling evolves with echo time, resulting in variation in spectral intensity. Consequently, this should be taken into account and integer multiples of the reciprocal value should be chosen as echo times for spectroscopy experiments. As an example, for lactate, the j coupling is 6.9 Hz, and the TE should be multiple of 1/J. As a result, the lactate doublet is at maximum intensity TEs of 144ms (inverted), and 288 ms (upright).⁹⁵

Localising MRS signals

Spectroscopic data can be acquired from a single volume element (voxel), or multiple voxels simultaneously. While the acquisition of data from multiple voxels is attractive, the localisation schemes involved are complex and can result in artefacts.

Single voxel, two dimensional and three dimensional MR spectroscopic imaging (MRSI)

The volume of interest is localised using three orthogonal pulses. Single voxel spectroscopy (SVS) provides measurements limited to only a few pre-determined anatomical regions of interest.^{94,98} Two dimensional and three-dimensional imaging phase-encoding gradients to encode spatial information after the RF pulses and the gradient of slice selection. Multivoxel spectroscopy is preferred for TBI as anatomically normal areas of the brain may show significant biochemical pathology.⁹⁹ MRSI is one such imaging modality which uses multiple phase encoding steps to localise a large volume within a selected slab of tissue, thus improving the utility of spectroscopic imaging.⁹⁹ The result of 2D MRSI is a matrix, called a spectroscopy grid (placed on a structural image), for localisation. The size of this grid corresponds to the previously determined field of view (FOV). The number voxels in a grid are directly proportional to the number of phase encoding steps, and more voxels give better spatial resolution but is time-consuming.^{93,95,100-103} These techniques are not used for the experiments in my thesis as they cannot image the whole brain.

Whole brain spectroscopy using Metabolite Imaging and Data Analysis System

In the 3D sequence, multiple grids are acquired within one FOV, as implemented in the Metabolite Imaging and Data Analysis System (MIDAS) by Maudsley et al. The MRSI data are acquired by volumetric spin echo acquisition that uses two-dimensional phase encoding, echoplanar readout, frequency selective water suppression and lipid inversion nulling.^{99,104-112} The MRSI data are acquired

using volumetric spin echo [TR/TE =1710/70 milliseconds, FOV 280x280x180mm³, 100 read, 50x50 phase encoding steps, 18 slices over a 135mm slab with an acquisition time of 26 minutes. This sequence also includes lipid inversion nulling, spin echo excitation for metabolite signal and 20° flip angle gradient echo for water reference acquired in an interleaved fashion. The T1 and MRSI are acquired at an angulation of +15° to the anterior commissure-posterior commissure line to improve field inhomogeneity caused by the paranasal air sinuses.

In this thesis, I have used MIDAS acquisition system. Metabolite data were reconstructed using MIDAS and resulted in images composed of 64x64x32 voxels with an individual voxel volume of approximately 1 ml. The acquisition time for this sequence was 26 minutes. In awake volunteers, this longer acquisition time limited the number of repetitions that can be performed to quantify the within-subject, intersubject, and between session variability of spectroscopic data acquisition.

Quantitation of proton magnetic resonance spectra

In a nutshell, quantitation methods enable an analysis of individual metabolite components from the free induction decay. Approaches to spectral quantitation may deal with data in the time domain (e.g. jMRUI) or frequency domain (e.g. MIDAS). Metabolite Imaging and Data Analysis System uses a frequency domain analysis with prior knowledge.^{96,113}

Peak ratios and absolute quantification

The total area under a metabolite resonance in a ¹H MR spectrum is directly proportional to the concentration of the metabolite. Metabolite concentrations are usually expressed as ratios (relative quantification) rather than as absolute concentrations. In vivo quantification methods include either an external reference method (a vial of known concentration of metabolite is placed next to the head, and simultaneously data is acquired for both). Alternatively a water reference image, which uses unsuppressed water concentrations from the same voxel as a reference, with unsuppressed spectra obtained before or after metabolite spectra.^{99,110} The MIDAS technique uses a water reference image for quantification. A summary of expected ¹H MRS changes in traumatic brain injury are given in Table 2-2.

Absolute quantitation versus metabolic ratios in proton spectroscopy

Absolute concentration of metabolites (Table 2-1) have been used more recently in experimental studies.^{100,114} This is due to the improvement in the quantitation methods (e.g. MIDAS), and the ability to independently quantitate the concentration with a good between and within-subject variability.¹¹³ In traumatic brain injury, it is important to quantitate the absolute concentration as it gives the ability to independently assess the metabolite changes rather than the ratio of metabolite peaks. Also, following TBI, there are independent changes in creatine, choline and NAA that mean that ratios may not be an appropriate method if WB ¹H MRS is used as a biomarker.

Metabolite	GM Mean (range)	WM Mean (range)	Mixed Mean (range)
N Acetyl Aspartate	8.8 (5.2-11)	9.6 (4.5-12)	
Creatine	8.6 (6.4-9.3)	7.0 (5.5-8.9)	
Choline	1.6 (1.0-2.0)	1.8 (1.3-2.5)	
Myo-inositol	5.6 (4.1-11)	5.2 (3.1-10)	
Glutamate	9.0 (8.2-11)	6.9 (5.1-8.1)	
Lactate			1.0(0.4-1.9)

Table 2-1 Normal whole brain concentrations in millimoles of metabolites quantified by in vivo proton spectroscopy in brain
Average values of metabolites averaged from various studies. (GM – grey matter, WM white matter, Mixed– mixed grey and white matter).

	Metric	Physical principles	Pathologic associations	Pathologic Changes in traumatic brain injury
Diffusion tensor imaging	Fractional anisotropy (FA)	Quantifies degree of anisotropy of diffusion process	Reflect loss or disruption of white matter	↓ FA
	Mean diffusivity (MD)	Quantifies overall diffusion independent of fibre direction	Reflect fibre disruption and neuronal swelling	↑ MD
	Radial diffusivity (RD)	Quantifies rate of diffusion in the transverse or perpendicular directions	Reflect the integrity of Myelin sheaths	↑ RD
	Axial diffusivity (AD)	Quantifies rate of diffusion along the fibre tract main direction	Reflect axonal degeneration	↑ AD
Proton spectroscopy	N acetyl aspartate (NAA)	Observed at 2.2 parts per million (ppm)	Reflect neuronal energy metabolism, integrity and death	↓ NAA
	Creatine (Cr)	Observed at 3.0 ppm	Reflect cellular energy metabolism	↓ Cr
	Choline (Cho)	Observed at 3.2 ppm	Reflect myelin degradation and or destruction	↑ Cho

Table 2-2 Metrics used in this thesis for diffusion tensor imaging and proton spectroscopy of the brain

The physical principles of acquisition, pathological association and changes seen in acute traumatic brain injury. Fractional anisotropy (FA), Mean diffusivity (MD), Radial diffusivity (RD), Axial diffusivity (AD), N acetyl aspartate (NAA), Creatine (Cr) and Choline (Cho)

Positron emission tomography

Physical principles

Positron emission tomography (PET) is unique and is referred to as “molecular imaging”, as it uses radiolabelled isotopes to image functional, biochemical and physiological properties within tissues. The tracer compounds used are produced from the isotopes of elements such as carbon, nitrogen, oxygen and fluorine, which are rich in excess protons.¹¹⁵ Although the technique is costly and associated with additional exposure to radiation, it has unique functional capabilities which are used for early detection, characterisation, and “real-time” monitoring of disease (e.g. ischaemia in head injury).^{22,26,116,117}

¹⁵Oxygen positron emission tomography

The oxygen-15 steady-state PET technique implemented within the WBIC utilises three ¹⁵O emission scans (H_2^{15}O , $^{15}\text{O}_2$ and C^{15}O), and appropriate arterial data, to produce three-dimensional quantitative parametric images of cerebral blood flow (CBF), cerebral blood volume (CBV), cerebral metabolic requirement of oxygen (CMRO_2) and oxygen extraction fraction (OEF).^{22,26,117-123}

Oxygen-15 has a half-life of 123 seconds, and consequently, it must be produced on the same site as the PET scanner using a cyclotron. In the Wolfson brain imaging centre (WBIC), oxygen-15 is produced through the bombardment of nitrogen-14 with deuterons.¹¹⁵ As oxygen-15 has an excess of nuclear charge, it decays through b+ decay, emitting a neutrino (a very weakly interacting particle) and a positron, which is the positively charged antiparticle of the electron. The positron travels a short distance in tissue (a few millimetres for oxygen-15), losing most of its kinetic energy through collisions with electrons before it annihilates with an electron. The kinetic and rest mass energy of the electron-positron system is converted into energy in the form of two photons, each with an energy of 511keV, that travel at almost 180° to each other.^{23,115} As the photons are emitted simultaneously, incidence detection can detect the pair of photons from the same annihilation selectively; the typical timing window within which photons are paired up is 12 nsecs. If this data is acquired for all lines through the tracer distribution over a 180° range, then tomographic image reconstruction can be performed to recover the three-dimensional tracer distribution from the measured data. These detectors consist of crystals that convert gamma radiation into scintillation light; the scanner used for this work (GE Advance) has 12096 bismuth germanate crystal elements. Within each detector block (6x6 crystal array, Figure 2-6), crystals are coupled to photomultiplier tubes that convert the scintillation light into an electrical signal that can be recorded by the PET scanner.

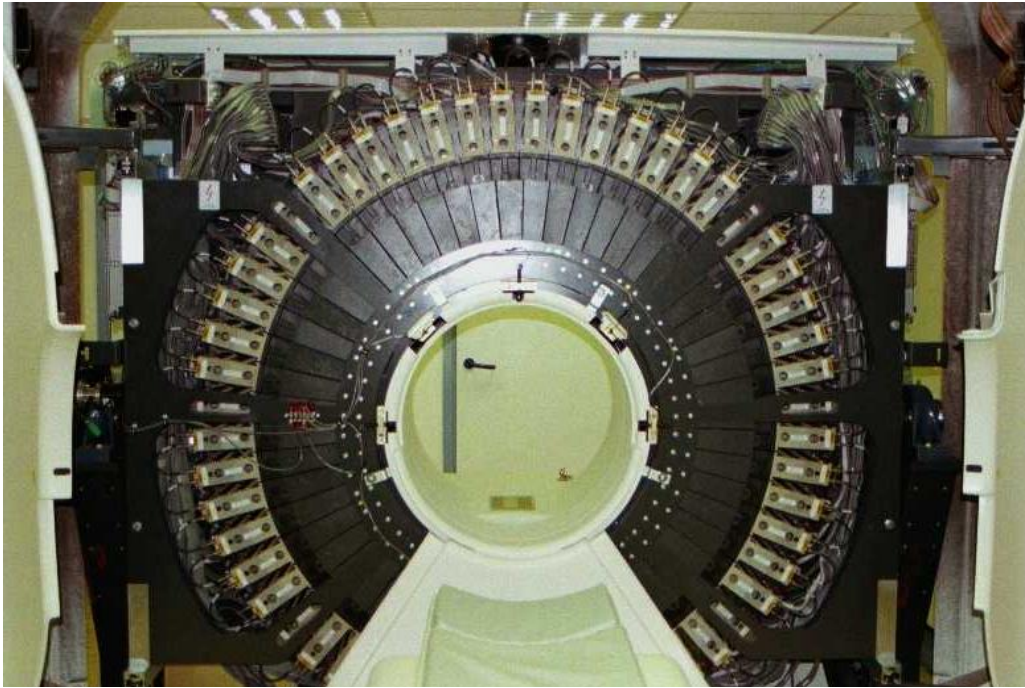


Figure 2-6 Array of detectors in positron emission tomography scanner used in this thesis
 Taken during repair of Wolfson brain imaging centre. (Adapted and redrawn from Veenith et al Current opinion in anaesthesiology)

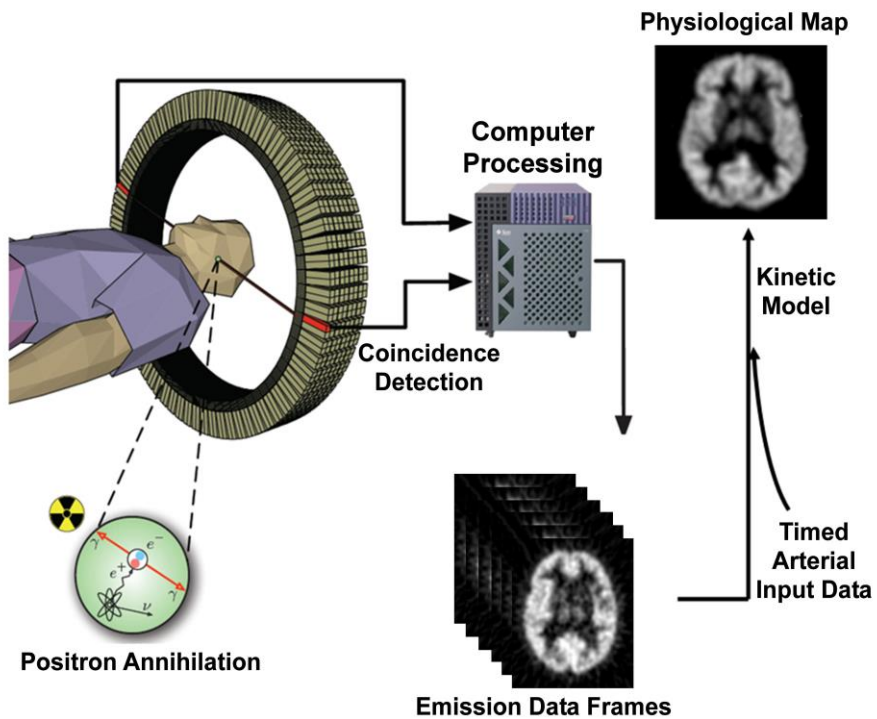


Figure 2-7 Acquisition and visualisation of the positron emission tomography image using an integrated approach
 Adapted and redrawn from veenith et al Current opinion in anaesthesiology

Steady-state model

The oxygen-15 steady-state PET technique implemented within the WBIC utilises three ^{15}O emission scans (H_2^{15}O , $^{15}\text{O}_2$ and C^{15}O), and appropriate arterial data, to produce three-dimensional quantitative parametric images of CBF, CBV, CMRO_2 and OEF (Figure 2-7). The time and spatially dependent concentration of radioactivity within the brain will be defined as C_T , and the time-dependent concentration of radioactivity within the arterial and venous blood will be defined as C_a and C_v , respectively. In the steady-state CBF technique, H_2^{15}O is administered intravenously over 10 minutes before data acquisition, during which time a state of dynamic equilibrium is reached.¹²⁴⁻¹²⁹

At this point, the continuous arrival of ^{15}O to the brain is balanced by its washout and the rate of radioactive decay. After the initial 10 minutes, and once a state of dynamic equilibrium is reached, the H_2^{15}O infusion is continued for a further 10 minutes to acquire the necessary PET emission data. At the WBIC, two five minute emission scans of the brain provide measurements of tissue radiotracer concentration (CT), and arterial radioactivity samples (C_a) are obtained at 10, 15 and 20 minutes after the start of infusion. Cerebral blood flow is calculated independently for each five-minute frame using the mathematical average of C_a [H_2^{15}O] measurements taken at 10 and 15 minutes and 15 and 20 minutes, respectively. For the measurement of CBV, labelled carbon monoxide (C^{15}O) is administered in trace amounts in the air by inhalation during a 60-second bolus. During this time the C^{15}O binds avidly to haemoglobin, in the form of carboxyhaemoglobin, and remains confined to the intravascular space. Following a minute for equilibration throughout the vascular compartment, emission data are collected over a single five-minute frame, and arterial radioactivity measurements are obtained at one and six minutes post inhalation. Regional CBV is calculated from the ratio of radioactivity in the brain to that within the peripheral blood.

Since the haematocrit is lower within the cerebral microvasculature compared to the peripheral blood, this difference must be taken into account in the final calculation of CBV. The tissue radioactivity measurement must be corrected for radioactive decay that occurs during the five-minute frame. Imaging is reconstructed in combination with data from a 60-minute blank scan acquired on the same day used to correct the emission data for photon attenuation.^{117,121-123,128,130} Images were reconstructed into $2.34 \times 2.34 \times 4.25$ mm voxels using a filtered back projection algorithm, with corrections applied for randoms, dead time, normalisation, scatter, attenuation and sensitivity. This resulted in images with isotropic resolution (6.7 mm FWHM) at the centre of the field of view. Emission images were then smoothed using an isotropic 4 mm Gaussian filter, resulting in a final spatial resolution of $\sim 7 - 8$ mm FWHM. Parametric maps of CBF, CBV, CMRO_2 and OEF were calculated by inputting simultaneous PET emission and arterial tracer activity measurements into standard models.

We used a blood-brain partition coefficient for $H_2^{15}O$ (r) of 0.95 based on previous in vitro data and a small to large vessel haematocrit ratio (r) of 0.85.

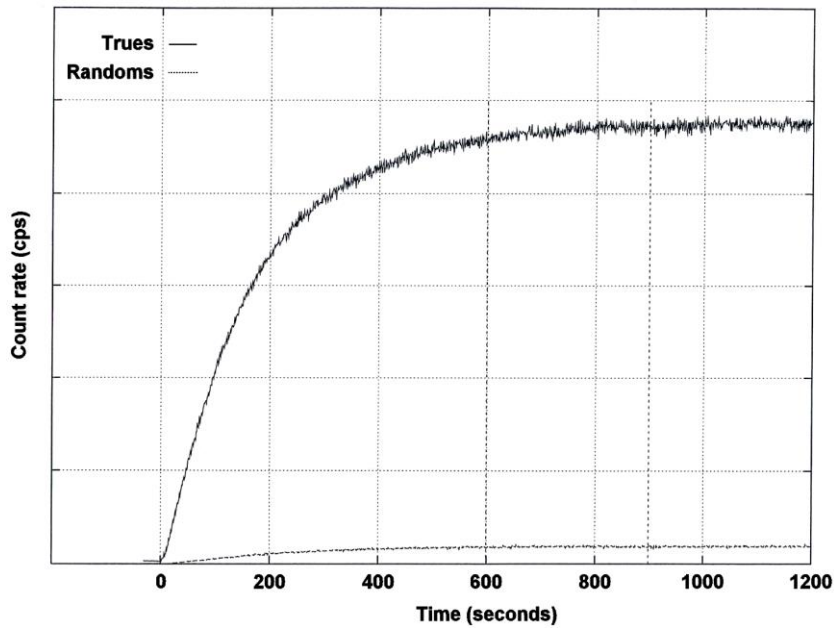


Figure 2-8 Steady-state $H_2^{15}O$ and $^{15}O_2$ used in PET studies.

Tissue radioactivity versus time curve obtained during a steady-state oxygen-15 protocol. After six hundred seconds (10 minutes) a state of dynamic equilibrium is achieved, after which two five minute emission frames (dotted lines) are obtained and arterial radioactivity measurements are obtained at 10, 15 and 20 minutes.

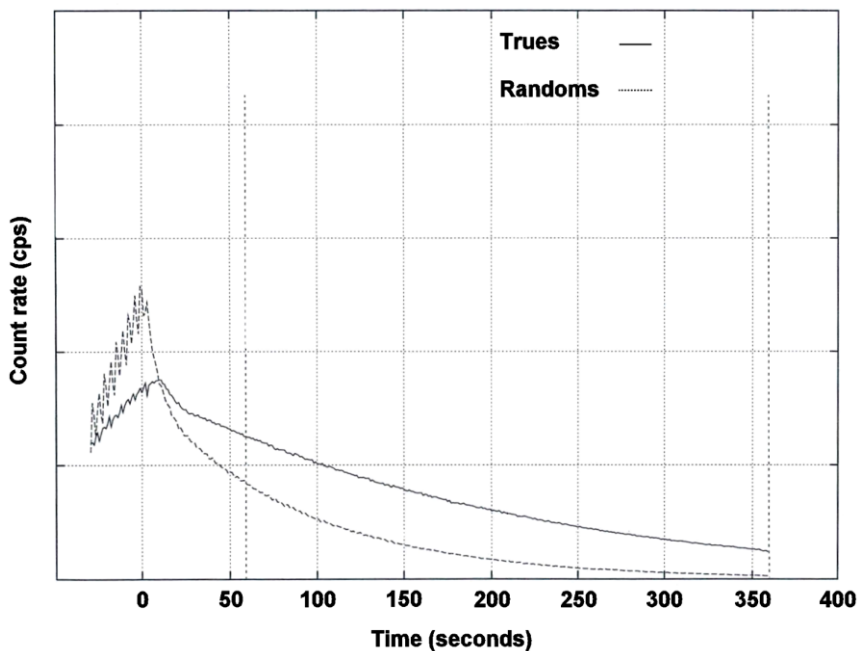


Figure 2-9 Bolus $C^{15}O$ used in PET studies

Tissue radioactivity versus time curve obtained following a sixty second bolus of $C^{15}O$. Regional CBV is calculated from the ratio of radioactivity in the brain during a single five minute frame (dotted lines), corrected for decay, to that within an arterial sample taken at the start of the emission frame.

Measurements of oxygen extraction fraction and oxygen metabolism

Measurements of OEF and $CMRO_2$ are obtained following a steady-state inhalation of $^{15}O_2$ (Figure 2-8). Trace amounts of labelled $^{15}O_2$ are inhaled in the air for 10 minutes until a state of dynamic equilibrium is achieved. As with the infusion of $H_2^{15}O$, the inhalation is continued for a further 10 minutes, during which time two five minute emission frames and arterial radioactivity measurements are obtained.

The tracer model used in the calculation of OEF and $CMRO_2$ describes the fate of the administered $^{15}O_2$. Since there are no stores of oxygen in the brain, $^{15}O_2$ extracted from the blood (approximately 40 %) is metabolised to produce $H_2^{15}O$, and subsequently washed out of the brain. The quantitative measurements of OEF and $CMRO_2$ thus require three emission scans ($H_2^{15}O$, $^{15}O_2$ and $C^{15}O$) (Figure 2-8 and Figure 2-9) in order to enable measurement of all these sources of ^{15}O activity.^{116,117,120,121,128,131} First, to obtain an expression for the OEF, one must divide the cerebral activity obtained during the $^{15}O_2$ inhalation by that obtained during the infusion of $H_2^{15}O$,

$$OEF = \frac{(C_T[H_2^{15}O]^O / C_T[H_2^{15}O]^H)(C_a[H_2^{15}O]^H / C_a[H_2^{15}O]^O) - 1}{(C_a[^{15}O]^O / C_a[H_2^{15}O]^O) - 1}$$

Finally, $CMRO_2$ can be derived from the following relationship.

$$CMRO_2 (\mu\text{mol}/100\text{ml}/\text{min}) = CBF \cdot OEF \cdot BOC$$

$$BOC = (1.34 \times Hb \times SpO_2 \times 0.01) + (0.023 \times PaO_2)$$

Where BOC is the blood oxygen content (given below) in $\mu\text{mol}/100\text{ml}$ calculated as, where Hb is haemoglobin (g/100ml), SaO_2 is the fractional oxygen saturation of arterial blood, and PaO_2 is the arterial partial pressure of oxygen (kPa).^{125,126,132-141}

^{18}F -fluoromisonidazole positron emission tomography

Tissue hypoxia can be imaged using the PET tracer ^{18}F Fluoromisonidazole ($[^{18}F]$ FMISO), which is trapped in hypoxic but viable tissue through oxygen-dependent bioreduction. This approach has been used in a variety of setting such as cancers, subarachnoid bleeds and embolic strokes to identify ischaemia and potentially salvageable brain tissue.¹⁴²⁻¹⁵⁴ This PET ligand has been used in this thesis to define the distribution and fate of hypoxic tissue in traumatic brain injury.

Positron emission tomography data using $[^{18}F]$ FMISO, are typically analysed by comparing potentially ischaemic tissue with known normal areas. The Cambridge PET imaging group have implemented kinetic tracer modelling of $[^{18}F]$ FMISO in animals, which has been extended to patients and volunteers. Also, we utilise a recently developed method (BAFPIC) for kinetic analysis of irreversible tracers, which will facilitate superior quantification of hypoxia from $[^{18}F]$ FMISO data through more robust estimation

of k_3 (trapping rate) and K_i (influx rate), especially at the voxel level compared to the nonlinear least squares (NLLS) modelling in hypoxic tissue.¹⁵⁵

[¹⁸F]FMISO injection (300 MBq) emission data were acquired in the 3D mode for 2.5 hours. Arterial plasma samples were obtained to provide the input function for kinetic analysis. Voxel-wise compartmental modelling utilised the irreversible version of bias-noise properties of the basis function method (BAFPIC a basis function approach to two tissue plasma input compartmental modelling). Hypoxia was mapped using the kinetic parameter (k_3) determined from BAFPIC, which denotes the trapping rate of [¹⁸F]FMISO in tissue.^{19,156,157}

Chapter 3 Aims and hypothesis

Evidence of ischaemic injury is common at autopsy in TBI, and ¹⁵O PET studies have shown that reduced perfusion represents true classical ischaemia, and treatments targeting this improves clinical outcome.^{29,120,158} Classical ischaemia is uncommon beyond 24 hours and does not robustly predict pan-necrosis in TBI.²⁷ Some PET studies have found abnormal energy metabolism after a TBI in the absence of classical ischaemia supporting a role for non-ischaemic pathophysiology.^{29,123,159} Understanding and reversing such non-ischaemic pathophysiologic processes may improve outcome.^{160,161} Conventional (e.g. jugular oximetry) and newer (e.g. microdialysis, brain tissue oxygen and cortical electrodes) monitoring techniques provide insights into pathophysiology.^{162,163} However, these techniques detect either global or localised abnormalities and can miss distant focal pathophysiology. Rational approaches to understanding pathophysiology predicate the need for advanced imaging using PET and MRI.^{19,23}

Post-mortem studies show widespread microvascular occlusion and perivascular oedema in TBI, associated with evidence of selective neuronal loss.¹²³ These findings may explain the relevance of antemortem ischaemia from the Cambridge group using ¹⁵O PET and brain tissue oximetry, which showed vascular to tissue gradients for oxygen tension in the injured brain.¹²³ Several recent studies have used microdialysis and brain tissue oxygen monitoring to show that increases in the fraction of inspired oxygen (FiO₂) can reduce extracellular fluid (ECF) lactate, although this may not result in an improvement in the lactate-pyruvate ratio.^{164,165} While the reversal of classical ischaemia is a theoretical mechanism for this finding; it seems more feasible that higher brain oxygen levels may overcome diffusion barriers to oxygen delivery, or compensate for mitochondrial dysfunction. Indeed, in regions of low oxygen tension, nitric oxide can competitively inhibit cytochrome oxidase and thereby render mitochondrial respiration dependent on the level of cellular oxygen.¹⁶⁶ Data also suggest that hyperoxia can improve oxygen metabolism, particularly within pericontusional and white matter regions, while a microdialysis study also found improvement in oxygen metabolism.¹⁶⁴ These studies showing an improvement in brain metabolism with hyperoxia require further confirmation.

Ex-vivo studies in clinical and experimental TBI suggest an impaired function of the mitochondria (typically < 4 hours) after injury.¹⁶⁷ Proton magnetic resonance spectroscopy (¹H MRS) provides imaging of n-acetylaspartate (NAA), a mitochondrial metabolite which is found almost exclusively in mature neurons.¹⁶⁸ Permanent reductions in NAA is suggestive of neuronal loss.¹⁶⁸ Diffusion hypoxia and mitochondrial dysfunction are potential mechanisms responsible for disorders in energy metabolism resulting in a neuronal loss that require further assessment using proton spectroscopy and PET imaging.^{29,164,166,167,169-172} Such an evaluation requires that we demonstrate a mismatch

between the distributions of classical ischaemia (characterised by reduced CBF and high oxygen extraction fraction (OEF) using ^{15}O PET) and tissue hypoxia.^{29,164,173}

Tissue pO_2 and microdialysis monitoring provide continuous but a focal sampling of brain tissue. Tissue hypoxia can be imaged across the whole brain using the PET tracer ^{18}F Fluoromisonidazole (^{18}F FMISO), which is trapped in hypoxic but viable tissue through oxygen-dependent bioreduction.¹⁷⁴⁻¹⁷⁶ This PET ligand has been used to study the distribution and fate of hypoxic tissue in ischaemic stroke, cerebral haemorrhage, and subarachnoid haemorrhage but not TBI.^{174,177} Combined ^{15}O and ^{18}F FMISO PET with ^1H MRS could be used to demonstrate whether transient reductions in NAA occur in brain regions without increased OEF or trapping of ^{18}F FMISO. Such data imply evidence of mitochondrial dysfunction rather than ischaemia (**Error! Reference source not found.**).

<i>Type of ischaemia</i>	<i>^{15}O PET</i>	<i>^1H MRS</i>	<i>^{18}F FMISO uptake</i>
Classical Ischaemia	CBF ↓ OEF ↑	NAA ↔ Lactate ↑ Creatine ↓ and ↔	↑
Microvascular Ischaemia	CBF ↓ OEF ↔	NAA ↔ Lactate ↑ Creatine ↓ and ↔	↑
Mitochondrial dysfunction	CBF ↔ OEF ↔ / ↓	NAA – Transient ↓ Lactate ↑ Creatine ↓	↔

Table 3-1 Mechanisms of energy failure following head injury

¹⁵oxygen positron emission tomography (^{15}O PET); proton magnetic resonance spectroscopy (^1H MRS); ^{18}F Fluoromisonidazole (^{18}F FMISO); cerebral blood flow (CBF), oxygen extraction fraction (OEF), n-acetylaspartate (NAA).

Aims and hypotheses

My studies have enrolled patients within a mechanistic and subsequent interventional cohort using normobaric hyperoxia as a neurotherapeutic option. Before the commencement of the interventional clinical studies, it was essential to address important methodological issues. The data from these studies provided a useful context for interpretation of the clinical datasets.

Methodological Aims

Inter-subject variability and reproducibility of Diffusion Tensor Imaging within and between different imaging sessions

These studies, which are presented in Chapter 4, aimed to provide reference data on intersubject variability and reproducibility of fractional anisotropy, apparent diffusion coefficient, radial and axial diffusivity measurements in a group of healthy volunteers. These data will inform the design of

interventional studies, where repeated measurements are conducted within the same session, and longitudinal studies, where assessments are repeated over time in several different imaging sessions.

Comparison of inter subject variability and reproducibility of whole brain proton spectroscopy

These studies, which are presented in Chapter 5, aimed to provide reference data on intersubject variability and reproducibility of commonly used metabolite ratios (Cho/Cr, NAA/Cho and NAA/Cr) and individual signal-intensity normalised metabolite concentrations (NAA, Cho and Cr) in a group of healthy volunteers using MIDAS. These data will inform the design of interventional studies, where repeated measurements are conducted within the same session and longitudinal studies where assessments are repeated over time in several different imaging sessions.

Experimental Hypotheses

Within the first patient cohort, I have described the mechanisms of energy failure seen following traumatic brain injury using ^{15}O and ^{18}F FMISO PET in comparison with MRI. The second patient cohort underwent a phase 2 evaluation of normobaric hyperoxia as a therapeutic option using DTI and whole brain (WB) ^1H MRS in the setting of acute TBI.

Hypothesis I: Tissue hypoxia can occur in the absence of conventional macrovascular ischaemia and is consistent with diffusion hypoxia resulting from microvascular ischaemia (Chapter 6)

Hypothesis II: Diffusion tensor imaging can be utilised to demonstrate the impact of normobaric hyperoxia (NH) within at-risk pericontusional tissue following traumatic brain injury (Chapter 7)

Hypothesis III: Normobaric hyperoxia will improve derangements in diffusion tensor imaging found distant from visible contusions following traumatic brain injury (Chapter 8)

Hypothesis IV: Normobaric hyperoxia will improve metabolic derangements identified by whole-brain proton spectroscopy following traumatic brain injury (Chapter 9)

Chapter 4 Inter-subject variability and reproducibility of Diffusion Tensor Imaging within and between different imaging sessions

Introduction

Diffusion tensor imaging (DTI) has been used to identify neuronal injury and predict outcome in a variety of neurological disorders such as traumatic brain injury,^{73,88,178-180} multiple sclerosis,¹⁸¹⁻¹⁸³ Alzheimer's dementia¹⁸⁴ and psychiatric disorders.^{185,186} Previous human studies using DTI have provided valuable reference data regarding typical values within different brain structures, and several groups have reported data comparing DTI measurements between subjects, between scanners in different centres, following service upgrades, and reproducibility within the same centre over time.¹⁸⁷⁻²⁰² However, there are limited data that compare intersubject variability and reproducibility of DTI measurements, or published studies that compare the reproducibility of DTI measurements obtained within the same imaging session (within session reproducibility) with that obtained during repeat imaging sessions on the same or different days (between session reproducibility) required to use DTI as an imaging biomarker.²⁰² This is of relevance for group comparisons with healthy volunteers, and longitudinal and interventional studies where DTI can be used as a non-invasive imaging biomarker of disease progression or response to therapy. The rational design and interpretation of such studies are hampered by lack of knowledge on the variability of DTI measurements in data obtained during the same scanning session compared with similar data obtained during a different session or day. In studies where consecutive measurements are performed on each subject under resting, and experimental conditions problems associated with variation between subjects due to individual differences (intersubject variability) can be limited. However, baseline DTI measurements may vary within an individual patient (intrasubject variability) and limit the ability to detect significant changes over time or following a therapeutic intervention. Where DTI is repeated after several days or weeks in different imaging sessions, the measurements may vary within an individual patient even in the absence of disease progression due to a combination of intrasubject and scanner variability.^{195,203} These studies aimed to provide reference data on intersubject variability and reproducibility of fractional anisotropy, apparent diffusion coefficient, radial and axial diffusivity measurements in a group of healthy volunteers. These data will inform the design of interventional studies, where repeated measurements are conducted within the same session, and longitudinal studies, where assessments are repeated over time in several different imaging sessions.

Materials and Methods

Ethics statement

Ethical approval was obtained from the Cambridgeshire 2 Research Ethics Committee (reference number 97/290) and written informed consent was obtained from all volunteers per the Declaration of Helsinki.

Imaging data acquisition

Twenty-six healthy volunteers without any history of neuropsychiatric disorder or substance abuse underwent imaging using a 3T Siemens Verio MRI scanner (Siemens AG, Erlangen, Germany) within the Wolfson Brain Imaging Centre (WBIC), University of Cambridge. All volunteers were right-handed (ten males and sixteen females) with mean (range) age of 34 (25 – 44) years and employed by Cambridge University Hospitals NHS Trust. Each subject was requested to attend two imaging sessions and undergo DTI twice during each session. Twenty-two volunteers attended a second imaging session within a mean (range) of 33 (3-181) days. Structural sequences included 3D T1-weighted magnetisation prepared rapid gradient echo (MPRAGE), fluid-attenuated inversion recovery (FLAIR), gradient echo and dual spin echo (proton density/T2-weighted). The DTI data were acquired using 63 non-collinear directions, $b=1000 \text{ s/mm}^2$ with one volume acquired without diffusion weighting ($b = 0$), echo time (TE) 106ms, repetition time (TR) 11700ms, 63 slices, field of view 192mm x 92mm, 2mm^3 isotropic voxels, and an acquisition time of 13:50 minutes. The two DTI sequences were interspersed within the structural sequences at different intervals within each imaging session in order to allow realistic comparison with clinical studies. In a single subject, the second DTI dataset from the baseline imaging session was not completed due to scanner malfunction, while four volunteers failed to attend the second imaging session within six months. Imaging data were checked for patient movement, and data sets degraded by motion artefact were excluded.^{59,72,178,179,204,205}

Image processing

Fractional anisotropy (FA), apparent diffusion coefficient (ADC) and axial diffusivity (AD) maps were created using the Oxford Centre for Functional MRI of the brain FSL Diffusion Toolbox, while radial (RD) diffusivity values were calculated as the mean of the second and third eigenvalues.^{206,207} To aid coregistration, the skull and extracranial soft tissue were stripped from the T1 weighted image using the Brain Extraction Tool of FSL.²⁰⁸ The diffusion weighted data were normalised using a two-step approach. First, volunteer T1 weighted images were coregistered to the Montreal Neurological Institute 152 (MNI152) template using the vtkCISG normalised mutual information algorithm.²⁰⁹ Using the $b = 0$ images, the diffusion weighted data were coregistered to the subjects own T1 weighted image obtained during the same session. The transformation matrix normalising the MPRAGE was then applied to the diffusion weighted data. Regions of interest (ROIs) from the Harvard Oxford

subcortical and MNI structural probabilistic atlases available within FSL were applied in normalised space (Figure 4-1).^{208,210} All normalised images were inspected using FSL View by a single experienced clinical investigator (TV) to confirm that data processing had completed successfully and that the ROIs were aligned and corresponded to the regions specified. The ROI template was modified by the erosion of a single voxel using `fslmaths` to improve spatial localisation and reduce the impact of coregistration, normalisation and partial volume errors. The FA, mean ADC, AD and RD values for the different ROIs were calculated using in-house software using Matlab (Mathworks, Natick, USA).

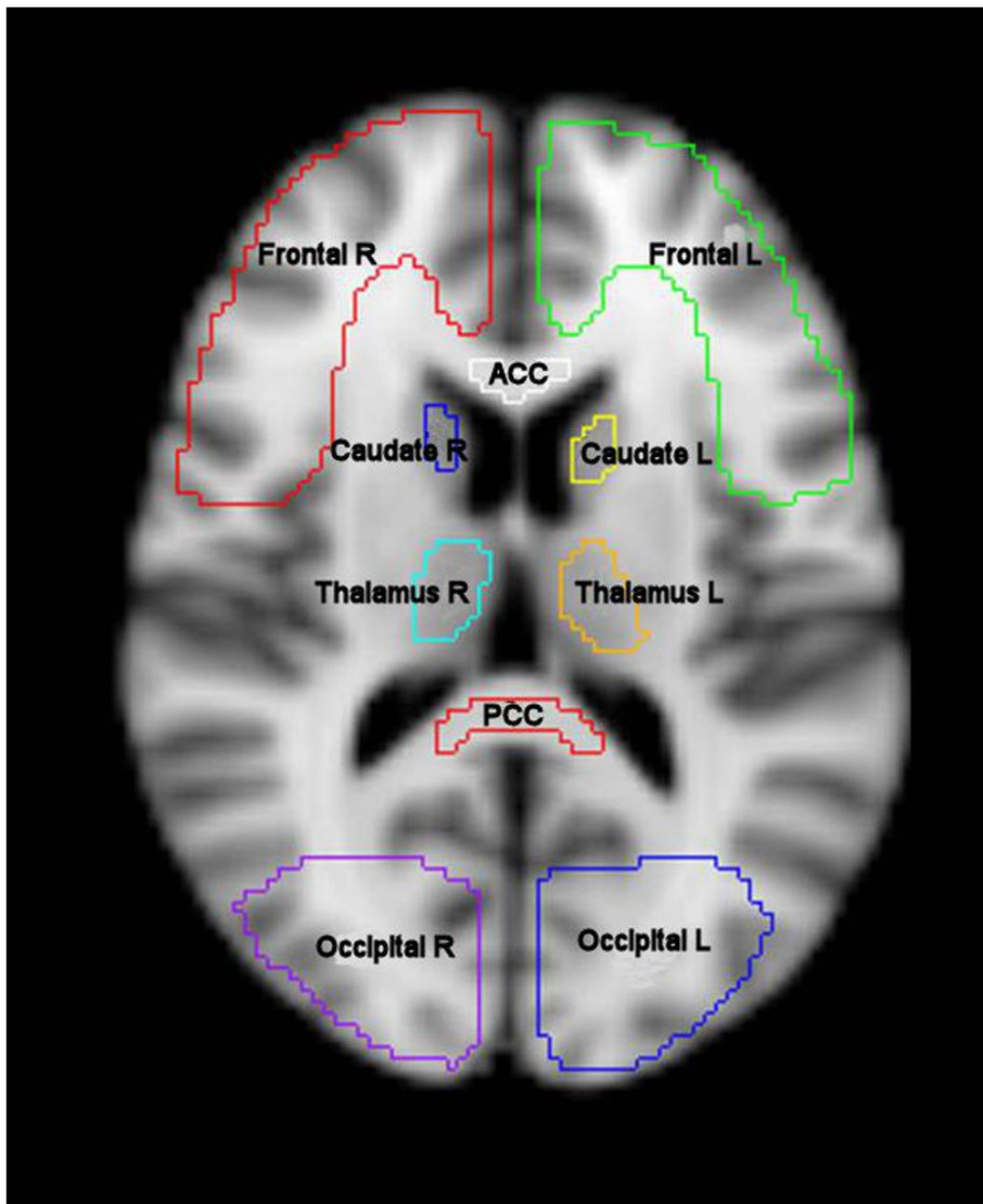


Figure 4-1 Region of interest template in MNI152 space used for intersubject, within and between session variability of diffusion tensor imaging
T1 weighted magnetic resonance image in MNI152 space (2mm resolution) showing frontal lobe left (Frontal L), frontal lobe right (Frontal R), anterior corpus callosum (ACC), caudate left (Caudate L), caudate right (Caudate R), thalamus left (Thalamus L), thalamus right (Thalamus R), posterior corpus callosum (PCC), occipital left (Occipital L) and occipital right (Occipital R). Additional regions not shown include body corpus callosum, ventral midbrain, dorsal midbrain, forceps minor, forceps major and bilateral regions covering the hippocampus, parietal lobe, temporal lobe, cerebral peduncle, pons, cerebellum, anterior thalamic radiation, superior longitudinal fasciculus, inferior longitudinal fasciculus, cingulum, uncinate fasciculus and corticospinal tract.

Analysis Strategy

The baseline data from all 26 volunteers were used to calculate the intersubject variability, while within the session and between-session reproducibility was calculated from available data. The acquisition of two sets of imaging data in each of the two imaging sessions allows the calculation of four independent sets of DTI data, which could be used to assess the reproducibility of measurements. We used the average SD for all DTI measurements obtained in 26 volunteers in both sessions to calculate the population 95% prediction interval (PI) for zero change (using two SD values). Although these average data are beneficial, the calculated SD could vary within different sessions and particular ROIs within subjects. It would, therefore, be helpful to have a more specific measure of variability within a session (within session reproducibility), and preferably for each ROI. While this is possible, the small sample numbers (two readings obtained in each of the two sessions) means that a current threshold of change higher than 2SD cannot be used to assess the statistical significance of changes in this context. While any estimate of variance based on a t distribution with two degrees of freedom must be treated with caution, the statistical theory suggests that a threshold of 4.3 SDs may provide an estimate of the 95% prediction interval for zero change. These within session measurements could, therefore, be used to assess the significance of the changes in DTI parameters following a therapeutic intervention within the same imaging session.

Statistical analysis: Statistical analyses were conducted using Statview (Version 5, 1998, SAS Institute Inc., Cary, North Carolina, USA) and SPSS[®] Statistics Version 21 (IBM[®] Corporation, New York, United States). All data are expressed and displayed as mean and standard deviation (SD) unless otherwise stated. To compare the reproducibility of DTI measurements, the SD and coefficient of variation (CoV) ($\text{CoV} = \text{SD}/\text{mean}$) of measurements were calculated within each ROI. Data were compared using paired t-tests, factorial analysis of variance (ANOVA) and intraclass correlation (ICC) as appropriate. Using ANOVA, the residual standard deviation was used to calculate the 95% prediction interval for zero change of repeat DTI studies. All p values are quoted after Bonferroni corrections for multiple comparisons (where appropriate).

Results

Intersubject variability of diffusion tensor imaging metrics

The intersubject variability of DTI measurements (Figure 4-2) is displayed in Table 4-1A for the predominantly white matter and Table 4-1B for mixed cortical and deep grey matter regions. The intersubject variability was high for all the calculated parameters with a mean (range) CoV across the ROIs for FA of 7.9 (3.3 – 31.7%) and 6.8 (3.3 – 19.2%), ADC of 7.3 (2.4 – 33.7%) and 7.1 (1.8 – 30.9%), AD of 4.5 (1.5 – 15.0%) and 6.0 (1.9 – 27.4%) and RD of 12.4 (3.6 – 63.2%) and 8.1 (2.6 – 33.3%) for the white matter and mixed cortical and deep grey matter regions respectively.

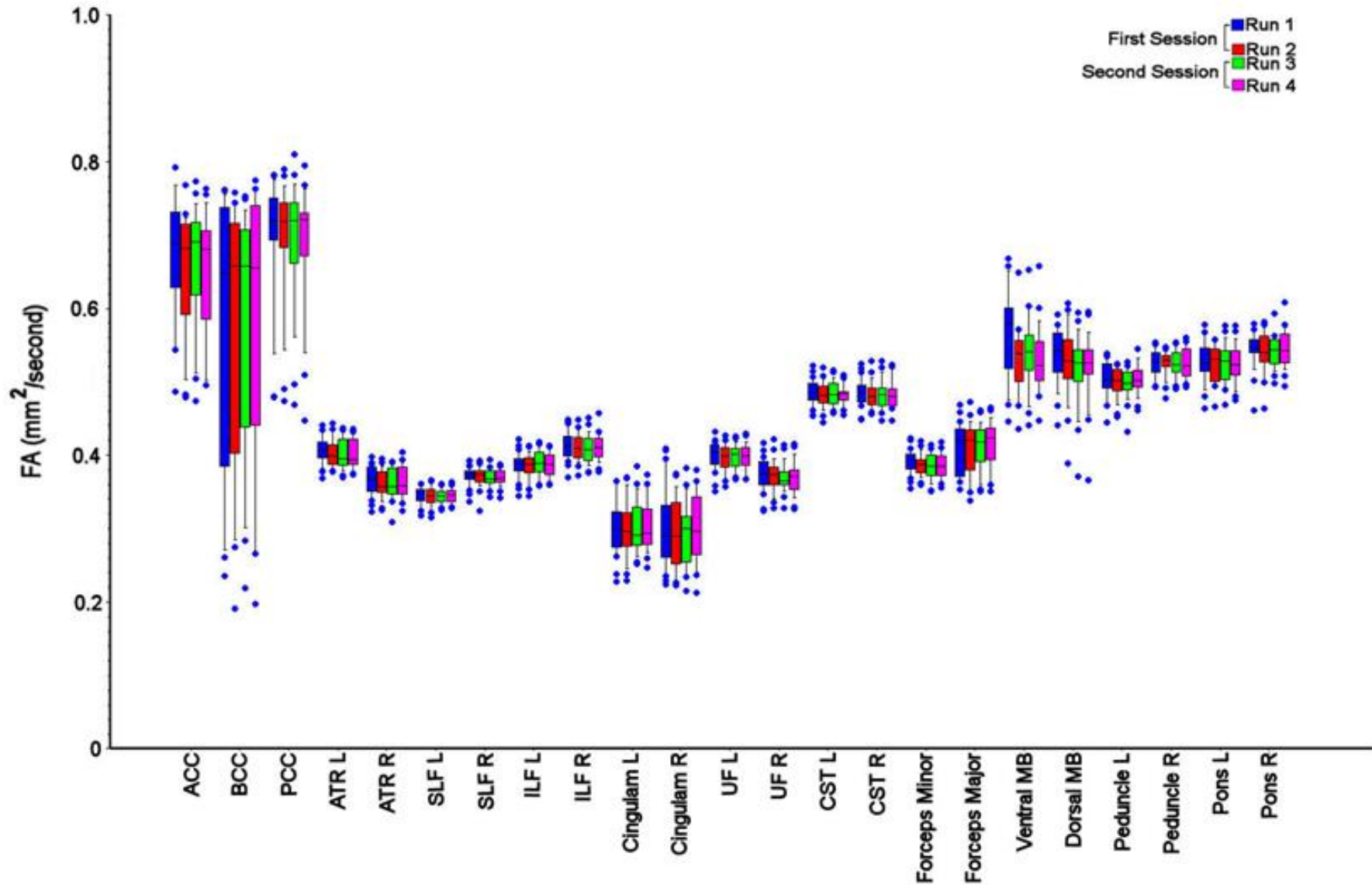


Figure 4-2 Variability in fractional anisotropy measurements

Box and whisker plot for fractional anisotropy values ($\text{mm}^2/\text{second}$) for the white matter region of interest (ROI) measurements. The spread of data within each ROI reflects inter subject variation, while the difference between runs 1 – 2 and 3 – 4 reflects within session reproducibility, and the change from first to second sessions reflects between session reproducibility. The central lines in each box denote median values, the lower and upper boundaries the 25th and 75th centile, the error bars the 10th and 90th centile, and the closed circles outlying data points. Anterior corpus callosum (ACC), body corpus callosum (BCC), posterior corpus callosum (PCC), left anterior thalamic radiation (ATR L), right anterior thalamic radiation (ATR R), left superior longitudinal fasciculus (SLF L), right superior longitudinal fasciculus (SLF R), left inferior longitudinal fasciculus (ILF L), right inferior longitudinal fasciculus (ILF R), left cingulum (Cingulum L), right cingulum (Cingulum R), left uncinate fasciculus (UFL), right uncinate fasciculus (UFR), left corticospinal tract (CST L), right corticospinal tract (CST R), dorsal midbrain (dorsal MB), ventral midbrain (ventral midbrain), left cerebral peduncle (CP L), right cerebral peduncle (CP R), left pons (pons L) and right pons (pons R).

Region of Interest (ROI)	FA (mm ² /second)			ADC (mm ² /second)			Axial diffusivity (mm ² /second)			Radial diffusivity (mm ² /second)		
	Mean	SD	CoV (%)	Mean	SD	CoV (%)	Mean	SD	CoV (%)	Mean	SD	CoV (%)
Ant corpus callosum	0.667162	0.079716	11.9	0.000828	0.000052	6.2	0.001604	0.000071	4.4	0.000440	0.000092	20.9
Body corpus callosum	0.564869	0.179244	31.7	0.000997	0.000187	18.7	0.001678	0.000091	5.4	0.000657	0.000286	43.5
Post corpus callosum	0.695110	0.101172	14.6	0.000993	0.000335	33.7	0.001812	0.000271	15.0	0.000584	0.000369	63.2
Ant thalamic radiation left	0.407562	0.019832	4.9	0.000833	0.000037	4.5	0.001198	0.000031	2.6	0.000652	0.000042	6.4
Ant thalamic radiation right	0.366557	0.019831	5.4	0.000936	0.000046	5.0	0.001274	0.000036	2.9	0.000768	0.000052	6.7
Sup longitudinal fasciculus left	0.345421	0.012185	3.5	0.000845	0.000027	3.2	0.001135	0.000027	2.4	0.000699	0.000029	4.1
Sup longitudinal fasciculus right	0.371603	0.012607	3.4	0.000828	0.000023	2.7	0.001146	0.000023	2.0	0.000669	0.000024	3.6
Inf longitudinal fasciculus left	0.387245	0.017434	4.5	0.000817	0.000020	2.4	0.001171	0.000018	1.5	0.000641	0.000026	4.0
Inf longitudinal fasciculus right	0.413091	0.019417	4.7	0.000860	0.000029	3.4	0.001258	0.000033	2.6	0.000660	0.000034	5.2
Cingulum left	0.301153	0.035238	11.7	0.000900	0.000051	5.6	0.001184	0.000049	4.1	0.000762	0.000058	7.6
Cingulum right	0.300470	0.051387	17.1	0.001013	0.000098	9.7	0.001311	0.000086	6.5	0.000861	0.000113	13.1
Uncinate fasciculus left	0.399732	0.018942	4.7	0.000816	0.000021	2.6	0.001177	0.000027	2.3	0.000636	0.000024	3.8
Uncinate fasciculus right	0.373047	0.022351	6.0	0.000915	0.000051	5.5	0.001273	0.000046	3.6	0.000736	0.000057	7.7
Corticospinal tract left	0.485927	0.016789	3.5	0.000838	0.000036	4.3	0.001275	0.000034	2.7	0.000621	0.000037	6.0
Corticospinal tract right	0.485927	0.018213	3.7	0.000819	0.000034	4.2	0.001256	0.000030	2.4	0.000603	0.000035	5.9
Forceps Minor	0.391980	0.015603	4.0	0.000895	0.000032	3.6	0.001269	0.000038	3.0	0.000706	0.000035	5.0
Forceps Major	0.410602	0.033072	8.1	0.000934	0.000077	8.2	0.001354	0.000082	6.0	0.000724	0.000082	11.3
Ventral Midbrain	0.575076	0.065234	11.3	0.000806	0.000102	12.6	0.001405	0.000147	10.4	0.000506	0.000089	17.5
Dorsal Midbrain	0.535710	0.037926	7.1	0.000778	0.000044	5.6	0.001262	0.000070	5.5	0.000536	0.000047	8.7
Cerebral peduncle left	0.504359	0.023937	4.7	0.000701	0.000027	3.9	0.001136	0.000041	3.6	0.000483	0.000027	5.6
Cerebral peduncle right	0.527349	0.017429	3.3	0.000683	0.000023	3.4	0.001132	0.000030	2.6	0.000459	0.000026	5.6
Pons left	0.528268	0.030525	5.8	0.000816	0.000091	11.2	0.001308	0.000094	7.2	0.000570	0.000092	16.2
Pons right	0.545961	0.027195	5.0	0.000792	0.000065	8.3	0.001300	0.000062	4.8	0.000537	0.000071	13.2
Mean	0.460182	0.038056	7.9	0.000854	0.000066	7.3	0.001301	0.000062	4.5	0.000631	0.000076	12.4

A

Region of Interest (ROI)	FA (mm ² /second)			ADC (mm ² /second)			Axial diffusivity (mm ² /second)			Radial diffusivity (mm ² /second)		
	Mean	SD	CoV (%)	Mean	SD	CoV (%)	Mean	SD	CoV (%)	Mean	SD	CoV (%)
Caudate left	0.245963	0.047207	19.2	0.001230	0.000379	30.9	0.001473	0.000403	27.4	0.001108	0.000369	33.3
Caudate right	0.293710	0.041241	14.0	0.000770	0.000106	13.8	0.000999	0.000116	11.6	0.000655	0.000106	16.2
Thalamus left	0.344843	0.016470	4.8	0.000781	0.000023	2.9	0.001054	0.000024	2.3	0.000645	0.000026	4.0
Thalamus right	0.352215	0.017537	5.0	0.000756	0.000013	1.8	0.001029	0.000020	1.9	0.000619	0.000016	2.6
Hippocampus left	0.284409	0.017636	6.2	0.001030	0.000061	5.9	0.001314	0.000059	4.5	0.000887	0.000063	7.2
Hippocampus right	0.291187	0.016893	5.8	0.001113	0.000073	6.6	0.001421	0.000073	5.2	0.000959	0.000075	7.8
Frontal lobe left	0.248031	0.010789	4.4	0.001015	0.000046	4.5	0.001234	0.000049	4.0	0.000905	0.000045	5.0
Frontal lobe right	0.241779	0.008078	3.3	0.001038	0.000048	4.6	0.001255	0.000049	3.9	0.000930	0.000048	5.2
Parietal lobe left	0.261730	0.010499	4.0	0.001016	0.000055	5.4	0.001250	0.000055	4.4	0.000899	0.000055	6.2
Parietal lobe right	0.260676	0.009041	3.5	0.001038	0.000051	4.9	0.001271	0.000051	4.0	0.000921	0.000051	5.5
Occipital lobe left	0.247951	0.014531	5.9	0.000952	0.000049	5.2	0.001171	0.000051	4.3	0.000842	0.000049	5.8
Occipital lobe right	0.240892	0.010980	4.6	0.000996	0.000053	5.3	0.001213	0.000054	4.5	0.000887	0.000052	5.9
Temporal lobe left	0.249815	0.017455	7.0	0.000903	0.000040	4.5	0.001127	0.000047	4.2	0.000791	0.000038	4.9
Temporal lobe right	0.257036	0.013190	5.1	0.000963	0.000027	2.8	0.001199	0.000026	2.2	0.000845	0.000028	3.4
Cerebellum left	0.234565	0.020717	8.8	0.000839	0.000063	7.5	0.001038	0.000069	6.6	0.000739	0.000060	8.2
Cerebellum right	0.230964	0.018121	7.8	0.000834	0.000058	7.0	0.001029	0.000057	5.5	0.000737	0.000060	8.1
Mean	0.267860	0.018149	6.8	0.000955	0.000072	7.1	0.001192	0.000075	6.0	0.000836	0.000071	8.1

B

Table 4-1A and 1B Intersubject variability for diffusion tensor imaging measurements

Intersubject variability for Fractional anisotropy (FA), apparent diffusion coefficient (ADC), axial and radial diffusivity. Data displayed were obtained in 26 subjects and show mean, standard deviation (SD) and coefficient of variation (CoV) for predominantly white matter (A) and mixed cortical and deep grey matter (B) regions of interest (ROI).

Within-session and between-session reproducibility of diffusion tensor imaging

The ROI data for within and between sessions reproducibility were variable across the different brain regions but lower than the values for intersubject variability (Table 4-2A, Table 4-2B, Table 4-2C and Table 4-2D). The within-session reproducibility measurements were significantly lower than between session reproducibility measurements for all the DTI parameters ($p < 0.001$, paired 't' test with Bonferroni correction). As an example, the difference between intersubject variability, within and between session reproducibility is displayed for FA in figure 4-2.

The mean (range) ROI ICC for within session measurements were for FA 0.79 (0.46 – 0.99) and 0.81 (0.57 – 0.93), ADC 0.91 (0.73 – 0.99) and 0.92 (0.74 – 0.98), AD 0.82 (0.59 – 0.98) and 0.89 (0.68 – 0.98), and for RD 0.89 (0.76 – 0.99) and 0.91 (0.59 – 0.99) for the white matter and mixed cortical and deep grey matter regions respectively. The between session measurements were for FA 0.78 (0.56 – 0.98) and 0.69 (0.42 – 0.93), ADC 0.79 (0.17 – 0.99) and 0.78 (0.40 – 0.98), AD 0.74 (0.47 – 0.98) and 0.68 (0.19 – 0.98), and for RD 0.82 (0.46 – 0.99) and 0.79 (0.48 – 0.99) for the white matter and mixed cortical and deep grey matter regions respectively.

	FA		ADC		AD		RD	
	Within session reproducibility	Between session reproducibility						
Ant corpus callosum	$2.0 \times 10^{-2} \pm 1.6 \times 10^{-2}$	$1.9 \times 10^{-2} \pm 1.7 \times 10^{-2}$	$1.2 \times 10^{-5} \pm 1.1 \times 10^{-5}$	$1.5 \times 10^{-5} \pm 1.2 \times 10^{-5}$	$2.2 \times 10^{-5} \pm 2.0 \times 10^{-5}$	$2.5 \times 10^{-5} \pm 2.1 \times 10^{-5}$	$1.9 \times 10^{-5} \pm 1.9 \times 10^{-5}$	$2.3 \times 10^{-5} \pm 2.3 \times 10^{-5}$
Body corpus callosum	$1.7 \times 10^{-2} \pm 1.5 \times 10^{-2}$	$1.8 \times 10^{-2} \pm 1.8 \times 10^{-2}$	$2.3 \times 10^{-5} \pm 2.2 \times 10^{-5}$	$3.2 \times 10^{-5} \pm 2.8 \times 10^{-5}$	$2.6 \times 10^{-5} \pm 2.8 \times 10^{-5}$	$3.5 \times 10^{-5} \pm 2.5 \times 10^{-5}$	$2.4 \times 10^{-5} \pm 2.4 \times 10^{-5}$	$3.3 \times 10^{-5} \pm 3.5 \times 10^{-5}$
Post corpus callosum	$1.0 \times 10^{-2} \pm 1.5 \times 10^{-2}$	$1.0 \times 10^{-2} \pm 8.2 \times 10^{-3}$	$2.2 \times 10^{-5} \pm 3.7 \times 10^{-5}$	$2.3 \times 10^{-5} \pm 2.4 \times 10^{-5}$	$2.1 \times 10^{-5} \pm 2.8 \times 10^{-5}$	$2.3 \times 10^{-5} \pm 2.0 \times 10^{-5}$	$2.2 \times 10^{-5} \pm 4.1 \times 10^{-5}$	$2.2 \times 10^{-5} \pm 2.9 \times 10^{-5}$
Ant thalamic radiation left	$3.6 \times 10^{-3} \pm 5.1 \times 10^{-3}$	$4.6 \times 10^{-3} \pm 4.6 \times 10^{-3}$	$6.4 \times 10^{-6} \pm 1.0 \times 10^{-5}$	$9.7 \times 10^{-6} \pm 9.9 \times 10^{-6}$	$7.4 \times 10^{-6} \pm 8.1 \times 10^{-6}$	$1.1 \times 10^{-5} \pm 9.2 \times 10^{-6}$	$6.5 \times 10^{-6} \pm 1.2 \times 10^{-5}$	$9.6 \times 10^{-6} \pm 1.1 \times 10^{-5}$
Ant thalamic radiation right	$4.5 \times 10^{-3} \pm 6.0 \times 10^{-3}$	$5.3 \times 10^{-3} \pm 4.9 \times 10^{-3}$	$8.7 \times 10^{-6} \pm 1.7 \times 10^{-5}$	$1.1 \times 10^{-5} \pm 1.4 \times 10^{-5}$	$8.8 \times 10^{-6} \pm 1.5 \times 10^{-5}$	$1.3 \times 10^{-5} \pm 1.2 \times 10^{-5}$	$9.5 \times 10^{-6} \pm 1.9 \times 10^{-5}$	$1.2 \times 10^{-5} \pm 1.5 \times 10^{-5}$
Sup longitudinal fasciculus left	$4.9 \times 10^{-3} \pm 1.9 \times 10^{-2}$	$4.4 \times 10^{-3} \pm 1.4 \times 10^{-2}$	$5.6 \times 10^{-6} \pm 2.2 \times 10^{-5}$	$8.2 \times 10^{-6} \pm 1.7 \times 10^{-5}$	$9.1 \times 10^{-6} \pm 3.8 \times 10^{-5}$	$1.2 \times 10^{-5} \pm 3.0 \times 10^{-5}$	$4.2 \times 10^{-6} \pm 1.4 \times 10^{-5}$	$6.7 \times 10^{-6} \pm 1.2 \times 10^{-5}$
Sup longitudinal fasciculus right	$5.4 \times 10^{-3} \pm 1.9 \times 10^{-2}$	$5.9 \times 10^{-3} \pm 1.4 \times 10^{-2}$	$3.3 \times 10^{-6} \pm 1.0 \times 10^{-5}$	$7.7 \times 10^{-6} \pm 1.0 \times 10^{-5}$	$6.6 \times 10^{-6} \pm 2.6 \times 10^{-5}$	$1.3 \times 10^{-5} \pm 2.2 \times 10^{-5}$	$2.5 \times 10^{-6} \pm 3.2 \times 10^{-6}$	$6.0 \times 10^{-6} \pm 5.6 \times 10^{-6}$
Inf longitudinal fasciculus left	$5.1 \times 10^{-3} \pm 1.7 \times 10^{-2}$	$4.9 \times 10^{-3} \pm 1.2 \times 10^{-2}$	$3.1 \times 10^{-6} \pm 2.7 \times 10^{-6}$	$6.1 \times 10^{-6} \pm 5.3 \times 10^{-6}$	$5.7 \times 10^{-6} \pm 1.6 \times 10^{-5}$	$7.9 \times 10^{-6} \pm 1.4 \times 10^{-5}$	$4.7 \times 10^{-6} \pm 9.9 \times 10^{-6}$	$7.3 \times 10^{-6} \pm 8.0 \times 10^{-6}$
Inf longitudinal fasciculus right	$5.2 \times 10^{-3} \pm 1.3 \times 10^{-2}$	$5.1 \times 10^{-3} \pm 9.6 \times 10^{-3}$	$4.3 \times 10^{-6} \pm 5.5 \times 10^{-6}$	$7.9 \times 10^{-6} \pm 6.4 \times 10^{-6}$	$7.0 \times 10^{-6} \pm 1.6 \times 10^{-5}$	$9.5 \times 10^{-6} \pm 1.3 \times 10^{-5}$	$6.2 \times 10^{-6} \pm 1.0 \times 10^{-5}$	$8.9 \times 10^{-6} \pm 8.1 \times 10^{-6}$
Cingulum left	$7.3 \times 10^{-3} \pm 8.3 \times 10^{-3}$	$7.9 \times 10^{-3} \pm 7.1 \times 10^{-3}$	$1.2 \times 10^{-5} \pm 1.4 \times 10^{-5}$	$1.3 \times 10^{-5} \pm 1.0 \times 10^{-5}$	$1.6 \times 10^{-5} \pm 2.0 \times 10^{-5}$	$1.6 \times 10^{-5} \pm 1.6 \times 10^{-5}$	$1.3 \times 10^{-5} \pm 1.5 \times 10^{-5}$	$1.4 \times 10^{-5} \pm 1.2 \times 10^{-5}$
Cingulum right	$8.0 \times 10^{-3} \pm 9.5 \times 10^{-3}$	$9.6 \times 10^{-3} \pm 8.3 \times 10^{-3}$	$1.9 \times 10^{-5} \pm 1.5 \times 10^{-5}$	$2.2 \times 10^{-5} \pm 1.8 \times 10^{-5}$	$2.4 \times 10^{-5} \pm 1.8 \times 10^{-5}$	$2.5 \times 10^{-5} \pm 1.9 \times 10^{-5}$	$1.9 \times 10^{-5} \pm 1.7 \times 10^{-5}$	$2.0 \times 10^{-5} \pm 1.8 \times 10^{-5}$
Uncinate fasciculus left	$4.6 \times 10^{-3} \pm 8.0 \times 10^{-3}$	$5.4 \times 10^{-3} \pm 6.7 \times 10^{-3}$	$4.7 \times 10^{-6} \pm 5.3 \times 10^{-6}$	$7.3 \times 10^{-6} \pm 6.8 \times 10^{-6}$	$6.4 \times 10^{-6} \pm 4.9 \times 10^{-6}$	$9.6 \times 10^{-6} \pm 8.3 \times 10^{-6}$	$6.6 \times 10^{-6} \pm 1.2 \times 10^{-5}$	$9.1 \times 10^{-6} \pm 1.0 \times 10^{-5}$
Uncinate fasciculus right	$4.8 \times 10^{-3} \pm 4.2 \times 10^{-3}$	$4.7 \times 10^{-3} \pm 3.4 \times 10^{-3}$	$7.7 \times 10^{-6} \pm 9.0 \times 10^{-6}$	$9.0 \times 10^{-6} \pm 8.5 \times 10^{-6}$	$8.2 \times 10^{-6} \pm 9.4 \times 10^{-6}$	$1.0 \times 10^{-5} \pm 8.5 \times 10^{-6}$	$9.7 \times 10^{-6} \pm 9.7 \times 10^{-6}$	$1.0 \times 10^{-5} \pm 8.9 \times 10^{-6}$
Corticospinal tract left	$6.7 \times 10^{-3} \pm 2.0 \times 10^{-2}$	$6.5 \times 10^{-3} \pm 1.5 \times 10^{-2}$	$6.4 \times 10^{-6} \pm 1.0 \times 10^{-5}$	$9.9 \times 10^{-6} \pm 1.0 \times 10^{-5}$	$1.0 \times 10^{-5} \pm 2.8 \times 10^{-5}$	$1.4 \times 10^{-5} \pm 2.2 \times 10^{-5}$	$6.8 \times 10^{-6} \pm 1.2 \times 10^{-5}$	$1.0 \times 10^{-5} \pm 1.1 \times 10^{-5}$
Corticospinal tract right	$6.4 \times 10^{-3} \pm 1.5 \times 10^{-2}$	$7.0 \times 10^{-3} \pm 1.2 \times 10^{-2}$	$5.3 \times 10^{-6} \pm 7.7 \times 10^{-6}$	$9.2 \times 10^{-6} \pm 9.6 \times 10^{-6}$	$8.9 \times 10^{-6} \pm 2.0 \times 10^{-5}$	$1.4 \times 10^{-5} \pm 1.8 \times 10^{-5}$	$6.0 \times 10^{-6} \pm 1.3 \times 10^{-5}$	$9.6 \times 10^{-6} \pm 1.3 \times 10^{-5}$
Forceps Minor	$5.5 \times 10^{-3} \pm 6.9 \times 10^{-3}$	$6.9 \times 10^{-3} \pm 6.2 \times 10^{-3}$	$7.9 \times 10^{-6} \pm 8.4 \times 10^{-6}$	$1.0 \times 10^{-5} \pm 8.2 \times 10^{-6}$	$9.4 \times 10^{-6} \pm 9.0 \times 10^{-6}$	$1.4 \times 10^{-5} \pm 1.1 \times 10^{-5}$	$8.9 \times 10^{-6} \pm 1.1 \times 10^{-5}$	$1.2 \times 10^{-5} \pm 8.7 \times 10^{-6}$
Forceps Major	$5.4 \times 10^{-3} \pm 1.5 \times 10^{-2}$	$4.3 \times 10^{-3} \pm 1.1 \times 10^{-2}$	$4.6 \times 10^{-6} \pm 6.6 \times 10^{-6}$	$7.3 \times 10^{-6} \pm 6.7 \times 10^{-6}$	$7.9 \times 10^{-6} \pm 2.1 \times 10^{-5}$	$1.0 \times 10^{-5} \pm 1.7 \times 10^{-5}$	$5.6 \times 10^{-6} \pm 7.5 \times 10^{-6}$	$7.4 \times 10^{-6} \pm 5.8 \times 10^{-6}$
Ventral Midbrain	$3.0 \times 10^{-2} \pm 3.7 \times 10^{-2}$	$2.6 \times 10^{-2} \pm 2.5 \times 10^{-2}$	$3.0 \times 10^{-5} \pm 2.6 \times 10^{-5}$	$4.3 \times 10^{-5} \pm 3.4 \times 10^{-5}$	$5.1 \times 10^{-5} \pm 5.1 \times 10^{-5}$	$6.3 \times 10^{-5} \pm 4.4 \times 10^{-5}$	$2.2 \times 10^{-5} \pm 1.8 \times 10^{-5}$	$2.9 \times 10^{-5} \pm 2.3 \times 10^{-5}$
Dorsal Midbrain	$1.3 \times 10^{-2} \pm 1.1 \times 10^{-2}$	$2.1 \times 10^{-2} \pm 1.8 \times 10^{-2}$	$1.3 \times 10^{-5} \pm 1.4 \times 10^{-5}$	$3.1 \times 10^{-5} \pm 3.7 \times 10^{-5}$	$1.6 \times 10^{-5} \pm 1.6 \times 10^{-5}$	$3.5 \times 10^{-5} \pm 3.5 \times 10^{-5}$	$1.9 \times 10^{-5} \pm 1.9 \times 10^{-5}$	$2.5 \times 10^{-5} \pm 2.8 \times 10^{-5}$
Cerebral peduncle left	$7.5 \times 10^{-3} \pm 7.6 \times 10^{-3}$	$9.3 \times 10^{-3} \pm 7.4 \times 10^{-3}$	$8.8 \times 10^{-6} \pm 1.1 \times 10^{-5}$	$1.5 \times 10^{-5} \pm 1.3 \times 10^{-5}$	$1.4 \times 10^{-5} \pm 1.5 \times 10^{-5}$	$2.0 \times 10^{-5} \pm 1.5 \times 10^{-5}$	$9.4 \times 10^{-6} \pm 1.0 \times 10^{-5}$	$1.4 \times 10^{-5} \pm 1.3 \times 10^{-5}$
Cerebral peduncle right	$5.9 \times 10^{-3} \pm 4.3 \times 10^{-3}$	$6.9 \times 10^{-3} \pm 5.0 \times 10^{-3}$	$7.4 \times 10^{-6} \pm 6.2 \times 10^{-6}$	$1.1 \times 10^{-5} \pm 8.7 \times 10^{-6}$	$1.2 \times 10^{-5} \pm 1.0 \times 10^{-5}$	$1.7 \times 10^{-5} \pm 1.2 \times 10^{-5}$	$8.5 \times 10^{-6} \pm 8.3 \times 10^{-6}$	$1.3 \times 10^{-5} \pm 1.6 \times 10^{-5}$
Pons left	$8.9 \times 10^{-3} \pm 8.1 \times 10^{-3}$	$1.2 \times 10^{-2} \pm 1.1 \times 10^{-2}$	$1.3 \times 10^{-5} \pm 1.2 \times 10^{-5}$	$3.1 \times 10^{-5} \pm 2.2 \times 10^{-5}$	$1.6 \times 10^{-5} \pm 1.5 \times 10^{-5}$	$3.6 \times 10^{-5} \pm 2.3 \times 10^{-5}$	$1.7 \times 10^{-5} \pm 1.6 \times 10^{-5}$	$2.8 \times 10^{-5} \pm 3.0 \times 10^{-5}$
Pons right	$7.7 \times 10^{-3} \pm 7.3 \times 10^{-3}$	$1.3 \times 10^{-2} \pm 7.4 \times 10^{-3}$	$1.1 \times 10^{-5} \pm 9.3 \times 10^{-6}$	$2.7 \times 10^{-5} \pm 2.1 \times 10^{-5}$	$1.5 \times 10^{-5} \pm 1.3 \times 10^{-5}$	$2.7 \times 10^{-5} \pm 2.4 \times 10^{-5}$	$1.4 \times 10^{-5} \pm 1.2 \times 10^{-5}$	$2.7 \times 10^{-5} \pm 2.6 \times 10^{-5}$
Mean	$7.1 \times 10^{-3} \pm 1.3 \times 10^{-2}$	$8.3 \times 10^{-3} \pm 1.1 \times 10^{-2}$	$1.0 \times 10^{-5} \pm 1.6 \times 10^{-5}$	$1.7 \times 10^{-5} \pm 2.1 \times 10^{-5}$	$1.4 \times 10^{-5} \pm 2.2 \times 10^{-5}$	$2.1 \times 10^{-5} \pm 2.5 \times 10^{-5}$	$1.1 \times 10^{-5} \pm 1.7 \times 10^{-5}$	$1.6 \times 10^{-5} \pm 2.1 \times 10^{-5}$

	FA		ADC		AD		RD	
	Within session reproducibility	Between session reproducibility						
Caudate left	$9.0 \times 10^{-3} \pm 7.5 \times 10^{-3}$	$9.1 \times 10^{-3} \pm 8.5 \times 10^{-3}$	$4.1 \times 10^{-5} \pm 4.1 \times 10^{-5}$	$4.2 \times 10^{-5} \pm 3.5 \times 10^{-5}$	$4.8 \times 10^{-5} \pm 4.5 \times 10^{-5}$	$4.9 \times 10^{-5} \pm 4.0 \times 10^{-5}$	$3.1 \times 10^{-5} \pm 3.5 \times 10^{-5}$	$3.0 \times 10^{-5} \pm 2.7 \times 10^{-5}$
Caudate right	$9.2 \times 10^{-3} \pm 8.1 \times 10^{-3}$	$9.7 \times 10^{-3} \pm 7.2 \times 10^{-3}$	$1.4 \times 10^{-5} \pm 1.9 \times 10^{-5}$	$1.9 \times 10^{-5} \pm 3.3 \times 10^{-5}$	$1.5 \times 10^{-5} \pm 1.9 \times 10^{-5}$	$2.1 \times 10^{-5} \pm 3.5 \times 10^{-5}$	$1.3 \times 10^{-5} \pm 1.9 \times 10^{-5}$	$1.7 \times 10^{-5} \pm 3.2 \times 10^{-5}$
Thalamus left	$6.1 \times 10^{-3} \pm 4.5 \times 10^{-3}$	$6.8 \times 10^{-3} \pm 4.9 \times 10^{-3}$	$7.9 \times 10^{-6} \pm 6.8 \times 10^{-6}$	$1.1 \times 10^{-5} \pm 8.4 \times 10^{-6}$	$1.1 \times 10^{-5} \pm 8.3 \times 10^{-6}$	$1.6 \times 10^{-5} \pm 1.1 \times 10^{-5}$	$7.8 \times 10^{-6} \pm 8.2 \times 10^{-6}$	$1.1 \times 10^{-5} \pm 1.6 \times 10^{-5}$
Thalamus right	$5.7 \times 10^{-3} \pm 4.9 \times 10^{-3}$	$6.9 \times 10^{-3} \pm 5.7 \times 10^{-3}$	$6.2 \times 10^{-6} \pm 4.8 \times 10^{-6}$	$8.8 \times 10^{-6} \pm 6.1 \times 10^{-6}$	$8.2 \times 10^{-6} \pm 7.8 \times 10^{-6}$	$1.4 \times 10^{-5} \pm 9.8 \times 10^{-6}$	$7.5 \times 10^{-6} \pm 7.9 \times 10^{-6}$	$1.1 \times 10^{-5} \pm 1.7 \times 10^{-5}$
Hippocampus left	$4.2 \times 10^{-3} \pm 4.8 \times 10^{-3}$	$4.8 \times 10^{-3} \pm 4.3 \times 10^{-3}$	$7.0 \times 10^{-6} \pm 8.4 \times 10^{-6}$	$1.3 \times 10^{-5} \pm 1.1 \times 10^{-5}$	$8.5 \times 10^{-6} \pm 8.1 \times 10^{-6}$	$1.4 \times 10^{-5} \pm 1.2 \times 10^{-5}$	$8.2 \times 10^{-6} \pm 1.2 \times 10^{-5}$	$1.4 \times 10^{-5} \pm 2.0 \times 10^{-5}$
Hippocampus right	$4.7 \times 10^{-3} \pm 6.7 \times 10^{-3}$	$5.7 \times 10^{-3} \pm 3.8 \times 10^{-3}$	$9.7 \times 10^{-6} \pm 9.8 \times 10^{-6}$	$1.6 \times 10^{-5} \pm 1.2 \times 10^{-5}$	$1.1 \times 10^{-5} \pm 9.0 \times 10^{-6}$	$1.6 \times 10^{-5} \pm 1.3 \times 10^{-5}$	$9.2 \times 10^{-6} \pm 1.2 \times 10^{-5}$	$1.6 \times 10^{-5} \pm 1.9 \times 10^{-5}$
Frontal lobe left	$3.1 \times 10^{-3} \pm 3.7 \times 10^{-3}$	$4.1 \times 10^{-3} \pm 4.1 \times 10^{-3}$	$9.1 \times 10^{-6} \pm 9.6 \times 10^{-6}$	$2.0 \times 10^{-5} \pm 1.6 \times 10^{-5}$	$1.1 \times 10^{-5} \pm 1.3 \times 10^{-5}$	$2.3 \times 10^{-5} \pm 2.0 \times 10^{-5}$	$9.6 \times 10^{-6} \pm 8.0 \times 10^{-6}$	$1.5 \times 10^{-5} \pm 1.3 \times 10^{-5}$
Frontal lobe right	$3.2 \times 10^{-3} \pm 3.0 \times 10^{-3}$	$3.9 \times 10^{-3} \pm 3.6 \times 10^{-3}$	$9.0 \times 10^{-6} \pm 8.4 \times 10^{-6}$	$2.0 \times 10^{-5} \pm 1.7 \times 10^{-5}$	$1.1 \times 10^{-5} \pm 1.1 \times 10^{-5}$	$2.4 \times 10^{-5} \pm 2.1 \times 10^{-5}$	$8.9 \times 10^{-6} \pm 7.7 \times 10^{-6}$	$1.6 \times 10^{-5} \pm 1.4 \times 10^{-5}$
Parietal lobe left	$3.7 \times 10^{-3} \pm 4.3 \times 10^{-3}$	$4.9 \times 10^{-3} \pm 4.9 \times 10^{-3}$	$7.3 \times 10^{-6} \pm 8.4 \times 10^{-6}$	$1.3 \times 10^{-5} \pm 1.2 \times 10^{-5}$	$9.1 \times 10^{-6} \pm 1.1 \times 10^{-5}$	$1.7 \times 10^{-5} \pm 1.6 \times 10^{-5}$	$7.1 \times 10^{-6} \pm 8.2 \times 10^{-6}$	$1.3 \times 10^{-5} \pm 1.3 \times 10^{-5}$
Parietal lobe right	$2.4 \times 10^{-3} \pm 2.8 \times 10^{-3}$	$4.0 \times 10^{-3} \pm 3.6 \times 10^{-3}$	$4.5 \times 10^{-6} \pm 3.3 \times 10^{-6}$	$1.2 \times 10^{-5} \pm 1.2 \times 10^{-5}$	$5.1 \times 10^{-6} \pm 4.3 \times 10^{-6}$	$1.4 \times 10^{-5} \pm 1.4 \times 10^{-5}$	$5.7 \times 10^{-6} \pm 6.3 \times 10^{-6}$	$1.2 \times 10^{-5} \pm 1.4 \times 10^{-5}$
Occipital lobe left	$5.0 \times 10^{-3} \pm 6.8 \times 10^{-3}$	$5.5 \times 10^{-3} \pm 5.2 \times 10^{-3}$	$6.5 \times 10^{-6} \pm 6.8 \times 10^{-6}$	$1.3 \times 10^{-5} \pm 9.4 \times 10^{-6}$	$9.3 \times 10^{-6} \pm 1.0 \times 10^{-5}$	$1.5 \times 10^{-5} \pm 1.2 \times 10^{-5}$	$6.4 \times 10^{-6} \pm 7.2 \times 10^{-6}$	$1.2 \times 10^{-5} \pm 1.4 \times 10^{-5}$
Occipital lobe right	$3.7 \times 10^{-3} \pm 4.7 \times 10^{-3}$	$4.4 \times 10^{-3} \pm 4.8 \times 10^{-3}$	$6.3 \times 10^{-6} \pm 6.6 \times 10^{-6}$	$1.3 \times 10^{-5} \pm 1.2 \times 10^{-5}$	$8.8 \times 10^{-6} \pm 9.2 \times 10^{-6}$	$1.5 \times 10^{-5} \pm 1.5 \times 10^{-5}$	$7.4 \times 10^{-6} \pm 8.1 \times 10^{-6}$	$1.4 \times 10^{-5} \pm 1.7 \times 10^{-5}$
Temporal lobe left	$6.7 \times 10^{-3} \pm 8.5 \times 10^{-3}$	$6.7 \times 10^{-3} \pm 7.5 \times 10^{-3}$	$1.0 \times 10^{-5} \pm 9.4 \times 10^{-6}$	$1.3 \times 10^{-5} \pm 1.1 \times 10^{-5}$	$1.4 \times 10^{-5} \pm 1.4 \times 10^{-5}$	$1.7 \times 10^{-5} \pm 1.6 \times 10^{-5}$	$8.6 \times 10^{-6} \pm 8.2 \times 10^{-6}$	$1.4 \times 10^{-5} \pm 1.6 \times 10^{-5}$
Temporal lobe right	$4.4 \times 10^{-3} \pm 5.1 \times 10^{-3}$	$4.7 \times 10^{-3} \pm 4.8 \times 10^{-3}$	$7.0 \times 10^{-6} \pm 5.4 \times 10^{-6}$	$1.1 \times 10^{-5} \pm 8.5 \times 10^{-6}$	$8.9 \times 10^{-6} \pm 8.1 \times 10^{-6}$	$1.3 \times 10^{-5} \pm 1.0 \times 10^{-5}$	$1.3 \times 10^{-5} \pm 4.4 \times 10^{-5}$	$1.5 \times 10^{-5} \pm 3.6 \times 10^{-5}$
Cerebellum left	$4.5 \times 10^{-3} \pm 4.7 \times 10^{-3}$	$1.3 \times 10^{-2} \pm 1.3 \times 10^{-2}$	$1.2 \times 10^{-5} \pm 1.5 \times 10^{-5}$	$3.5 \times 10^{-5} \pm 3.8 \times 10^{-5}$	$1.5 \times 10^{-5} \pm 1.9 \times 10^{-5}$	$4.4 \times 10^{-5} \pm 4.9 \times 10^{-5}$	$1.3 \times 10^{-5} \pm 1.4 \times 10^{-5}$	$2.4 \times 10^{-5} \pm 2.7 \times 10^{-5}$
Cerebellum right	$4.0 \times 10^{-3} \pm 4.4 \times 10^{-3}$	$1.2 \times 10^{-2} \pm 1.2 \times 10^{-2}$	$8.9 \times 10^{-6} \pm 1.1 \times 10^{-5}$	$3.1 \times 10^{-5} \pm 3.4 \times 10^{-5}$	$1.2 \times 10^{-5} \pm 1.3 \times 10^{-5}$	$4.0 \times 10^{-5} \pm 4.2 \times 10^{-5}$	$1.2 \times 10^{-5} \pm 1.2 \times 10^{-5}$	$2.4 \times 10^{-5} \pm 2.4 \times 10^{-5}$
Mean	$5.0 \times 10^{-3} \pm 5.8 \times 10^{-3}$	$6.6 \times 10^{-3} \pm 7.2 \times 10^{-3}$	$1.0 \times 10^{-5} \pm 1.6 \times 10^{-5}$	$1.8 \times 10^{-5} \pm 2.2 \times 10^{-5}$	$1.3 \times 10^{-5} \pm 1.8 \times 10^{-5}$	$2.2 \times 10^{-5} \pm 2.7 \times 10^{-5}$	$1.1 \times 10^{-5} \pm 1.8 \times 10^{-5}$	$1.6 \times 10^{-5} \pm 2.2 \times 10^{-5}$

4B

	FA		ADC		AD		RD	
	Within session reproducibility	Between session reproducibility						
Ant corpus callosum	3.2 ± 2.6	3.0 ± 2.7	1.5 ± 1.3	1.9 ± 1.4	1.4 ± 1.3	1.6 ± 1.3	4.3 ± 4.6	5.2 ± 5.0
Body corpus callosum	3.6 ± 3.6	3.8 ± 4.2	2.4 ± 2.4	3.1 ± 2.7	1.6 ± 1.7	2.1 ± 1.6	3.9 ± 4.6	5.2 ± 5.7
Post corpus callosum	1.6 ± 2.1	1.5 ± 1.3	2.2 ± 3.4	2.2 ± 2.1	1.1 ± 1.4	1.3 ± 1.0	3.8 ± 6.6	4.0 ± 4.2
Ant thalamic radiation left	0.9 ± 1.3	1.1 ± 1.1	0.8 ± 1.2	1.2 ± 1.2	0.6 ± 0.7	0.9 ± 0.8	1.0 ± 1.8	1.4 ± 1.6
Ant thalamic radiation right	1.3 ± 1.6	1.5 ± 1.4	0.9 ± 1.8	1.2 ± 1.4	0.7 ± 1.2	1.0 ± 0.9	1.2 ± 2.3	1.5 ± 1.8
Sup longitudinal fasciculus left	1.7 ± 7.4	1.4 ± 5.5	0.7 ± 3.0	1.0 ± 2.3	0.9 ± 4.0	1.1 ± 3.1	0.6 ± 2.3	1.0 ± 1.8
Sup longitudinal fasciculus right	1.7 ± 6.3	1.7 ± 4.7	0.4 ± 1.4	1.0 ± 1.3	0.6 ± 2.6	1.1 ± 2.2	0.4 ± 0.5	0.9 ± 0.9
Inf longitudinal fasciculus left	1.4 ± 5.0	1.3 ± 3.6	0.4 ± 0.3	0.7 ± 0.7	0.5 ± 1.4	0.7 ± 1.2	0.7 ± 1.5	1.1 ± 1.2
Inf longitudinal fasciculus right	1.3 ± 3.5	1.3 ± 2.5	0.5 ± 0.7	0.9 ± 0.7	0.6 ± 1.3	0.8 ± 1.1	0.9 ± 1.6	1.4 ± 1.2
Cingulum left	2.5 ± 2.8	2.7 ± 2.3	1.3 ± 1.5	1.4 ± 1.1	1.3 ± 1.6	1.4 ± 1.3	1.7 ± 1.9	1.9 ± 1.6
Cingulum right	2.7 ± 3.0	3.2 ± 2.6	1.9 ± 1.5	2.2 ± 1.8	1.8 ± 1.4	1.9 ± 1.5	2.2 ± 1.9	2.4 ± 2.0
Uncinate fasciculus left	1.2 ± 2.1	1.4 ± 1.8	0.6 ± 0.6	0.9 ± 0.8	0.5 ± 0.4	0.8 ± 0.7	1.0 ± 1.8	1.4 ± 1.5
Uncinate fasciculus right	1.3 ± 1.2	1.3 ± 0.9	0.8 ± 1.0	1.0 ± 0.9	0.6 ± 0.8	0.8 ± 0.7	1.3 ± 1.4	1.4 ± 1.2
Corticospinal tract left	1.5 ± 4.8	1.4 ± 3.5	0.8 ± 1.4	1.2 ± 1.3	0.8 ± 2.4	1.1 ± 1.9	1.1 ± 1.9	1.9 ± 1.8
Corticospinal tract right	1.4 ± 3.6	1.5 ± 2.9	0.7 ± 1.0	1.1 ± 1.2	0.7 ± 1.7	1.1 ± 1.5	1.0 ± 2.1	1.6 ± 2.1
Forceps Minor	1.5 ± 1.9	1.8 ± 1.7	0.9 ± 0.9	1.1 ± 0.9	0.7 ± 0.7	1.1 ± 0.8	1.3 ± 1.5	1.6 ± 1.2
Forceps Major	1.5 ± 4.4	1.1 ± 3.2	0.5 ± 0.8	0.8 ± 0.8	0.6 ± 1.8	0.8 ± 1.4	0.8 ± 1.1	1.0 ± 0.8
Ventral Midbrain	5.5 ± 6.6	4.7 ± 4.4	3.9 ± 3.5	5.7 ± 4.5	3.8 ± 4.0	4.7 ± 3.4	4.3 ± 3.6	5.8 ± 4.5
Dorsal Midbrain	2.5 ± 2.2	4.0 ± 3.4	1.7 ± 1.7	3.8 ± 4.4	1.3 ± 1.2	2.7 ± 2.5	3.3 ± 3.0	4.5 ± 4.9
Cerebral peduncle left	1.5 ± 1.6	1.8 ± 1.5	1.3 ± 1.6	2.2 ± 1.9	1.2 ± 1.4	1.8 ± 1.4	1.9 ± 2.1	3.0 ± 2.6
Cerebral peduncle right	1.1 ± 0.9	1.3 ± 0.9	1.1 ± 0.9	1.7 ± 1.3	1.0 ± 0.9	1.5 ± 1.1	1.8 ± 1.7	2.8 ± 3.3
Pons left	1.7 ± 1.6	2.3 ± 2.1	1.5 ± 1.5	3.8 ± 2.8	1.2 ± 1.2	2.8 ± 1.8	2.9 ± 2.6	4.9 ± 5.4
Pons right	1.4 ± 1.4	2.3 ± 1.4	1.4 ± 1.2	3.4 ± 2.6	1.2 ± 1.0	2.1 ± 1.8	2.6 ± 2.0	4.8 ± 4.4
Mean	1.9 ± 3.7	2.1 ± 3.0	1.2 ± 1.9	1.9 ± 2.4	1.1 ± 1.9	1.5 ± 1.9	1.9 ± 2.9	2.6 ± 3.5

4C

	FA		ADC		AD		RD	
	Within session reproducibility	Between session reproducibility						
Caudate left	3.8 ± 3.4	3.9 ± 4.0	3.3 ± 3.3	3.6 ± 3.0	3.2 ± 2.9	3.4 ± 2.8	2.9 ± 3.2	3.0 ± 2.8
Caudate right	3.2 ± 2.9	3.4 ± 2.5	1.7 ± 2.2	2.2 ± 3.0	1.4 ± 1.7	2.0 ± 2.6	1.9 ± 2.5	2.2 ± 3.4
Thalamus left	1.8 ± 1.3	2.0 ± 1.5	1.0 ± 0.9	1.4 ± 1.1	1.0 ± 0.8	1.5 ± 1.0	1.2 ± 1.2	1.6 ± 2.3
Thalamus right	1.6 ± 1.4	2.0 ± 1.6	0.8 ± 0.6	1.2 ± 0.8	0.8 ± 0.8	1.3 ± 1.0	1.2 ± 1.1	1.8 ± 2.5
Hippocampus left	1.5 ± 1.7	1.7 ± 1.6	0.7 ± 0.8	1.2 ± 1.1	0.6 ± 0.6	1.1 ± 0.9	0.9 ± 1.3	1.6 ± 2.2
Hippocampus right	1.6 ± 2.3	2.0 ± 1.4	0.9 ± 0.9	1.4 ± 1.1	0.8 ± 0.6	1.1 ± 0.9	1.0 ± 1.3	1.7 ± 2.0
Frontal lobe left	1.2 ± 1.5	1.7 ± 1.6	0.9 ± 1.0	1.9 ± 1.6	0.9 ± 1.0	1.9 ± 1.6	1.1 ± 0.9	1.6 ± 1.5
Frontal lobe right	1.4 ± 1.2	1.6 ± 1.5	0.9 ± 0.8	2.0 ± 1.7	0.9 ± 0.9	1.9 ± 1.7	1.0 ± 0.8	1.7 ± 1.5
Parietal lobe left	1.4 ± 1.6	1.9 ± 1.9	0.7 ± 0.8	1.3 ± 1.2	0.7 ± 0.9	1.3 ± 1.2	0.8 ± 0.9	1.4 ± 1.4
Parietal lobe right	0.9 ± 1.1	1.6 ± 1.4	0.4 ± 0.3	1.2 ± 1.2	0.4 ± 0.3	1.2 ± 1.2	0.6 ± 0.6	1.3 ± 1.5
Occipital lobe left	2.1 ± 2.8	2.2 ± 2.1	0.7 ± 0.7	1.3 ± 1.0	0.8 ± 0.8	1.3 ± 1.0	0.7 ± 0.8	1.4 ± 1.6
Occipital lobe right	1.6 ± 2.0	1.9 ± 2.0	0.6 ± 0.6	1.3 ± 1.2	0.7 ± 0.7	1.3 ± 1.2	0.8 ± 0.8	1.5 ± 1.8
Temporal lobe left	2.7 ± 3.4	2.8 ± 3.0	1.1 ± 1.0	1.5 ± 1.2	1.3 ± 1.2	1.5 ± 1.4	1.1 ± 1.0	1.8 ± 1.9
Temporal lobe right	1.7 ± 2.0	1.9 ± 1.9	0.7 ± 0.6	1.2 ± 0.9	0.7 ± 0.7	1.1 ± 0.9	1.8 ± 6.9	1.9 ± 5.3
Cerebellum left	2.1 ± 2.5	5.9 ± 6.4	1.5 ± 2.1	4.3 ± 4.9	1.5 ± 2.1	4.4 ± 5.1	1.7 ± 1.9	3.3 ± 3.8
Cerebellum right	1.9 ± 2.2	5.5 ± 6.3	1.1 ± 1.4	3.8 ± 4.0	1.2 ± 1.4	4.0 ± 4.2	1.6 ± 1.7	3.2 ± 3.1
Mean	1.9 ± 2.3	2.6 ± 3.3	1.1 ± 1.5	1.9 ± 2.4	1.1 ± 1.4	1.9 ± 2.4	1.3 ± 2.3	1.9 ± 2.7

4D

Table 4-2 Within and between session variability of diffusion tensor imaging region of interest measurements

Individual white matter (A and C) and mixed cortical and deep grey matter (B and D) region of interest measurements for within session reproducibility obtained in the first and second imaging sessions in 26 and 22 subjects respectively, and the between session reproducibility for those 22 subjects who underwent imaging at both sessions. Data displayed are standard deviation (A and B) and percentage coefficient of variation (C and D) of measurements for fractional anisotropy (FA), apparent diffusion coefficient (ADC), axial (AD) and radial (RD) diffusivity

Calculation of 95% prediction interval for zero change

Using the four DTI measurements obtained from both sessions, we used ANOVA to determine the significance of the differences (Table 4-3). These confirm that there is a significant difference between regions and subjects and that there is a significant interaction between brain region and subject. The residual variance of the DTI measurements which could not be accounted for by the known independent variables is shown in Table 4-3, and the calculated SD for FA, ADC, AD and RD were 1.2×10^{-2} , 3.2×10^{-5} , 3.2×10^{-5} and 8.4×10^{-5} mm²/second respectively. The overall population 95% prediction intervals for zero change (based on two SD values) were therefore 2.4×10^{-2} , 6.3×10^{-5} , 6.3×10^{-5} and 1.7×10^{-4} mm²/second for FA, ADC, AD and RD respectively. The calculated SD for the within-session measurements were 7.1×10^{-3} , 1.0×10^{-5} , 1.4×10^{-5} and 1.1×10^{-5} mm²/second for FA, ADC, AD and RD respectively. An estimate of the overall 95% prediction interval for zero change (based on 4.3 SD values) within a single imaging session was therefore 3.1×10^{-2} , 4.5×10^{-5} , 5.9×10^{-5} and 4.7×10^{-5} mm²/second for FA, ADC, AD and RD respectively.

Parameter	Session	DF	Sum of Squares	Mean Square	F Value	p Value
FA	ROI	38	5.4×10^1	1.4	9.6×10^3	<.0001
	subject	21	3.5×10^{-1}	1.7×10^{-2}	1.1×10^2	<.0001
	ROI * subject	798	5.3	6.6×10^{-3}	4.4×10^1	<.0001
	Residual	2574	3.8×10^{-1}	1.5×10^{-4}		
ADC	ROI	38	4.6×10^{-5}	1.2×10^{-6}	2.1×10^3	<.0001
	subject	21	2.2×10^{-6}	1.1×10^{-7}	1.9×10^2	<.0001
	ROI * subject	798	2.9×10^{-5}	3.6×10^{-8}	6.4×10^1	<.0001
	Residual	2574	1.5×10^{-6}	5.7×10^{-10}		
AD	ROI	38	9.5×10^{-5}	2.5×10^{-6}	3.0×10^3	<.0001
	subject	21	1.9×10^{-6}	8.9×10^{-8}	1.1×10^2	<.0001
	ROI * subject	798	2.7×10^{-5}	3.4×10^{-8}	4.1×10^1	<.0001
	Residual	2574	2.1×10^{-6}	8.3×10^{-10}		
RD	ROI	38	7.3×10^{-5}	1.9×10^{-6}	2.8×10^2	<.0001
	subject	21	2.0×10^{-6}	9.5×10^{-8}	1.4	<.0001
	ROI * subject	798	2.5×10^{-5}	3.2×10^{-8}	4.6	<.0001
	Residual	2574	1.8×10^{-5}	6.9×10^{-9}		

Table 4-3 Analysis of variance table for diffusion tensor imaging parameters

Data (mm²/second) were obtained from 26 volunteers using the region of interest (ROI) template for fractional anisotropy (FA), apparent diffusion coefficient (ADC), axial diffusivity (AD), and radial diffusivity (RD). Degrees of freedom (DF).

Discussion

This study provides additional reference data concerning intersubject variability and reproducibility of DTI conducted within the same imaging session (within a session) and different imaging sessions (between session) in a group of healthy volunteers. As reported previously, we found that intersubject variability was high,²⁰² with substantial variability across the brain for all the calculated parameters. While the DTI measurements were stable with CoV values of $\sim 5\%$, the repeated DTI sequences obtained during the same session (within session) had lower CoV values than those obtained from measurements obtained in a different imaging session separated by up to six months. The calculated 95% prediction intervals for zero change of repeat DTI measurements were similar for the data obtained within the same session and that calculated from all the measurements obtained over both imaging sessions. These prediction intervals can be calculated for individual ROIs and utilised in interventional studies to quantify change within a single imaging session, or to assess the significance of the change in longitudinal studies of brain injury and disease. The factors affecting the reproducibility of DTI parameters include changes within the MR scanner or individual subjects. Features related to the scanner include B_0 field inhomogeneities, scanner drift, gradient coil stability, signal to noise ratio and software upgrades. Such factors may be more significant when imaging is acquired within different imaging sessions, rather than repeat acquisitions within the same session where such parameters are more likely to be similar. Regular servicing and daily quality assurance measurements seek to ensure that an MR scanner is operating normally. There were no upgrades or changes in MR scanner hardware or software during the period of this study. Also, daily signal to noise ratio measurements was not significantly different for the six months of this study ($p = 0.08$, Friedman test. Data not shown).

There are individual subject factors such as head movements, and positioning within the scanner field was minimised to limit variability. All subjects were positioned within the head coil according to the standard operating procedure, and their alignment was confirmed before imaging. We monitored subject movement, and all data were checked during acquisition and processing for evidence of motion artefact. While no subject was excluded during acquisition or processing in these analyses, DTI had to be repeated in one subject during an imaging session due to subject movement. We performed all analyses following image coregistration and spatial normalisation to MNI standard space. We used a standard ROI template covering the whole brain from the Harvard Oxford subcortical and MNI structural probabilistic atlases available within FSL. Finally, all ROIs were manually inspected to ensure that they were aligned with the imaging data and corresponded to the regions specified. In summary, we considered possible sources of DTI variability within our centre and attempted to limit their impact and ensure that the data we acquired were comparable within and between the different imaging sessions.

While our results for DTI reproducibility are in line with published data,²¹¹ we report data specifically concerning the difference between intersubject variability, within session and between-session reproducibility. Our data for healthy volunteers are broadly concordant with results from other groups, and show that these are high, with mean (range) CoV of 7% (3 – 32) for FA, 7% (2 – 34) for ADC, 5% (2 – 27) for axial diffusivity and 11% (3 – 63) for radial diffusivity. To be sure that DTI values derived from an individual patient are significantly lower, with a confidence of 95%, these figures suggest that we need to have mean ROI FA values (for example) that are at least 14% lower than volunteer means. This estimate and the secure distinction of a patient group as abnormal is further confounded by the fact that intersubject CoV in patients with neurological disorders is larger, and is variable across different brain regions. These figures underline the difficulty of using DTI in small groups of patients with various causes of neurological disease who have variable pathophysiology. In practice, however, estimated sample sizes in such studies are moderated by the fact that the changes in DTI are often dramatic, and significance is often detected with manageable numbers,^{59,212,213} despite the large intersubject variability in volunteer and patients groups.

However, it is essential to point out that these figures are largely irrelevant when considering the power and design of clinical studies, were the subject is his or her own control, and the relevant parameter is intrasubject variability or reproducibility. Our data show that these figures for CoV are much smaller than those obtained from the discussion in the previous paragraph. Also, we provide reference data for FA, ADC, AD and RD in healthy volunteers demonstrating that the CoV for within-session reproducibility is lower than between session reproducibility (Table 4-2). These data provide helpful guidance for designing clinical studies and suggest that it should be possible to detect differences of approximately 5 to 10% with confidence, particularly within single session interventional studies. For example, although the reproducibility of measurements is variable for the different brain regions, we can use these data to calculate sample sizes for interventional and longitudinal clinical studies. Even when we consider the brain region with the highest CoV (ventral midbrain), we should be able to detect a 10% change in DTI with 95% power at a significance level of 1% within a group of 10 subjects within a single interventional or longitudinal study design. Such estimates only strictly apply to our scanner and institution, but they provide a useful starting point for study design. There are several factors particular to our scanning protocols and institutional setup that limit the use of the reproducibility measurements that we provide. These include, but might not be limited to, scanner, acquisition protocols, data correction and reconstruction, and processing. Despite these variations, it should be possible for other groups to use the methodology that we describe to derive ‘in house’ data for their studies. Also, although these data guide designing further clinical

studies, particular groups of subjects (including those with brain injury) may require sedation and control of ventilation as part of clinical care.^{213,214}

Methodological limitations

While we were able to obtain multiple DTI datasets on up to two occasions in this group of volunteers, scanner availability and subject tolerance prevented us from acquiring further DTI datasets within the same session and additional scanning sessions. We found that the within-session reproducibility measurements were lower than between session reproducibility measurements obtained over six months. The expected change in DTI in healthy volunteers of a similar age over up to six months is small and unlikely to have resulted in the differences we have found.^{215,216} The 95% prediction intervals for zero change for the within-session DTI measurements were similar to that calculated from the DTI measurements obtained within all sessions. The lack of difference between these measures could be related to the fact that we were only able to obtain two sets of DTI within each session and that the 95% prediction interval for zero change for within-session measurements is based on 4.3 rather than 2 SDs. These overall prediction intervals for zero change are calculated from all the ROI data, but can easily be calculated for individual ROIs using the same technique and used as a method for determining the significance of changes following an intervention or longitudinal change over time.

There were differences in the intersubject variability and reproducibility of DTI across the different brain regions. These differences are demonstrated in Table 4-1, Table 4-2 and Figure 4-2 and are particularly relevant within the corpus callosum, caudate, cingulum and midbrain structures. The increase in variability and lower reproducibility of these regions may be related to partial volume errors within these relatively small structures secondary to variation in the quality of coregistration and spatial normalisation within individual subjects. We tried to limit these errors by eroding the ROI template by a single voxel to improve accuracy. Despite this, errors remain within some ROIs where DTI values differ in closely adjacent brain regions. However, the purpose of this study was to determine the variability of measurements using an ROI template and standard processing pipeline. While variability in the fitting of template ROIs in individual subjects may result in higher intersubject variability for particular brain regions, this is less likely for measurements of reproducibility within the same subject. Here any differences in ROI template fitting between the sessions are likely to be small. However, these regional differences underline that DTI studies seeking to compare different subject groups or assess interventional or longitudinal change should compare data from within the same brain region using the same data processing technique.

Conclusions

This study provides additional reference data concerning intersubject variability and reproducibility of DTI conducted in a group of healthy volunteers. The CoV for repeat DTI measurements obtained during the same session was lower than those obtained from measurements obtained in a different imaging session separated by up to six months. These data can be used to calculate the 95% prediction interval for zero change and may inform the design of interventional studies to quantify change within a single imaging session or to assess the significance of the change in longitudinal studies.

Chapter 5 Comparison of inter subject variability and reproducibility of whole brain proton spectroscopy

Introduction

Proton magnetic resonance spectroscopic imaging (^1H MRS) can be used in the diagnosis, assessment of progression and prediction of outcome in a variety of neurological disorders such as brain tumours,²¹⁷ traumatic brain injury,^{108,110,218} multiple sclerosis,^{219,220} motor neuron disease,²²¹ Alzheimer's dementia²²² and psychiatric disorders.^{223,224} The metabolites reliably measured with proton spectroscopy (^1H MRS) at medium to long echo times include N-acetylaspartate (NAA), Creatine (Cr) and Choline (Cho) containing compounds. These provide a measure of neuronal integrity, metabolism and a marker of neuronal breakdown and turnover, respectively.^{168,225} While targeted imaging of regions of interest (with single voxel or two dimensional ^1H MRS) allows evaluation of local neuronal loss and glial proliferation; whole brain imaging provides an assessment of the global burden of neurological disease even in regions that appear structurally normal. Proton magnetic resonance spectroscopy has been used to non-invasively evaluate normal appearing brain in a variety of neurological disorders, including multiple sclerosis and head injury.^{226,227} Whole brain proton spectroscopy (WB ^1H MRS) data acquired with Metabolic Imaging and Data Acquisition Software (MIDAS)^{96,228,229} provides a fully automated pipeline for processing and interpreting WB ^1H MRS data. Previous studies using MIDAS and other ^1H MRS techniques have provided invaluable reference data regarding normal values within different brain regions and reproducibility of such data.^{109,230,231} However, there are limited data comparing intersubject variability and reproducibility of WB ^1H MRS measurements within the same imaging session (within session reproducibility) and those obtained during repeat imaging sessions on different days (between session reproducibility). This is of relevance for group comparisons with healthy controls, and longitudinal and interventional studies where WB ^1H MRS is used as a biomarker of disease progression or response to therapy. The rational design and interpretation of such studies are hampered by lack of knowledge regarding how the variability of WB ^1H MRS measurements in data obtained during the same scanning session differs when compared with similar data obtained during a different session or day. In studies where consecutive measurements are performed on each subject under resting, and experimental conditions problems associated with variation between subjects due to individual differences (intersubject variability) can be limited. However, baseline MIDAS WB ^1H MRS measurements may vary within an individual patient (intrasubject variability) and limit the ability to detect significant changes over time or following a therapeutic intervention. Where imaging is repeated after several days or weeks in different sessions,

the measurements may vary within an individual patient even in the absence of disease progression due to a combination of intrasubject and scanner variability.^{113,232} Without knowledge of such differences, it is difficult to accurately determine the clinical significance of pathophysiological changes, as they evolve following various causes of brain injury or disease.

These studies aimed to provide reference data on intersubject variability and reproducibility of commonly used metabolite ratios (Cho/Cr, NAA/Cho and NAA/Cr) and individual signal-intensity normalised metabolite concentrations (NAA, Cho and Cr) in a group of healthy volunteers using MIDAS. These data will inform the design of interventional studies, where repeated measurements are conducted within the same session and longitudinal studies where assessments are repeated over time in several different imaging sessions.

Materials and Methods

Ethics statement

Ethical approval was obtained from the Cambridgeshire 2 Research Ethics Committee (reference number 97/290) and written informed consent was obtained from all volunteers in accordance with the Declaration of Helsinki.

Imaging data acquisition

Thirty-two healthy volunteers without any history of neuropsychiatric disorder or substance abuse underwent imaging using a 3T Siemens Verio MRI scanner (Siemens AG, Erlangen, Germany) with 12 channel detection within the Wolfson Brain Imaging Centre (WBIC), University of Cambridge. All volunteers were right-handed (fourteen males and eighteen females) with mean (range) age of 34 (25 – 50) years and were employed by Cambridge University Hospitals NHS Trust. Twenty-two volunteers attended a second imaging session within a mean (range) of 33 (3 – 181) days. At each imaging session subjects were imaged twice with MIDAS along with standard structural imaging. Structural sequences included 3D T1-weighted magnetisation prepared rapid gradient echo (MPRAGE), fluid attenuated inversion recovery (FLAIR), gradient echo and dual spin echo (proton density/T2-weighted). Whole brain spectroscopy data were acquired using a volumetric spin echo (TR/TE 1710/70 milliseconds, flip angle of 73°, 50 phase encoding steps and a field of view of 280x280x180mm³) covering the whole brain with an acquisition time of 26 minutes as described by Maudsley et al.^{96,228,233} This sequence also included lipid inversion nulling and an unsuppressed water spectroscopy dataset acquired with 20° flip angle acquired in an interleaved fashion. The MIDAS and MPRAGE were acquired at an angulation of +15 to +20° to the AC-PC line to improve brain coverage and limit field inhomogeneities from the frontal and sphenoid air sinuses. The MPRAGE (TR/TE 2150/4.4 and flip angle 8°) was acquired within each imaging session with one-millimetre isotropic resolution.

Spectroscopic data processing

Parametric maps were created using the automated pipeline of MIDAS and the data for NAA, Cho and Cr were individual signal-intensity normalised to institutional units (iu) based on the tissue water signal derived from the water reference dataset. Metabolite data were reconstructed using MIDAS and resulted in images composed of 64x64x32 voxels with an individual voxel volume of approximately 1ml. Voxel data with line width greater than 12 Hz were excluded from further analysis as previously described by Maudsley et al.^{109,111,228} The WB ¹H MRS parametric maps were spatially normalised using a two-step approach using FSL.^{206,207} First, control T1 weighted images were coregistered to water spectroscopic images using FMRIB's Linear Image Registration Tool (FLIRT).²³⁴ This was followed by coregistration of control T1 weighted images to the MNI152 template using FMRIB's Non-linear Image Registration Tool (FNIRT).²³⁴ Combined transformation matrixes were then applied to all parametric images used in the analyses. Representative white matter, deep grey and mixed regions of interest (ROIs) from the Harvard Oxford subcortical and MNI structural probabilistic atlases available within FSL were then applied in normalised space (Figure 5-1). All coregistered images were subsequently inspected to ensure that the ROIs were correctly aligned and corresponded to the regions specified. The ROI template was modified by the erosion of a single voxel using FSL to improve spatial localisation and reduce the impact of coregistration, normalisation and partial volume errors. The mean values for metabolites for each ROI were calculated using in-house software written in Matlab (Mathworks, Natick, USA).

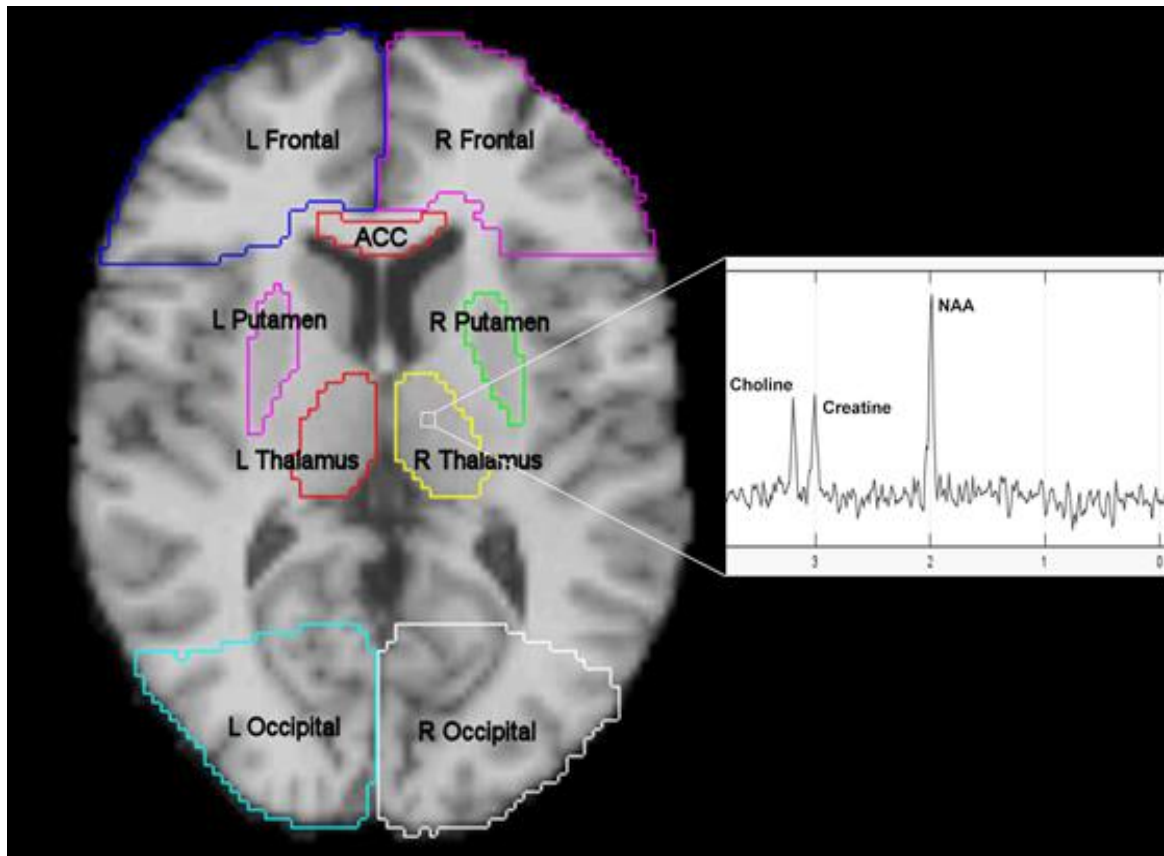


Figure 5-1 Region of interest template with a representative spectra from right thalamus used for calculating metabolite ratios for whole brain proton spectroscopy

T1 weighted magnetic resonance image in MNI152 space (2mm resolution) showing frontal lobe left (L Frontal), frontal lobe right (R Frontal), anterior corpus callosum (ACC), thalamus left (L Thalamus), thalamus right (R Thalamus), occipital left (L Occipital), occipital right (R Occipital), putamen left (L Putamen) and putamen right (R Putamen). Additional regions not shown include body corpus callosum, posterior corpus callosum, dorsal mid brain, ventral mid brain and bilateral regions covering the corticospinal tract, anterior thalamic radiation, inferior longitudinal fasciculus, superior longitudinal fasciculus, pallidum, hippocampus, parietal lobe, temporal lobe, cerebral peduncle and pons.

Analysis Strategy

Each of the 32 volunteers were invited to attend two separate imaging sessions where two MIDAS sequences were obtained. This resulted in a maximum of four independent sets of WB ^1H MRS data (runs) for each subject, which could be used to assess the reproducibility of measurements. Twenty-two subjects underwent imaging in both sessions. The baseline data from all 32 volunteers were used to calculate intersubject variability. For the repeat MIDAS measurements obtained in the same subject, the data were split into that obtained during the same imaging session and that obtained in two different imaging sessions to calculate within session and between session reproducibility respectively. Therefore, the available paired data from each session (run 1 & 2 and 3 & 4 respectively) were used to calculate within session reproducibility, and the available combinations of the four datasets from the different sessions were used to calculate between session reproducibility (runs 1 & 3, 1 & 4, 2 & 3, and 2 & 4). The inclusion of all potential combinations ensures that any variation in the

order of the individual sequences obtained within each particular session is accounted for within the calculated average measurement of between session reproducibility and reflects clinical practice.

In order to help design any future interventional study using proton spectroscopy, we need to know how much deviation in a repeat measurement we would accept as no or zero change. We used the SD of measurements obtained in this healthy volunteer study to calculate a 'confidence interval' for zero change of a repeat measurement in the same subject. We used the average SD for all measurements obtained in 32 volunteers in both sessions to calculate the population 95% prediction interval (PI) for zero change (using two SD values).^{113,116,118,232} These calculated thresholds are prediction intervals for assuming no changes from zero with the repeat WB ¹H MRS measurement rather than confidence intervals for the variability of the measurement. This estimate for the variation in repeat measurements means that we would accept a positive or negative change in a patient as being indicative of zero change as long as it were less than two times the standard deviation of the repeat measurement obtained in our healthy volunteer group. Although these average data are extremely useful, the calculated SD could vary within different sessions and particular ROIs within subjects. It would, therefore, be helpful to have a more specific measure of variability within a session (within session reproducibility), and preferably for each ROI. While this is possible, the small sample numbers (two readings obtained in each of the two sessions) means that a conventional threshold of change greater than 2SD cannot be used to assess the statistical significance of changes in this context. For a *t* distribution with two degrees of freedom, the statistical theory suggests that an estimate of the 95% prediction interval for zero change may be provided by a threshold of 4.3 SDs. These within session measurements could, therefore, be used to assess the significance of the changes in WB ¹H MRS parameters following a therapeutic intervention within the same imaging session. We have previously published this analysis strategy for diffusion tensor imaging and ¹⁵O positron emission tomography.^{116,118,232}

Statistical analysis

Statistical analyses were conducted using Statview (Version 5, 1998, SAS Institute Inc., Cary, North Carolina, USA) and SPSS[®] Statistics Version 21 (IBM[®] Corporation, New York, United States). All data are expressed and displayed as mean and standard deviation (SD), unless otherwise stated. To compare the reproducibility of WB ¹H MRS measurements, the SD and coefficient of variation (CoV) (CoV = SD/mean) of measurements were calculated within each ROI. Data were compared using paired *t*-tests, factorial analysis of variance (ANOVA) and intraclass correlation (ICC) as appropriate. Using ANOVA, the residual standard deviation was used to calculate the 95% prediction interval for zero change of repeat WB ¹H MRS studies. All *p* values are quoted after Bonferroni corrections for multiple comparisons (where appropriate).

Results

Intersubject variability for whole brain proton spectroscopic imaging

The intersubject variability of the metabolite ratios (Cho/Cr, NAA/Cr and NAA/Cho) and concentrations (NAA, Cho and Cr) using the ROI template (Figure 5-1) are displayed in Table 5-1 and 5-2 respectively. In Figure 5-2 NAA, Cr and Cho signal-intensity normalised metabolite concentration parametric maps are displayed in comparison with a structural image. The intersubject variability was high with a mean (range) CoV across the ROIs for Cho/Cr of 21 (11 – 62%), NAA/Cho 17 (11 – 55%), NAA/Cr 13 (8 – 37%), NAA 12 (6 – 23%), choline of 31 (13 – 69%) and creatine 19 (7 – 61%) (Figure 5-3 and Figure 5-4).

Region of Interest	Choline/Creatine			NAA/Choline			NAA/Creatine		
	Mean	SD	CoV %	Mean	SD	CoV %	Mean	SD	CoV %
Anterior corpus callosum	0.63	0.39	61.81	5.23	2.85	54.58	1.79	0.67	37.35
Body of corpus callosum	0.27	0.07	24.47	6.45	0.93	14.47	1.59	0.23	14.35
Posterior corpus callosum	0.28	0.05	17.04	6.78	0.78	11.53	1.81	0.23	12.86
Corticospinal tract right	0.29	0.04	13.57	4.98	0.67	13.41	1.40	0.14	10.26
Corticospinal tract left	0.29	0.06	21.11	4.85	0.56	11.57	1.37	0.12	8.62
Anterior thalamic radiation right	0.32	0.06	18.37	5.29	0.67	12.68	1.44	0.12	8.30
Anterior thalamic radiation left	0.31	0.07	22.61	5.54	0.68	12.26	1.46	0.11	7.63
Inferior longitudinal fasciculus right	0.24	0.04	17.26	7.16	0.81	11.35	1.49	0.12	8.09
Inferior longitudinal fasciculus left	0.22	0.03	13.13	6.65	0.78	11.68	1.38	0.12	8.46
Superior longitudinal fasciculus right	0.23	0.03	11.93	6.77	0.83	12.30	1.50	0.13	8.57
Superior longitudinal fasciculus left	0.21	0.03	12.51	6.26	0.78	12.52	1.36	0.11	8.17
Thalamus right	0.31	0.05	15.84	5.37	0.68	12.58	1.59	0.18	11.57
Thalamus left	0.30	0.05	15.62	5.58	0.67	12.08	1.63	0.20	12.09
Pallidum right	0.29	0.05	16.50	5.71	0.84	14.67	1.49	0.12	8.23
Pallidum left	0.30	0.07	22.54	5.82	0.79	13.66	1.54	0.16	10.18
Putamen right	0.28	0.04	15.62	5.75	0.84	14.65	1.47	0.14	9.88
Putamen left	0.30	0.06	20.25	5.70	0.74	12.95	1.50	0.15	10.18
Dorsal Mid Brain	0.37	0.08	21.14	4.84	0.94	19.49	1.71	0.22	13.10
Ventral Midbrain	0.35	0.08	21.93	5.11	0.78	15.34	1.64	0.14	8.33
Frontal lobe right	0.21	0.06	27.24	4.42	0.87	19.79	0.97	0.13	13.79
Frontal lobe left	0.22	0.09	40.53	4.25	0.90	21.13	0.92	0.14	15.03
Hippocampus right	0.33	0.06	16.57	4.97	0.95	19.14	1.49	0.21	13.87
Hippocampus left	0.33	0.04	13.19	4.88	0.91	18.59	1.50	0.23	15.24
Occipital right	0.17	0.08	45.79	9.27	1.89	20.34	1.47	0.26	17.76
Occipital left	0.16	0.05	29.32	7.97	1.67	20.96	1.30	0.21	15.95
Parietal right	0.18	0.04	21.17	6.37	1.16	18.27	1.24	0.18	14.25
Parietal left	0.17	0.03	16.75	5.92	1.01	17.05	1.15	0.14	12.19
Peduncle right	0.28	0.04	14.32	4.69	0.65	13.80	1.27	0.17	13.37
Peduncle left	0.28	0.05	18.23	4.59	0.56	12.20	1.23	0.15	12.00
Pons right	0.45	0.11	24.90	3.94	0.90	22.73	1.74	0.42	24.08
Pons left	0.46	0.12	26.18	4.18	1.18	28.24	1.78	0.48	27.16
Temporal right	0.19	0.02	11.00	4.60	0.75	16.22	1.04	0.13	12.94
Temporal left	0.18	0.02	12.62	4.20	0.73	17.33	0.95	0.14	14.65
Mean	0.29	0.06	21.24	5.58	0.93	16.96	1.43	0.19	13.30

Table 5-1 Intersubject variability of metabolite ratios for whole brain proton spectroscopy

Intersubject variability for Choline /Creatine, N-Acetyl aspartate (NAA)/Choline and N-Acetyl aspartate/Creatine. Data displayed were obtained in 32 subjects and show mean, standard deviation (SD) and percentage coefficient of variation (CoV%) for each region of interest (ROI).

Region of Interest	NAA			Cho			Cr		
	Mean	SD	CoV %	Mean	SD	CoV %	Mean	SD	CoV %
Anterior corpus callosum	11778.3	2644.6	22.5	3928.9	1593.9	40.6	9561.7	3934.6	41.1
Body of corpus callosum	14215.7	1799.0	12.7	2535.7	1131.0	44.6	9357.7	2010.0	21.5
Posterior corpus callosum	14769.6	1782.9	12.1	2256.2	377.8	16.7	8508.9	1788.5	21.0
Corticospinal tract right	12802.3	765.3	6.0	2660.9	334.7	12.6	8612.0	561.5	6.5
Corticospinal tract left	12545.5	691.9	5.5	2651.9	407.9	15.4	8667.5	804.0	9.3
Anterior thalamic radiation right	11825.9	882.6	7.5	2973.8	1568.1	52.7	9130.7	3498.9	38.3
Anterior thalamic radiation left	12371.3	722.3	5.8	2958.6	1307.1	44.2	8946.8	1674.1	18.7
Inferior longitudinal fasciculus right	13292.0	1147.9	8.6	2220.6	817.6	36.8	9015.0	1466.9	16.3
Inferior longitudinal fasciculus left	12006.4	1119.4	9.3	1976.1	437.8	22.2	8232.2	794.6	9.7
Superior longitudinal fasciculus right	13347.6	992.9	7.4	2067.6	302.5	14.6	8578.7	613.6	7.2
Superior longitudinal fasciculus left	11969.7	1139.7	9.5	1905.6	285.7	15.0	7986.0	675.7	8.5
Thalamus right	12445.6	1926.6	15.5	2417.1	474.5	19.6	8043.5	1531.9	19.0
Thalamus left	12371.1	2000.5	16.2	2313.6	442.4	19.1	7825.0	1594.3	20.4
Pallidum right	12804.3	1312.2	10.2	2517.1	542.8	21.6	8952.5	1091.4	12.2
Pallidum left	13159.7	1388.3	10.5	2554.0	509.3	19.9	8877.8	1140.2	12.8
Putamen right	13276.7	1546.3	11.6	2601.2	647.9	24.9	9356.6	1079.3	11.5
Putamen left	13664.1	1426.8	10.4	2791.6	742.0	26.6	9473.1	1071.1	11.3
Dorsal Mid Brain	13584.3	2699.4	19.9	3003.7	791.2	26.3	8169.9	1740.5	21.3
Ventral Mid brain	13478.7	1588.7	11.8	2840.5	546.8	19.3	8576.1	1110.9	13.0
Frontal lobe right	7793.6	767.3	9.8	1991.8	1156.6	58.1	6519.3	2158.9	33.1
Frontal lobe left	7724.7	818.0	10.6	2042.6	1261.6	61.8	6379.4	1701.0	26.7
Hippocampus right	12640.0	1255.2	9.9	3121.1	928.0	29.7	9388.5	1823.7	19.4
Hippocampus left	12628.8	1315.5	10.4	3257.6	1660.3	51.0	9433.9	2998.5	31.8
Occipital right	12968.4	1817.8	14.0	1667.8	1146.9	68.8	8480.5	1905.3	22.5
Occipital left	11378.9	1562.1	13.7	1507.6	627.7	41.6	7655.5	1042.3	13.6
Parietal right	11321.4	1039.0	9.2	1668.9	532.8	31.9	7682.2	914.2	11.9
Parietal left	10300.9	977.7	9.5	1550.0	468.8	30.2	7164.8	834.4	11.6
Peduncle right	16640.8	1451.7	8.7	3771.9	618.9	16.4	13721.4	2252.4	16.4
Peduncle left	16388.9	1198.7	7.3	3760.7	927.0	24.6	13589.7	1511.0	11.1
Pons right	14199.4	2778.6	19.6	3757.8	918.3	24.4	8322.3	1989.1	23.9
Pons left	14712.8	2663.6	18.1	4076.3	1777.4	43.6	9308.0	5645.1	60.6
Temporal right	9137.6	1119.4	12.3	1834.7	341.9	18.6	6849.1	881.4	12.9
Temporal left	8266.0	1267.6	15.3	1683.3	344.8	20.5	6203.0	751.6	12.1
Mean	12479.1	1442.7	11.6	2571.7	787.0	30.7	8683.9	1654.3	19.0

Table 5-2 Intersubject variability of metabolite concentrations for whole brain proton spectroscopy

Intersubject variability for N-Acetyl aspartate (NAA), Choline (Cho) and Creatine (Cr). Data displayed were obtained in 32 subjects and show mean, standard deviation (SD) and percentage coefficient of variation (CoV%) for each region of interest (ROI).

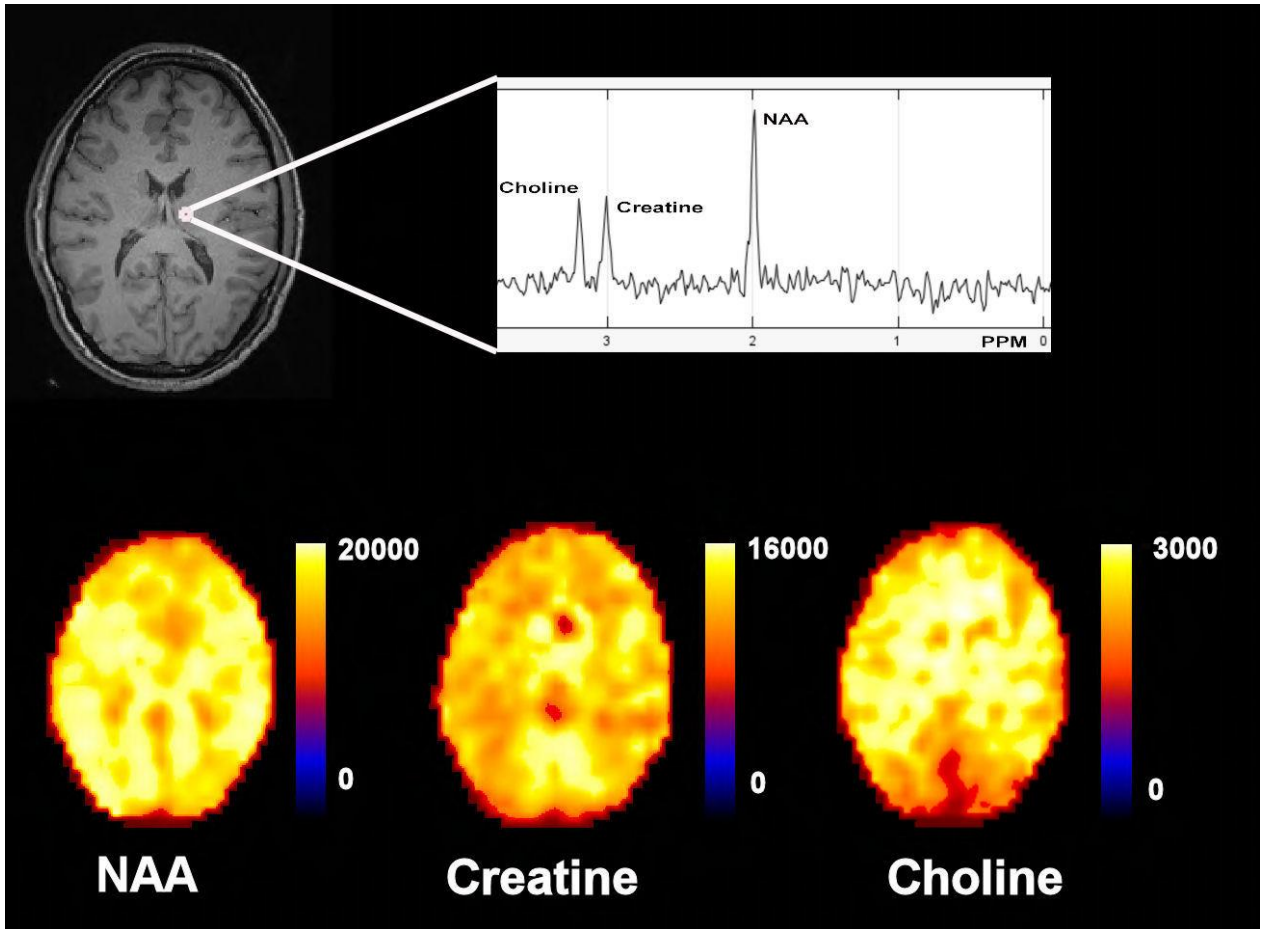


Figure 5-2 Region of interest template with a representative spectra from right thalamus

T1 weighted magnetic resonance image in MNI152 space (2mm resolution) with a representative spectra from the right thalamus and N-acetyl aspartate (NAA), Creatine (Cr) and Choline (Cho) signal-intensity normalised metabolite concentration parametric maps. PPM (parts per million).

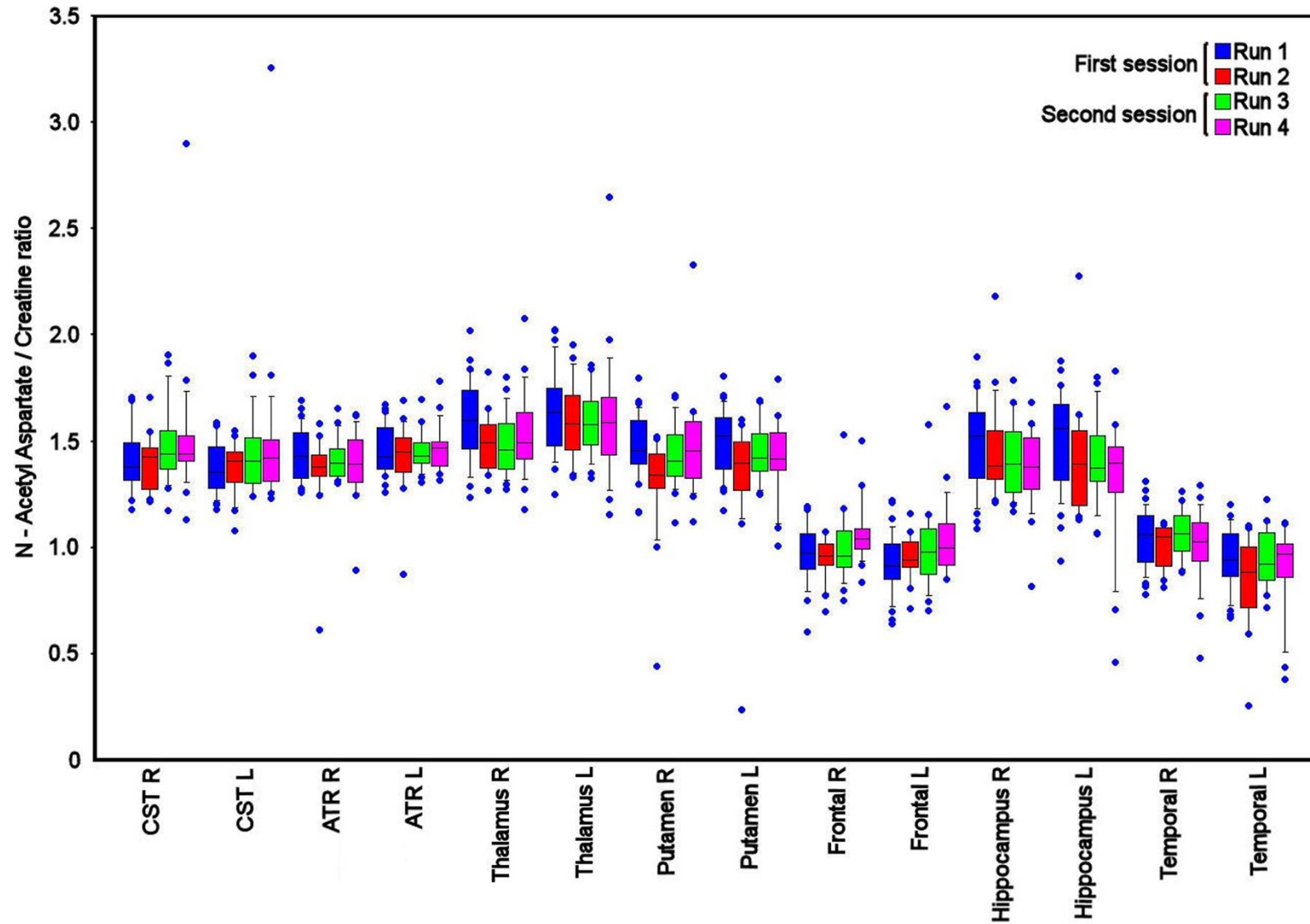


Figure 5-3 Variability in N Acetyl Aspartate / Creatine ratio measurements

Box and whisker plot for N Acetyl Aspartate / Creatine ratio for a selection of the regions of interest (ROI), including right (R) and left (L) corticospinal (CST), anterior thalamic radiation (ATR), thalamus, putamen, frontal lobe, hippocampus and temporal lobe. The spread of data within each ROI reflects inter subject variation, while the difference between runs 1 – 2 and 3 – 4 reflects within session reproducibility, and the change from first to second sessions reflects between session reproducibility. The central lines in each box denote median values, the lower and upper boundaries the 25th and 75th centile, the error bars the 10th and 90th centile, and the closed circles outlying data points.

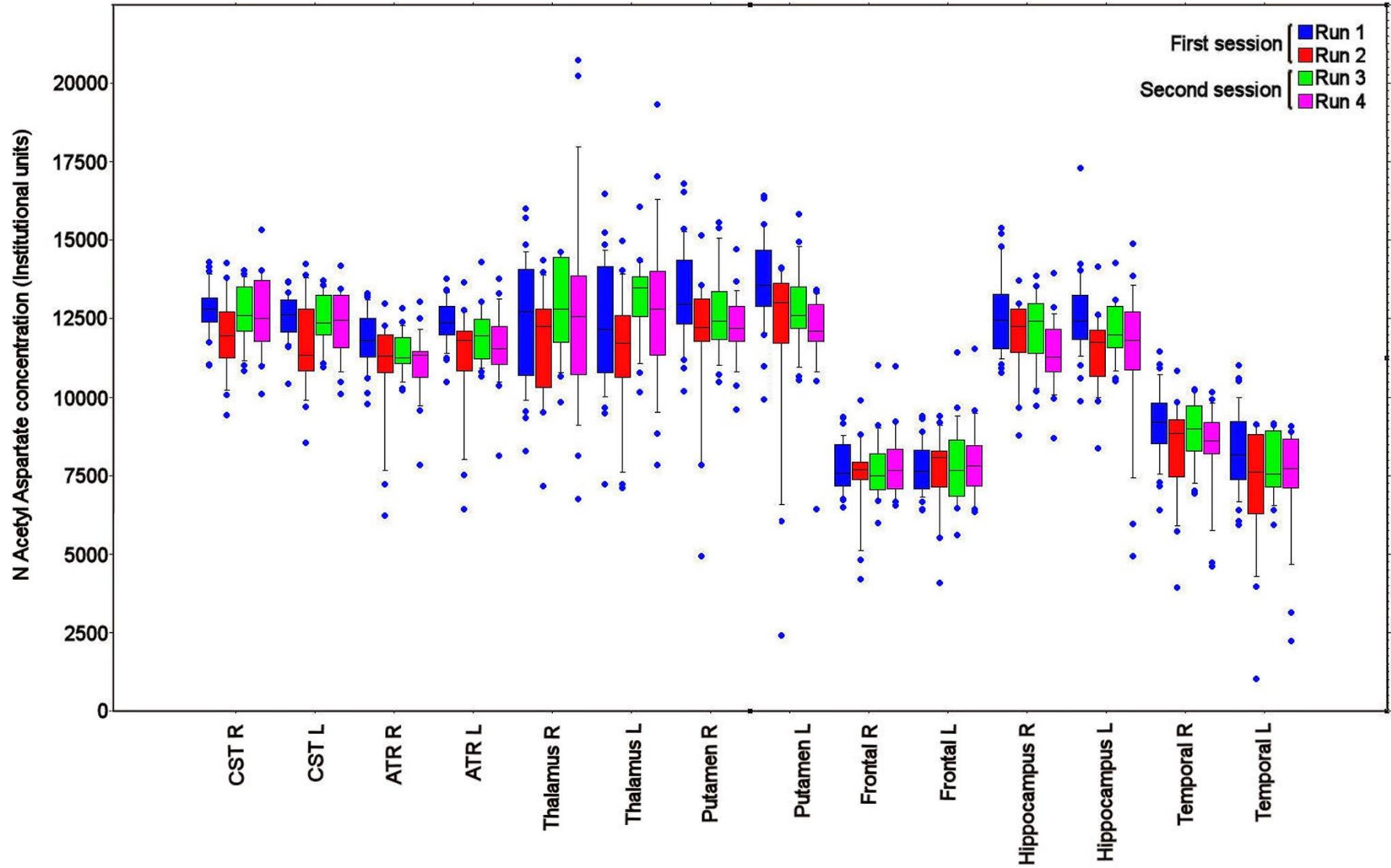


Figure 5-4 Variability in N Acetyl Aspartate concentration

Box and whisker plot for N Acetyl Aspartate for a selection of the regions of interest (ROI), including right (R) and left (L) corticospinal (CST), anterior thalamic radiation (ATR), thalamus, putamen, frontal lobe, hippocampus and temporal lobe. The spread of data within each ROI reflects inter subject variation, while the difference between runs 1 – 2 and 3 – 4 reflects within session reproducibility, and the change from first to second sessions reflects between session reproducibility. The central lines in each box denote median values, the lower and upper boundaries the 25th and 75th centile, the error bars the 10th and 90th centile, and the closed circles outlying data points.

Within session and between session reproducibility of whole brain proton spectroscopic imaging

The individual ROI data for within and between session reproducibility were variable across the different brain regions, but lower than the values for intersubject variability (Table 5-3). The within and between session reproducibility measurements were similar for Cho/Cr, NAA/Choline, Cho and Cr (11.9%, 11.4%, 14.3 and 10.6% vs. 11.8%, 11.4%, 13.5% and 10.5%, and $p = 0.44, 0.87, 0.08$ and 0.86 respectively, paired 't' tests), but for NAA/Creatine and NAA between session reproducibility was lower than within session reproducibility (9.3% and 9.1% vs. 10.1% and 9.9%, $p < 0.05$ paired 't' test with Bonferroni correction). The difference between intersubject variability, within and between session reproducibility is displayed for a selection of ROIs for the metabolite ratios and concentrations in figure 5-3 and 5-4, respectively.

The intraclass correlation coefficient (ICC) for within and between session reproducibility within brain regions of mixed cortical and deep grey, and white matter are displayed in Table 5-4.

A

	Cho/Cr		NAA/Cho		NAA/Cr	
	Within Session	Between Session	Within Session	Between Session	Within Session	Between Session
Anterior corpus callosum	0.21 ± 0.21	0.23 ± 0.20	1.73 ± 1.40	2.63 ± 2.86	0.48 ± 0.42	0.50 ± 0.47
Body of corpus callosum	0.03 ± 0.03	0.05 ± 0.06	0.69 ± 0.65	0.68 ± 0.64	0.18 ± 0.16	0.16 ± 0.14
Posterior corpus callosum	0.04 ± 0.08	0.05 ± 0.08	0.51 ± 0.50	0.55 ± 0.56	0.25 ± 0.30	0.25 ± 0.31
Corticospinal tract right	0.03 ± 0.05	0.02 ± 0.03	0.52 ± 0.63	0.60 ± 0.70	0.09 ± 0.15	0.10 ± 0.15
Corticospinal tract left	0.03 ± 0.03	0.03 ± 0.05	0.48 ± 0.58	0.46 ± 0.55	0.11 ± 0.21	0.09 ± 0.17
Anterior thalamic radiation right	0.04 ± 0.08	0.05 ± 0.08	0.32 ± 0.37	0.32 ± 0.26	0.09 ± 0.13	0.06 ± 0.10
Anterior thalamic radiation left	0.04 ± 0.05	0.04 ± 0.04	0.29 ± 0.22	0.35 ± 0.33	0.06 ± 0.08	0.06 ± 0.06
Inferior longitudinal fasciculus right	0.03 ± 0.07	0.03 ± 0.09	0.50 ± 0.59	0.52 ± 0.48	0.07 ± 0.10	0.06 ± 0.09
Inferior longitudinal fasciculus left	0.02 ± 0.05	0.02 ± 0.04	0.50 ± 0.69	0.44 ± 0.53	0.08 ± 0.14	0.06 ± 0.09
Superior longitudinal fasciculus right	0.01 ± 0.02	0.01 ± 0.02	0.59 ± 0.74	0.61 ± 0.68	0.07 ± 0.07	0.06 ± 0.06
Superior longitudinal fasciculus left	0.01 ± 0.02	0.01 ± 0.01	0.38 ± 0.40	0.44 ± 0.34	0.06 ± 0.08	0.06 ± 0.06
Thalamus right	0.03 ± 0.03	0.03 ± 0.03	0.52 ± 0.45	0.46 ± 0.48	0.12 ± 0.12	0.12 ± 0.10
Thalamus left	0.03 ± 0.02	0.03 ± 0.03	0.56 ± 0.46	0.61 ± 0.51	0.14 ± 0.16	0.14 ± 0.13
Pallidum right	0.04 ± 0.04	0.03 ± 0.03	0.57 ± 0.66	0.51 ± 0.58	0.13 ± 0.17	0.12 ± 0.15
Pallidum left	0.05 ± 0.06	0.04 ± 0.05	1.11 ± 1.12	0.99 ± 0.95	0.18 ± 0.24	0.15 ± 0.17
Putamen right	0.03 ± 0.03	0.03 ± 0.03	0.66 ± 0.62	0.48 ± 0.52	0.12 ± 0.14	0.11 ± 0.13
Putamen left	0.04 ± 0.04	0.04 ± 0.04	0.74 ± 0.84	0.73 ± 0.80	0.14 ± 0.18	0.13 ± 0.15
Dorsal mid brain	0.04 ± 0.07	0.04 ± 0.07	0.46 ± 0.42	0.54 ± 0.45	0.27 ± 0.42	0.26 ± 0.40
Ventral mid brain	0.06 ± 0.06	0.05 ± 0.05	0.62 ± 0.58	0.55 ± 0.64	0.22 ± 0.32	0.20 ± 0.28
Frontal lobe right	0.04 ± 0.04	0.03 ± 0.04	0.47 ± 0.28	0.57 ± 0.48	0.07 ± 0.06	0.08 ± 0.08
Frontal lobe left	0.05 ± 0.05	0.04 ± 0.05	0.38 ± 0.31	0.50 ± 0.47	0.06 ± 0.05	0.07 ± 0.08
Hippocampus right	0.03 ± 0.03	0.02 ± 0.03	0.48 ± 0.33	0.49 ± 0.38	0.14 ± 0.11	0.13 ± 0.10
Hippocampus left	0.03 ± 0.04	0.03 ± 0.03	0.53 ± 0.48	0.52 ± 0.46	0.18 ± 0.15	0.16 ± 0.15
Occipital right	0.03 ± 0.08	0.05 ± 0.13	1.09 ± 1.09	1.22 ± 1.13	0.09 ± 0.13	0.11 ± 0.14
Occipital left	0.03 ± 0.07	0.03 ± 0.06	0.91 ± 0.92	0.90 ± 0.86	0.09 ± 0.10	0.09 ± 0.09
Parietal right	0.03 ± 0.08	0.03 ± 0.08	0.72 ± 0.68	0.81 ± 0.74	0.10 ± 0.13	0.12 ± 0.13
Parietal left	0.02 ± 0.04	0.02 ± 0.03	0.49 ± 0.50	0.69 ± 0.60	0.09 ± 0.14	0.11 ± 0.15
Peduncle right	0.10 ± 0.26	0.06 ± 0.19	0.43 ± 0.38	0.42 ± 0.38	0.17 ± 0.19	0.15 ± 0.17
Peduncle left	0.09 ± 0.33	0.08 ± 0.28	0.42 ± 0.39	0.39 ± 0.42	0.13 ± 0.22	0.12 ± 0.21
Pons right	0.06 ± 0.06	0.05 ± 0.04	0.63 ± 1.02	0.54 ± 0.79	0.21 ± 0.16	0.17 ± 0.15
Pons left	0.06 ± 0.06	0.06 ± 0.05	0.68 ± 1.23	0.53 ± 0.96	0.24 ± 0.19	0.22 ± 0.18
Temporal right	0.02 ± 0.04	0.02 ± 0.03	0.32 ± 0.33	0.39 ± 0.33	0.07 ± 0.08	0.05 ± 0.07
Temporal left	0.02 ± 0.02	0.02 ± 0.02	0.44 ± 0.55	0.39 ± 0.48	0.10 ± 0.13	0.08 ± 0.10
Mean	0.04 ± 0.10	0.04 ± 0.09	0.60 ± 0.73	0.63 ± 0.87	0.14 ± 0.20	0.13 ± 0.20

B

	Cho/Cr		NAA/Cho		NAA/Cr	
	Within Session	Between Session	Within Session	Between Session	Within Session	Between Session
Anterior corpus callosum	39.56 ± 34.49	46.44 ± 35.47	41.96 ± 40.19	47.03 ± 38.81	40.69 ± 40.56	38.17 ± 37.48
Body of corpus callosum	10.71 ± 7.72	14.59 ± 13.44	10.33 ± 9.86	10.53 ± 9.64	11.09 ± 9.58	9.92 ± 7.66
Posterior corpus callosum	10.36 ± 15.49	12.99 ± 15.49	7.78 ± 8.39	8.35 ± 8.72	12.93 ± 14.36	12.68 ± 14.41
Corticospinal tract right	8.15 ± 11.83	7.24 ± 8.49	8.92 ± 8.72	10.75 ± 11.00	5.57 ± 6.83	6.54 ± 7.48
Corticospinal tract left	8.21 ± 8.91	8.54 ± 11.98	8.63 ± 8.73	8.59 ± 8.94	6.50 ± 9.37	5.98 ± 7.99
Anterior thalamic radiation right	12.29 ± 17.17	12.49 ± 16.87	6.63 ± 8.65	6.34 ± 5.97	6.68 ± 11.84	4.62 ± 8.63
Anterior thalamic radiation left	11.74 ± 12.45	11.06 ± 11.21	5.39 ± 4.66	6.58 ± 6.58	4.45 ± 6.73	4.45 ± 4.72
Inferior longitudinal fasciculus right	7.47 ± 11.18	9.01 ± 14.85	7.70 ± 10.50	7.79 ± 8.22	5.17 ± 8.28	4.08 ± 6.72
Inferior longitudinal fasciculus left	8.80 ± 11.95	7.51 ± 9.58	8.80 ± 15.09	7.60 ± 11.26	6.50 ± 13.10	5.12 ± 9.11
Superior longitudinal fasciculus right	5.26 ± 7.34	5.46 ± 6.46	7.80 ± 8.51	8.47 ± 8.18	4.27 ± 3.98	3.94 ± 3.93
Superior longitudinal fasciculus left	5.99 ± 6.54	6.16 ± 5.52	6.32 ± 8.12	7.14 ± 6.22	4.37 ± 7.11	4.86 ± 5.35
Thalamus right	9.10 ± 7.04	9.05 ± 8.39	9.83 ± 8.49	8.38 ± 8.82	7.56 ± 7.23	7.91 ± 6.52
Thalamus left	8.44 ± 7.22	9.67 ± 8.10	10.16 ± 8.33	11.01 ± 9.07	8.81 ± 8.51	8.35 ± 7.58
Pallidum right	12.54 ± 12.38	10.84 ± 9.75	11.90 ± 18.78	9.93 ± 14.88	10.00 ± 16.35	8.58 ± 13.02
Pallidum left	14.69 ± 18.61	12.82 ± 15.19	20.59 ± 25.85	17.26 ± 20.01	14.13 ± 22.87	11.12 ± 16.82
Putamen right	11.28 ± 9.83	10.19 ± 10.22	13.04 ± 15.64	9.20 ± 12.42	8.98 ± 13.40	8.15 ± 11.15
Putamen left	11.96 ± 13.74	12.21 ± 13.27	14.48 ± 20.63	13.15 ± 16.67	11.21 ± 18.53	9.47 ± 14.13
Dorsal mid brain	10.58 ± 12.20	9.68 ± 11.80	9.89 ± 9.67	11.15 ± 9.24	14.38 ± 17.92	13.82 ± 15.09
Ventral mid brain	17.27 ± 16.76	14.07 ± 13.13	13.50 ± 17.99	10.99 ± 15.45	13.97 ± 21.91	12.09 ± 17.39
Frontal lobe right	16.12 ± 13.73	14.71 ± 15.11	10.03 ± 6.45	12.96 ± 11.93	6.84 ± 6.76	8.15 ± 8.28
Frontal lobe left	18.83 ± 15.03	17.00 ± 16.07	8.56 ± 7.40	11.34 ± 12.00	6.50 ± 5.81	7.34 ± 8.24
Hippocampus right	8.44 ± 9.05	7.71 ± 7.78	9.88 ± 6.36	9.92 ± 7.17	9.88 ± 8.01	9.03 ± 7.43
Hippocampus left	11.08 ± 15.17	8.87 ± 11.62	12.05 ± 12.26	11.51 ± 11.51	13.80 ± 13.84	11.98 ± 13.01
Occipital right	11.27 ± 15.53	13.04 ± 22.14	13.52 ± 17.83	13.83 ± 14.95	6.99 ± 12.66	7.68 ± 10.33
Occipital left	11.35 ± 18.54	11.08 ± 17.57	12.81 ± 15.86	12.21 ± 13.82	6.89 ± 9.52	7.13 ± 7.67
Parietal right	8.37 ± 13.84	10.15 ± 13.54	10.61 ± 9.97	12.15 ± 10.74	7.22 ± 8.23	9.06 ± 8.90
Parietal left	7.77 ± 12.53	9.27 ± 11.44	7.92 ± 8.51	11.36 ± 9.84	6.81 ± 8.96	9.02 ± 10.03
Peduncle right	16.93 ± 25.85	13.01 ± 19.52	9.75 ± 10.40	9.45 ± 9.10	12.55 ± 14.44	11.24 ± 11.89
Peduncle left	12.33 ± 21.86	12.20 ± 18.94	9.79 ± 10.34	8.91 ± 10.24	9.18 ± 10.44	8.93 ± 10.51
Pons right	12.89 ± 12.02	10.61 ± 8.31	13.10 ± 15.61	11.86 ± 13.39	12.72 ± 10.05	9.57 ± 9.16
Pons left	13.78 ± 12.87	14.85 ± 11.69	14.52 ± 15.40	11.69 ± 14.43	15.22 ± 12.94	12.61 ± 11.73
Temporal right	8.35 ± 12.58	8.46 ± 10.05	7.86 ± 9.41	9.07 ± 8.80	7.07 ± 9.77	5.63 ± 8.36
Temporal left	11.18 ± 13.93	9.34 ± 11.57	13.12 ± 20.92	10.86 ± 16.65	12.94 ± 18.93	9.63 ± 15.11
Mean	11.91 ± 15.77	11.83 ± 15.65	11.43 ± 15.62	11.44 ± 14.77	10.06 ± 15.29	9.30 ± 13.43

C

	NAA		Cho		Cr	
	Within Session	Between Session	Within Session	Between Session	Within Session	Between Session
Anterior corpus callosum	3279.9 ± 2703.7	2968.5 ± 2697.1	1878.8 ± 2338.6	1719.7 ± 2458.7	3697.5 ± 2975.4	3814.5 ± 3818.6
Body of corpus callosum	1141.0 ± 815.6	1314.2 ± 1162.3	492.2 ± 1191.7	656.2 ± 1355.5	1201.2 ± 1391.4	1317.6 ± 1327.6
Posterior corpus callosum	1091.4 ± 989.5	1186.1 ± 1089.6	318.2 ± 376.5	323.3 ± 387.4	1309.3 ± 1398.6	1432.2 ± 1454.5
Corticospinal tract right	702.9 ± 734.4	590.2 ± 608.4	284.2 ± 646.5	256.6 ± 500.8	519.4 ± 671.9	504.0 ± 614.5
Corticospinal tract left	673.5 ± 700.7	558.0 ± 625.5	231.7 ± 240.5	196.4 ± 194.1	521.8 ± 544.5	378.7 ± 465.1
Anterior thalamic radiation right	827.2 ± 912.2	740.0 ± 775.1	422.3 ± 422.9	523.5 ± 598.9	716.5 ± 565.6	904.9 ± 1558.5
Anterior thalamic radiation left	789.7 ± 1023.5	727.1 ± 938.9	387.9 ± 374.1	424.0 ± 536.9	604.6 ± 677.1	731.0 ± 860.9
Inferior longitudinal fasciculus right	798.9 ± 929.8	816.7 ± 881.6	179.7 ± 175.5	287.8 ± 607.3	627.6 ± 553.7	712.5 ± 901.6
Inferior longitudinal fasciculus left	802.6 ± 1058.1	775.9 ± 969.3	207.5 ± 431.0	202.7 ± 317.7	419.8 ± 430.0	466.5 ± 498.6
Superior longitudinal fasciculus right	548.9 ± 655.5	624.2 ± 673.6	208.5 ± 285.7	216.2 ± 226.4	465.4 ± 459.7	471.0 ± 454.4
Superior longitudinal fasciculus left	623.6 ± 768.8	657.1 ± 726.0	197.0 ± 190.2	177.3 ± 178.5	493.8 ± 529.0	478.7 ± 508.6
Thalamus right	1307.2 ± 1442.7	1214.1 ± 1308.9	294.7 ± 242.3	266.5 ± 269.1	864.7 ± 682.2	968.4 ± 780.6
Thalamus left	1219.0 ± 1244.6	1301.8 ± 1171.3	330.9 ± 304.3	399.7 ± 438.0	996.5 ± 757.5	1079.0 ± 894.7
Pallidum right	1211.9 ± 1209.2	1087.1 ± 1259.3	427.3 ± 354.7	334.5 ± 299.4	847.8 ± 581.4	722.5 ± 635.1
Pallidum left	1457.9 ± 1760.3	1212.6 ± 1515.8	453.0 ± 300.8	365.3 ± 314.9	935.8 ± 814.1	829.6 ± 789.2
Putamen right	1154.7 ± 1145.8	1084.7 ± 1280.7	368.4 ± 404.2	317.3 ± 407.0	794.9 ± 720.1	770.7 ± 726.4
Putamen left	1286.2 ± 1634.9	1289.1 ± 1553.6	416.5 ± 365.3	413.6 ± 434.6	804.7 ± 763.3	775.7 ± 788.2
Dorsal Mid Brain	2179.9 ± 2135.5	1996.1 ± 1847.3	423.3 ± 328.8	415.8 ± 311.8	1160.2 ± 1060.2	1229.0 ± 881.1
Ventral Midbrain	1348.3 ± 1791.0	1184.9 ± 1597.5	412.7 ± 360.1	316.6 ± 315.8	947.6 ± 939.3	901.7 ± 835.9
Frontal lobe right	451.9 ± 529.9	548.9 ± 575.8	379.3 ± 499.0	409.2 ± 396.5	700.7 ± 667.7	756.8 ± 912.2
Frontal lobe left	516.0 ± 575.2	596.0 ± 565.1	537.9 ± 560.2	430.3 ± 463.8	826.1 ± 826.4	739.7 ± 591.6
Hippocampus right	861.7 ± 658.3	845.6 ± 764.6	388.7 ± 341.1	289.6 ± 226.4	797.4 ± 555.3	676.4 ± 532.2
Hippocampus left	1050.0 ± 1232.9	1001.4 ± 1147.3	380.9 ± 300.4	338.5 ± 278.2	853.3 ± 765.6	790.2 ± 659.6
Occipital right	658.8 ± 781.0	749.0 ± 837.7	235.3 ± 368.6	390.9 ± 986.0	526.1 ± 653.5	770.4 ± 1264.1
Occipital left	582.0 ± 799.6	567.2 ± 692.2	277.4 ± 611.4	269.8 ± 644.9	496.8 ± 542.5	545.5 ± 717.1
Parietal right	528.1 ± 648.3	536.3 ± 609.6	232.4 ± 445.5	208.5 ± 334.0	465.2 ± 594.3	494.0 ± 540.5
Parietal left	507.5 ± 598.6	527.3 ± 610.9	177.0 ± 216.8	152.8 ± 192.4	487.6 ± 581.7	491.7 ± 535.7
Peduncle right	1578.9 ± 1632.0	1470.6 ± 1444.0	770.9 ± 1507.8	541.6 ± 1107.7	1199.7 ± 1218.9	1295.7 ± 1422.0
Peduncle left	1357.3 ± 1592.7	1337.8 ± 1269.4	960.6 ± 3271.4	862.4 ± 2572.0	1065.0 ± 1330.2	1230.5 ± 1142.6
Pons right	1590.4 ± 1560.1	1617.1 ± 1589.4	411.3 ± 295.7	395.4 ± 384.1	990.4 ± 638.2	1048.3 ± 776.8
Pons left	1569.6 ± 1464.3	1401.8 ± 1561.0	553.4 ± 612.4	368.8 ± 474.5	1532.3 ± 2594.0	985.7 ± 797.7
Temporal right	843.6 ± 924.7	768.5 ± 884.4	185.3 ± 137.6	176.5 ± 204.3	513.8 ± 503.8	557.1 ± 551.7
Temporal left	892.9 ± 1170.0	839.5 ± 1017.6	196.4 ± 159.4	183.8 ± 192.8	545.4 ± 674.7	522.7 ± 591.2
Mean	1073.7 ± 1350.1	1034.4 ± 1280.9	412.8 ± 896.0	388.8 ± 835.9	876.6 ± 1163.6	890.7 ± 1223.2

D

	NAA		Cho		Cr	
	Within Session	Between Session	Within Session	Between Session	Within Session	Between Session
Anterior corpus callosum	38.0 ± 41.5	33.1 ± 38.1	44.6 ± 37.8	40.5 ± 37.9	42.1 ± 38.2	37.5 ± 37.2
Body of corpus callosum	8.6 ± 6.2	9.5 ± 8.4	15.8 ± 17.8	18.8 ± 22.3	13.7 ± 14.0	14.6 ± 13.9
Posterior corpus callosum	8.0 ± 7.4	8.4 ± 7.8	13.9 ± 13.7	13.9 ± 14.7	16.1 ± 15.7	17.6 ± 16.9
Corticospinal tract right	5.7 ± 6.2	4.8 ± 5.2	8.8 ± 13.6	8.1 ± 11.1	6.1 ± 7.5	5.9 ± 7.0
Corticospinal tract left	5.7 ± 6.3	4.7 ± 5.6	8.7 ± 8.3	7.6 ± 7.3	6.4 ± 7.9	4.7 ± 6.7
Anterior thalamic radiation right	7.9 ± 9.7	6.9 ± 8.1	14.5 ± 12.9	16.9 ± 14.8	8.5 ± 7.0	9.5 ± 10.4
Anterior thalamic radiation left	7.2 ± 10.4	6.5 ± 9.1	13.0 ± 10.7	14.7 ± 15.6	7.0 ± 7.6	8.4 ± 9.6
Inferior longitudinal fasciculus right	6.6 ± 8.2	6.6 ± 7.5	8.3 ± 7.0	9.6 ± 13.1	7.0 ± 5.8	7.6 ± 7.8
Inferior longitudinal fasciculus left	7.6 ± 11.5	7.1 ± 10.1	8.5 ± 11.2	8.7 ± 9.4	5.4 ± 6.1	5.8 ± 6.5
Superior longitudinal fasciculus right	4.4 ± 5.8	5.0 ± 5.8	10.1 ± 11.7	10.5 ± 10.0	5.6 ± 6.1	5.8 ± 6.1
Superior longitudinal fasciculus left	5.5 ± 7.7	5.8 ± 7.2	10.4 ± 9.5	9.5 ± 9.3	6.5 ± 8.3	6.4 ± 7.9
Thalamus right	10.5 ± 11.0	9.9 ± 9.8	12.5 ± 10.6	11.6 ± 11.5	10.7 ± 9.0	12.3 ± 10.4
Thalamus left	10.2 ± 11.5	10.9 ± 10.3	14.3 ± 13.0	16.7 ± 16.5	12.7 ± 10.9	13.7 ± 11.8
Pallidum right	11.1 ± 14.4	9.6 ± 13.2	16.7 ± 13.3	13.1 ± 12.3	10.1 ± 7.8	8.8 ± 9.1
Pallidum left	14.3 ± 23.4	11.0 ± 18.4	19.3 ± 15.3	15.5 ± 14.9	12.5 ± 16.6	10.6 ± 14.1
Putamen right	10.0 ± 12.0	9.0 ± 11.9	14.2 ± 13.0	12.3 ± 14.0	9.1 ± 8.6	8.9 ± 9.1
Putamen left	12.1 ± 19.4	11.1 ± 16.4	16.6 ± 14.3	16.0 ± 16.0	10.0 ± 12.3	9.3 ± 12.0
Dorsal Mid Brain	15.5 ± 15.3	14.2 ± 12.1	14.0 ± 11.9	14.1 ± 10.7	13.2 ± 12.1	14.8 ± 10.8
Ventral Midbrain	13.0 ± 24.1	10.3 ± 18.6	16.4 ± 16.1	12.5 ± 13.7	12.9 ± 16.3	11.8 ± 13.4
Frontal lobe right	6.3 ± 8.6	7.6 ± 9.0	18.3 ± 16.7	20.8 ± 17.4	11.0 ± 10.1	11.6 ± 11.8
Frontal lobe left	7.1 ± 9.0	8.1 ± 8.6	23.4 ± 16.2	20.7 ± 19.7	12.3 ± 10.9	11.7 ± 9.7
Hippocampus right	7.4 ± 5.9	7.1 ± 6.6	13.0 ± 8.6	10.5 ± 8.1	8.7 ± 5.9	7.8 ± 6.3
Hippocampus left	9.6 ± 12.8	8.7 ± 11.4	12.9 ± 10.4	12.1 ± 10.0	9.1 ± 7.5	9.0 ± 7.7
Occipital right	5.6 ± 7.5	6.1 ± 7.1	11.4 ± 14.1	13.0 ± 18.8	5.9 ± 7.3	7.7 ± 9.8
Occipital left	5.6 ± 8.9	5.4 ± 7.9	11.3 ± 16.0	11.4 ± 15.7	6.1 ± 6.7	6.6 ± 7.4
Parietal right	4.7 ± 5.9	4.8 ± 5.5	10.3 ± 11.9	10.0 ± 10.7	5.8 ± 7.6	6.4 ± 7.2
Parietal left	4.8 ± 5.7	5.1 ± 5.8	9.7 ± 8.8	8.5 ± 8.5	6.6 ± 8.6	6.9 ± 7.9
Peduncle right	10.9 ± 13.0	9.8 ± 11.0	15.9 ± 19.1	12.0 ± 15.5	10.1 ± 12.7	9.9 ± 11.5
Peduncle left	9.8 ± 13.3	9.2 ± 10.3	13.3 ± 22.2	12.3 ± 18.7	8.9 ± 14.0	9.7 ± 11.5
Pons right	13.5 ± 16.4	12.1 ± 13.2	12.7 ± 11.4	11.7 ± 11.8	13.4 ± 9.6	13.4 ± 10.4
Pons left	12.9 ± 14.9	10.5 ± 13.0	14.5 ± 16.7	11.1 ± 15.5	15.7 ± 16.7	12.7 ± 11.4
Temporal right	10.8 ± 13.5	9.2 ± 12.1	10.6 ± 7.4	9.5 ± 9.0	8.5 ± 9.2	8.6 ± 8.8
Temporal left	14.4 ± 24.0	12.0 ± 19.1	13.6 ± 14.3	12.1 ± 14.0	11.2 ± 17.4	10.0 ± 14.4
Mean	9.9 ± 15.4	9.1 ± 13.4	14.3 ± 15.9	13.5 ± 16.2	10.6 ± 13.8	10.5 ± 13.2

Table 5-3 Within session and between session variability of metabolites for whole brain proton spectroscopy

Individual region of interest measurements for within session reproducibility obtained in the first and second imaging sessions in 17 and 16 subjects respectively, and the between session reproducibility for those 22 subjects who underwent imaging at both sessions. Data displayed are standard deviation (A & C) and percentage coefficient of variation (B & D) for metabolite ratios (Choline (Cho)/Creatine (Cr), N-Acetyl aspartate (NAA)/ Choline and NAA/Cr and metabolite concentrations (NAA, Cho

	Mixed		White	
	Within	Between	Within	Between
Cho/Cr	0.76(0.72 – 0.80)	0.71(0.68 – 0.75)	0.50(0.41 – 0.58)	0.58(0.53 – 0.63)
NAA/Cho	0.84(0.82 – 0.87)	0.82(0.80 – 0.84)	0.78(0.74 – 0.82)	0.56(0.51 – 0.61)
NAA/Cr	0.76(0.72 – 0.80)	0.79(0.76 – 0.81)	0.60(0.52 – 0.66)	0.55(0.49 – 0.60)
NAA	0.81(0.77 – 0.84)	0.80(0.78 – 0.83)	0.63(0.56 – 0.68)	0.58(0.53 – 0.63)
Cho	0.84(0.81 – 0.86)	0.75(0.71 – 0.78)	0.53(0.44 – 0.60)	0.61(0.56 – 0.66)
Cr	0.84(0.81 – 0.86)	0.77(0.74 – 0.79)	0.73(0.68 – 0.77)	0.66(0.61 – 0.70)

Table 5-4 Within session and between session intraclass correlation coefficient for metabolites

Data displayed are mean (95% Confidence interval) intraclass correlation coefficient for metabolite ratios (Choline (Cho)/Creatine (Cr), N Acetyl Aspartate (NAA)/Cho, NAA/Cr) and metabolites (NAA, Cho and Cr) for mixed cortical and deep grey, and white matter brain regions.

Calculation of 95% prediction interval for zero change

Using the four WB ¹H MRS measurements obtained from both sessions, we used ANOVA to determine the significance of the differences (Table 5-5). These confirm that there is a significant difference between regions and subjects, and that there is a significant interaction between brain region and subject. The residual variance of the measurements that cannot be accounted for by the known independent variables is shown in Table 5-5. The calculated SD values were 0.10, 1.03 and 0.28 for Cho/Cr, NAA/Cho, NAA/Cr and 1709.7, 913.2 and 1521.4 iu for NAA, Cho and Cr respectively. The overall population 95% prediction interval for zero change (based on two SD values) were therefore 0.20, 2.06 and 0.56 for Cho/Cr, NAA/Cho and NAA/Cr and 3419.4, 1826.4 and 3042.8 iu for NAA, Cho and Cr respectively. For the within session measurements the calculated SD values were 0.10, 1.11 and 0.23 for Cho/Cr, NAA/Cho, NAA/Cr and 1399.7, 1115.9 and 1292.8 iu for NAA, Cho and Cr respectively and were similar to the data obtained from all four sessions. These data can be used to calculate prediction intervals within individual ROIs. For the within session data (Table 5-3A&C) an estimate of the 95% prediction intervals for zero change within individual ROIs should be based on 4.3 SD values. As an example, this results in a 95% prediction interval for zero change for NAA, Cho and Cr within a single imaging session of 3839.5, 844.5 and 2345.2 iu for the left temporal, and 3557.0, 1815.9 and 3081.0 iu for the right anterior thalamic radiation respectively. These prediction intervals can be used to assess the impact of therapeutic interventions within a single session, but also to assess the impact of treatment and disease progression over time within different imaging sessions.

A

Parameter	Session	DF	Sum of Squares	Mean Square	F Value	p Value
Cho/Cr	ROI	32	17.18	0.54	52.86	<.0001
	subject	31	2.86	0.09	9.07	<.0001
	ROI * subject	992	14.70	0.01	1.46	<.0001
	Residual	1815	18.44	0.01		
NAA/Cho	ROI	32	3105.79	97.06	91.19	<.0001
	subject	31	657.96	21.22	19.94	<.0001
	ROI * subject	992	1264.47	1.27	1.2	0.0006
	Residual	1815	1931.76	1.06		
NAA/Cr	ROI	32	113.60	3.55	61.42	<.0001
	subject	31	24.16	0.78	13.48	<.0001
	ROI * subject	992	83.45	0.08	1.46	<.0001
	Residual	1815	104.90	0.08		

B

Parameter	Session	DF	Sum of Squares	Mean Square	F Value	p Value
NAA	ROI	32	8.3×10^9	2.6×10^8	89.1	<.0001
	subject	31	1.2×10^9	3.7×10^7	12.8	<.0001
	ROI * subject	992	3.7×10^9	3.7×10^6	1.3	<.0001
	Residual	1815	5.3×10^9	2.9×10^6		
Cho	ROI	32	1.2×10^9	3.7×10^7	43.9	<.0001
	subject	31	3.5×10^8	1.1×10^7	13.4	<.0001
	ROI * subject	992	1.5×10^9	1.5×10^6	1.9	<.0001
	Residual	1815	1.5×10^9	8.3×10^5		
Cr	ROI	32	4.7×10^9	1.5×10^8	63.3	<.0001
	subject	31	1.0×10^9	3.3×10^7	14.1	<.0001
	ROI * subject	992	4.4×10^9	4.4×10^6	1.9	<.0001
	Residual	1815	4.2×10^9	2.3×10^6		

Table 5-5 Analysis of variance table for whole brain proton magnetic resonance spectroscopy

Data were obtained from 32 volunteers using the region of interest (ROI) template for metabolite ratios (A) and metabolite concentrations (B). Choline – Cho, Creatine – Cr, N acetyl aspartate – NAA and DF – Degrees of freedom.

Discussion

This study provides additional reference data concerning intersubject variability and reproducibility of metabolite ratios, and individual signal-intensity normalised metabolite concentrations obtained using WB ^1H MRS conducted within the same imaging session (within session) and different imaging sessions (between session) in a group of healthy volunteers. As reported previously, we found that intersubject variability was high.²³¹ The reproducibility of metabolite ratios and concentrations were lower than intersubject variability (10 – 15% vs. 15 – 30%), but there was substantial variability across the brain for all the calculated parameters. The within and between session reproducibility measurements were similar for Cho/Cr, NAA/Cho, Cho and Cr but for NAA/Creatine and NAA between session reproducibility was lower than within session reproducibility. The calculated overall population 95% prediction intervals for zero change of repeat MIDAS measurements were 0.20, 2.06 and 0.56 for metabolite ratios (Cho/Cr, NAA/Cho and NAA/Cr) and 3419.4, 1826.4 and 3042.8 iu for

metabolite concentrations (NAA, Cho and Cr) respectively. These prediction intervals can be calculated for individual ROIs and utilised in interventional studies where the response to therapy can be assessed, or to assess the significance of the change from disease progression within longitudinal studies of nervous system disorders.

The factors affecting the reproducibility of WB ^1H MRS parameters include changes within the MR scanner or individual subjects. Features related to the scanner include B_0 field inhomogeneities (heating during the long acquisition process), scanner drift, gradient coil stability, signal to noise ratio and software upgrades. Such factors may be more significant when imaging is acquired within different imaging sessions, rather than repeat acquisitions within the same session where such parameters are more likely to be similar. Regular servicing and daily quality assurance measurements seek to ensure that an MR scanner is operating normally. It is necessary to monitor such changes, and where possible, take steps to limit their impact on the spectroscopic data obtained. Importantly, there were no upgrades or changes in MR scanner hardware or software during the period of this study. While scanner variability is important there are individual subject factors that can induce substantial variability in WB ^1H MRS. These include head movements and positioning within the scanner field of view. In particular, data acquisition within the volume of interest is sensitive to inhomogeneities that can result from proximity to the sphenoid and frontal sinuses. We undertook standard procedures to limit such variability. All subjects were positioned within the head coil according to standard operating procedures within our institution and the alignment confirmed before commencing imaging.

Following standard imaging for localisation, we monitored subject movement, and all data were checked during processing for movement artefact. No data sets were excluded in these analyses due to subject motion during the scan. Also, we performed all analyses following image coregistration and spatial normalisation to MNI standard space. We used a standard ROI template covering the whole brain from the Harvard Oxford subcortical and MNI structural probabilistic atlases available within FSL. While the use of this analysis strategy sought to reduce variability within our comparisons, we eroded the ROI template by a single voxel within FSL in order to improve spatial localisation and reduce the impact of coregistration, normalisation and partial volume errors. Finally, all ROIs were manually inspected to ensure that they were correctly aligned with the imaging data and corresponded to the regions specified. In summary, we considered possible sources of WB ^1H MRS variability within our centre and attempted to limit their impact and ensure that the data we acquired were comparable within and between the different imaging sessions.

While our results for WB ^1H MRS reproducibility are in line with published data, we report data specifically concerning the difference between intersubject variability, within session and between

session reproducibility. It is useful to consider the sources of variability in WB ^1H MRS data in the setting where we are trying to address the significance of changes between normal physiology and disease states, or changes that are the consequence of a therapeutic intervention. In the first case, the relevant sources of error are the intersubject variability in the patient and volunteer groups. Our data for healthy volunteers are broadly concordant with results from other groups,¹¹¹ and show that these are high, with mean (range) CoV for Cho/Cr 21 (11 – 62%), NAA/Cho 17 (11 – 55%), NAA/Cr 13 (8 – 37%), NAA 12 (6 – 23%), Cho 31 (13 – 69%) and Cr 19 (7 – 61%). To be certain that WB ^1H MRS values derived from an individual patient are significantly lower, with a confidence of 95%, these figures suggest that we need to have mean ROI NAA values (for example) that are at least 23% lower than volunteer means. This estimate and the secure distinction of a patient group as abnormal is confounded by the fact that intersubject CoV in patients with neurological disorders is likely to be larger than controls, and variable across different brain regions. These figures underline the difficulty of using WB ^1H MRS in small groups of patients with different causes of neurological disease who have variable pathophysiology. In practice, the estimated study sample size is moderated by the dramatic changes in metabolite concentration that occur in patients. For example, following mild traumatic brain injury there is approximately a 20% reduction in NAA and increase in Cho even where structural imaging appears normal, and in severe traumatic brain injury changes of up to a 50% can occur.^{171,172,235-239} Hence the significance of metabolite change is often detected with manageable numbers, despite the large intersubject variability in volunteer and patients groups.

However, it is important to point out that these figures are largely irrelevant when considering the power and design of clinical studies, when WB ^1H MRS is being used to monitor changes within the same subject in the same scanning session (within session reproducibility) or during longitudinal assessments over time in several different imaging sessions (between session reproducibility). In such settings, the subject is his or her own control, and the relevant parameter is intrasubject variability or reproducibility. Our data show that these figures for CoV are smaller than those obtained from the discussion in the previous paragraph. Also, we provide reference data for metabolites in healthy volunteers, demonstrating that the CoV for within session reproducibility is broadly comparable to that obtained in different imaging sessions (Table 5-3 and Table 5-4). While the reproducibility of NAA/Creatine and NAA was significantly lower for between session compared to within session measurements, the absolute differences were small. This finding is not consistent with the lack of difference for the other metabolites and is unlikely to be clinically relevant. We found no evidence to suggest that within session reproducibility was smaller than between session reproducibility measurements. These data provide helpful guidance for designing clinical studies and suggest that for NAA or NAA/Cr it should be possible to detect differences of 20% with confidence. For example,

although the reproducibility of measurements is variable for the different brain regions, we can use these data to calculate sample sizes for interventional and longitudinal clinical studies.²⁴⁰ For a lobar ROI such as the right frontal region the between session CoV was 8% for NAA, and we should be able to detect a 20% change with 95% power at a significance level of 1% within a group of 10 subjects within a single interventional or longitudinal study design. Such estimates only strictly apply to our scanner and institution, but they provide a useful starting point for any spectroscopic study design. There are several factors particular to our scanning protocols and institutional setup that limit the use of the reproducibility measurements that we provide. These include, but might not be limited to, scanner, acquisition protocols, data correction and reconstruction, and processing. Despite these variations, it should be possible for other groups to use the methodology that we describe to derive 'in house' data for their studies. Also, although these data guide designing clinical studies, particularly in groups of subjects (including those with brain injury) that may require sedation and control of ventilation as part of clinical care. While such patient groups may appear complex and difficult to manage within the context of an imaging study the fact that they remain completely immobile and have stable physiology should result in lower CoV for reproducibility measurements and an increase in the sensitivity of interventional studies.¹¹⁶

Methodological limitations

The volunteers included in this study ranged in aged from 25 – 50 years, and since metabolite levels are associated with age,^{106,221} this may account for some of the variability in the intersubject analysis. While we were able to obtain multiple WB ¹H MRS datasets on up to two occasions in this group of volunteers, scanner availability and subject tolerance (duration and noise) prevented us from acquiring further WB ¹H MRS datasets within the same session and additional scanning sessions. A repeat imaging session was performed within a mean (range) of 33 (3 – 181) days, and variation in this interval could result in biological differences between the datasets obtained within a few days compared to those obtained after several months. However, any expected change in WB ¹H MRS in healthy volunteers of a similar age over up to six months is small and unlikely to have resulted in the differences we have found.²⁴¹ In addition, we found no relationship between scan reproducibility and the interval between the two imaging sessions.

We found variability in the ¹H MRS measurements and their reproducibility across the different brain regions. In addition, there was more variability in metabolite data involving choline, which probably reflects the lower concentration of choline within the brain.²⁴² These differences are demonstrated in Table 5-1, Table 5-2, Table 5-3, Figure 5-3 and Figure 5-4 were particularly relevant for the corpus

callosum, deep grey matter, midbrain, frontal, occipital and some white matter regions. We found no relationship between the ROI volume and intersubject variability and reproducibility of ^1H MRS for any of the metabolites (data not shown). Despite this, the cause of these differences may in part be related to inhomogeneities in the B_0 field induced by the frontal and sphenoidal air sinuses, partial volume errors within relatively small regions, locally variant metabolite concentrations, and variation in the quality of coregistration and spatial normalisation within individual subjects. We tried to limit these errors through careful review of all the transformed imaging datasets, shimming the scanner before each MIDAS data acquisition, and eroding the ROI template by a single voxel to improve accuracy. Despite this, errors remain within some ROIs where ^1H MRS values differ in closely adjacent brain regions. However, the purpose of this study was to determine the variability of measurements using an ROI template and standard processing pipeline. While variability in the fitting of template ROIs in individual subjects may result in higher intersubject variability for particular brain regions, this should be less likely for measurements of reproducibility within the same subject. Here any differences in ROI template fitting between the sessions should be small. These regional differences underline that ^1H MRS studies should compare data within the same brain region using the same data processing technique. Our figures for reproducibility are higher than that reported by Maudsley et al. using the same acquisition sequence.¹⁰⁹ This reflects our inclusion of a larger study group and that we utilised a standard processing pipeline and ROI template covering the whole brain within normalised space that we would typically apply to patient studies. While the data we report are specific to our methods, the reproducibility measurements that we report provide a useful starting point for study design.

Conclusions

This study provides additional reference data concerning intersubject variability and reproducibility of WB ^1H MRS conducted in a group of healthy volunteers. The CoV for repeat WB ^1H MRS measurements obtained during the same session were similar to that obtained from measurements obtained in a different imaging session separated by up to six months. These data can be used to calculate the 95% prediction interval for zero change and may inform the design of interventional studies to quantify change within a single imaging session or to assess the significance of the change in longitudinal studies.

Chapter 6 Pathophysiological mechanisms of cerebral ischaemia and diffusion hypoxia in traumatic brain injury

Introduction

The Cambridge group have previously used ^{15}O oxygen positron emission tomography (^{15}O PET) to define evidence of cerebral ischaemia following early clinical head injury.^{118,120} While ischaemia was related to regions of structural injury, it was distributed across the brain and found in regions that appeared structurally normal.²⁴³ While other ^{15}O PET studies have found less convincing evidence of ischaemia, these typically demonstrate evidence of metabolic dysfunction that correlates with focal microdialysis and brain tissue oxygen monitoring derangements, and ultimately, were associated with late cognitive decline and cerebral atrophy.^{160,244} Brain tissue oxygen and microdialysis identify evidence of tissue hypoxia and metabolic dysfunction, particularly within perilesional regions following traumatic brain injury (TBI), and protocol-driven management has been shown to improve outcome.^{159,164,245-250} We have previously used brain tissue oxygen and ^{15}O PET to demonstrate an increased gradient for oxygen diffusion within hypoxic brain regions in the absence of classical ischaemia.¹²³ This is consistent with microvascular ischaemia and is supported by ex-vivo clinical and experimental studies demonstrating perivascular oedema, microvascular thrombosis and occlusion associated with selective neuronal loss.²⁵⁰⁻²⁵³

^{18}F Fluoromisonidazole (^{18}F FMISO) is a hypoxia PET tracer that undergoes selective bioreduction within hypoxic cells where it becomes irreversibly bound. This imaging modality has been used to investigate and identify severely hypoxic but viable tissue following stroke.^{144,254-256} There are no published data concerning the use of ^{18}F FMISO PET following TBI or direct comparison with ^{15}O PET. This study aimed to compare the burden and distribution of classical ischaemia using ^{15}O PET with regional tissue hypoxia as defined by ^{18}F Fluoromisonidazole PET in patients following early head injury.

Materials and methods

Ethical approval was obtained from the Cambridge Central Research Ethics Committee (06/Q108/359) and written informed consent, or consultee agreement from next-of-kin where appropriate were obtained in all cases in accordance with the Declaration of Helsinki. Also, approval was obtained from the Administration of Radioactive Substances Advisory Committee (83/2050/21530).

Subjects

Ten adult patients (9 males) with a mean (range) age 52 (30 – 68) years with TBI were recruited from the Neurosciences Critical Care Unit, Addenbrooke's Hospital, Cambridge, UK. Patients presented with a mean (range) post-resuscitation Glasgow Coma Score (GCS) of 7 (3 – 12) but deteriorated to a GCS < 8 requiring sedation and ventilation for control of intracranial pressure (ICP) (Table 6-1). Patients were recruited to this imaging study between days 1 – 8 post-injury at a time when they were still sedated and ventilated to facilitate ICP control. All patients were managed by protocol-driven care; which included sedation, paralysis and ventilation aiming for ICP < 20 mmHg, cerebral perfusion pressure > 65 mmHg, and where available BtpO₂ values > 15 mmHg. Physiological stability was meticulously ensured during imaging through the titration of fluids and vasoactive agents and the presence of a critical care physician and nurse. Patients who received the surgical intervention (cerebral spinal fluid (CSF) drainage or decompressive craniectomy) or second-tier medical therapies (barbiturate coma or moderate hypothermia (33–35°C)) prior imaging are specified in Table 6-1. Outcome was evaluated using the Glasgow outcome scale (GOS) at six months. All patients admitted to the neurocritical care unit requiring sedation, paralysis and ventilation for the maintenance of ICP control were considered for this study to avoid selection bias. The recruitment rate for this study was low because of duration of study (three hours) and the inherent complexity of triple oxygen PET scan. Patients were recruited over one year.

Ten healthy volunteers (8 males) with mean (range) age of 45 (29 – 59) years underwent ¹⁵O PET and another ten healthy volunteers (8 males) with mean (range) age of 55 (41 – 76) years underwent [¹⁸F]FMISO PET. We used two separate volunteer groups (¹⁵O and [¹⁸F]FMISO PET) for this study because of the combined duration of triple oxygen and FMISO PET acquisition and discomfort for unsedated patients.

Subject	Age	Sex	Mechanism	Injury	GCS	Marshall	APACHE	ISS	Neurosurgery	Second tier medical therapies	Days to Imaging	GOS
1	47	M	Assault	Contusions	8	5d	19	16	DC		5	SD
2	59	M	Fall	Contusions and SDH	4	5c	24	38	DC		1	D
3	34	M	Fall	Contusions, SDH and DAI	6	5b	25	16	EVD, DC		5	MD
4	60	F	RTA	EDH and tSAH	4	5a	25	20	C	Hypothermia	2	GR
5	30	M	RTA	Contusions, SDH and DAI	3	5b	17	29	DC		1	MD
6	65	M	Assault	Contusions, SDH and tSAH	12	6d	11	25			8	GR
7	58	M	Fall	Contusions, SDH, tSAH and DAI	8	6c	20	34			8	GR
8	66	M	RTA	Contusions, SDH and DAI	10	6d	15	13		Hypothermia	3	MD
9	31	M	Fall	Contusions, SDH and DAI	5	6d	16	42	EVD, DC	Hypothermia	5	SD
10	68	M	Fall	Contusions, EDH, SDH and tSAH	11	6d	17	29			5	GR

Table 6-1 Patient Characteristics

C, craniotomy; D, death; DAI, diffuse axonal injury; DC, decompressive craniectomy; EDH, extradural hemorrhage; EVD, external ventricular drain; F, female; GCS, Glasgow coma score; GOS, Glasgow outcome score; GR, good recovery; M, male; MD, moderate disability; RTA, road traffic accident; SD, severe disability; SDH, subdural hemorrhage; tSAH, traumatic subarachnoid hemorrhage.

Imaging

All subjects underwent structural imaging for coregistration with magnetic resonance imaging (MRI) using a 3T Siemens Verio MRI scanner (Siemens AG, Erlangen, Germany) within the Wolfson Brain Imaging Centre, University of Cambridge. The sequences obtained included a 3D T1-weighted magnetisation prepared rapid gradient echo (MPRAGE), fluid-attenuated inversion recovery (FLAIR), gradient echo (GE), susceptibility weighted (SWI), dual spin echo (proton density/T2-weighted) and diffusion tensor imaging (DTI).²³²

Positron emission tomography (PET) studies were undertaken on a General Electric Advance scanner (GE Medical Systems, Milwaukee, USA). Image reconstruction included corrections for attenuation, scatter, randoms and dead time.¹²⁰

¹⁵Oxygen PET: Emission data were acquired in 3D mode during a 20 minute steady state infusion of 800 MBq of H₂¹⁵O (two five minute frames at the end of the administration), following a 60-second inhalation of 300 MBq of C¹⁵O (single 5 minute frame), and in 2D mode during a 20 minute steady state inhalation of 7200 MBq of ¹⁵O₂ (two five minute frames at the end of the administration). Parametric maps of cerebral blood flow (CBF), cerebral blood volume (CBV), cerebral oxygen metabolism (CMRO₂) and oxygen extraction fraction (OEF) were calculated by inputting simultaneous PET and arterial tracer activity measurements into standard models previously described by Coles et al.^{116,131} We used a blood-brain partition coefficient for H₂¹⁵O (ρ) of 0.95 based on the previous *in vitro* data and a small to large haematocrit ratio (r) of 0.85.¹²⁰

¹⁸Fluoromisonidazole PET: Following [¹⁸F]FMISO injection emission data were acquired in the 3D mode for up to 2.5 hours. Arterial plasma input function was used for kinetic analysis, and binding was quantified using BAFPIC²⁵⁷ (a basis function approach to two tissue irreversible compartmental modelling and Patlak graphical analyses to derive kinetic parameters from the dynamic [¹⁸F]FMISO PET emission. Parametric maps of K₁, k₃ and K_i were calculated. The rate constants K₁ and k₃ reflect tracer delivery to the brain and trapping within hypoxic tissue, respectively. The steady state uptake rate constant $K_i = K_1 k_3 / (k_2 + k_3)$, where k₂ is efflux of the tracer from tissue to blood.

Image processing: The PET data were processed using custom designed automated software (PETAN^{128,258}) incorporating elements of Statistical Parametric Mapping (SPM), Matlab (MathWorks, Inc., Natick, Maryland, USA) and Analyze (AnalyzeDirect, Inc., Lenexa, Kansas, USA). To aid coregistration, the skull and extracranial soft tissue were stripped from the T1 weighted image using the Brain Extraction Tool of FSL.²⁵⁹ Subsequently; this extracted brain was registered to the summed [¹⁸F]FMISO and H₂¹⁵O PET emission using SPM.²⁶⁰ In order to exclude brain tissue with irreversible injury from further analyses, we used a threshold value of CBF < 2.36 ml/100ml/min based on a

positive predictive value of 0.95 for non-viable tissue.²⁷ Subsequently, we created a brain mask using the coregistered extracted T1 weighted image following removal of the CSF segment and the CBF threshold for non-viable tissue. This brain mask was applied to the parametric PET images and used to generate corrected parametric maps.

Region of interest analysis

Lesions were defined on native FLAIR and segregated into core, contusion and pericontusion using FLAIR, MPRAGE, GE and SWI images. Lesion core was identified as a region of mixed signal intensity consistent with haemorrhage and necrotic tissue and excluded from subsequent analyses. Contusion was identified as an area of high FLAIR signal consistent with oedema, and pericontusion as 1 cm border zone of normal-appearing tissue surrounding a contusion. The FLAIR images were coregistered to PET space using SPM8, and coregistration parameters applied to lesion ROIs. For comparison, a region of normal appearing mixed grey and white matter was defined in patients.

Ischaemic brain volume

We used OEF to assess the burden of classical ischaemia in order to avoid the confounding effects of drug and injury-induced metabolic suppression on CBF and CMRO₂. Although it is difficult to find data that identify critical increases in OEF levels that still allow survival in the setting of ischaemia, we have previously validated a technique for patients with TBI.^{120,261,262} We estimated an individualised critical OEF threshold (OEF_{crit}; which equated to a cerebral venous oxygen content (CvO₂) of 3.5 ml/100ml) for each subject as follows:

$$OEF_{crit} = \frac{(CaO_2 - 3.5)}{CaO_2}$$

where,

$$CaO_2 = 1.34Hb.SaO_2 + 0.0225PaO_2$$

CaO₂ is arterial oxygen content, Hb is the haemoglobin in g/100ml, SaO₂ is the fractional arterial oxygen saturation, and PaO₂ is the partial pressure of oxygen (kPa). Application of these thresholds to OEF images allowed us to calculate the volume of voxels with CvO₂ values below this threshold and hence allowed estimation of the ischaemic brain volume (IBV).

Hypoxic brain volume

We used k_3 to assess the burden of tissue hypoxia since it is the rate constant for FMISO trapping under hypoxic conditions. Using the mean and standard deviation (SD) of voxel k_3 values within the whole brain of each healthy volunteer we calculated the upper 99% confidence interval (CI) threshold using the mean plus three SDs. We used the volume of the brain with k_3 values above this threshold to calculate the hypoxic brain volume (HBV). The volume, spatial location and mismatch between the HBV and IBV were examined.

Comparison with tissue pO_2 : For subjects who underwent BtpO₂ monitoring, this was monitored continuously with values recorded every 5 - 10 minutes throughout PET. A 20mm diameter ROI was drawn around the LICOX[®] sensor tip (Integra Neurosciences), and [¹⁸F]FMISO k_3 compared with BtpO₂.

Statistical analysis: Statistical analyses were conducted using Statview (Version 5, 1998, SAS Institute Inc.). Data are expressed as median (range) unless otherwise stated. Data were compared using Mann Whitney U and Spearman's rank tests and p values quoted after Bonferroni correction (where appropriate), with corrected p values < .05 considered significant. The Dice similarity coefficient was used to measure the degree of spatial overlap between IBV and HBV.

Results

Regional physiology

Physiology was highly variable even within regions that appeared structurally normal (Figure 6-1). When compared to data from healthy volunteers, contusions showed lower CBF and CMRO₂ ($p < 0.01$ Mann Whitney U test with Bonferroni correction), while CBV and OEF were variable but similar to control. Pericontusional tissue and regions that appeared structurally normal had lower CMRO₂ than healthy volunteers ($p < 0.01$ Mann Whitney U test with Bonferroni correction), while CBF, CBV and OEF were similar to control.

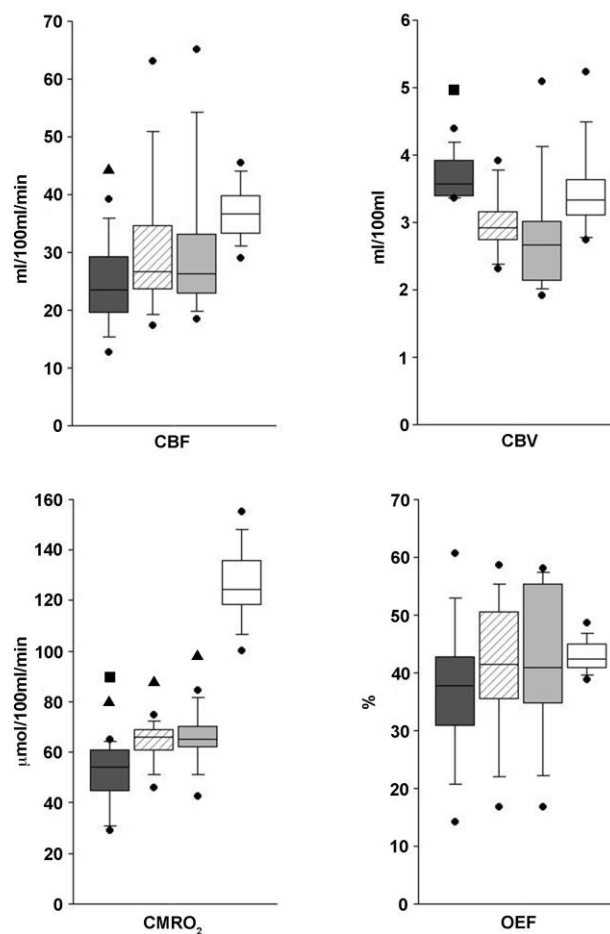


Figure 6-1 Regional physiology

- Box and whisker plots of cerebral blood flow (CBF), cerebral blood volume (CBV), cerebral oxygen metabolism (CMRO₂), and oxygen extraction fraction (OEF) in brain regions identified as contusion (dark grey), perilesion (diagonal), normal appearing (light grey) and healthy volunteers (white). The central lines in each box denote median values, the lower and upper boundaries the 25th and 75th centile, the error bars the 10th and 90th centile, and the closed circles outlying data points. ▲ $p < 0.01$ and ■ $p < 0.05$, Mann Whitney U test with Bonferroni correction for comparison with control values from healthy volunteers and normal appearing regions within patients respectively.

Ischaemic brain volume

When compared to healthy volunteers, patient IBV was significantly higher (56 (9 – 281) ml vs 1 (0 – 11) ml; $p < 0.001$, Mann Whitney U test). While much of the IBV was close to visible lesions, with 23 (4 – 65)% found within contusional and pericontusional regions, it was also distributed across the normal appearing brain (Figure 6-2). Physiology within the IBV is shown in Figure 6-3. There was no relationship between the IBV and days since injury or age ($p = 0.49$ and 0.34 , respectively, Spearman's rank test).

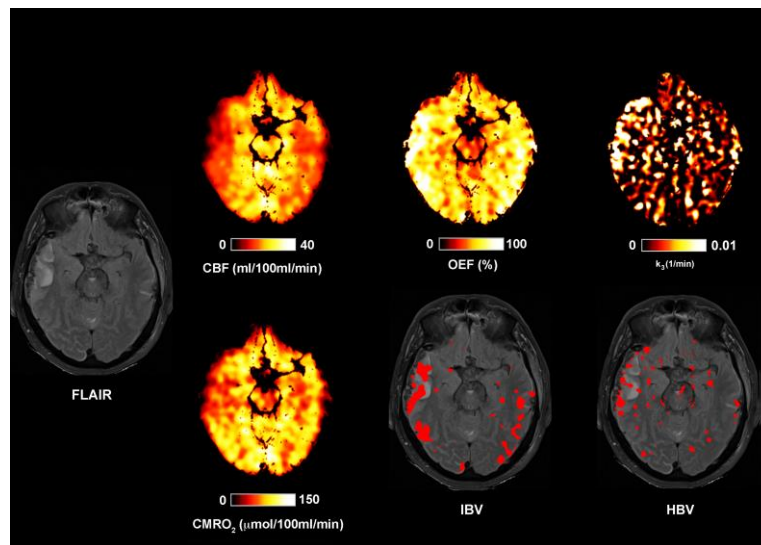


Figure 6-2 ¹⁵O Evidence of cerebral ischaemia using ¹⁵O positron emission tomography following head injury

Fluid-attenuated inversion recovery (FLAIR), cerebral blood flow (CBF), cerebral oxygen metabolism (CMRO₂), oxygen extraction fraction (OEF), ischaemic brain volume (IBV), ¹⁸F-fluoromisonidazole trapping rate (k₃) and hypoxic brain volume (HBV) in patient 10 who sustained a head injury following a fall. During imaging cerebral perfusion pressure was 82 and intracranial pressure 12 mmHg. The FLAIR image demonstrates bilateral contusions within the temporal and parietal lobes on the right and the temporal lobe on the left. Cerebral blood flow is low in these regions, particularly on the right side. Cerebral oxygen metabolism is mildly reduced within the right temporal region, but there is a large increase in the OEF particularly within the right but also within the left temporal and parietal cortices. Increased k₃ is found within the right temporal region but also across other injured and normal appearing regions. The region with a critical increase in OEF above the individually calculated ischaemic threshold (IBV) and the HBV are both shown in red overlying the FLAIR image. Within the total IBV of 131ml in this patient the mean CBF was 14 ml/100ml/min, CBV 3.4 ml/100ml, CMRO₂ 84 µmol/100ml/min and OEF 90 %. The total HBV in this patient was 70ml and had mean CBF was 13 ml/100ml/min, CBV 2.2 ml/100ml, CMRO₂ 47 µmol/100ml/min and OEF 49 %. The volume of overlap between these two tissues classes in this subject was 6ml.

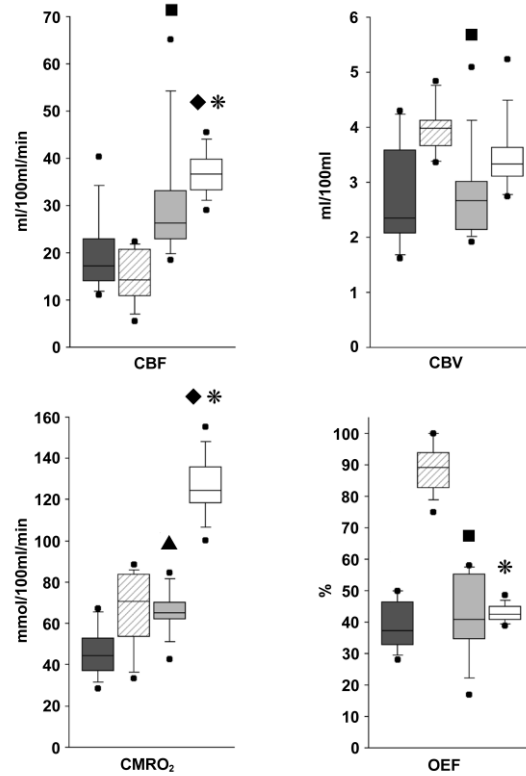


Figure 6-3 Comparison of physiology within the ischaemic brain volume and hypoxic brain volume

Box and whisker plots of cerebral blood flow (CBF), cerebral blood volume (CBV), cerebral oxygen metabolism (CMRO₂), and oxygen extraction fraction (OEF) in brain tissue constituting the hypoxic brain volume (HBV) (dark grey), ischaemic brain volume (IBV) (diagonal), brain that appeared structurally normal (light grey) and healthy volunteers (white). The central lines in each box denote median values, the lower and upper boundaries the 25th and 75th centile, the error bars the 10th and 90th centile, and the closed circles outlying data points. ▲ $p < 0.05$, for comparison between the HBV and brain that appeared structurally normal within patients. ■ $p < 0.01$, for comparison between the IBV and brain that appeared structurally normal within patients. ◆ $p < 0.01$, for comparison between the HBV and healthy volunteers. * $p < 0.01$, for comparison between the IBV and healthy volunteers. For all comparisons between the HBV or IBV, and brain that appeared structurally normal in patients or healthy volunteers Mann Whitney U tests with Bonferroni correction were used.

Hypoxic Brain Volume

The HBV was variable, but significantly higher in patients compared with healthy volunteers, with a median (range) of 29 (0 – 106) ml vs 9 (1 – 24) ml ($p = 0.016$, Mann Whitney U test). A trend for correlation between the IBV and HBV failed to achieve significance ($\rho = 0.61$ and $p = 0.07$, Spearman's rank test). The overlap volume between these two pathophysiological tissue classes was 1 (0 – 19) ml, and there was substantial spatial mismatch (Dice similarity coefficient of 0 (0 – 0.1)) (Figure 6-2 and Figure 6-4). While the HBV was often related to visible lesions, with 37 (21 – 57)% found within contusional and pericontusional regions, it was also seen within the normal appearing brain (figures 6-2 and 6-4). Figure 6-3 shows a comparison of summary physiological data from the IBV and HBV tissue classes, the tissue that appeared structurally normal and was in neither of these classes and tissue from healthy volunteers. When tissue constituting the HBV was compared to that within the IBV (figure 6-3) it showed similar CBF ($p = 0.22$), CBV ($p = 0.09$) and CMRO₂ ($p = 0.14$), but lower OEF ($p < 0.001$; Mann Whitney U tests with Bonferroni correction). Cerebral metabolism below

published ^{15}O PET thresholds for irreversible injury ($37.6 \mu\text{mol}/100\text{ml}/\text{min}$) in TBI was observed in three of 10 patients in the HBV tissue class compared to one within the IBV tissue class. There was no relationship between the HBV and days since injury or age ($p = 0.70$ and 0.90 respectively, Spearman's rank test).

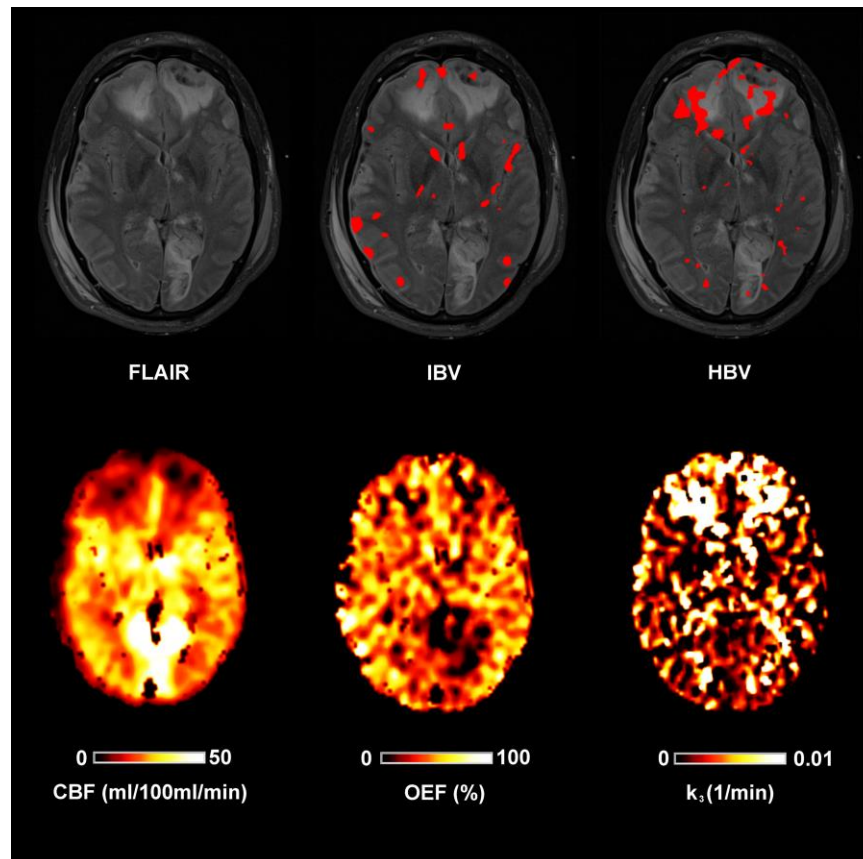


Figure 6-4 Evidence of tissue hypoxia using ^{18}F fluoromisonidazole positron emission tomography

Fluid-attenuated inversion recovery (FLAIR), cerebral blood flow (CBF), oxygen extraction fraction (OEF), ischaemic brain volume (IBV), and ^{18}F -fluoromisonidazole trapping rate (k_3) and hypoxic brain volume (HBV) in patient 9 who sustained a head injury following a fall. During imaging cerebral perfusion pressure was 80 and intracranial pressure 21 mmHg. The FLAIR image demonstrates haemorrhagic contusions with surrounding vasogenic oedema within bilateral frontal and right temporal regions. Additional areas of high signal consistent with injury are evident within the left thalamus and bilateral occipital regions. Finally, there are thin subdural haematomas over the right cortex and left frontal region. Cerebral blood flow is low within the frontal regions and is associated with increased k_3 in the absence of an increase in OEF consistent with conventional macrovascular ischaemia. The HBV (100ml) in this subject had a mean CBF of $14 \text{ ml}/100\text{ml}/\text{min}$, CBV $2.1 \text{ ml}/100\text{ml}$, CMRO_2 $27 \mu\text{mol}/100\text{ml}/\text{min}$ and OEF 35 % and did not match the region of brain within the IBV (149ml) that had CBF of $15 \text{ ml}/100\text{ml}/\text{min}$, CBV $3.4 \text{ ml}/100\text{ml}$, CMRO_2 $63 \mu\text{mol}/100\text{ml}/\text{min}$ and OEF 88 %. The volume of overlap between these two tissues classes in this subject was 10ml.

Comparison with tissue pO_2 measurements

Tissue pO_2 was available in five subjects, and measurements during PET were 34 (16 – 55) mmHg. The ROI around the LICOX probe tip showed no values of ^{18}F FMISO k_3 or OEF that exceeded our HBV and IBV thresholds.

Discussion

Combining ^{15}O and $[^{18}\text{F}]\text{FMISO}$ PET, we demonstrate evidence of conventional macrovascular cerebral ischaemia and tissue hypoxia up to a week post-TBI. Spatial matching of these two tissue classes was poor, with voxels contributing to the HBV more frequent within the vicinity of lesions. The IBV and HBV voxels showed comparable reductions in CBF, but the HBV tissue class showed a trend for lower CBV and CMRO_2 , and significantly lower OEF. Further, the HBV more frequently exhibited CMRO_2 values within the range of irreversible injury. While the IBV identifies conventional macrovascular ischaemia, the coexistence of normal OEF (identified by ^{15}O PET) and low tissue pO_2 (identified by high $[^{18}\text{F}]\text{FMISO}$ trapping) in the HBV is the typical signature of diffusion barrier hypoxia, which, along with lower CBV, implies microvascular collapse and ischaemia as an underlying mechanism. These findings confirm the existence of diffusion hypoxia, characterise its pathophysiological signature as distinct from macrovascular ischaemia, and show that the two have an incomplete spatial concordance. This is a potential target for future novel neuroprotective strategies.

While ^{15}O and $[^{18}\text{F}]\text{FMISO}$ PET have been used separately to identify ischaemia,^{255,256,263,264} we combined both tracers to interrogate pathophysiological derangements following TBI. For $[^{18}\text{F}]\text{FMISO}$ PET, we used kinetic analysis to calculate k_3 as a measure of hypoxia. While K_i , the influx rate constants²⁶⁵ often used to quantify irreversible trapping/metabolism of a tracer in tissue, it is sensitive to changes in tracer delivery, which is CBF dependent. This confounding issue is obviated through estimation of k_3 , the rate constant for tissue $[^{18}\text{F}]\text{FMISO}$ trapping, and in the context of low CBF in the vicinity of contusions,^{28,266} k_3 is more suited to represent trapping of $[^{18}\text{F}]\text{FMISO}$ within the hypoxic brain.^{155,267} The HBV was calculated from the total volume of voxels with k_3 values larger than the upper 99% CI value from control data.

Since derangements are common across the whole brain following TBI,^{120,266,268} we cannot utilise a similar approach used following an ischaemic stroke that defined increased $[^{18}\text{F}]\text{FMISO}$ trapping greater than the upper 99% CI value from the contralateral brain.²⁶⁹ Other studies used voxel-wise statistical testing to compare with controls following spatial normalisation.^{144,256} These are less applicable to TBI since structural distortions are usually larger, making spatial normalisation less dependable. We sought to identify $[^{18}\text{F}]\text{FMISO}$ trapping within areas of obvious injury and normal appearing regions, and therefore, used native PET space analyses to avoid artefacts from such processing techniques.^{72,179} The volumes of the hypoxic brain with increased $[^{18}\text{F}]\text{FMISO}$ trapping in our subjects were similar to those seen in ischaemic stroke,²⁵⁵ with a mean HBV of 47 ml in our patients, and four patients with a $\text{HBV} \geq 5\%$ of brain volume.

We removed lesion core using MR and excluding CBF voxels < 2.36 ml/100ml/min based on a positive predictive value of 0.95 for non-viable tissue in TBI.²⁷ Following TBI increased FLAIR signal can disappear on sequential imaging²⁷⁰ and is not predictive of pan-necrosis for all lesion voxels.²⁷ Since derangements are often found in normal-appearing regions,²⁶⁸ we examined the whole brain, but highlighted when these were found within the vicinity of lesions using standard MR sequences. The mean HBV found outside contusion and pericontusion was 30 (0 – 75) ml, and four subjects had >50 ml of such tissue.

These results have implications for our understanding of oxygen delivery and utilisation in clinical TBI. Although the HBV and IBV showed some overlap, most IBV voxels did not show significant [¹⁸F]FMISO trapping. This suggests that at least some of the voxels with OEF in excess of our threshold CvO₂ values could maintain tissue pO₂ levels above those that result in irreversible bioreduction of [¹⁸F]FMISO. The pO₂ at which this occurs is unclear, but *in vitro* data show that, while FMISO bioreduction shows some enhancement with pO₂ < 60 mmHg, it rises steeply at a pO₂ < 10 mmHg.²⁷¹ Given that the normal BtpO₂ is ~ 25 mmHg,^{272,273} it is possible that many IBV voxels had BtpO₂ values in the 10 – 20 mmHg range, and our HBV threshold may simply be a more stringent physiological marker of tissue hypoxia. In comparison with the IBV, CMRO₂ below thresholds, we have previously identified for survival²⁷ were more common in the HBV. While [¹⁸F]FMISO trapping does not occur within necrotic tissue²⁵⁴ a proportion of these voxels may be destined for infarction, and the HBV may provide a more specific marker of tissue on the cusp of survival.

To explore the relationship between OEF and [¹⁸F]FMISO k₃ within viable brain, we excluded voxels at high risk of infarction based on the lower 95% confidence interval for non-lesion brain following TBI, using a CMRO₂ threshold of 37.6 μ mol/100ml/min.²⁷ In Figure 6-5, the subsequent relationship between OEF and k₃ within individual patients is shown using locally weighted scatterplot smoothing (LOWESS)^{27,274,275} This shows variability between patients, with a subset showing increased [¹⁸F]FMISO trapping above an OEF threshold of $\sim 60 - 70\%$, broadly consistent with conventional ischaemia. It is important to emphasise that levels of [¹⁸F]FMISO trapping were, in most cases, below our HBV thresholds and equivalent to tissue pO₂ levels of $\sim 10 - 25$ mmHg.²⁷¹

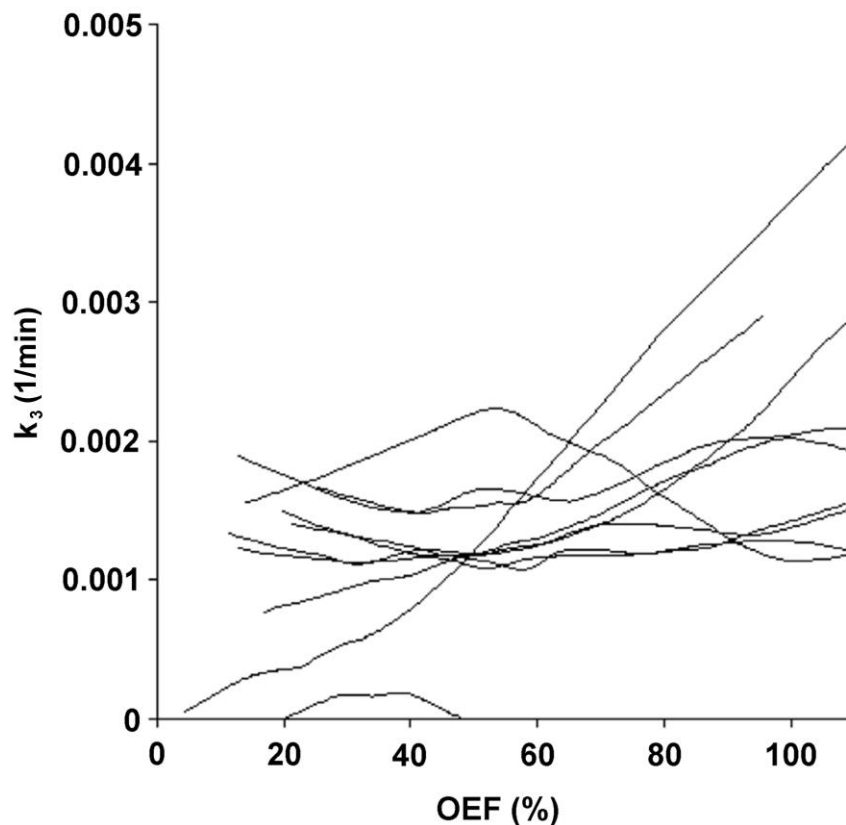


Figure 6-5 Relationship between PET parameters

The relationship between oxygen extraction fraction (OEF) and $[^{18}\text{F}]$ FMISO trapping rate (k_3) within voxels across the whole brain of individual patients ($n=10$) plotted using locally weighted scatterplot smoothing (Lowess) with 66% tension using Statview. Lowess is an outlier resistant method based on local polynomial fits. For this comparison voxels with cerebral oxygen metabolism less than $37.6 \mu\text{mol}/100\text{ml}/\text{min}$ were excluded based on the lower 95% confidence limits for non-lesion voxels following head injury.

Given that these data provide a transition zone between normal tissue and that which shows increased $[^{18}\text{F}]$ FMISO trapping, it would be useful to have a physiological characterisation of tissue that shows pathological levels of $[^{18}\text{F}]$ FMISO trapping. While subjects showed increased $[^{18}\text{F}]$ FMISO trapping across the whole brain, there was none within the vicinity of focal BtpO₂ monitoring probes. Clinically significant reductions in BtpO₂ are typically reported below 10 – 15 mmHg,²⁷⁶ and our local treatment protocol aim to maintain values > 15 mmHg, which were achieved in all subjects. The lowest BtpO₂ level recorded during the PET was 16mmHg. In terms of the threshold value at which $[^{18}\text{F}]$ FMISO trapping occurs in TBI, we can conclude that pO₂ values within the HBV may have been $\leq 10 - 15$ mmHg.

The proportion of HBV voxels that had high OEF meeting the criteria for macrovascular ischaemia (IBV) was small (8%). This may relate to the fact that we imaged patients between days 1 – 8 post-injury, at a time when conventional ischaemia is less prevalent,^{122,130,277} but lesions remain at risk of expansion. This may have meant that many tissue regions showed complex and varying mixtures of macrovascular

ischaemia and diffusion hypoxia, making detection of clear OEF thresholds for [¹⁸F]FMISO trapping challenging. Our study has limitations. This study recruited a small number of patients due to the inherent complexity of conduct of the trial. The temporal variability in neurophysiology after TBI during the recruitment window may have played a role in the final results, but we attempted to minimise variations in physiology by only recruiting patients undergoing aggressive therapy for ICP management in the critical care unit.

Our characterisation of prominent [¹⁸F]FMISO trapping in perilesional regions is worth highlighting. Previous PET studies have shown severe derangements within and around cerebral contusions, but that increases in OEF consistent with cerebral ischaemia are not always identified.^{27,28} We found that tissue within the vicinity of such lesions is hypoxic but does not fulfil the criteria for conventional macrovascular ischaemia. An explanation for these findings comes from studies showing widespread microvascular occlusion and perivascular oedema after TBI,^{250,252,278} associated with selective neuronal loss.²⁵¹ Conventional physiology dictates that to maintain CMRO₂ in the face of low CBF, OEF must be increased.^{130,263} However, hypoxic regions may be less able to increase OEF due to an increased gradient for oxygen diffusion.¹²³ This could explain our findings of low OEF and CBV despite evidence of low CBF and tissue hypoxia. Other studies have used DTI to demonstrate contusion expansion, and that a rim of low apparent diffusion coefficient consistent with cytotoxic oedema is often found surrounding contusions.⁷² This may characterise a region of microvascular failure, and represent a ‘traumatic penumbra’ that may be rescued by effective therapy such as hyperoxia,^{25,179} or be subsumed as the contusion enlarges.

These findings confirm the existence of diffusion hypoxia, characterise its pathophysiological signature as distinct from conventional macrovascular ischaemia, and show that the two have an incomplete spatial concordance. This physiological signature is consistent with microvascular ischaemia, and importantly, this mechanism is also found within regions that appear structurally normal. Such findings require further scrutiny and are relevant to the development of future neuroprotective strategies.

Chapter 7 Use of diffusion tensor imaging to assess the impact of normobaric hyperoxia within at-risk pericontusional tissue following traumatic brain injury

Introduction

Structural damage due to ischaemia and tissue hypoxia remains an important cause of neuronal loss following traumatic brain injury (TBI)¹²¹ as shown in the previous chapter. The Cambridge group have previously used ¹⁵O positron emission tomography (¹⁵O PET) to show that normobaric hyperoxia increases oxygen utilisation in “at-risk” regions of metabolically compromised tissue, typically in pericontusional regions and white matter.^{19,25} However, while previous studies demonstrate a consistent effect of hyperoxia in increasing brain tissue oxygen levels, reports of the impact on brain metabolism have been inconsistent, regionally variant, and dependent on the underlying metabolic state of the tissue concerned.^{25,164,279,280} Additional concerns have been raised regarding the potential deleterious effects on pulmonary function and worsening of neuronal injury due to oxidative stress. Studies within other pathologies such as stroke and myocardial infarction have also shown conflicting evidence of benefit and harm.²⁸¹⁻²⁹⁰ Given this background, it is clear that further study of the regional effects of normobaric hyperoxia is warranted before definitive clinical trials of the intervention following traumatic brain injury (TBI).

Diffusion tensor imaging has shown benefit in a variety of neurological disease states in predicting both local tissue and functional outcome.^{60,61,88,181,182,212,213,216,291-295} Studies following TBI have demonstrated evidence of traumatic axonal injury that is not evident using conventional imaging techniques.^{49-51,56,57,61,180,296-299} Diffusion tensor imaging (DTI) images dynamic metabolic processes, including cytotoxic oedema associated with cellular metabolic failure, and experience in stroke shows that these imaging changes are dynamic and reversible, suggesting that they may be able to image acute treatment effects.^{250,300,301} We have therefore used DTI to assess the impact of normobaric hyperoxia in this context, and provide data for the planning and design of future therapeutic trials of hyperoxia therapy for patients with a head injury.

Materials and methods

Ethical approval was obtained from the Cambridgeshire Research Ethics Committee (reference numbers 97/290 and 02/293) and written informed consent, or consultee agreement from next-of-kin where appropriate were obtained in all cases in accordance with the Declaration of Helsinki.

Subjects

Patients: Fourteen adult patients (12 males and two females) with a mean (range) age 41 (21 – 70) years with head injury were recruited from the Neurosciences Critical Care Unit (NCCU), Addenbrooke's Hospital, Cambridge, UK between 2010 and 2012. Patients presented with median (range) post-resuscitation Glasgow Coma Score (GCS) of 7 (3 – 14) but deteriorated to a GCS < 8 requiring sedation and ventilation for control of intracranial pressure (ICP) (Table 7-1). Patients were recruited to this imaging study between days one and nine post-injury and underwent imaging while sedated. Patients were excluded from this study if they had suffered a previous TBI, other neurological diseases, or had any contraindication to magnetic resonance imaging (MRI). All patients were managed by protocol-driven care; which included sedation, paralysis and ventilation to ensure that ICP < 20 mmHg and cerebral perfusion pressure > 65 mmHg were maintained. Physiological stability was meticulously ensured during imaging through the titration of fluids and vasoactive agents and the presence of a critical care physician and nurse. Patients who received the surgical intervention (CSF drainage or decompressive craniectomy) or second-tier medical therapies (barbiturate coma or moderate hypothermia (33–35°C)) before imaging are specified in Table 7-1. No other major changes occurred in the management of patients on the day of study.

Subject	Age	Sex	Mechanism	Injury	GCS	Marshall score	APACHE II	ISS	Neurosurgery	Second tier therapies	Days to MRI	GOS
1	53	M	RTA	Multiple contusions and DAI	4	NEML	17	34	-		4	MD
2	34	M	RTA	tSAH, SDH and IVH	4	NEML	21	20	EVD		3	VS
3	34	M	Assault	Multiple contusions	8	EML	25	16	DC		3	SD
4	21	M	RTA	Multiple contusions	10	NEML	21	50	-	Hypothermia	2	MD
5	31	M	RTA	Multiple SDH	6	EML	17	29	DC		1	MD
6	29	M	Assault	Multiple contusions	10	EML	17	16	DC, EVD	Hypothermia	2	GR
7	58	M	Fall	Multiple contusions	10	NEML	20	34	-	-	4	GR
8	26	M	RTA	SDH and Multiple contusions	3	NEML	17	75	-		3	MD
9	28	M	Assault	SDH and EDH	12	EML	24	36	DC		3	GR
10	61	M	Fall	Multiple contusions	5	NEML	22	75	-		9	Not available
11	60	M	Fall	Multiple contusions	14	NEML	8	34	-	-	3	MD
12	31	F	Fall	Multiple contusions	3	EML	25	75	DC	Hypothermia	4	VS
13	70	F	RTA	Multiple contusions	3	NEML	21	34	-		1	GR
14	27	M	RTA	Multiple contusions	7	NEML	16	25	-		4	GR

Table 7-1 Patient characteristics

M, male; F, female; RTA, road traffic accident, DAI, diffuse axonal injury; tSAH, traumatic subarachnoid haemorrhage, SDH, subdural haemorrhage; IVH, intraventricular haemorrhage; EDH, extradural haemorrhage, GCS, Glasgow coma score; NEML, non-evacuated mass lesion; EML, evacuated mass lesion; EVD external ventricular drain; DC, decompressive craniectomy; MRI, magnetic resonance imaging; GOS, Glasgow Outcome Score; MD, moderate disability; VS, vegetative state; SD, severe disability, GR, good recovery

Following acquisition of baseline diffusion tensor imaging (DTI) at a partial pressure of oxygen (PaO_2) of approximately 75 – 90 torr (10 – 12 kPa) the fraction of inspired oxygen (FiO_2) was increased to a maximum of 0.8 in order to achieve a PaO_2 of approximately 225 – 260 mmHg (30 – 35 kPa). Following 60 minutes to allow impact of higher PaO_2 (and by inference, brain pO_2) levels on cerebral metabolism, repeat DTI was obtained within the same imaging session without moving the patient.

Controls: Seven controls (four females and three males) with a mean (range) age of 31 (22 – 42) years were exposed to graded oxygen therapy (21%, 60% and 100% inspired oxygen) delivered via a venturi mask (Flexicare Medical Limited, Mid Glamorgan, Wales). Diffusion tensor imaging was obtained at each level following an equilibration period of 15 minutes to assess the impact of oxygen therapy on the normal brain.

Imaging

All subjects were scanned using a 3T Siemens Verio MRI scanner (Siemens AG, Erlangen, Germany) within the Wolfson Brain Imaging Centre (WBIC), University of Cambridge. During the study period, there were no significant changes or upgrades to the scanner or software. The sequences obtained were structural sequences including a 3D T1-weighted magnetisation prepared rapid gradient echo (MPRAGE), fluid-attenuated inversion recovery (FLAIR), gradient echo (GE), susceptibility weighted (SWI) and dual spin echo (proton density/T2-weighted). The DTI data were acquired using 63 non-collinear directions, $b=1000 \text{ s/mm}^2$ with one volume acquired without diffusion weighting ($b = 0$), echo time (TE) 106ms, repetition time (TR) 11700ms, 63 slices, field of view 192mm x 92mm, 2mm^3 isotropic voxels, and an acquisition time of 13:50 minutes. A specialist neuroradiologist reviewed all acquired images as a part of clinical care.

Image processing: Apparent diffusion coefficient (ADC) maps were created using the Oxford Centre for Functional MRI of the brain FSL Diffusion Toolbox. To aid coregistration, the skull and extracranial soft tissue were stripped from the T1 weighted image using the Brain Extraction Tool of FSL.^{206,207,259} The diffusion weighted data were normalised using a two-step approach. First, T1 weighted images were coregistered to the Montreal Neurological Institute 152 (MNI152) template using the vtkCISG normalised mutual information algorithm.²⁰⁹ The $b = 0$ images were subsequently coregistered to the subject's T1 weighted image as described previously.^{113,232} The transformation matrix normalising the MPRAGE was then applied to the $b = 0$ images. All coregistered and normalised images were visually checked to ensure that they were aligned.

Region of interest analysis

Standard template in controls: Regions of interest (ROIs) from the Harvard Oxford subcortical and MNI structural probabilistic atlases available within FSL were applied in normalised space. All coregistered images were inspected to ensure that the ROIs were aligned and corresponded to the regions specified. The ROI template was modified by the erosion of a single voxel using `fslmaths` to improve spatial localisation and reduce the impact of coregistration, normalisation and partial volume errors. The ADC values for the different ROIs were calculated using in-house software using Matlab (Mathworks, Natick, USA).

Lesion-based analysis in patients:

Lesions were defined in native FLAIR space (hand-drawn) by a single author (JG, sense checked and confirmed for concordance by other authors TV and JPC), and segregated into regions defined as core, contusion and pericontusion using patient FLAIR, MPRAGE, GE and SWI images. SWI (three dimensional) and GE (two dimensional) were used to identify areas of bleeding and necrotic core in the contusion along with the structural imaging.

Lesion core was identified as a region of mixed signal intensity consistent with haemorrhage and necrotic tissue, contusion as an area of high signal on FLAIR, and pericontusion as a 1 cm border zone of tissue surrounding the contusion (Figure 7-1). Where visible, we also defined a rim of cytotoxic oedema ('traumatic penumbra') on ADC images that we have previously reported around contusions using DTI (figure 7-2). The ROIs were drawn using Analyze 8.5 (Analyze Direct, Lenexa, KS, USA). FLAIR images were coregistered to T1 space using SPM8, and the coregistration matrix subsequently applied to the individual lesion ROIs. For comparison, a comparable region of the brain composed of mixed grey and white matter was defined in controls.

Statistical analysis

Statistical analyses were conducted using Statview (Version 5, 1998, SAS Institute Inc., Cary, North Carolina, USA). All data are expressed and displayed as mean and standard deviation (SD) unless otherwise stated. Individual ROIs were treated independently, since they represented a clinically relevant method of segmenting the brain, with specific location being irrelevant to this analysis. Data were compared using unpaired and paired t-tests and ANOVA. All p values are quoted after Bonferroni corrections (where appropriate) and corrected p values < .05 were considered significant.

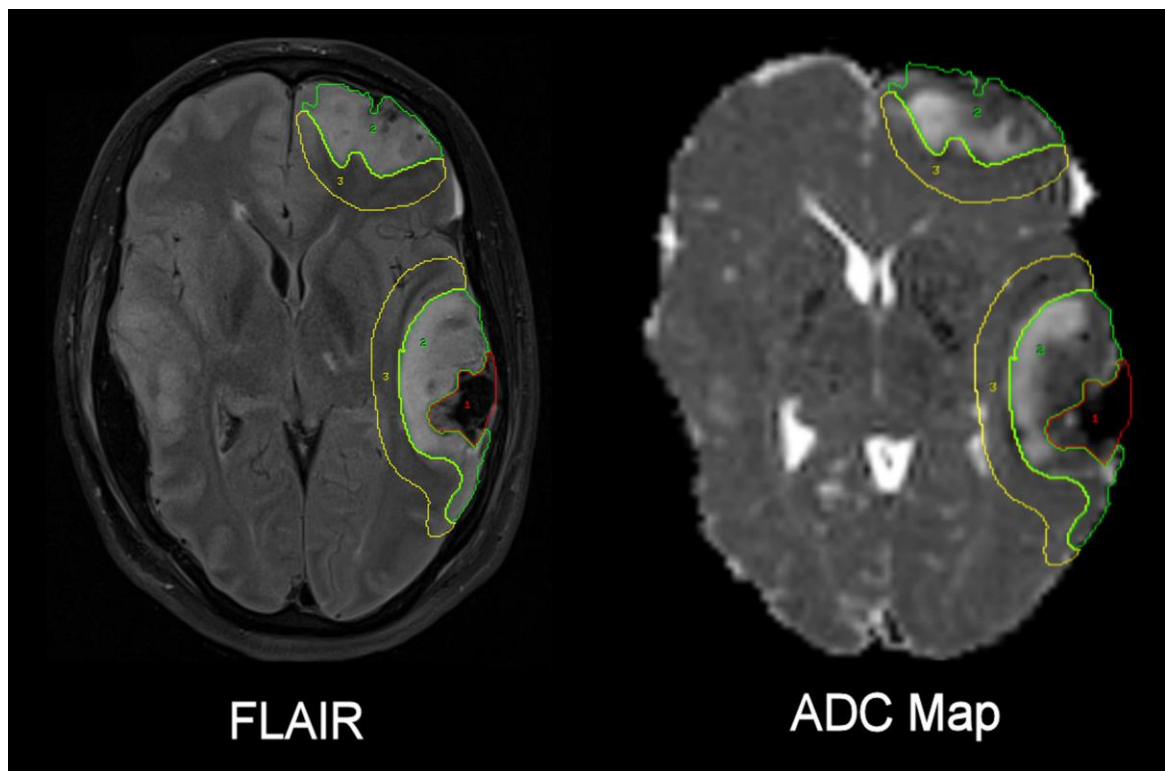


Figure 7-1 Lesion regions of Interest drawn using Fluid attenuated inversion recovery (FLAIR) and apparent diffusion coefficient (ADC) images. In FLAIR and ADC images lesion core (red), contusion (green) and perilesion (yellow) are identified on a single axial slice.

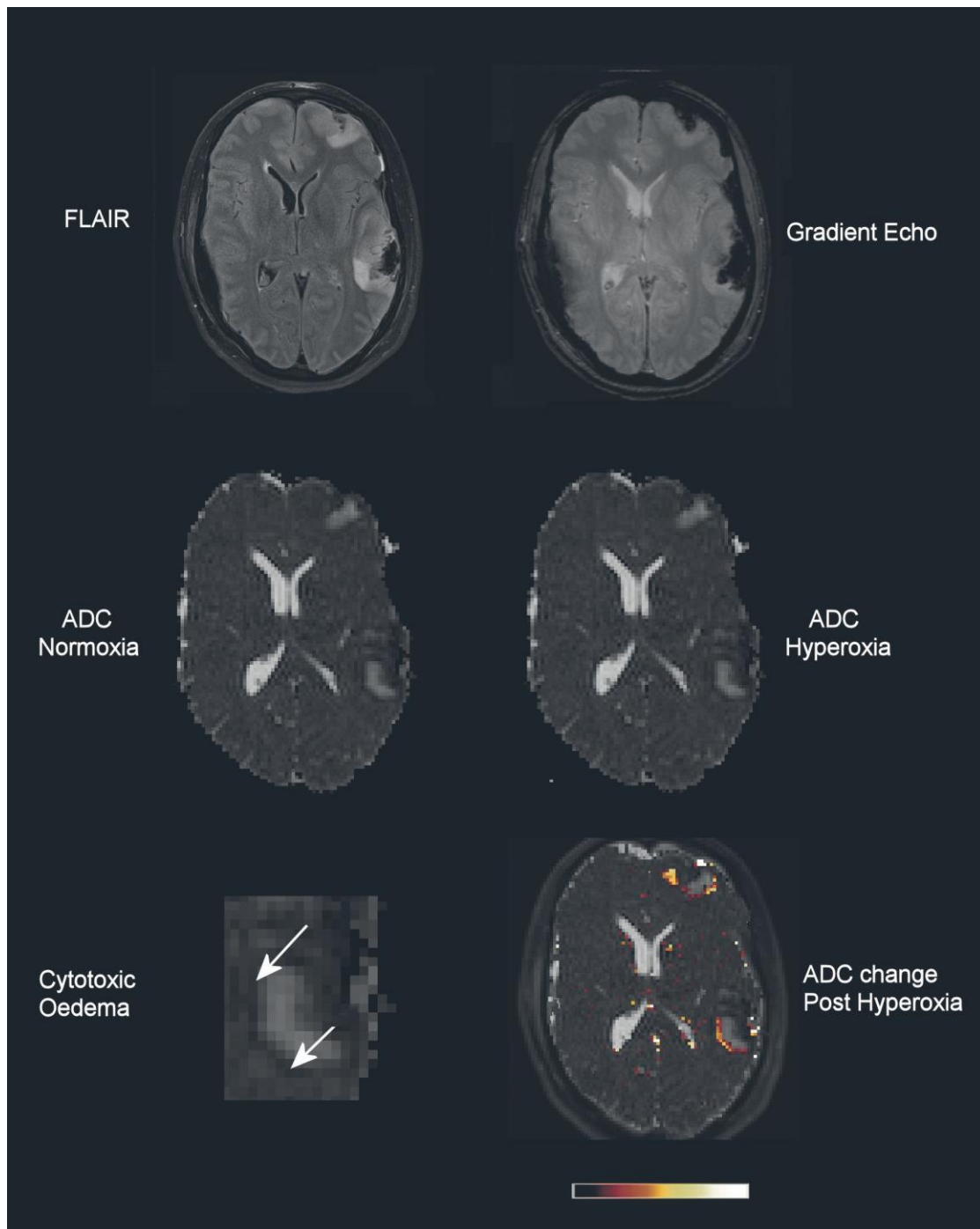


Figure 7-2 Impact of hyperoxia on traumatic penumbra in apparent diffusion coefficient (ADC) image

Fluid attenuated inversion recovery (FLAIR), gradient echo and ADC images at normoxia and hyperoxia demonstrating contusions within the left frontal and temporal parietal regions. These lesions have a haemorrhagic core shown by low signal on the gradient echo corresponding to the presence of blood degradation products, surrounded by a region of 'vasogenic oedema' with high signal on FLAIR and ADC. Around these lesions is a hypointense rim consistent with 'cytotoxic oedema', an example of which is shown at higher magnification and identified by the arrows. The final image has a colour map showing the ADC increase calculated from the difference between the ADC images following hyperoxia. This highlights that the increase in ADC occurs predominantly within this border zone immediately surrounding the contusions.

Results

Impact of oxygen therapy on diffusion tensor imaging in healthy volunteers

There was no significant ADC change using the standard template ROI for an increase in the inspired fraction of oxygen (FiO_2) ($p > 0.99$, ANOVA). The mean (SD) ADC was 8.98×10^{-4} (1.37×10^{-4}), 9.21×10^{-4} (1.37×10^{-4}) and 9.20×10^{-4} (1.35×10^{-4}) mm²/second for a FiO_2 of 0.21, 0.6 and 1.0 respectively.

Injured brain regions

The mean (SD) ADC in contusional and pericontusional ROIs was 1.11×10^{-3} (1.41×10^{-4}) and 1.08×10^{-3} (1.79×10^{-4}) respectively, and was significantly higher than controls (9.21×10^{-4} (2.78×10^{-5} , $p < 0.01$, ANOVA with Bonferroni correction). There was no significant change in ADC following hyperoxia within contusional ROIs ($p = 0.16$), but an increase within pericontusional ROIs ($p < 0.05$, paired t-test with Bonferroni correction). One subject with low pericontusional ADC showed an increase to within the normal range. The data are displayed compared to the mixed grey and white matter region from controls (figure 7-3). There was a rim of low ADC around brain contusions consistent with cytotoxic oedema in 13 subjects with a mean (range) volume of 8 (1 - 20) ml (figure 7-2). There was a significant increase in ADC towards the normal range (7.04×10^{-4} vs 8.28×10^{-4} $p = 0.02$, paired t-test). The data are displayed compared to a mixed grey and white matter region from controls, and shows that while all subjects demonstrate an increase this is to within or more than the normal range in four subjects (figure 7-4).

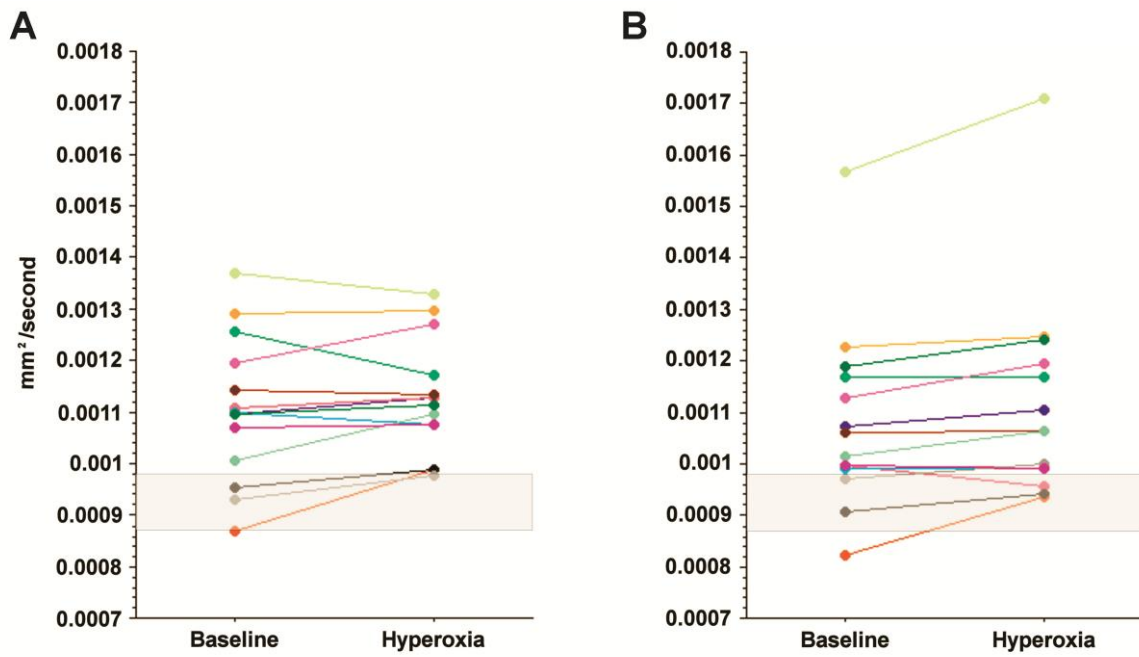


Figure 7-3 Lesion based analysis

Apparent diffusion coefficient (ADC) within brain tissue identified as contusion (A) and pericontusion (B) at baseline and following normobaric hyperoxia. The shaded box represents the 95% confidence interval for healthy controls from a region of mixed grey and white matter.

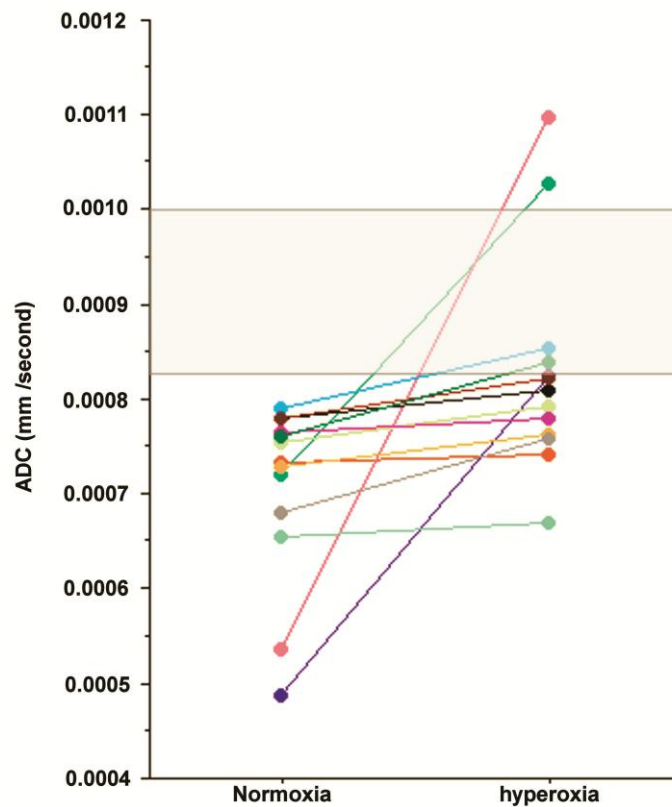


Figure 7-4 Impact of hyperoxia within traumatic penumbra

Changes in Apparent Diffusion Coefficient for the rim of cytotoxic oedema surrounding visible brain lesions in 13 subjects. The shaded box represents the 99% confidence interval for healthy controls from a region of mixed grey and white matter.

Discussion

In this study, we used DTI to examine whether an increase in the fraction of inspired oxygen had any beneficial effects within the injured brain. We found no significant change in healthy volunteers and no evidence of benefit within lesion brain identified on structural imaging. The rim of cytotoxic oedema that we have previously defined as a region of 'traumatic penumbra' around brain contusions⁷² demonstrated a significant increase in ADC values towards normal. While an increase in the fraction of inspired oxygen has been reported to increase brain tissue partial pressure of oxygen, reduce microdialysis lactate and lactate-pyruvate ratio and improve brain metabolism, we show evidence of benefit within 'at risk' traumatic penumbral regions of the injured brain.^{164,165,302} While these data are provisional; they provide a framework to use DTI as an intermediate endpoint to assess the impact of changes in brain oxygenation and metabolism on lesion expansion and local tissue outcome over time within the injured brain. Further studies should address whether there is a benefit in using hyperoxia therapy over a more extended period of days in patients with a head injury.³⁰³

Previous studies have demonstrated that patients with an increase in the severity, number and duration of episodes of tissue hypoxia tend to suffer poor outcome following head injury and evidence suggests that therapy guided by measurement of brain tissue oxygen levels may be associated with improved outcome.^{162,304,305} Interventional studies have demonstrated that an increase in the fraction of inspired oxygen can result in improvements in brain tissue oxygen levels, and reductions in brain lactate using microdialysis.^{248,306} While significant, the changes in lactate did not necessarily result in an improvement in oxidative metabolism since the lactate/pyruvate was not consistently lowered.

The effects that result from an improvement in tissue oxygenation are clearly dependent on oxygen delivery and (probably) diffusion gradients in the injured brain.³⁰⁷ Pathophysiological derangements within the injured brain are spatially variant and are not limited to regions that appear structurally injured.³⁰⁷ Therefore, an adequate definition of the effects of hyperoxia across the injured brain demands measurement of regional and global cerebral metabolism using a physiological imaging

technique such as ^{15}O oxygen positron emission tomography (^{15}O PET). A ^{15}O PET study showed that ventilation with 100% oxygen in a group of 5 patients within 24 hours of severe head injury resulted in no change in hemispheric cerebral blood flow (CBF) or oxygen metabolism (CMRO_2).³⁰⁸ These results are in contrast to a further study that demonstrated that a brief intervention (~ one hour) of normobaric hyperoxia resulted in an increase of CMRO_2 within brain regions at the most significant risk of infarction. This analysis included perilesional and white matter regions of the injured brain. While these data suggest that the impact of hyperoxia may be dependent on the underlying physiological characteristics of different regions of the injured brain, another study using near-infrared spectroscopy has suggested that short term therapy with hyperoxia can improve oxygen metabolism within a frontal brain region.^{309,310}

An explanation for these findings comes from post-mortem studies showing widespread microvascular occlusion and perivascular oedema following TBI, associated with selective neuronal loss.^{250,251} The relevance of these findings to antemortem ischaemia is explained by ^{15}O PET and brain tissue oximetry studies which show increased vascular to tissue gradients for oxygen tension in the injured brain.²⁵ We have previously used DTI to demonstrate contusion expansion, and that a rim of low ADC consistent with cytotoxic oedema is often found surrounding a region of high ADC (vasogenic oedema). This rim of hypodensity may characterise a region of microvascular failure resulting in cytotoxic oedema, and represent a 'traumatic penumbra' that may be rescued by effective therapy or be subsumed as the contusion enlarges. Higher brain oxygen levels may overcome diffusion barriers to oxygen delivery, or compensate for mitochondrial dysfunction. Indeed, in regions of low oxygen tension, nitric oxide can competitively inhibit cytochrome oxidase and thereby render mitochondrial respiration dependent on the level of cellular oxygen.⁶⁷ Ex-vivo studies in clinical and experimental head injury tissue show impaired function in mitochondria (typically < 4 hours of injury).^{170,311} Experimental data also show that mitochondrial ATP production is preserved and that this is associated with improved cognitive recovery and reduce neuronal cell loss in the hippocampus

following injury and treatment with hyperbaric and normobaric hyperoxia.³¹² Experimental data also report that hyperoxia has neuroprotective and anti-inflammatory effects within the injured and ischaemic brain.³¹³ Our clinical data are suggestive of normalisation of ADC values in such regions following a brief period of hyperoxia. However, we have no data on whether such an increase is beneficial in terms of preventing lesion expansion and improving functional outcome. Indeed, in two subjects, the increase in ADC was greater than the 95% confidence interval for controls and could reflect tissue injury.

While the use of high partial pressures of oxygen may be beneficial in a variety of disease states and following brain injury, there may be a relatively narrow margin of safety due to the known toxic effects. The maximum FiO_2 in this interventional study was limited to 0.8 to reduce potential side effects, including alveolar atelectasis and pulmonary injury. However, clinical studies in TBI have used short exposures of normobaric and hyperbaric hyperoxia and failed to demonstrate increased oxidative stress.^{314,315} While these clinical studies suggest that the use of high concentrations of inspired oxygen in this context may be safe, further studies are required to calculate the risk-benefit ratio and determine whether such therapy has a beneficial impact on patient outcome. Such data may permit a rational design of future clinical trials.

While evidence of significant changes in brain oxygenation and metabolism and suggestions that improved outcome may be associated with targeted therapy are encouraging,^{249,316,317} a firm recommendation for clinical use of the intervention requires a clinical trial. Previous studies have suggested that hyperoxia therapy in TBI can improve mortality, but not a favourable outcome. A recently published phase II study^{315,318} from Rockswold et al. provided valuable evidence of the risks and benefits of hyperoxia therapy over several days. This study compared 60 minutes of hyperbaric hyperoxia (1.5 atmospheres) with three hours of 100% oxygen and standard care in a group of 69 patients with a severe head injury. Patients received therapy on three consecutive days, starting within 27 hours of injury. While there was no change in global CMRO_2 , those patients with low baseline

CBF showed an increase in global CMRO₂ following both hyper and normobaric hyperoxia. The microdialysate L/P ratio was also decreased in both treatment groups, and in the hyperbaric group, these changes were associated with a reduction in intracranial pressure (ICP). It was also noted that the beneficial effects on brain tissue oxygenation, CBF, CMRO₂ and ICP lasted until the next treatment period. Importantly, there were no signs of pulmonary or cerebral toxicity. Another publication from the same group suggests that a combination of daily hyperbaric (60 minutes at 1.5 atmospheres) followed by three hours of normobaric hyperoxia (FiO₂ 1.0) can improve favourable outcome³¹⁵.

Despite the promising findings, the studies by Rockswold et al. do not provide definitive evidence of an improvement in clinical outcome. Evidence of a change in tissue fate may come from DTI, but evidence of improved outcome will require a large Phase II trial. Previous studies have shown serial DTI changes in grey and white matter following a head injury that represent microstructural injury. Our study addressed this within the time frame of metabolic changes that we have previously demonstrated with short term hyperoxia but was only able to show improvement in DTI parameters within a rim of potentially vulnerable tissue around brain contusions. However, we can use the data from this study and the recent Rockswold studies to refine the design of a future therapeutic trial of hyperoxia therapy following clinical head injury. In the studies published by Rockswold et al. subjects received daily exposure to hyperoxia within the first four days following injury, and we have shown that evolution of DTI signal changes within pericontusional tissue is maximal within the first 72 hours.^{318,319} In our study, 9 of 14 subjects underwent intervention within 72 hours of injury, and only two subjects were studied within 24 hours of injury. Previous studies have demonstrated that evidence of ischaemia is more evident at earlier time points following injury. However, derangements in brain metabolism continue for many days post-injury, may be particularly prominent in white matter regions, and have shown evidence of improvement following hyperoxia therapy. In our study, changes in DTI parameters did not differ between those subjects imaged at earlier compared to later time points ($p = 0.32$). While Rockswold et al. used daily exposures of normo and hyperbaric hyperoxia,

the subjects in our study only underwent an intervention lasting approximately one hour using a FiO_2 of 0.8. The partial pressure of oxygen delivered and the duration of exposure may be relevant in determining the impact on the outcome, but we must balance the potential benefits with the lack of robust safety data beyond three days' worth of treatment.

Future studies should seek to confirm whether exposing patients with brain injury to high fractions of inspired oxygen during the management of raised ICP over several days is beneficial. This assessment could focus on DTI progression around cerebral contusions and within white matter regions³¹⁹ as an intermediate endpoint, and as a cause of neurocognitive deficits at outcome.^{59,205} This would require a longitudinal study with imaging at regular intervals and correlation with structural imaging at outcome and neurocognitive assessment at 6 - 12 months post-injury. Such evidence would be useful in the design of any future large clinical trial. We have previously reported on the reproducibility of DTI measurements and found that for ADC, the SD of ROI measurements was 3.16×10^{-5} mm²/second. Using such data to calculate sample sizes for interventional and longitudinal clinical studies we should be able to detect a 10% change in ADC with 95% power at a significance level of 1% within a group of 15 subjects within a single interventional or longitudinal study design.^{232,320}

Conclusions

Previous studies have suggested that cerebral metabolism can be improved through an increase in the fraction of inspired oxygen. Using DTI, we demonstrate that a short interval of normobaric hyperoxia may result in benefit within the rim of cytotoxic oedema around brain contusions. Future longitudinal studies should address whether a longer period of hyperoxia therapy during the time that patients require critical care management of raised ICP has a favourable impact on the evolution of tissue injury.

Chapter 8 Normobaric hyperoxia does not improve derangements in diffusion tensor imaging found distant from visible contusions following acute traumatic brain injury

Introduction

While normobaric hyperoxia (NH) has been used to increase brain tissue oxygen partial pressure (BtpO₂) following traumatic brain injury (TBI), it is not used as a routine therapy.^{248,321,322} Reductions in BtpO₂ are associated with worse outcome, and interventions aimed at optimising oxygen delivery have shown benefit.³²³ ¹⁵O positron emission tomography (¹⁵O PET) has been used to show that NH can improve oxygen utilisation in “at-risk” regions of metabolically compromised tissue in pericontusional and white matter regions.¹⁶⁴ Also, evidence obtained using diffusion tensor imaging (DTI) show how cytotoxic oedema within a rim of pericontusional tissue can be ameliorated with a short NH intervention.²⁰⁴

These results are in conflict with evidence demonstrating increases in microdialysis glutamate, and studies showing an association between arterial hyperoxia and poor outcome following severe TBI. These highlight the potential deleterious effects on pulmonary function and worsening neuronal injury due to oxidative stress.^{290,324-326} Given this background, it is clear that further study of the regional effects of normobaric hyperoxia across the injured brain is warranted to ensure it is used appropriately.

Diffusion tensor imaging has been used to demonstrate evidence of traumatic axonal injury following TBI even when conventional imaging appears normal.^{74,180} Imaging findings are dynamic and potentially reversible, suggesting that DTI could be used as a biomarker of the effectiveness of therapeutic interventions in TBI.²⁰⁴ In this study, we aimed to address the impact of NH distant from visible contusions. Such data should help inform the design and conduct of any future clinical trial of this intervention in TBI.

Materials and methods

Ethical approval was obtained from the Cambridgeshire Research Ethics Committee (reference numbers 97/290 and 02/293), and assent from next-of-kin with later written informed consent, where appropriate, obtained in all cases in accordance with the Declaration of Helsinki.

Subjects

Patients

Fourteen adult patients (12 males and two females) with median (range) age 33 (21 – 70) years with TBI were recruited from the Neurosciences Critical Care Unit (NCCU), Addenbrooke's Hospital, Cambridge, UK between 2010 and 2012. Patients presented with median (range) post-resuscitation Glasgow Coma Score (GCS) of 7 (3 – 14), but all subsequently had a GCS < 8 requiring sedation and ventilation for control of intracranial pressure (ICP) (Table 2). Patients were recruited between day 1 and day 9 post-injury (mean 3.3 days) and underwent imaging while sedated and ventilated. Patients with previous TBI, other neurological diseases, or contraindication to magnetic resonance imaging (MRI) were excluded. All patients were managed by protocol-driven care; which included sedation, paralysis and ventilation to ensure that intracranial pressure (ICP) < 20 mmHg and cerebral perfusion pressure > 60 mmHg were maintained.²⁵ Physiological stability was meticulously ensured during imaging through the titration of fluids and vasoactive agents and the presence of a critical care physician and nurse. Patients who received surgical intervention (CSF drainage or decompressive craniectomy) or second-tier medical therapies (barbiturate coma or moderate hypothermia (33 – 35°C)) before imaging are specified in Table 8-1.

Based on previous imaging studies we acquired baseline DTI at a partial pressure of oxygen (PaO_2) of approximately 75 – 90 mmHg (10 – 12 kPa) and then increased the FiO_2 to a maximum of 0.8 in order to achieve a PaO_2 of approximately 225 – 260 mmHg (30 – 35 kPa). Following 60 minutes to allow the impact of higher PaO_2 (and by inference, brain pO_2) levels on cerebral metabolism, repeat DTI was obtained within the same imaging session without moving the patient.

Subject	Age	Sex	Mechanism	Summary of MRI findings	Parenchymal lesion volume (ml)	DAI	GCS	Marshall score	APACHE II	ISS	Neurosurgery	Second tier therapies	Days to MRI	GOS
1	53	M	RTA	Bitemporal, basal ganglia & cortical contusions. Bilateral frontal SDH	100	Yes	4	NEML	17	34	-		4	MD
2	34	M	RTA	Bilateral subcortical & deep white matter, corpus callosum, R thalamus, midbrain & cerebellar contusions. IVH, L occipital & fronto-temporal SDH	20	Yes	4	NEML	21	20	EVD		3	VS
3	34	M	Assault	Bilateral frontal, temporal, R occipital, thalamus & L cerebellar contusions. IVH	607	No	8	EML	25	16	DC, R SDH EVD		3	SD
4	21	M	RTA	Bilateral cortical, corpus callosum, dorsal midbrain & pons contusions	46	Yes	10	NEML	21	50	-	H	2	MD
5	31	M	RTA	Bilateral frontal, temporal & L occipito-parietal & midbrain contusions	259	No	6	EML	17	29	DC, R SDH		1	MD
6	29	M	Assault	Bilateral frontal & temporal contusions. Bilateral temporal SDH	444	No	10	EML	17	16	DC, EVD	H	2	GR
7	58	M	Fall	Bilateral frontal, temporal & R parietal contusions. Bifrontal SDH & tSAH	122	No	10	NEML	20	34	-	-	4	GR
8	26	M	RTA	Bilateral frontal & temporal contusions. R temporal & L frontotemporal SDH	346	No	3	NEML	17	75	-		3	MD
9	28	M	Assault	R frontotemporal contusions & R SDH	38	No	12	EML	24	36	DC		3	GR
10	61	M	Fall	Bilateral frontal & temporal, corpus callosum & midbrain contusions. L SDH & IVH	358	No	5	NEML	22	75	-		9	NA
11	60	M	Fall	L Frontal, Temporal & Parietal contusions. L SDH	236	No	14	NEML	8	34	-	-	3	MD
12	31	F	Fall	R frontal, temporal, parietal, occipital, bilateral thalamic & midbrain contusions R SDH & IVH	599	No	3	EML	25	75	DC, R SDH	H	4	VS
13	70	F	RTA	Bilateral frontal, parietal, corpus callosum & midbrain contusions. tSAH & IVH	23	Yes	3	2	21	34	-		1	GR
14	27	M	RTA	Bifrontal contusions. R frontal SDH	52	No	7	NEML	16	25	-		4	GR

Table 8-1 Patient characteristics

C, craniotomy; D, death; DAI, diffuse axonal injury; DC, decompressive craniectomy; EDH, extradural hemorrhage; EVD, external ventricular drain; F, female; GCS, Glasgow coma score; GOS, Glasgow outcome score; GR, good recovery; M, male; MD, moderate disability; RTA, road traffic accident; SD, severe disability; SDH, subdural hemorrhage; tSAH, traumatic subarachnoid hemorrhage.

Controls

A total of 32 healthy volunteers (19 females and 13 males) with a median (range) age of 34 (22 – 52) underwent DTI breathing room air. Six of these volunteers were exposed to graded oxygen therapy (60% and 100% inspired oxygen) delivered via a venturi mask (Flexicare Medical Limited, Mid Glamorgan, Wales) and underwent repeat DTI within the same imaging session. Diffusion tensor imaging and whole brain proton spectroscopy were obtained at each level of inspired oxygen (21%, 60% and 100%) following an equilibration period of 15 minutes. The baseline data obtained breathing room air in all 32 subjects, and the graded oxygen therapy data in the six healthy volunteers, are presented in the results section of this manuscript. As part of a previously published study, 26 of these volunteers underwent DTI on up to 4 occasions within two imaging sessions separated by a maximum of six months. The reproducibility data from this historical cohort have been published and are used in the subsequent analyses (see Chapter 4).

Imaging

All subjects were scanned using a 3T Siemens Verio MRI scanner (Siemens AG, Erlangen, Germany) within the WBIC, University of Cambridge. During the study period, there were no major changes or upgrades to the scanner or software. Sequences included a 3D T1-weighted magnetisation prepared rapid gradient echo (MPRAGE), fluid attenuated inversion recovery (FLAIR), gradient echo (GE), susceptibility weighted (SWI), dual spin echo (proton density/T2-weighted) and whole brain proton spectroscopy (26 minutes). The DTI data were acquired over 13:50 minutes using 63 non-collinear directions, $b=1000 \text{ s/mm}^2$ with one volume acquired without diffusion weighting ($b = 0$), echo time (TE) 106ms, repetition time (TR) 11700ms, 63 slices, field of view 192mm x 92mm, and $2 \times 2 \times 2 \text{ mm}^3$ isotropic voxels. All imaging was reviewed by a specialist clinical neuroradiologist.

Image processing

Fractional anisotropy, MD and AD maps were created using the Oxford Centre for Functional MRI of the brain FSL Diffusion Toolbox. While RD values were calculated as the mean of the second and third eigenvalues. To aid coregistration, the skull and extracranial soft tissue were stripped from the MPRAGE image using the Brain Extraction Tool of FSL. The diffusion weighted data were normalised to the Montreal Neurological Institute 152 (MNI152) template using the non-linear vtkCISG normalised mutual information algorithm. Using the same non-linear algorithm, the T1 weighted images were coregistered to the MNI152 template and each subject's $b = 0$ image subsequently coregistered to the individual T1 weighted image. The transformation matrix normalising the MPRAGE was then applied

to the $b = 0$ images. All coregistered and normalised images were visually checked to ensure that they were aligned.

Region of interest analysis

Lesions were defined in native FLAIR space (hand-drawn) by a single author (JG, sense checked and confirmed for concordance by other authors TV and JPC), and segregated into regions defined as core, contusion and pericontusion using patient FLAIR, MPRAGE, GE and SWI images. SWI (three dimensional), GE (two dimensional) were used to identify areas of necrotic core in the contusion along with the structural imaging. Lesion core was identified as a region of mixed signal intensity consistent with haemorrhage and necrotic tissue (GE, SWI and FLAIR) and contusion as an area of high signal on FLAIR (Figure 8-1). The ROIs were drawn using Analyze 8.5 (Analyze Direct, Lenexa, KS, USA). FLAIR images were coregistered to T1 space using SPM8, and the coregistration matrix applied to the individual lesion ROIs.

Regions of interest from the Harvard Oxford subcortical and MNI structural probabilistic atlases available within FSL were applied in normalised space. The ROI template was modified by the erosion of a single voxel using the `fslmaths` tool within FSL to improve spatial localisation and reduce the impact of coregistration, normalisation and partial volume errors as previously described in this thesis²³². In patients, these analyses were performed on “lesion free” brain by the exclusion of lesion core and contusion tissue following the transformation of the lesion ROI to normalised space (Figure 8-2). While this resulted in the removal of a few regions were a lesion covered the entire ROI, normal appearing tissue from within the remaining volume of brain of each region was retained for subsequent analyses. The FA, MD, AD and RD values for the different ROIs were calculated using in-house software using Matlab (Mathworks, Natick, USA).

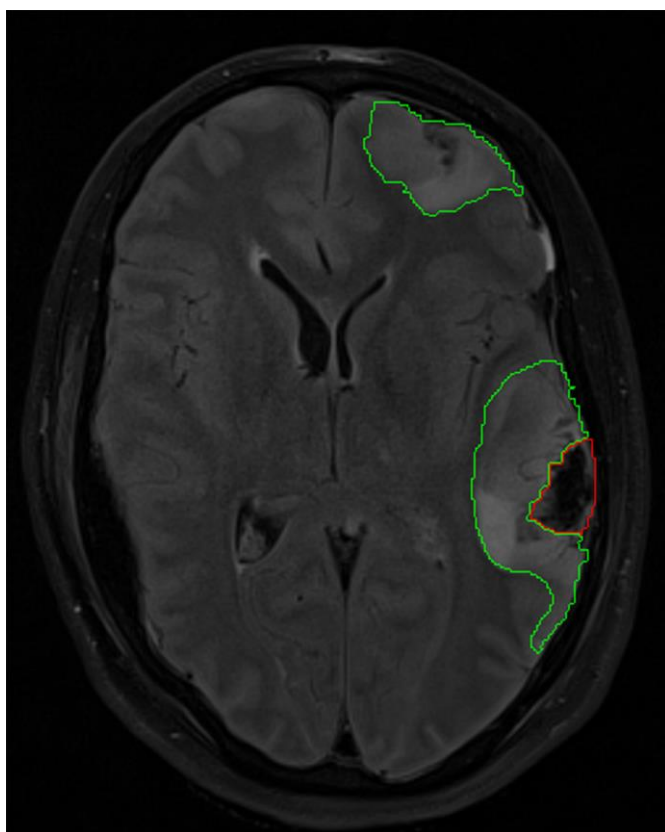


Figure 8-1 Lesion regions of Interest
Fluid attenuated inversion recovery (FLAIR) image from subject 8 with lesion core and contusion highlighted on a single axial slice

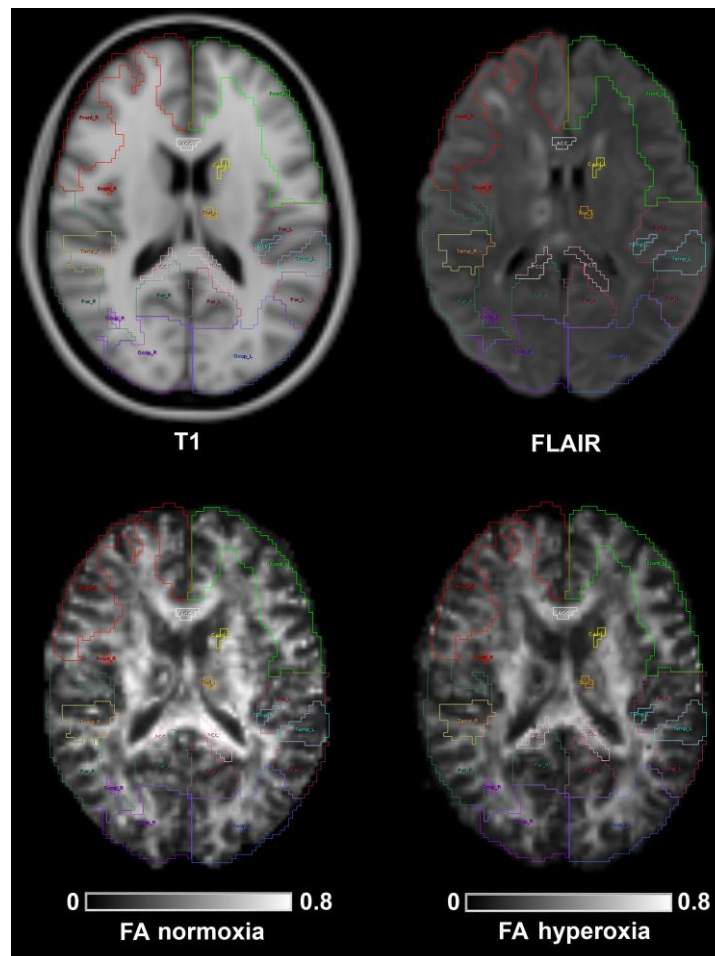


Figure 8-2 Individualised template regions of interest

Standard T1 weighted magnetic resonance image and patient fluid attenuated inversion recovery (FLAIR), fractional anisotropy (FA) at baseline normoxia and following hyperoxia; all images are displayed in Montreal Neurological Institute 152 (MNI152) space. The region of interest (ROI) template for this subject (subject 1) has been individualised by the exclusion of lesion core and contusion tissue. On the FLAIR image slice shown lesions can be seen within the right frontal and temporal cortex, white matter, right caudate and right thalamus. On this axial slice regions shown include frontal left (Front_L), frontal right (Front_R), temporal left (Temp_L), temporal right (Temp_R), parietal left (Par_L), parietal right (Par_R), occipital left (Occip_L), occipital right (Occip_R), anterior corpus callosum (ACC), posterior corpus callosum (PCC), caudate left (Caud_L) and thalamus left (Thal_L).

Impact of hyperoxia

Using published DTI reproducibility data from the historical cohort of 26 volunteers included in this manuscript (Chapter 4), we assessed the significance of changes in DTI parameters following NH. Based on the standard deviation (SD) of DTI measurements the overall population 99% PIs for zero change (based on three SD values) were 9.6×10^{-5} , 9.6×10^{-5} and 2.5×10^{-4} mm²/second for AD, RD and MD respectively, and 3.6×10^{-2} for FA. We calculated the percentage of ROIs in patients with increases or decreases in DTI parameters greater than the overall 99% Prediction interval for zero change. Since measurements of reproducibility can vary depending on the brain region examined, we also used an estimate of the regional 99% prediction interval for zero change calculated for each ROI. As this is

based on the four independent measurements obtained for each ROI in isolation, we must be more cautious. For a *t* distribution with 3 degrees of freedom, this should be based on 5.8 SD values, and this estimate was used for each individual ROI value in calculating the regional 99% prediction interval for zero change.^{179,232}

Data and statistical analysis

Statistical analyses were conducted using Statview (Version 5, 1998, SAS Institute Inc., Cary, North Carolina, USA). All data are expressed and displayed as mean and SD unless otherwise stated. Individual ROIs were treated independently, since they represented a clinically relevant method of segmenting the brain, with specific location being irrelevant to this analysis. Data were compared using unpaired and paired *t*-tests and ANOVA. All *p* values are quoted after Bonferroni correction (where appropriate), and *p* values that remained < .05 following multiplication by the number of tests performed were considered significant.

Results

Effect of graduated oxygen therapy on diffusion tensor imaging in healthy volunteers

The DTI data at each level of inspired oxygen are displayed in Table 8-2 and 8-3 for white and mixed cortical and deep grey matter regions, respectively. As expected, there were significant differences between the brain regions for fractional anisotropy (FA), axial diffusivity (AD), radial diffusivity (RD) and mean diffusivity (MD) ($p < 0.001$ for all comparisons using ANOVA with Bonferroni correction). While the DTI parameters were variable across the different brain regions there were no significant changes in FA, AD, RD and MD with an increase in the fraction of inspired oxygen (F_{iO_2}) within white matter ($p = 0.82, 0.87, 0.70$ and 0.68 respectively, analysis of variance (ANOVA)) and mixed cortical and deep grey matter regions of interest (ROIs) ($0.66, 0.32, 0.47$ and 0.40 respectively, ANOVA).

	<i>FA</i>			<i>AD</i>			<i>RD</i>			<i>MD</i>		
	21%	60%	100%	21%	60%	100%	21%	60%	100%	21%	60%	100%
ACC	0.50221 ± 0.14227	0.51701 ± 0.13994	0.51598 ± 0.12946	0.00147 ± 0.00014	0.00151 ± 0.00012	0.00153 ± 0.00010	0.00063 ± 0.00014	0.00063 ± 0.00017	0.00065 ± 0.00014	0.00091 ± 0.00007	0.00093 ± 0.00009	0.00094 ± 0.00006
BCC	0.62040 ± 0.18813	0.61152 ± 0.17453	0.60411 ± 0.18935	0.00163 ± 0.00021	0.00163 ± 0.00019	0.00162 ± 0.00020	0.00054 ± 0.00019	0.00056 ± 0.00018	0.00057 ± 0.00021	0.00091 ± 0.00010	0.00091 ± 0.00008	0.00092 ± 0.00012
PCC	0.72065 ± 0.06245	0.70915 ± 0.06939	0.72249 ± 0.05558	0.00169 ± 0.00018	0.00169 ± 0.00018	0.00166 ± 0.00013	0.00045 ± 0.00019	0.00046 ± 0.00018	0.00041 ± 0.00010	0.00086 ± 0.00018	0.00087 ± 0.00018	0.00083 ± 0.00010
ATR left	0.41352 ± 0.01627	0.41092 ± 0.01820	0.41295 ± 0.01898	0.00116 ± 0.00002	0.00116 ± 0.00002	0.00117 ± 0.00002	0.00061 ± 0.00002	0.00061 ± 0.00002	0.00062 ± 0.00003	0.00079 ± 0.00002	0.00080 ± 0.00002	0.00080 ± 0.00002
ATR right	0.38022 ± 0.01080	0.38072 ± 0.01289	0.37752 ± 0.01495	0.00123 ± 0.00002	0.00123 ± 0.00002	0.00124 ± 0.00002	0.00071 ± 0.00002	0.00071 ± 0.00003	0.00072 ± 0.00003	0.00088 ± 0.00002	0.00089 ± 0.00003	0.00090 ± 0.00003
SLF left	0.35047 ± 0.00847	0.34760 ± 0.01557	0.34740 ± 0.01195	0.00113 ± 0.00003	0.00113 ± 0.00003	0.00113 ± 0.00003	0.00069 ± 0.00003	0.00069 ± 0.00003	0.00070 ± 0.00003	0.00083 ± 0.00003	0.00084 ± 0.00003	0.00084 ± 0.00003
SLF right	0.37194 ± 0.01291	0.37352 ± 0.01132	0.37423 ± 0.01091	0.00114 ± 0.00003	0.00115 ± 0.00002	0.00114 ± 0.00002	0.00066 ± 0.00002	0.00067 ± 0.00002	0.00067 ± 0.00002	0.00082 ± 0.00002	0.00083 ± 0.00002	0.00083 ± 0.00002
ILF left	0.39235 ± 0.00718	0.39099 ± 0.01296	0.39078 ± 0.01037	0.00116 ± 0.00003	0.00116 ± 0.00004	0.00116 ± 0.00005	0.00062 ± 0.00002	0.00063 ± 0.00003	0.00062 ± 0.00003	0.00080 ± 0.00002	0.00080 ± 0.00003	0.00080 ± 0.00004
ILF right	0.41145 ± 0.02079	0.40903 ± 0.02208	0.41097 ± 0.01977	0.00122 ± 0.00003	0.00122 ± 0.00003	0.00123 ± 0.00003	0.00064 ± 0.00003	0.00064 ± 0.00003	0.00064 ± 0.00003	0.00083 ± 0.00003	0.00083 ± 0.00003	0.00084 ± 0.00002
C left	0.31285 ± 0.04658	0.31081 ± 0.04683	0.31204 ± 0.05076	0.00117 ± 0.00005	0.00117 ± 0.00004	0.00116 ± 0.00005	0.00072 ± 0.00005	0.00073 ± 0.00005	0.00072 ± 0.00005	0.00087 ± 0.00003	0.00088 ± 0.00002	0.00087 ± 0.00002
C right	0.31179 ± 0.07048	0.30697 ± 0.07175	0.31259 ± 0.06668	0.00131 ± 0.00007	0.00132 ± 0.00008	0.00131 ± 0.00006	0.00084 ± 0.00012	0.00085 ± 0.00012	0.00083 ± 0.00013	0.00100 ± 0.00009	0.00100 ± 0.00009	0.00099 ± 0.00010
UF left	0.39901 ± 0.01733	0.39133 ± 0.02412	0.39329 ± 0.01869	0.00115 ± 0.00003	0.00115 ± 0.00004	0.00115 ± 0.00004	0.00061 ± 0.00003	0.00062 ± 0.00004	0.00062 ± 0.00004	0.00079 ± 0.00003	0.00080 ± 0.00003	0.00080 ± 0.00004
UF right	0.39146 ± 0.03456	0.39149 ± 0.03235	0.38938 ± 0.03364	0.00124 ± 0.00005	0.00124 ± 0.00005	0.00125 ± 0.00004	0.00068 ± 0.00005	0.00068 ± 0.00006	0.00069 ± 0.00005	0.00087 ± 0.00004	0.00087 ± 0.00005	0.00088 ± 0.00004
CT left	0.48057 ± 0.01368	0.47754 ± 0.00970	0.47619 ± 0.01439	0.00130 ± 0.00003	0.00129 ± 0.00003	0.00130 ± 0.00003	0.00064 ± 0.00004	0.00064 ± 0.00004	0.00065 ± 0.00004	0.00086 ± 0.00004	0.00086 ± 0.00003	0.00087 ± 0.00004
CT right	0.48926 ± 0.00934	0.48504 ± 0.00208	0.48648 ± 0.00921	0.00126 ± 0.00004	0.00126 ± 0.00004	0.00127 ± 0.00003	0.00059 ± 0.00004	0.00060 ± 0.00004	0.00060 ± 0.00003	0.00081 ± 0.00004	0.00082 ± 0.00004	0.00082 ± 0.00003
F Mi	0.36611 ± 0.01964	0.36525 ± 0.02001	0.36728 ± 0.01612	0.00122 ± 0.00003	0.00122 ± 0.00004	0.00124 ± 0.00002	0.00071 ± 0.00004	0.00071 ± 0.00004	0.00072 ± 0.00003	0.00088 ± 0.00003	0.00088 ± 0.00004	0.00089 ± 0.00003
F Ma	0.41639 ± 0.03417	0.41371 ± 0.04138	0.41553 ± 0.03673	0.00130 ± 0.00006	0.00130 ± 0.00006	0.00130 ± 0.00005	0.00068 ± 0.00005	0.00068 ± 0.00005	0.00068 ± 0.00005	0.00088 ± 0.00004	0.00089 ± 0.00004	0.00088 ± 0.00003
VM	0.55563 ± 0.05028	0.54126 ± 0.04962	0.53096 ± 0.05866	0.00139 ± 0.00017	0.00137 ± 0.00021	0.00141 ± 0.00021	0.00049 ± 0.00019	0.00050 ± 0.00019	0.00054 ± 0.00025	0.00079 ± 0.00018	0.00079 ± 0.00020	0.00083 ± 0.00024
DM	0.51031 ± 0.05171	0.50918 ± 0.05721	0.49917 ± 0.05955	0.00124 ± 0.00006	0.00125 ± 0.00005	0.00128 ± 0.00008	0.00054 ± 0.00009	0.00054 ± 0.00008	0.00058 ± 0.00009	0.00077 ± 0.00007	0.00078 ± 0.00007	0.00081 ± 0.00008
CP left	0.50069 ± 0.02066	0.50010 ± 0.01832	0.48834 ± 0.01827	0.00112 ± 0.00009	0.00112 ± 0.00008	0.00112 ± 0.00006	0.00047 ± 0.00005	0.00048 ± 0.00005	0.00049 ± 0.00003	0.00069 ± 0.00006	0.00069 ± 0.00006	0.00070 ± 0.00004
CP right	0.52664 ± 0.01868	0.52488 ± 0.01068	0.52953 ± 0.02562	0.00115 ± 0.00006	0.00115 ± 0.00007	0.00113 ± 0.00008	0.00046 ± 0.00001	0.00046 ± 0.00002	0.00045 ± 0.00003	0.00069 ± 0.00003	0.00069 ± 0.00004	0.00068 ± 0.00004
P left	0.54257 ± 0.03019	0.52804 ± 0.04279	0.53039 ± 0.03928	0.00128 ± 0.00007	0.00127 ± 0.00010	0.00127 ± 0.00014	0.00051 ± 0.00006	0.00052 ± 0.00007	0.00052 ± 0.00008	0.00077 ± 0.00006	0.00077 ± 0.00008	0.00077 ± 0.00010
P right	0.47292 ± 0.02088	0.45338 ± 0.04297	0.46720 ± 0.02883	0.00125 ± 0.00010	0.00126 ± 0.00016	0.00126 ± 0.00013	0.00059 ± 0.00007	0.00061 ± 0.00012	0.00060 ± 0.00010	0.00081 ± 0.00008	0.00083 ± 0.00013	0.00082 ± 0.00011
Mean	0.45389 ± 0.11151	0.44998 ± 0.10941	0.45021 ± 0.10944	0.00127 ± 0.00017	0.00127 ± 0.00017	0.00128 ± 0.00017	0.00061 ± 0.00012	0.00062 ± 0.00013	0.00062 ± 0.00013	0.00083 ± 0.00010	0.00084 ± 0.00010	0.00084 ± 0.00010

Table 8-2 Impact of oxygen therapy on diffusion tensor imaging parameters in healthy volunteers within white matter regions

Data are mean ± standard deviation using the atlas regions of interest applied in normalised space for fractional anisotropy (FA), mean diffusivity (MD) mm²/second, axial (AD) mm²/second and radial diffusivity (RD) mm²/second for six volunteers. Anterior corpus callosum (ACC), body corpus callosum (BCC), posterior corpus callosum (PCC), anterior thalamic radiation (ATR), superior longitudinal fasciculus (SLF), inferior longitudinal fasciculus (ILF), Cingulum (C), uncinate fasciculus (UF), corticospinal tract (CT), forceps minor (F Mi), forceps major (F Ma), ventral midbrain (VM), dorsal midbrain (DM), cerebral peduncle (CP), pons (P).

	<i>FA</i>			<i>AD</i>			<i>RD</i>			<i>MD</i>		
	21%	60%	100%	21%	60%	100%	21%	60%	100%	21%	60%	100%
Caud left	0.31673 ± 0.02508	0.30618 ± 0.01805	0.30588 ± 0.02167	0.00098 ± 0.00004	0.00098 ± 0.00005	0.00098 ± 0.00005	0.00060 ± 0.00002	0.00062 ± 0.00002	0.00062 ± 0.00004	0.00073 ± 0.00002	0.00074 ± 0.00003	0.00074 ± 0.00004
Caud right	0.25826 ± 0.01186	0.26358 ± 0.01362	0.26141 ± 0.01089	0.00100 ± 0.00005	0.00100 ± 0.00005	0.00101 ± 0.00005	0.00070 ± 0.00003	0.00070 ± 0.00004	0.00070 ± 0.00001	0.00080 ± 0.00003	0.00080 ± 0.00004	0.00081 ± 0.00002
Thal left	0.34176 ± 0.01511	0.34810 ± 0.01540	0.35057 ± 0.01520	0.00102 ± 0.00003	0.00103 ± 0.00003	0.00103 ± 0.00002	0.00062 ± 0.00002	0.00061 ± 0.00001	0.00061 ± 0.00001	0.00075 ± 0.00002	0.00075 ± 0.00001	0.00075 ± 0.00001
Thal right	0.33759 ± 0.01271	0.34540 ± 0.00680	0.33842 ± 0.01065	0.00107 ± 0.00004	0.00108 ± 0.00001	0.00108 ± 0.00002	0.00066 ± 0.00002	0.00066 ± 0.00002	0.00067 ± 0.00001	0.00080 ± 0.00002	0.00080 ± 0.00001	0.00081 ± 0.00002
H left	0.27931 ± 0.01450	0.28370 ± 0.01449	0.28669 ± 0.01327	0.00130 ± 0.00005	0.00131 ± 0.00005	0.00132 ± 0.00006	0.00088 ± 0.00005	0.00089 ± 0.00004	0.00089 ± 0.00005	0.00102 ± 0.00004	0.00103 ± 0.00004	0.00103 ± 0.00005
H right	0.28173 ± 0.01553	0.28166 ± 0.01753	0.28907 ± 0.01828	0.00144 ± 0.00005	0.00146 ± 0.00007	0.00146 ± 0.00005	0.00098 ± 0.00005	0.00099 ± 0.00006	0.00099 ± 0.00004	0.00113 ± 0.00005	0.00115 ± 0.00006	0.00115 ± 0.00004
F left	0.24207 ± 0.00387	0.24104 ± 0.00709	0.24324 ± 0.00745	0.00124 ± 0.00008	0.00126 ± 0.00008	0.00125 ± 0.00007	0.00092 ± 0.00007	0.00093 ± 0.00007	0.00092 ± 0.00006	0.00102 ± 0.00008	0.00104 ± 0.00007	0.00103 ± 0.00006
F right	0.23650 ± 0.00423	0.23606 ± 0.00211	0.23572 ± 0.00646	0.00128 ± 0.00007	0.00128 ± 0.00007	0.00128 ± 0.00005	0.00096 ± 0.00006	0.00095 ± 0.00006	0.00096 ± 0.00005	0.00106 ± 0.00006	0.00106 ± 0.00006	0.00106 ± 0.00005
P left	0.25733 ± 0.00825	0.25441 ± 0.01647	0.25662 ± 0.01468	0.00126 ± 0.00011	0.00127 ± 0.00010	0.00127 ± 0.00010	0.00091 ± 0.00010	0.00092 ± 0.00009	0.00092 ± 0.00009	0.00103 ± 0.00010	0.00104 ± 0.00009	0.00104 ± 0.00009
P right	0.25676 ± 0.00769	0.25622 ± 0.01135	0.25826 ± 0.01062	0.00129 ± 0.00007	0.00130 ± 0.00007	0.00130 ± 0.00006	0.00094 ± 0.00006	0.00095 ± 0.00006	0.00095 ± 0.00006	0.00106 ± 0.00006	0.00107 ± 0.00006	0.00106 ± 0.00006
Temp left	0.23648 ± 0.00696	0.23727 ± 0.01211	0.23691 ± 0.00850	0.00109 ± 0.00003	0.00111 ± 0.00004	0.00111 ± 0.00003	0.00077 ± 0.00003	0.00078 ± 0.00004	0.00079 ± 0.00003	0.00088 ± 0.00003	0.00089 ± 0.00004	0.00090 ± 0.00003
Temp right	0.25081 ± 0.00664	0.25316 ± 0.00908	0.25276 ± 0.00909	0.00118 ± 0.00002	0.00119 ± 0.00002	0.00120 ± 0.00002	0.00083 ± 0.00002	0.00084 ± 0.00002	0.00084 ± 0.00003	0.00094 ± 0.00002	0.00096 ± 0.00002	0.00096 ± 0.00003
O left	0.24035 ± 0.01366	0.24140 ± 0.01701	0.24371 ± 0.01533	0.00115 ± 0.00005	0.00116 ± 0.00004	0.00116 ± 0.00004	0.00083 ± 0.00005	0.00084 ± 0.00004	0.00084 ± 0.00005	0.00094 ± 0.00005	0.00095 ± 0.00004	0.00095 ± 0.00005
O right	0.23499 ± 0.01004	0.23343 ± 0.01326	0.23542 ± 0.01063	0.00118 ± 0.00005	0.00119 ± 0.00003	0.00119 ± 0.00003	0.00086 ± 0.00004	0.00087 ± 0.00003	0.00087 ± 0.00003	0.00096 ± 0.00004	0.00098 ± 0.00003	0.00097 ± 0.00003
Cereb left	0.22897 ± 0.01667	0.22951 ± 0.01207	0.23166 ± 0.01633	0.00103 ± 0.00009	0.00104 ± 0.00009	0.00106 ± 0.00008	0.00074 ± 0.00009	0.00075 ± 0.00009	0.00076 ± 0.00008	0.00084 ± 0.00009	0.00085 ± 0.00009	0.00086 ± 0.00008
Cereb right	0.22549 ± 0.01729	0.22826 ± 0.01589	0.22658 ± 0.01788	0.00102 ± 0.00007	0.00103 ± 0.00008	0.00103 ± 0.00008	0.00074 ± 0.00007	0.00075 ± 0.00009	0.00075 ± 0.00008	0.00083 ± 0.00007	0.00085 ± 0.00009	0.00084 ± 0.00008
Mean	0.26407 ± 0.03850	0.26496 ± 0.03954	0.26581 ± 0.03910	0.00116 ± 0.00014	0.00117 ± 0.00014	0.00117 ± 0.00014	0.00081 ± 0.00013	0.00082 ± 0.00013	0.00082 ± 0.00013	0.00092 ± 0.00013	0.00093 ± 0.00013	0.00093 ± 0.00013

Table 8-3 Impact of oxygen therapy on diffusion tensor imaging parameters in healthy volunteers within mixed cortical and deep grey matter regions

Data are mean ± standard deviation using the atlas regions of interest applied in normalised space for fractional anisotropy (FA), mean diffusivity (MD) mm²/second, axial (AD) mm²/second and radial diffusivity (RD) mm²/second for six volunteers. Caudate (Caud), thalamus (Thal), hippocampus (H), frontal (F), parietal (P), temporal (Temp), occipital (O), cerebellum (Cereb).

Diffusion tensor imaging in patients and healthy volunteers

Patient characteristics are shown in Table 8-1. For the 14 patients and 32 healthy volunteers, there was no significant difference in age ($p = 0.48$, Mann-Whitney U test). The baseline ROI data for healthy volunteers and normoxic patients from predominantly white matter, and mixed cortical and deep grey matter are summarised in Table 8-4 and 8-5, respectively. These demonstrate that baseline patient data show lower FA, MD, AD and RD values than healthy volunteers in a variety of normal appearing white and mixed cortical and deep grey matter regions ($p < 0.05$, unpaired t-tests with Bonferroni correction).

	FA			AD			RD			MD		
	Control	Normoxia	p value									
ACC	0.63677 ± 0.12020	0.49887 ± 0.20845	0.0095	0.00158 ± 0.00011	0.00136 ± 0.00053	0.034	0.00048 ± 0.00013	0.00050 ± 0.00023	0.6457	0.00085 ± 0.00007	0.00080 ± 0.00030	0.3749
BCC	0.58257 ± 0.18841	0.33346 ± 0.20998	0.0004	0.00166 ± 0.00012	0.00117 ± 0.00055	<0.0001	0.00064 ± 0.00028	0.00062 ± 0.00027	0.8352	0.00097 ± 0.00019	0.00081 ± 0.00034	0.0438
PCC	0.70273 ± 0.08119	0.57710 ± 0.13015	0.0004	0.00177 ± 0.00022	0.00139 ± 0.00029	<0.0001	0.00056 ± 0.00035	0.00045 ± 0.00015	0.2763	0.00095 ± 0.00027	0.00078 ± 0.00014	0.0280
ATR left	0.40868 ± 0.01945	0.35482 ± 0.07519	0.0004	0.00119 ± 0.00003	0.00105 ± 0.00018	<0.0001	0.00064 ± 0.00004	0.00057 ± 0.00009	0.0003	0.00083 ± 0.00004	0.00074 ± 0.00011	0.0002
ATR right	0.36912 ± 0.01944	0.29968 ± 0.09557	0.0003	0.00127 ± 0.00004	0.00107 ± 0.00035	0.0035	0.00076 ± 0.00005	0.00065 ± 0.00023	0.0139	0.00093 ± 0.00005	0.00081 ± 0.00025	0.0115
SLF left	0.34637 ± 0.01184	0.31853 ± 0.06529	0.0229	0.00113 ± 0.00003	0.00106 ± 0.00022	0.0638	0.00070 ± 0.00003	0.00064 ± 0.00014	0.0255	0.00084 ± 0.00003	0.00078 ± 0.00017	0.0380
SLF right	0.37167 ± 0.01266	0.32277 ± 0.05725	<0.0001	0.00114 ± 0.00002	0.00104 ± 0.00017	0.0014	0.00067 ± 0.00002	0.00061 ± 0.00010	0.0017	0.00083 ± 0.00002	0.00076 ± 0.00012	0.0020
ILF left	0.38820 ± 0.01635	0.32670 ± 0.09123	0.0005	0.00117 ± 0.00002	0.00101 ± 0.00028	0.0029	0.00064 ± 0.00003	0.00056 ± 0.00016	0.0061	0.00081 ± 0.00002	0.00072 ± 0.00019	0.0059
ILF right	0.41278 ± 0.01966	0.31476 ± 0.13090	0.0001	0.00125 ± 0.00004	0.00099 ± 0.00041	0.0008	0.00066 ± 0.00004	0.00053 ± 0.00022	0.0026	0.00085 ± 0.00003	0.00069 ± 0.00028	0.0025
C left	0.30335 ± 0.03759	0.30404 ± 0.04193	0.9562	0.00118 ± 0.00005	0.00113 ± 0.00021	0.2290	0.00075 ± 0.00006	0.00070 ± 0.00015	0.1165	0.00089 ± 0.00005	0.00085 ± 0.00017	0.1613
C right	0.30259 ± 0.05510	0.26216 ± 0.07964	0.0573	0.00131 ± 0.00008	0.00108 ± 0.00033	0.0006	0.00086 ± 0.00012	0.00070 ± 0.00024	0.0040	0.00101 ± 0.00010	0.00084 ± 0.00027	0.0029
UF left	0.39960 ± 0.01869	0.28661 ± 0.11856	<0.0001	0.00117 ± 0.00003	0.00091 ± 0.00037	0.0002	0.00063 ± 0.00003	0.00051 ± 0.00020	0.0014	0.00081 ± 0.00002	0.00066 ± 0.00023	0.0006
UF right	0.37650 ± 0.02579	0.24896 ± 0.13432	<0.0001	0.00127 ± 0.00005	0.00090 ± 0.00049	0.0001	0.00073 ± 0.00006	0.00053 ± 0.00029	0.0005	0.00091 ± 0.00005	0.00069 ± 0.00032	0.0004
CT left	0.48492 ± 0.01647	0.44921 ± 0.05182	0.0009	0.00128 ± 0.00003	0.00118 ± 0.00012	<0.0001	0.00063 ± 0.00004	0.00058 ± 0.00006	0.0011	0.00084 ± 0.00004	0.00078 ± 0.00007	0.0002
CT right	0.48655 ± 0.01715	0.43681 ± 0.06783	0.0003	0.00126 ± 0.00003	0.00113 ± 0.00015	<0.0001	0.00060 ± 0.00004	0.00053 ± 0.00007	<0.0001	0.00082 ± 0.00004	0.00073 ± 0.00009	<0.0001
F Mi	0.38713 ± 0.01928	0.29800 ± 0.11998	0.0002	0.00126 ± 0.00004	0.00105 ± 0.00043	0.0093	0.00071 ± 0.00004	0.00061 ± 0.00026	0.0413	0.00089 ± 0.00003	0.00077 ± 0.00029	0.0266
F Ma	0.41169 ± 0.03333	0.37233 ± 0.05808	0.0056	0.00134 ± 0.00008	0.00120 ± 0.00019	0.0005	0.00072 ± 0.00008	0.00064 ± 0.00011	0.0137	0.00093 ± 0.00008	0.00083 ± 0.00013	0.0028
VM	0.56403 ± 0.06007	0.51104 ± 0.17386	0.1515	0.00139 ± 0.00015	0.00109 ± 0.00036	0.0006	0.00050 ± 0.00011	0.00040 ± 0.00015	0.0104	0.00080 ± 0.00012	0.00064 ± 0.00021	0.0029
DM	0.53050 ± 0.04129	0.45870 ± 0.09509	0.0014	0.00125 ± 0.00007	0.00116 ± 0.00021	0.0341	0.00054 ± 0.00006	0.00055 ± 0.00012	0.6100	0.00077 ± 0.00005	0.00075 ± 0.00014	0.4959
CP left	0.50314 ± 0.02263	0.51864 ± 0.03881	0.1092	0.00113 ± 0.00006	0.00113 ± 0.00005	0.8293	0.00048 ± 0.00003	0.00047 ± 0.00004	0.3588	0.00070 ± 0.00004	0.00069 ± 0.00004	0.6371
CP right	0.52636 ± 0.01760	0.52704 ± 0.02997	0.9257	0.00114 ± 0.00004	0.00113 ± 0.00006	0.8368	0.00046 ± 0.00002	0.00046 ± 0.00004	0.7512	0.00068 ± 0.00002	0.00069 ± 0.00004	0.8190
P left	0.53110 ± 0.02903	0.52361 ± 0.06831	0.6193	0.00129 ± 0.00008	0.00121 ± 0.00018	0.0567	0.00056 ± 0.00009	0.00052 ± 0.00011	0.1752	0.00079 ± 0.00007	0.00075 ± 0.00013	0.1399
P right	0.52891 ± 0.03832	0.51575 ± 0.05788	0.3833	0.00128 ± 0.00007	0.00118 ± 0.00012	0.0009	0.00055 ± 0.00007	0.00051 ± 0.00007	0.1515	0.00079 ± 0.00007	0.00073 ± 0.00008	0.0212
Mean	0.45335 ± 0.11535	0.39476 ± 0.14502		0.00129 ± 0.00018	0.00112 ± 0.00032		0.00063 ± 0.00015	0.00056 ± 0.00018		0.00085 ± 0.00011	0.00075 ± 0.00020	

Table 8-4 Region of interest data within white matter regions in healthy volunteers and normoxic patients

Data are mean ± standard deviation using the atlas regions of interest applied in normalised space for fractional anisotropy (FA), mean diffusivity (MD) mm²/second, axial (AD) mm²/second and radial diffusivity (RD) mm²/second for 32 healthy volunteers and 14 patients with head injury. Anterior corpus callosum (ACC), body corpus callosum (BCC), posterior corpus callosum (PCC), anterior thalamic radiation (ATR), superior longitudinal fasciculus (SLF), inferior longitudinal fasciculus (ILF), Cingulum (C), uncinate fasciculus (UF), corticospinal tract (CT), forceps minor (F Mi), forceps major (F Ma), ventral midbrain (VM), dorsal midbrain (DM), cerebral peduncle (CP), pons (P). For the comparison between normoxic patients and healthy controls unpaired t-tests with Bonferroni correction for multiple comparisons were utilised, and a p < 0.0022 was considered significant. Significant results are highlighted in bold.

	FA			AD			RD			MD		
	Control	Normoxia	p value	Control	Normoxia	p value	Control	Normoxia	p value	Control	Normoxia	p value
Caud left	0.26092 ± 0.05327	0.29957 ± 0.07987	0.0688	0.00137 ± 0.00042	0.00098 ± 0.00021	0.0027	0.00101 ± 0.00039	0.00060 ± 0.00014	0.0005	0.00112 ± 0.00041	0.00074 ± 0.00014	0.0016
Caud right	0.28511 ± 0.04115	0.22121 ± 0.08821	0.0025	0.00100 ± 0.00012	0.00103 ± 0.00054	0.8329	0.00066 ± 0.00010	0.00074 ± 0.00045	0.3801	0.00078 ± 0.00010	0.00085 ± 0.00046	0.4196
Thal left	0.34373 ± 0.01600	0.34940 ± 0.09018	0.7457	0.00105 ± 0.00003	0.00098 ± 0.00028	0.2294	0.00064 ± 0.00003	0.00056 ± 0.00019	0.0205	0.00078 ± 0.00003	0.00070 ± 0.00022	0.0755
Thal right	0.34814 ± 0.01676	0.33398 ± 0.09947	0.4630	0.00104 ± 0.00003	0.00111 ± 0.00038	0.3440	0.00063 ± 0.00002	0.00067 ± 0.00028	0.4024	0.00077 ± 0.00002	0.00082 ± 0.00031	0.3799
H left	0.28230 ± 0.01721	0.27675 ± 0.04647	0.5754	0.00131 ± 0.00006	0.00119 ± 0.00027	0.0278	0.00089 ± 0.00006	0.00078 ± 0.00020	0.0120	0.00103 ± 0.00006	0.00092 ± 0.00023	0.0221
H right	0.28868 ± 0.01590	0.24806 ± 0.07484	0.0084	0.00143 ± 0.00006	0.00114 ± 0.00040	0.0005	0.00096 ± 0.00007	0.00075 ± 0.00028	0.0003	0.00112 ± 0.00006	0.00090 ± 0.00031	0.0008
F left	0.24658 ± 0.01024	0.23134 ± 0.04662	0.1028	0.00124 ± 0.00006	0.00116 ± 0.00024	0.1240	0.00091 ± 0.00005	0.00084 ± 0.00018	0.0605	0.00102 ± 0.00005	0.00095 ± 0.00020	0.0974
F right	0.24100 ± 0.00749	0.20716 ± 0.06476	0.0086	0.00126 ± 0.00005	0.00111 ± 0.00036	0.0287	0.00094 ± 0.00005	0.00081 ± 0.00028	0.0166	0.00105 ± 0.00005	0.00092 ± 0.00029	0.0267
P left	0.26126 ± 0.01020	0.25815 ± 0.02866	0.6087	0.00125 ± 0.00007	0.00114 ± 0.00020	0.0093	0.00090 ± 0.00006	0.00079 ± 0.00017	0.0020	0.00102 ± 0.00007	0.00091 ± 0.00018	0.0047
P right	0.26039 ± 0.00906	0.25118 ± 0.03396	0.1827	0.00127 ± 0.00005	0.00117 ± 0.00015	0.0015	0.00092 ± 0.00005	0.00082 ± 0.00012	0.0001	0.00104 ± 0.00005	0.00094 ± 0.00012	0.0005
Temp left	0.24581 ± 0.01440	0.20667 ± 0.08940	0.0277	0.00112 ± 0.00005	0.00093 ± 0.00042	0.0173	0.00079 ± 0.00004	0.00064 ± 0.00030	0.0100	0.00090 ± 0.00004	0.00075 ± 0.00033	0.0191
Temp right	0.25492 ± 0.01031	0.19311 ± 0.09262	0.0011	0.00120 ± 0.00003	0.00089 ± 0.00043	0.0005	0.00084 ± 0.00003	0.00062 ± 0.00030	0.0002	0.00096 ± 0.00003	0.00072 ± 0.00034	0.0007
O left	0.24578 ± 0.01287	0.25494 ± 0.01641	0.0544	0.00117 ± 0.00005	0.00108 ± 0.00013	0.0029	0.00084 ± 0.00005	0.00075 ± 0.00011	0.0002	0.00095 ± 0.00005	0.00086 ± 0.00011	0.0007
O right	0.23925 ± 0.01151	0.23656 ± 0.07214	0.8468	0.00120 ± 0.00006	0.00103 ± 0.00030	0.0042	0.00088 ± 0.00005	0.00072 ± 0.00020	<0.0001	0.00099 ± 0.00005	0.00082 ± 0.00023	0.0008
Cereb left	0.23434 ± 0.01828	0.22973 ± 0.04483	0.6374	0.00104 ± 0.00007	0.00097 ± 0.00013	0.0419	0.00074 ± 0.00007	0.00069 ± 0.00010	0.0432	0.00084 ± 0.00007	0.00078 ± 0.00011	0.0477
Cereb right	0.22928 ± 0.01782	0.22957 ± 0.02782	0.9674	0.00103 ± 0.00006	0.00099 ± 0.00008	0.0848	0.00074 ± 0.00006	0.00070 ± 0.00007	0.0920	0.00084 ± 0.00006	0.00080 ± 0.00008	0.0919
Mean	0.26672 ± 0.04034	0.25173 ± 0.07812		0.00119 ± 0.00017	0.00106 ± 0.00031		0.00083 ± 0.00016	0.00072 ± 0.00024		0.00095 ± 0.00016	0.00084 ± 0.00025	

Table 8-5 Region of interest data within mixed cortical and deep grey matter regions in healthy volunteers and normoxic patients

Data are mean ± standard deviation using the atlas regions of interest applied in normalised space for fractional anisotropy (FA), mean diffusivity (MD) mm²/second, axial (AD) mm²/second and radial diffusivity (RD) mm²/second for 32 healthy volunteers and 14 patients with head injury. Caudate (Caud), thalamus (Thal), hippocampus (H), frontal (F), parietal (P), temporal (Temp), occipital (O), cerebellum (Cereb). For the comparison between normoxic patients and healthy controls unpaired t-tests with Bonferroni correction for multiple comparisons were utilised, and a p < 0.0031 was considered significant. Significant results are highlighted in bold

Impact of hyperoxia in patients

The ROI data in patients at normoxia and following hyperoxia for white matter and mixed cortical and deep grey matter are shown in Table 8-6 and 8-7 respectively. These demonstrate that there were no changes in AD and MD. Within white matter, FA was lower and RD higher within the left uncinate fasciculus ($p < 0.05$, paired t-tests with Bonferroni correction). Within mixed cortical and deep grey matter, FA was significantly lower following hyperoxia within the right caudate and occipital regions ($p < 0.05$, paired t tests with Bonferroni correction).

	FA			AD			RD			MD		
	Normoxia	Hyperoxia	p value	Normoxia	Hyperoxia	p value	Normoxia	Hyperoxia	p value	Normoxia	Hyperoxia	p value
ACC	0.49887 ± 0.20845	0.46601 ± 0.19273	0.0334	0.00136 ± 0.00053	0.00131 ± 0.00052	0.0529	0.00050 ± 0.00023	0.00050 ± 0.00024	0.8849	0.00080 ± 0.00030	0.00077 ± 0.00031	0.0554
BCC	0.33346 ± 0.20998	0.33884 ± 0.21408	0.4982	0.00117 ± 0.00055	0.00116 ± 0.00054	0.2799	0.00062 ± 0.00027	0.00060 ± 0.00025	0.1193	0.00081 ± 0.00034	0.00079 ± 0.00032	0.0456
PCC	0.57710 ± 0.13015	0.57336 ± 0.12501	0.7631	0.00139 ± 0.00029	0.00137 ± 0.00032	0.7383	0.00045 ± 0.00015	0.00045 ± 0.00015	0.5701	0.00078 ± 0.00014	0.00076 ± 0.00018	0.3469
ATR left	0.35482 ± 0.07519	0.33935 ± 0.06744	0.0220	0.00105 ± 0.00018	0.00103 ± 0.00018	0.0114	0.00057 ± 0.00009	0.00056 ± 0.00010	0.2084	0.00074 ± 0.00011	0.00072 ± 0.00013	0.0613
ATR right	0.29968 ± 0.09557	0.28401 ± 0.09722	0.0061	0.00107 ± 0.00035	0.00107 ± 0.00034	0.4104	0.00065 ± 0.00023	0.00065 ± 0.00022	0.4066	0.00081 ± 0.00025	0.00079 ± 0.00026	0.0466
SLF left	0.31853 ± 0.06529	0.31750 ± 0.06472	0.8144	0.00106 ± 0.00022	0.00106 ± 0.00022	0.9032	0.00064 ± 0.00014	0.00064 ± 0.00014	0.9765	0.00078 ± 0.00017	0.00078 ± 0.00017	0.8687
SLF right	0.32277 ± 0.05725	0.32151 ± 0.05791	0.7934	0.00104 ± 0.00017	0.00104 ± 0.00018	0.9763	0.00061 ± 0.00010	0.00061 ± 0.00010	0.6550	0.00076 ± 0.00012	0.00075 ± 0.00013	0.6819
ILF left	0.32670 ± 0.09123	0.32196 ± 0.08965	0.0556	0.00101 ± 0.00028	0.00101 ± 0.00028	0.3297	0.00056 ± 0.00016	0.00056 ± 0.00016	0.9433	0.00072 ± 0.00019	0.00071 ± 0.00020	0.1586
ILF right	0.31476 ± 0.13090	0.30828 ± 0.12736	0.0448	0.00099 ± 0.00041	0.00099 ± 0.00041	0.7629	0.00053 ± 0.00022	0.00053 ± 0.00022	0.1948	0.00069 ± 0.00028	0.00068 ± 0.00028	0.2155
C left	0.30404 ± 0.04193	0.29809 ± 0.03727	0.2383	0.00113 ± 0.00021	0.00110 ± 0.00018	0.1035	0.00070 ± 0.00015	0.00068 ± 0.00015	0.0484	0.00085 ± 0.00017	0.00082 ± 0.00016	0.0695
C right	0.26216 ± 0.07964	0.23905 ± 0.07162	0.0130	0.00108 ± 0.00033	0.00104 ± 0.00033	0.0988	0.00070 ± 0.00024	0.00068 ± 0.00024	0.2510	0.00084 ± 0.00027	0.00080 ± 0.00027	0.0910
UF left	0.28661 ± 0.11856	0.27719 ± 0.11528	0.0011	0.00091 ± 0.00037	0.00091 ± 0.00037	0.6681	0.00051 ± 0.00020	0.00052 ± 0.00020	0.0021	0.00066 ± 0.00023	0.00065 ± 0.00026	0.3428
UF right	0.24896 ± 0.13432	0.24308 ± 0.13207	0.0097	0.00090 ± 0.00049	0.00090 ± 0.00049	0.7409	0.00053 ± 0.00029	0.00053 ± 0.00030	0.3017	0.00069 ± 0.00032	0.00065 ± 0.00036	0.1331
CT left	0.44921 ± 0.05182	0.44727 ± 0.04226	0.8566	0.00118 ± 0.00012	0.00119 ± 0.00009	0.5719	0.00058 ± 0.00006	0.00059 ± 0.00004	0.2257	0.00078 ± 0.00007	0.00079 ± 0.00005	0.3778
CT right	0.43681 ± 0.06783	0.43413 ± 0.06456	0.8495	0.00113 ± 0.00015	0.00114 ± 0.00014	0.6354	0.00053 ± 0.00007	0.00054 ± 0.00006	0.2061	0.00073 ± 0.00009	0.00074 ± 0.00009	0.5114
F Mi	0.29800 ± 0.11998	0.28593 ± 0.11483	0.0120	0.00105 ± 0.00043	0.00105 ± 0.00043	0.8826	0.00061 ± 0.00026	0.00062 ± 0.00025	0.0090	0.00077 ± 0.00029	0.00077 ± 0.00031	0.5523
F Ma	0.37233 ± 0.05808	0.36734 ± 0.05747	0.0326	0.00120 ± 0.00019	0.00119 ± 0.00019	0.7544	0.00064 ± 0.00011	0.00064 ± 0.00011	0.5321	0.00083 ± 0.00013	0.00083 ± 0.00013	0.9731
VM	0.51104 ± 0.17386	0.41313 ± 0.15136	0.0208	0.00109 ± 0.00036	0.00098 ± 0.00036	0.0344	0.00040 ± 0.00015	0.00036 ± 0.00014	0.0326	0.00064 ± 0.00021	0.00057 ± 0.00021	0.0213
DM	0.45870 ± 0.09509	0.45470 ± 0.09622	0.6912	0.00116 ± 0.00021	0.00115 ± 0.00022	0.5138	0.00055 ± 0.00012	0.00054 ± 0.00012	0.3076	0.00075 ± 0.00014	0.00074 ± 0.00015	0.3755
CP left	0.51864 ± 0.03881	0.50183 ± 0.03786	0.2359	0.00113 ± 0.00005	0.00110 ± 0.00008	0.2290	0.00047 ± 0.00004	0.00046 ± 0.00005	0.2358	0.00069 ± 0.00004	0.00067 ± 0.00005	0.1441
CP right	0.52704 ± 0.02997	0.51477 ± 0.03095	0.1299	0.00113 ± 0.00006	0.00112 ± 0.00006	0.4128	0.00046 ± 0.00004	0.00046 ± 0.00005	0.9786	0.00069 ± 0.00004	0.00068 ± 0.00005	0.5297
P left	0.52361 ± 0.06831	0.49732 ± 0.08016	0.1299	0.00121 ± 0.00018	0.00118 ± 0.00020	0.0358	0.00052 ± 0.00011	0.00050 ± 0.00012	0.1257	0.00075 ± 0.00013	0.00073 ± 0.00014	0.0394
P right	0.51575 ± 0.05788	0.48313 ± 0.07295	0.0630	0.00118 ± 0.00012	0.00116 ± 0.00014	0.2579	0.00051 ± 0.00007	0.00051 ± 0.00009	0.9642	0.00073 ± 0.00008	0.00073 ± 0.00010	0.6623
Mean	0.39476 ± 0.14502	0.38033 ± 0.13861		0.00112 ± 0.00032	0.00110 ± 0.00031		0.00056 ± 0.00018	0.00055 ± 0.00018		0.00075 ± 0.00020	0.00074 ± 0.00021	

Table 8-6 Region of interest data within white matter regions in normoxic and hyperoxic patients

Data are mean ± standard deviation using the atlas regions of interest applied in normalised space for fractional anisotropy (FA), mean diffusivity (MD) mm²/second, axial (AD) mm²/second and radial diffusivity (RD) mm²/second for 14 patients with head injury. Anterior corpus callosum (ACC), body corpus callosum (BCC), posterior corpus callosum (PCC), anterior thalamic radiation (ATR), superior longitudinal fasciculus (SLF), inferior longitudinal fasciculus (ILF), Cingulum (C), uncinate fasciculus (UF), corticospinal tract (CT), forceps minor (F Mi), forceps major (F Ma), ventral midbrain (VM), dorsal midbrain (DM), cerebral peduncle (CP), pons (P). For the comparison between normoxic and hyperoxic patients paired t-tests with Bonferroni correction for multiple comparisons were utilised, and a p < 0.0022 was considered significant. Significant results are highlighted in bold.

	FA			AD			RD			MD		
	Normoxia	Hyperoxia	p value	Normoxia	Hyperoxia	p value	Normoxia	Hyperoxia	p value	Normoxia	Hyperoxia	p value
Caud left	0.26092 ± 0.05327	0.27767 ± 0.07919	0.0545	0.00137 ± 0.00042	0.00097 ± 0.00022	0.2827	0.00101 ± 0.00039	0.00061 ± 0.00013	0.8614	0.00112 ± 0.00041	0.00073 ± 0.00016	0.3045
Caud right	0.28511 ± 0.04115	0.19793 ± 0.08400	0.0010	0.00100 ± 0.00012	0.00103 ± 0.00054	0.7154	0.00066 ± 0.00010	0.00076 ± 0.00044	0.3644	0.00078 ± 0.00010	0.00085 ± 0.00047	0.9001
Thal left	0.34373 ± 0.01600	0.34006 ± 0.09364	0.3427	0.00105 ± 0.00003	0.00096 ± 0.00025	0.2320	0.00064 ± 0.00003	0.00054 ± 0.00016	0.3468	0.00078 ± 0.00003	0.00068 ± 0.00019	0.2857
Thal right	0.34814 ± 0.01676	0.31502 ± 0.09599	0.1183	0.00104 ± 0.00003	0.00107 ± 0.00034	0.2343	0.00063 ± 0.00002	0.00065 ± 0.00023	0.5554	0.00077 ± 0.00002	0.00079 ± 0.00026	0.3623
H left	0.28230 ± 0.01721	0.26040 ± 0.04050	0.0268	0.00131 ± 0.00006	0.00118 ± 0.00027	0.2343	0.00089 ± 0.00006	0.00079 ± 0.00020	0.1988	0.00103 ± 0.00006	0.00092 ± 0.00022	0.7549
H right	0.28868 ± 0.01590	0.22844 ± 0.07136	0.0244	0.00143 ± 0.00006	0.00115 ± 0.00039	0.5317	0.00096 ± 0.00007	0.00077 ± 0.00028	0.1794	0.00112 ± 0.00006	0.00090 ± 0.00031	0.8673
F left	0.24658 ± 0.01024	0.22486 ± 0.02626	0.3944	0.00124 ± 0.00006	0.00117 ± 0.00021	0.7043	0.00091 ± 0.00005	0.00085 ± 0.00017	0.1921	0.00102 ± 0.00005	0.00096 ± 0.00019	0.7320
F right	0.24100 ± 0.00749	0.19822 ± 0.05414	0.1786	0.00126 ± 0.00005	0.00111 ± 0.00033	0.7611	0.00094 ± 0.00005	0.00082 ± 0.00026	0.2848	0.00105 ± 0.00005	0.00092 ± 0.00028	0.7473
P left	0.26126 ± 0.01020	0.24623 ± 0.02936	0.1439	0.00125 ± 0.00007	0.00114 ± 0.00020	0.9095	0.00090 ± 0.00006	0.00080 ± 0.00016	0.3040	0.00102 ± 0.00007	0.00091 ± 0.00017	0.5460
P right	0.26039 ± 0.00906	0.24493 ± 0.03334	0.2826	0.00127 ± 0.00005	0.00118 ± 0.00013	0.9294	0.00092 ± 0.00005	0.00084 ± 0.00010	0.2873	0.00104 ± 0.00005	0.00095 ± 0.00011	0.5020
Temp left	0.24581 ± 0.01440	0.18931 ± 0.08033	0.0098	0.00112 ± 0.00005	0.00091 ± 0.00041	0.7466	0.00079 ± 0.00004	0.00065 ± 0.00029	0.6335	0.00090 ± 0.00004	0.00074 ± 0.00033	0.2284
Temp right	0.25492 ± 0.01031	0.17901 ± 0.08160	0.0203	0.00120 ± 0.00003	0.00088 ± 0.00041	0.3056	0.00084 ± 0.00003	0.00063 ± 0.00030	0.5390	0.00096 ± 0.00003	0.00071 ± 0.00034	0.1902
O left	0.24578 ± 0.01287	0.24138 ± 0.01921	0.0185	0.00117 ± 0.00005	0.00107 ± 0.00012	0.3962	0.00084 ± 0.00005	0.00075 ± 0.00011	0.3149	0.00095 ± 0.00005	0.00086 ± 0.00011	0.8351
O right	0.23925 ± 0.01151	0.21773 ± 0.06625	0.0025	0.00120 ± 0.00006	0.00101 ± 0.00029	0.5054	0.00088 ± 0.00005	0.00072 ± 0.00020	0.9072	0.00099 ± 0.00005	0.00082 ± 0.00023	0.5505
Cereb left	0.23434 ± 0.01828	0.22161 ± 0.03535	0.2294	0.00104 ± 0.00007	0.00098 ± 0.00011	0.1807	0.00074 ± 0.00007	0.00070 ± 0.00009	0.0878	0.00084 ± 0.00007	0.00079 ± 0.00010	0.1024
Cereb right	0.22928 ± 0.01782	0.22366 ± 0.02530	0.1595	0.00103 ± 0.00006	0.00099 ± 0.00011	0.2355	0.00074 ± 0.00006	0.00071 ± 0.00007	0.0806	0.00084 ± 0.00006	0.00080 ± 0.00007	0.1561
Mean	0.26672 ± 0.04034	0.23795 ± 0.07417		0.00119 ± 0.00017	0.00105 ± 0.00030		0.00083 ± 0.00016	0.00072 ± 0.00023		0.00095 ± 0.00016	0.00083 ± 0.00025	

Table 8-7 Region of interest data within mixed cortical and deep grey matter regions in normoxic and hyperoxic patients

Data are mean ± standard deviation using the atlas regions of interest applied in normalised space for fractional anisotropy (FA), mean diffusivity (MD) mm²/second, axial (AD) mm²/second and radial diffusivity (RD) mm²/second for 14 patients with head injury. Caudate (Caud), thalamus (Thal), hippocampus (H), frontal (F), parietal (P), temporal (Temp), occipital (O), cerebellum (Cereb). For the comparison between normoxic and hyperoxic patients paired t-tests with Bonferroni correction for multiple comparisons were utilised, and a p < 0.0031 was considered significant. Significant results are highlighted in bold.

The percentage of white and mixed cortical and deep grey matter ROIs in patients and healthy volunteers exposed to hyperoxia showing a change in DTI parameters following NH that was greater than the overall population and regional 99% prediction intervals (PIs) for zero change are summarised in figure 8-3 and 8-4 respectively. In healthy volunteers, these changes are shown from baseline air to 100% oxygen. Using the overall population 99% PI, significant decreases in FA were found within 16% of white matter ROIs from 9/14 patients and in 14% of mixed cortical and deep grey matter ROIs from 8/14 patients. Changes in the other DTI parameters were less frequent; some regions showed significant decreases in AD and MD while RD was generally unchanged.

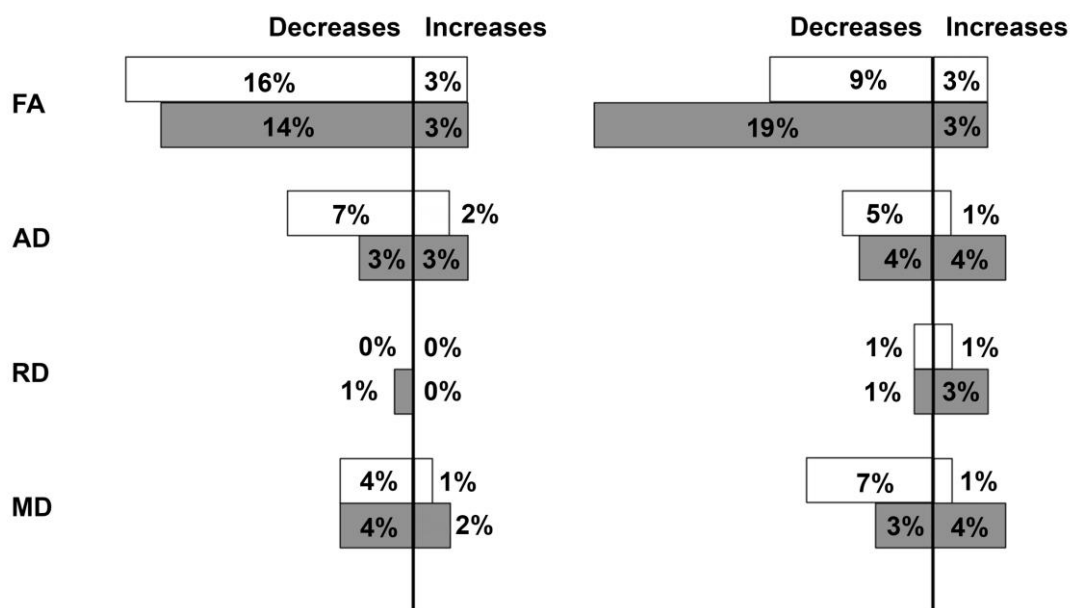


Figure 8-3 Impact of hyperoxia in patients

Fractional anisotropy (FA), axial diffusivity (AD), radial diffusivity (RD) and mean diffusivity (MD) within atlas regions of interest (ROI) applied in normalised space for 14 patients using “lesion free” brain by exclusion of lesion core and contusion tissue. Data displayed are the percentage number of white (white) and mixed cortical and deep grey matter (grey) ROIs showing a change greater than the overall population (left panel) and individual regional (right panel) 99% prediction interval (PI) for zero change. The total number of regions in this cohort was 320 and 223 for white matter and mixed cortical and deep grey matter respectively.

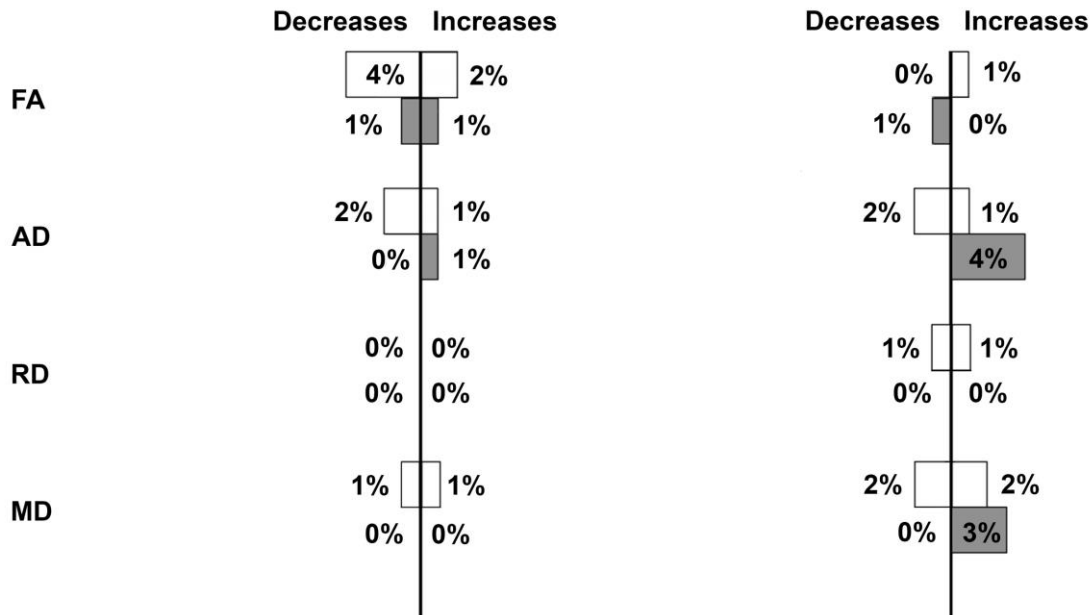


Figure 8-4 Impact of hyperoxia in healthy volunteers

Fractional anisotropy (FA), axial diffusivity (AD), radial diffusivity (RD) and mean diffusivity (MD) within atlas regions of interest (ROI) applied in normalised space for 6 healthy volunteers. Data displayed are the percentage number of white (white) and mixed cortical and deep grey matter (grey) ROIs showing a change greater than the overall population (left panel) and individual regional (right panel) 99% prediction interval (PI) for zero change. The total number of regions in this cohort was 138 and 96 for white matter and mixed cortical and deep grey matter respectively.

Table 8-8 and Table 8-9 provide a detailed list of which patients and regions showed significant change for white and mixed cortical and deep grey matter regions respectively. Decreases in FA were found across the whole brain in many different brain regions. Table 8-10 and Table 8-11 provide the equivalent data for the 6 healthy volunteers who underwent graded exposure to oxygen. The results using the individual ROI reproducibility data were similar and demonstrate significant FA decreases in 9% of white and 19% of mixed cortical and deep grey matter ROIs respectively (see figure 8-3 and 8-4). Table 8-12 and Table 8-13 provide a detailed list of the regions showing significant change for white and mixed cortical and deep grey matter in patients, while Table 8-14 and Table 8-15 show the equivalent for healthy volunteers.

Subject	FA		AD		RD		MD	
	Increases	Decreases	Increases	Decreases	Increases	Decreases	Increases	Decreases
1		VM, P right, ACC, CP left, DM, P left, CP right, C right, CT right, ATR left		VM, ACC, P right, CP left, P left				
2		VM, P right, P left, ATR right, CP left, F Mi						
3								
4		VM		VM				VM
5		VM, CP left, ATR right, ACC, CT right, DM		DM, PCC, SLF R, F Ma, VM				PCC, UF right, DM, SLF right
6	VM, CT right, PCC, CT left, CP left, BCC, DM, SLF right, SLF left, P left	C right	PCC, CT right, CT left, VM, CP left	C right, C left			CT left, CT right, PCC	C right, C left, UF left, ATR left, UF right
7								
8			VM					
9								
10		VM, C right, P left, CP right, CP left		VM, C right				
11		VM, ATR right, ACC, P right, P left, ATR left, CP right, CP left, CT right	P right				P right	VM
12								
13	BCC	VM, P right, ACC, C right, P right, C left, CP right, CP left, CT left, ATR left		VM, ACC, PCC, P left				VM
14		VM						
N (%) regions	11 (3)	50 (16)	7 (2)	22 (7)	0	0	4 (1)	14 (4)

Table 8-8 Patient white matter regions demonstrating a change following hyperoxia using the population 99% prediction interval

Regions showing a significant increase or decrease following hyperoxia that was greater than the overall population 99% prediction interval (PI) are shown for 14 patients with head injury for fractional anisotropy (FA), mean diffusivity (MD), axial (AD) and radial diffusivity (RD). The total number of regions in this patient cohort was 320, and the number (N) and percentage (%) of this total showing a change is provided in the table. Anterior corpus callosum (ACC), body corpus callosum (BCC), posterior corpus callosum (PCC), anterior thalamic radiation (ATR), superior longitudinal fasciculus (SLF), inferior longitudinal fasciculus (ILF), Cingulum (C), uncinate fasciculus (UF), corticospinal tract (CT), forceps minor (F Mi), forceps major (F Ma), ventral midbrain (VM), dorsal midbrain (DM), cerebral peduncle (CP), pons (P).

Subject	<i>FA</i>		<i>AD</i>		<i>RD</i>		<i>MD</i>	
	Increases	Decreases	Increases	Decreases	Increases	Decreases	Increases	Decreases
1		H left, H right, Thal left, Temp right, P right, O right, O left, Thal right, Temp left						
2		Temp right, H right, Temp left, O right		Caud right				Caud right
3								
4								H right
5		Thal right, Cereb left, Thal left, Caud right, O right	Caud right	O right, P right, Temp left	Caud right		Caud right, Thal right	Temp right, F right
6	F left, P left, F right, Thal left, P right, Thal right	H right, Caud left	P right, P left, F right, F left, H right	Thal right, Thal left		Thal right, Thal left	P right, P left, H right	Thal right, Thal left, Caud right, Caud left
7								
8		Caud left						
9								
10			Caud right					
11		Caud left, Caud right, Thal right, Thal left		Caud left				
12								
13		Temp left, H left, Caud right, Caud left, F right						
14		Caud right						
N (%) regions	6 (3)	31 (14)	7(3)	7 (3)	1 (0)	2 (1)	5(2)	8 (4)

Table 8-9 Patient mixed cortical and deep grey matter regions demonstrating a change following hyperoxia using the population 99% prediction interval

Regions showing a significant increase or decrease following hyperoxia that was greater than the overall population 99% prediction interval (PI) are shown for 14 patients with head injury for fractional anisotropy (FA), mean diffusivity (MD), axial (AD) and radial diffusivity (RD). The total number of regions in this patient cohort was 223, and the number (N) and percentage (%) of this total showing a change is provided in the table. Caudate (Caud), thalamus (Thal), hippocampus (H), frontal (F), parietal (P), temporal (Temp), occipital (O), cerebellum (Cereb).

Volunteer	FA		AD		RD		MD	
	Increases	Decreases	Increases	Decreases	Increases	Decreases	Increases	Decreases
1	ACC	P left	ACC	P left				
2	PCC	BCC		PCC				PCC
3	ACC							
4								
5		VM		VM				
6		ACC, VM, P right	VM				VM	
N (%) regions	3 (2)	6 (4)	2(1)	3 (2)	0	0	1(1)	1 (1)

Table 8-10 Healthy volunteer white matter regions demonstrating a change following hyperoxia using the population 99% prediction interval

Regions showing a significant increase or decrease following hyperoxia that was greater than the overall population 99% prediction interval (PI) are shown for 6 controls for fractional anisotropy (FA), mean diffusivity (MD), axial (AD) and radial diffusivity (RD). The total number of regions in this patient cohort was 138, and the number (N) and percentage (%) of this total showing a change is provided in the table. Anterior corpus callosum (ACC), body corpus callosum (BCC), posterior corpus callosum (PCC), anterior thalamic radiation (ATR), superior longitudinal fasciculus (SLF), inferior longitudinal fasciculus (ILF), Cingulum (C), uncinate fasciculus (UF), corticospinal tract (CT), forceps minor (F Mi), forceps major (F Ma), ventral midbrain (VM), dorsal midbrain (DM), cerebral peduncle (CP), pons (P).

Volunteer	FA		AD		RD		MD	
	Increases	Decreases	Increases	Decreases	Increases	Decreases	Increases	Decreases
1								
2								
3								
4								
5								
6	Caud right	Caud left	Caud right					
N (%) regions	1 (1)	1 (1)	1(1)	0	0	0	0	0

Table 8-11 Healthy volunteer mixed cortical and deep grey matter regions demonstrating a change following hyperoxia using the population 99% prediction interval

Regions showing a significant increase or decrease following hyperoxia that was greater than the overall population 99% prediction interval (PI) are shown for 6 controls for fractional anisotropy (FA), mean diffusivity (MD), axial (AD) and radial diffusivity (RD). The total number of regions in this patient cohort was 96, and the number (N) and percentage (%) of this total showing a change is provided in the table. Caudate (Caud), thalamus (Thal), hippocampus (H), frontal (F), parietal (P), temporal (Temp), occipital (O), cerebellum (Cereb).

Subject	FA		AD		RD		MD	
	Increases	Decreases	Increases	Decreases	Increases	Decreases	Increases	Decreases
1		ACC, ATR left, ATR right, ILF right, C right, CT right, VM, CP left, CP right, P left, P right		ACC, VM, CP left, P right				ACC
2		ATR right						
3								
4		VM						
5		ATR left, ATR right, VM, CP left		PCC, SLF left, SLF right, ILF left, UF left, F Ma, DM	ATR right	SLF right		PCC, ATR left, SLF right, IFL left, IFL right, UF right, F Mi, F Ma
6	PCC, ATR left, SLF left, SLF right, CT left, CT right, VM, CP left		PCC, CT left, CT right, CP left	C left, C right	CT left, CT right	ATR left, C left, C right	CT left, CT right	ATR left, ATR right, ILF left, ILF right, C left, C right, UF left, UF right
7								ILF L, UF L, UF R
8								
9								
10		C right						
11		ACC, ATR left, ATR right, VM, P left, P right		ACC, ATR left, VM				
12								
13		ATR left, C left, C right, VM, CP right, P left		C left				C left
14								
N (%) regions	8 (3)	30 (9)	4(1)	17 (5)	3 (1)	4 (1)	2(1)	21 (7)

Table 8-12 Patient white matter regions demonstrating a change following hyperoxia using the regional 99% prediction interval

Regions showing a significant increase or decrease following hyperoxia that was greater than the regional 99% prediction interval (PI) are shown for 14 patients with head injury for fractional anisotropy (FA), mean diffusivity (MD), axial (AD) and radial diffusivity (RD). The total number of regions in this patient cohort was 320, and the number (N) and percentage (%) of this total showing a change is provided in the table. Anterior corpus callosum (ACC), body corpus callosum (BCC), posterior corpus callosum (PCC), anterior thalamic radiation (ATR), superior longitudinal fasciculus (SLF), inferior longitudinal fasciculus (ILF), Cingulum (C), uncinate fasciculus (UF), corticospinal tract (CT), forceps minor (F Mi), forceps major (F Ma), ventral midbrain (VM), dorsal midbrain (DM), cerebral peduncle (CP), pons (P).

Subject	FA		AD		RD		MD	
	Increases	Decreases	Increases	Decreases	Increases	Decreases	Increases	Decreases
1		Thal left, Thal right, H left, H right, P left, P right, Temp left, Temp right, O left, O right		Thal R, H left				Thal right
2		H left, H right, F left, F right, P left, Temp left, Temp right, O left, O right		Caud right		Caud right		Caud right
3								
4								H right
5		Thal left, Thal right, F left, F right, P left, P right, O right	Caud R, Thal R	P right, Temp L, O right	Caud right, Thal right		Caud right, Thal right, P right, Temp right, O right	
6	Thal left, Thal right, F left, F right, P left, P right	Caud left, H left, H right	H right, F left, F right, P left, P right, Temp R, O left, O right	Thal L, Thal R	H right, F right, P left, P right	Thal left, Thal right	H right, P left, P right	Caud right, Thal left, Thal right
7								
8								
9								
10		P left, O right						
11		Caud left, Caud right, Thal left, Thal right						
12								
13		H left, F left, F right, P left, Temp left, O left, O right						
14		O right						
N (%) regions	6 (3)	43 (19)	10(4)	8 (4)	6 (3)	3 (1)	8(4)	6 (3)

Table 8-13 Patient mixed cortical and deep grey matter regions demonstrating a change following hyperoxia using the regional 99% prediction interval

Regions showing a significant increase or decrease following hyperoxia that was greater than the regional 99% prediction interval (PI) are shown for 14 patients with head injury for fractional anisotropy (FA), mean diffusivity (MD), axial (AD) and radial diffusivity (RD). The total number of regions in this patient cohort was 223, and the number (N) and percentage (%) of this total showing a change is provided in the table. Caudate (Caud), thalamus (Thal), hippocampus (H), frontal (F), parietal (P), temporal (Temp), occipital (O), cerebellum (Cereb).

Volunteer	<i>FA</i>		<i>AD</i>		<i>RD</i>		<i>MD</i>	
	Increases	Decreases	Increases	Decreases	Increases	Decreases	Increases	Decreases
1			ACC	ILF left, P left			ACC	ILF left
2	PCC			PCC		PCC	P left	PCC, CP right
3								
4								
5								
6					VM		P right	
N (%) regions	1 (1)	0	1 (1)	3 (2)	1 (1)	1 (1)	3(2)	3 (2)

Table 8-14 Healthy volunteer white matter regions demonstrating a change following hyperoxia using the regional 99% prediction interval

Regions showing a significant increase or decrease following hyperoxia that was greater than the regional 99% prediction interval (PI) are shown for 6 controls for fractional anisotropy (FA), mean diffusivity (MD), axial (AD) and radial diffusivity (RD). The total number of regions in this patient cohort was 138, and the number (N) and percentage (%) of this total showing a change is provided in the table. Anterior corpus callosum (ACC), body corpus callosum (BCC), posterior corpus callosum (PCC), anterior thalamic radiation (ATR), superior longitudinal fasciculus (SLF), inferior longitudinal fasciculus (ILF), Cingulum (C), uncinate fasciculus (UF), corticospinal tract (CT), forceps minor (F Mi), forceps major (F Ma), ventral midbrain (VM), dorsal midbrain (DM), cerebral peduncle (CP), pons (P).

Volunteer	<i>FA</i>		<i>AD</i>		<i>RD</i>		<i>MD</i>	
	Increases	Decreases	Increases	Decreases	Increases	Decreases	Increases	Decreases
1			Temp right				Temp right	
2								
3								
4			Thal right				Thal right	
5								
6		Caud left	Caud right, P right				P right	
N (%) regions	0	1 (1)	4 (4)	0	0	0	3(3)	0

Table 8-15 Healthy volunteer mixed cortical and deep grey matter regions demonstrating a change following hyperoxia using the regional 99% prediction interval

Regions showing a significant increase or decrease following hyperoxia that was greater than the regional 99% prediction interval (PI) are shown for 6 controls for fractional anisotropy (FA), mean diffusivity (MD), axial (AD) and radial diffusivity (RD). The total number of regions in this patient cohort was 96, and the number (N) and percentage (%) of this total showing a change is provided in the table. Caudate (Caud), thalamus (Thal), hippocampus (H), frontal (F), parietal (P), temporal (Temp), occipital (O), cerebellum (Cereb).

Discussion

In this study we used DTI to examine whether an increase in the fraction of inspired oxygen had any beneficial effects within deep grey and mixed cortical, and white matter regions distant from visible contusions following TBI. Baseline patient data showed evidence of traumatic injury with lower MD and FA in several regions compared with healthy volunteers, consistent with cytotoxic oedema and axonal injury, respectively. Exposure to a brief period of NH had no effect on healthy volunteers, and did not ameliorate these findings in patients with some regions showing further FA decreases following the intervention. Using published reproducibility data from a historical cohort of 26 healthy volunteers we demonstrated that 16% of white matter and 14% of deep grey and mixed cortical regions in patients showed a reduction in FA more than the expected population 99% PI for zero change. The mechanistic basis for some of the DTI findings are unclear but implies that a short period of NH has no beneficial impact within the brain that appears normal using conventional structural imaging. To confirm these findings and investigate further will require a longer duration of hyperoxia with serial DTI and conventional MRI in comparison with clinical outcome.

Monitoring of focal tissue oxygen and brain metabolism using microdialysis has shown that hyperoxia can correct derangements and may be associated with improved outcome.^{165,179,306,327} Further, a ¹⁵O PET study suggested that improvements in metabolism with hyperoxia may be particularly relevant within brain regions with physiology consistent with the greatest risk of infarction.¹⁶⁴ We have also used DTI to demonstrate contusion expansion within a rim of low MD consistent with cytotoxic oedema that surrounds a region of high MD (vasogenic oedema), and a short interval of normobaric hyperoxia can increase MD values towards normal within this perilesional rim.¹⁷⁹ Both these imaging studies demonstrate how a short period of exposure to normobaric hyperoxia (~60 minutes) can result in potential benefit. Such findings suggest improvements in oxygen delivery that may relate to evidence of microvascular injury¹⁹ within the 'traumatic penumbra' and are consistent with post mortem studies showing microvascular occlusion and perivascular oedema associated with selective neuronal loss post-TBI. Increased brain oxygen levels may overcome diffusion barriers to oxygen delivery or improve mitochondrial function where low oxygen tension allows nitric oxide to competitively inhibit cytochrome oxidase.⁶⁷ Mitochondrial dysfunction has been shown in ex vivo clinical, and experimental TBI studies,¹⁷⁰ and mitochondrial function can be preserved using hyperoxia.³²⁸ Other studies demonstrate that hyperoxia has neuroprotective and anti-inflammatory effects within the injured brain.^{170,312,313}

While these changes are most evident within perilesional regions, pathophysiological derangements are also evident in regions distant from visible injury based on conventional structural imaging.^{120,268,329} Several PET studies have shown evidence of ischaemia and other metabolic derangements within the brain that may initially appear structurally normal but ultimately demonstrates late atrophy, and is associated with poor outcome.^{120,160,244,330} Further, benefit shown with normobaric hyperoxia in the ¹⁵O PET study by Nortje et al. within the brain demonstrating physiology consistent with the greatest risk of infarction included normal appearing white matter.¹⁶⁴ Studies using DTI are particularly relevant in this regard since evidence of cytotoxic oedema, and traumatic axonal injury is often identified using this technique when conventional structural imaging appears normal.⁴⁷ Our findings were consistent with these data. Despite the exclusion of visible contusions and other areas of brain injury, the patient regional baseline data demonstrated significant DTI abnormalities consistent with cytotoxic oedema and axonal injury in comparison with healthy controls. Such regions were the focus of this study, and our expectation was that we might see an amelioration of cytotoxic oedema and other DTI signal changes in brain distant from contusions following hyperoxia secondary to an improvement in oxygen delivery and/or mitochondrial function. It is important to acknowledge that any change must be sustained if it is to result in improved neuronal survival and better functional outcome for patients, but it is likely that this will require a much longer period of exposure to NH. However, we wished to demonstrate whether it was possible to use DTI as a biomarker of the trajectory of such injury or its recovery in the assessment of therapeutic interventions such as hyperoxia. Previous imaging studies have limited exposure to NH to one hour,^{164,204} and have conducted repeat imaging within a single session in which changes in other physiological and patient-related factors can be minimised. There are also concerns regarding excessive exposure to NH since it can result in atelectasis and pulmonary injury, increased oxidative stress and potential harm in critically ill patients. In this context, a further preliminary study of the impact of NH on the injured brain was warranted.

Experimental and clinical ischaemia following middle cerebral artery occlusion results in early evidence of cytotoxic oedema with a reduction in MD, and while AD and RD are typically reduced, it has been hypothesised that oligodendrite swelling can compress the axoplasm and result in a greater decrease in RD than AD within the white matter.^{331,332} This may explain why acute ischaemia can result in an initial increase in white matter FA if imaging is conducted within 4.5 hours of acute stroke.^{332,333} Later, loss of cellular integrity results in large decreases in white matter FA.³³² These findings are relevant to ischaemic stroke, but were hyperoxia to improve oxygen delivery and attenuate cytotoxic oedema following TBI, MD should increase towards normal and, in theory, an increase in RD that was greater than AD could result in an initial *reduction* in white matter FA. While we did find evidence of

low MD in TBI patients at baseline consistent with cytotoxic oedema, we did not see evidence of an increase in MD towards normal within white or grey matter regions following exposure to hyperoxia. This suggests that the intervention was ineffective, or that a longer period of hyperoxia was needed to demonstrate any effect. Also, the lack of evidence for a reversal of cytotoxic oedema cannot explain our finding of a reduction in FA within the white or grey matter.

We exposed healthy volunteers to oxygen therapy since oxygen has a known paramagnetic effect and could have resulted in systematic changes to our DTI findings.³³⁴ We saw no relationship between a step increase in administered oxygen and any of the DTI parameters. Healthy volunteers received oxygen via a venturi mask, in comparison with TBI patients who received fixed concentrations of inspired oxygen via a closed ventilatory circuit as they had been intubated and ventilated as part of routine clinical care. The Venturi mask provides a means of reliably titrating the FiO_2 in spontaneously breathing subjects,³³⁵ and while arterial blood gases were not monitored in healthy volunteers each step increase in delivered oxygen will have resulted in higher PaO_2 . Following 15 minutes of breathing, 60% oxygen volunteers underwent ~ 45 minutes of imaging (DTI and whole brain proton spectroscopy) while continuing to breath 60% oxygen. Then, following an additional 15 minutes breathing 100% oxygen imaging was repeated for the last time. So, by the final DTI sequence subjects had been breathing an increased fraction of inspired oxygen for over 60 minutes. At this stage, the PaO_2 of the healthy volunteers would have been at least as high as that achieved in patients.²⁰⁴

In patients, we looked for regions where changes in DTI were more significant than the 99% PI for zero change using published data from 26 healthy historical volunteers who underwent DTI on up to four occasions within two imaging sessions.²³² Both patients and volunteers underwent scanning within the Wolfson Brain Imaging Centre (WBIC) using the same scanner, software version and scanner sequences. Since patients underwent baseline and post-intervention imaging during the same session the expected variability in patients, who were also sedated and paralysed during imaging, is likely to be at least as good as that found in awake spontaneously breathing healthy volunteers who underwent repeat DTI during two sessions separated by up to six months.²³²

Patients suffered a TBI and the presence of brain lesions will produce errors in spatial processing, particularly where non-linear algorithms are used to co-register and transform data to a standard template. The ROI template was eroded by a single voxel to limit problems resulting from co-registration, normalisation and partial volume errors. Visible areas of injury were manually delineated in native space, and subsequently, a normalised binary mask of the lesions was used to exclude this volume of brain tissue from the individualised standard ROI template of each patient. All registered datasets were reviewed to ensure that the spatial processing had not resulting in significant errors,

and no subjects were excluded on this basis. While these concerns may lead to an overestimate of the difference between regional DTI values in patients compared to healthy volunteers, it is important to emphasise that the focus of this study was to compare change following NH within individual subjects during the same imaging session. There were no structural differences between the baseline and post NH datasets, and therefore, any small errors in registration and normalisation would have been replicated in both datasets. Patients were sedated, paralysed and ventilated throughout imaging sessions as part of routine care. This would have prevented movement artefact and helped optimise data collection, processing and subsequent analyses. Under these circumstances, small changes within individual ROIs that relate to problems with spatial processing would be unlikely to introduce systematic errors between baseline and post NH intervention imaging within individual subjects. While it is possible that the DTI changes we found occurred purely by chance, we cannot ignore the fact that over 10% of all patient regions showed a fall in FA greater than the 99% PI for zero change following NH.

While the significance of a fall in FA following brief exposure to hyperoxia is unknown, it still represents some detectable and reversible change in the local tissue environment that did not occur in healthy volunteers exposed to a similar intervention. Given the concern regarding the use of hyperoxia, it would be important to exclude the possibility, however small, that this could represent some early evidence of axonal injury within white matter resulting from oxidative stress. In chronic TBI a reduction of FA within white matter is consistent with axonal injury, with the extent of changes dependent on the time since ictus.³²⁹ Interestingly, late cortical FA increases can also occur and may relate to scarring post mild TBI.^{336,337} Clearly, it would be important to undertake serial MRI with DTI to understand how these DTI parameters evolve within both grey and white matter following exposure to longer periods of NH. At the very least these findings demonstrate how such measurements could be used to assess the impact of a longer duration of therapeutic NH and should be compared with the evidence of late tissue fate based on structural MR and clinical outcome. Finally, since AD and RD are parameters that relate to the orientation of white matter fibres the small changes we found within mixed cortical and deep grey matter following hyperoxia are of little consequence.

Patients underwent imaging between days 1 – 9 (mean 3.3 days) post-injury, and DTI changes may reflect different trajectories within individual subjects with a resolution of cytotoxic and vasogenic oedema (Figure 2-3, page 30), temporal variability in microvascular ischaemia and neurophysiology along with the loss of tissue integrity within established lesions. Despite this concern, there was no significant interaction between FA changes following hyperoxia and the time since injury ($p = 0.59$, ANOVA). We did not measure the temporal impact of neurophysiology in this study but patients in

this cohort sustained TBI severe enough to require intensive care management of raised intracranial pressure and had comparable imaging patterns of injury. Despite this, the outcome was variable, and it is possible that the changes in DTI parameters seen may reflect individual variability within this small cohort. However, reductions in FA were seen in over half the patients and the majority of brain regions with no apparent relationship to injury type or eventual outcome. Nevertheless, definitive statements concerning the significance of DTI changes would require data from a larger cohort of patients showing evidence of sustained reductions in FA associated with poor functional outcome in comparison with a control arm before it could be concluded that they were indicative of axonal injury.³³⁸ Sequential imaging could be used as a biomarker of the trajectory of such injury or its recovery in the assessment of therapeutic interventions such as hyperoxia.

Previous clinical studies have suggested that the use of high partial pressures of oxygen may be beneficial,^{248,318} but there may be a relatively narrow margin of safety.²⁹⁰ We limited the maximum FiO_2 in this interventional study to 0.8 to minimise direct side effects such as alveolar atelectasis and pulmonary injury. Clinical studies show little evidence of increased oxidative stress when therapy is applied in a controlled manner within the first three days post-injury.³¹⁴ We show how changes in DTI can be detected in patients following NH based on reproducibility data from a historical group of healthy volunteers. The pathophysiological basis and significance of any fall in FA following exposure to NH remain unknown, particularly following such a brief intervention.

Nevertheless, any potentially adverse effect should be considered, and further studies should incorporate serial DTI to help determine how and when this intervention should be used within a precision medicine approach to optimise the beneficial impact on patient outcome. Such data could be invaluable in the design of any future clinical trial since studies to date do not provide definitive evidence of an improvement in clinical outcome.³¹⁵

Prior TBI studies have suggested that an increase in the fraction of inspired oxygen can improve cerebral metabolism within perilesional and normal appearing white matter,^{164,309} and using DTI, result in benefit within the rim of cytotoxic oedema found around brain contusions.¹⁷⁸ Using DTI, we showed evidence of cytotoxic oedema and traumatic axonal injury distant from visible lesions with no improvement following the short-term administration of normobaric hyperoxia. To confirm these findings and investigate further will require a longer duration of hyperoxia with serial DTI and conventional MRI in comparison with clinical outcome.

Chapter 9 Impact of normobaric hyperoxia on the metabolic derangements identified by whole-brain proton spectroscopy following severe traumatic brain injury

Introduction

Classical cerebral ischaemia and late energy failure remain a significant cause of neuronal loss after traumatic brain injury (TBI). We have previously used diffusion tensor imaging (DTI) and ^{15}O positron emission tomography (^{15}O PET) to show that normobaric hyperoxia increases oxygen utilisation and may benefit “at risk” regions such as the rim of cytotoxic oedema found in the vicinity of contusions following head injury. The response to normobaric hyperoxia depends on the underlying regional metabolic derangements within brain tissue.¹⁶⁴ While hyperoxia has shown benefit in some studies after brain injury, there are concerns regarding the deleterious effects of hyperoxia on the brain and other organ systems such as lungs and heart.^{290,339-349} These concerns justify further study of the regional metabolic effects of normobaric hyperoxia before large scale clinical trials are commenced. We have used structural MR imaging and diffusion tensor imaging to identify “at risk brain regions” regions with evidence of structural injury, vasogenic and cytotoxic oedema. Whole brain proton spectroscopy (WB ^1H MRS) and diffusion tensor imaging provide insights into progression and outcome in a variety of neurological disorders, including traumatic brain injury.^{113,179,232,243,350}

Metabolites reliably measured with whole brain proton spectroscopy (WB ^1H MRS) at an echo time of 70 milliseconds include N-acetyl aspartate (NAA) a metabolite reflecting neuronal integrity, exclusively found in brain, Creatine (Cr) a putative marker of phosphate metabolism and Choline (Cho) containing compounds indicating breakdown and turnover of neuronal membrane.^{99,108,109,112,113,168,228,233} Whole brain proton spectroscopy (WB ^1H MRS) data acquired with Metabolic Imaging and Data Acquisition Software (MIDAS) provides a fully automated pipeline for processing and interpreting WB ^1H MRS data.⁹⁶ Whole brain proton spectroscopic imaging data can be used to quantify dynamic metabolic processes, neuronal integrity, and metabolic fate of tissue after traumatic brain injury.^{103,168,351-354} This would be the first study to use WB ^1H MRS to assess the impact of a neurotherapeutic option such as normobaric hyperoxia on the regional metabolic state in patients following traumatic brain injury. This study could also provide insights into the metabolic fate of injured brain tissue and potential impact on outcome following TBI.

Material and Methods

Ethical approval was obtained from the Cambridgeshire Research Ethics Committee (reference numbers 97/290 and 02/293) and written informed consent, or written assent from next-of-kin where appropriate were obtained in all cases following the Declaration of Helsinki.

Subjects

Patients

Twelve adult patients (10 males and two females) with a mean (range) age 41.5 (21 – 70) years with head injury were recruited from the Neurosciences Critical Care Unit (NCCU), Addenbrooke's Hospital, Cambridge, UK. Recruited patients presented with a median (range) post-resuscitation Glasgow Coma Score (GCS) of 7 (3 – 14) with deterioration to a GCS < 8 requiring sedation and ventilation for control of intracranial pressure (ICP) (Table 9-1).

Patients were recruited to this imaging study between mean (range) days 3 (1 – 9) post-injury and underwent imaging while they were sedated in the critical care unit. Patients were excluded from this study if they had suffered a previous TBI, any other neurological disease or had any contraindication to magnetic resonance imaging (MRI). Patients were managed by protocol-driven care, which included sedation, paralysis and ventilation to ensure that intracranial pressure (ICP) < 20 mmHg and cerebral perfusion pressure > 65 mmHg were maintained. Physiological stability was meticulously ensured during imaging through the titration of fluids and vasoactive agents by a critical care physician and specialist neurocritical care nurse. Patients who received the surgical intervention (CSF drainage or decompressive craniectomy) or second-tier medical therapies (barbiturate coma or moderate hypothermia (33–35°C) before imaging are specified in Table 9-1. No other significant changes occurred in the management of patients on the day of study.

Following the acquisition of baseline WB ¹H MRS at a partial pressure of oxygen (PaO₂) of approximately 10 – 12 KPa (75-90 mmHg) the fraction of inspired oxygen (FiO₂) was increased to a maximum of 0.8 to achieve a PaO₂ of approximately 30 – 35 KPa (225-260 mmHg). Following a 60-minute equilibration period (and by inference, brain pO₂) a repeat WB ¹H MRS was obtained within the same imaging session without moving the patient.

Controls

Two groups of healthy volunteers underwent WB ¹H MRS. Seven controls (four females and three males) with a mean (range) age of 31 (22 – 42) years were exposed to graded oxygen therapy (room air, 60% and 100% inspired oxygen) delivered via a venturi mask (Flexicare Medical Limited, Mid Glamorgan, Wales). WB ¹H MRS was obtained at each level following an equilibration period of 15

minutes as described previously in my thesis.¹⁷⁹ This equilibration time was double the time taken for normobaric hyperoxia to equilibrate with brain tissue oxygenation (PtbO₂) in patients with severe traumatic brain injury with brain tissue oxygen monitoring system in situ (LICOX[®], Integra Life Sciences Corporation, Plainsboro, NJ). A further 11 healthy volunteers (six males and four females) with mean (range) age of 34 (25 – 44) years underwent WB ¹H MRS on up to four occasions within two imaging sessions separated by a maximum of six months to look at the test-retest variability of WB ¹H MRS when repeated up to four occasions.

Subject	Age	Sex	Mechanism	Summary of MRI findings	Parenchymal lesion volume (ml)	DAI	GCS	Marshall score	APACHE II	ISS	Neurosurgery	Second tier therapies	Days to MRI	GOS
1	53	M	RTA	Bitemporal, basal ganglia & cortical contusions. Bilateral frontal SDH	100	Yes	4	NEML	17	34	-		4	MD
2	34	M	RTA	Bilateral subcortical & deep white matter, corpus callosum, R thalamus, midbrain & cerebellar contusions. IVH, L occipital & fronto-temporal SDH	20	Yes	4	NEML	21	20	EVD		3	VS
3	34	M	Assault	Bilateral frontal, temporal, R occipital, thalamus & L cerebellar contusions. IVH	607	No	8	EML	25	16	DC, R SDH EVD		3	SD
4	21	M	RTA	Bilateral cortical, corpus callosum, dorsal midbrain & pons contusions	46	Yes	10	NEML	21	50	-	H	2	MD
5	31	M	RTA	Bilateral frontal, temporal & L occipito-parietal & midbrain contusions	259	No	6	EML	17	29	DC, R SDH		1	MD
6	29	M	Assault	Bilateral frontal & temporal contusions. Bilateral temporal SDH	444	No	10	EML	17	16	DC, EVD	H	2	GR
7	58	M	Fall	Bilateral frontal, temporal & R parietal contusions. Bifrontal SDH & tSAH	122	No	10	NEML	20	34	-	-	4	GR
8	26	M	RTA	Bilateral frontal & temporal contusions. R temporal & L frontotemporal SDH	346	No	3	NEML	17	75	-		3	MD
9	28	M	Assault	R frontotemporal contusions & R SDH	38	No	12	EML	24	36	DC		3	GR
10	61	M	Fall	Bilateral frontal & temporal, corpus callosum & midbrain contusions. L SDH & IVH	358	No	5	NEML	22	75	-		9	NA
11	31	F	Fall	R frontal, temporal, parietal, occipital, bilateral thalamic & midbrain contusions. R SDH & IVH	599	No	3	EML	25	75	DC, R SDH	H	4	VS
12	70	F	RTA	Bilateral frontal, parietal, corpus callosum & midbrain contusions. tSAH & IVH	23	Yes	3	2	21	34	-		1	GR

Table 9-1 Patient characteristics

C, craniotomy; D, death; DAI, diffuse axonal injury; DC, decompressive craniectomy; EDH, extradural hemorrhage; EVD, external ventricular drain; F, female; GCS, Glasgow coma score; GOS, Glasgow outcome score; GR, good recovery; M, male; MD, moderate disability; RTA, road traffic accident; SD, severe disability; SDH, subdural hemorrhage; tSAH, traumatic subarachnoid hemorrhage.

Image processing

Lesion analysis: Lesions were defined in native FLAIR space (hand-drawn) by a single author (JG, sense checked and confirmed for concordance by other authors TV and JPC), and segregated into regions defined as core, contusion and pericontusion using patient FLAIR, MPRAGE, GE and SWI images. SWI (three dimensional) and GE (two dimensional) were used to identify areas of bleeding and necrotic core in the contusion along with the structural imaging. Lesion core was identified as a region of mixed signal intensity consistent with haemorrhage and necrotic tissue, contusion as an area of high FLAIR signal, and pericontusion as a 1 cm border zone surrounding the contusion, as described previously in this thesis.^{113,204,232} Where visible, we also defined a rim of cytotoxic oedema ('traumatic penumbra') on ADC images (figure 9-1). The FLAIR images were coregistered to unsuppressed water image space using FSL, and the coregistration matrix subsequently applied to the lesion ROIs. For comparison, a comparable region of the normal appearing brain composed of mixed grey and white matter was defined. Parametric maps for NAA, Cho and Cr were created using the automated pipeline of MIDAS and were signal intensity normalised to institutional units (iu) based on the tissue water signal derived from the water reference dataset.^{96,113}

Voxel data with line width greater than 13 Hz were excluded from further analysis as previously described by Maudsley et al. combined transformation matrices were then applied to all parametric images used in the analyses. Spectroscopic data were analysed by the following with an additional false discovery rate (FDR) of 0.01 used to correct for the number of regions of interest (equivalent to uncorrected $p < 0.0023$).

Lesion free ROI analysis: Parametric maps of NAA, choline and Creatine were created with MIDAS.^{96,106,107,109,111-113,221,355} The WB ¹H MRS parametric maps were spatially normalised using a two-step approach using FSL.^{206,207} First, control T1 weighted images were coregistered to water spectroscopic images using FMRIB's Linear Image Registration Tool (FLIRT).²³⁴ This was followed by coregistration of control T1 weighted images to the MNI152 template using FMRIB's Non-linear Image Registration Tool (FNIRT).²³⁴ The "lesion free" analysis was performed by the exclusion of lesion core and contusion tissue following the transformation of the lesion ROI to normalised space. Combined transformation matrices were then applied to all parametric images used in the analyses. Representative white matter, deep grey and mixed regions of interest (ROIs) from the Harvard Oxford subcortical and MNI structural probabilistic atlases available within FSL were then applied in normalised space. All coregistered images were subsequently inspected to ensure that the ROIs were correctly aligned and corresponded to the regions specified. Prior to statistical tests, voxels were excluded based on the following quality criteria as previously described by Maudsley et al. (i) fitted

metabolite linewidth >13 Hz; (ii) having an outlying value >2.5 times the standard deviation of all valid voxels over the image; and (iii) having a Cramér-Rao Lower Bounds for fitting of Cr of >40%; and (iv) having >30% CSF contribution to the voxel volume. All coregistered images were subsequently inspected to ensure that the ROIs were correctly aligned and corresponded to the regions specified. The mean values for NAA, Cho and Cr in institutional units for each ROI were calculated using in-house software written in Matlab (Mathworks, Natick, USA).^{356,357}

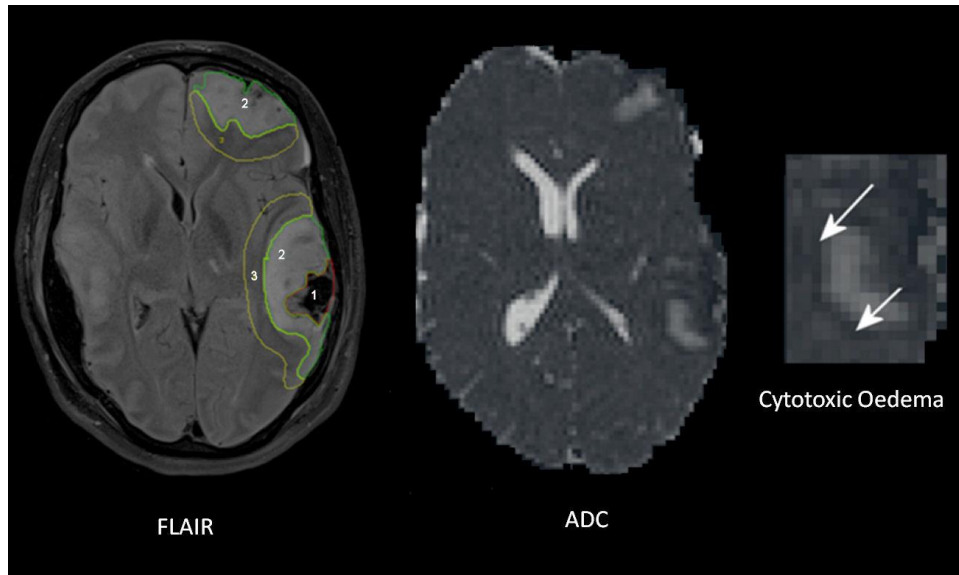


Figure 9-1 Lesion based regions of interest
Fluid attenuation inversion recovery (FLAIR) with lesion core (1, red), contusion (2, green) and pericontusion (3, yellow), and an apparent diffusion coefficient (ADC) map depicting the rim of cytotoxic oedema (low signal) surrounding the region of vasogenic oedema (high signal) related to the contusion following head injury. These show the brain tissue that represents the cytotoxic and vasogenic regions of interest used in the analyses.

Results

Impact of oxygen therapy on whole brain proton spectroscopy in healthy volunteers

The effect of an increase in the fraction of inspired oxygen on WB ¹H MRS parameters in healthy volunteers using the standard template ROI is shown in Table 9-2 and Figure 9-2 . There were no significant changes in any of the WB ¹H MRS parameters using the standard template ROI with an increase in the FiO₂ (p values were 0.16, 0.86, and 0.77 for NAA, creatine, and choline respectively using ANOVA with Bonferroni correction).

	Inspired oxygen concentration		
	Room air	Sixty	Hundred
NAA	10850.5 ± 2961.4	10277.8 ± 3087.4	10254.5 ± 3251.1
Creatine	8094.7 ± 3100.4	8194.9 ± 3130.1	8051.4 ± 2823.8
Choline	2457.6 ± 1571.8	2480.4 ± 1583.9	2391.1 ± 1233.8

Table 9-2 Impact of oxygen therapy on whole brain proton spectroscopy metabolite concentrations in healthy volunteers
Data are mean ± standard deviation of the standard template regions of interest for N acetyl aspartate (NAA), Creatine and Choline for seven volunteers

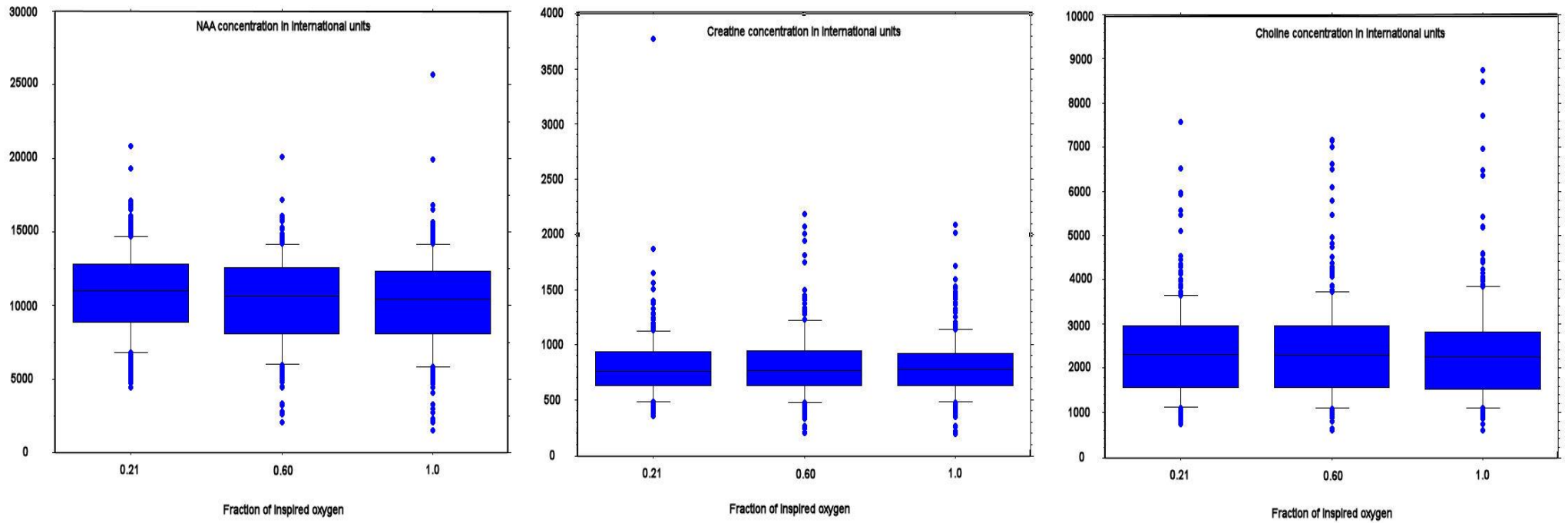


Figure 9-2 Metabolite concentration in healthy volunteers at room air, sixty and hundred percentage of oxygen

Box and whisker plots within healthy volunteers for N Acetyl aspartate (NAA), Creatine and Choline. The central lines in each box denote median values, the lower and upper boundaries the 25th and 75th centile, the error bars the 10th and 90th centile, and the closed circles outlying data points. There were no statistically significant differences at various oxygen concentrations in volunteers.

Baseline metabolite concentration in at-risk regions after TBI

The metabolic profile across the injured brain (Figure 9-3) and in healthy volunteers at normoxia is shown in Table 9-3 and Figure 9-4. There were no differences between the normal appearing brain in patients and healthy volunteers for NAA, creatine or choline (p values > 0.8). In patients, NAA was lower within contusion, pericontusion and vasogenic oedema regions, while creatine was lower within contusion and vasogenic oedema regions compared to normal appearing brain.

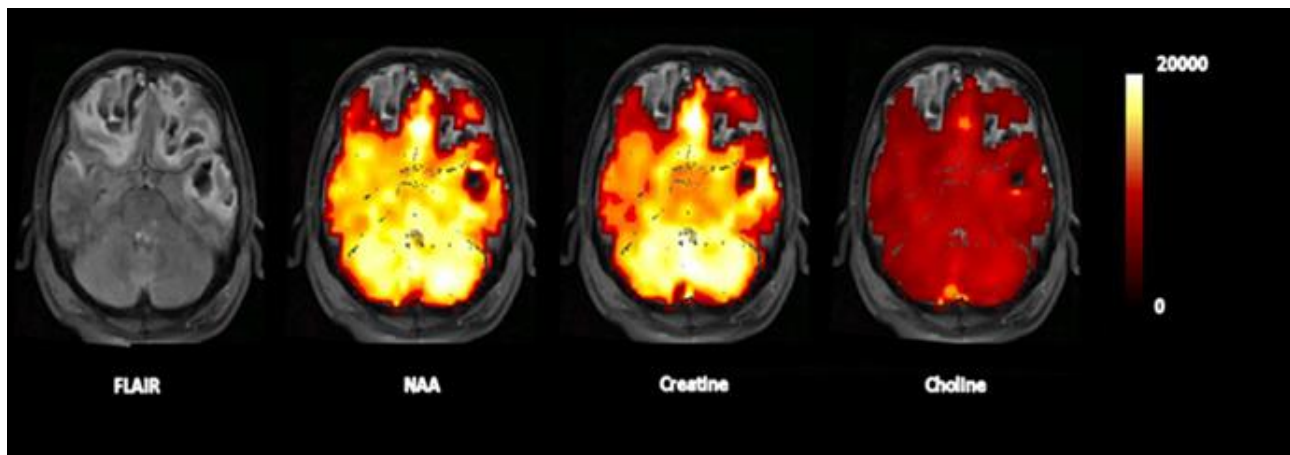


Figure 9-3 Parametric maps of metabolites in a patient with traumatic brain injury

Fluid attenuation inversion recovery (FLAIR) magnetic resonance image demonstrating extensive bilateral frontal and temporal contusions which extend to the parietal region on the left side of the brain. The haemorrhagic lesion core has low signal on FLAIR corresponding to the presence of blood degradation products. The parametric maps obtained at normoxia show spatial variation of n-acetyl aspartate (NAA), creatine and choline related to these traumatic lesions.

		Normoxia		Hyperoxia		Controls	
		Mean (SD)	Range	Mean (SD)	Range	Mean (SD)	Range
NAA	Contusion	8909.2 ± 2603.9	5769.1 - 13454.3	8524.4 ± 2591.5	4447.9 - 12279.2	13161.8 ± 993.9	11100 - 14700
	Pericontusion	10916.9 ± 2059.8	5992.8 - 13416	10662.6 ± 1654.1	7937.1 - 12626.3		
	Cytotoxic oedema	11217.2 ± 2991.8	795.7 - 16551.6	10178.5 ± 2372.6	5692.6 - 13592.6		
	Vasogenic oedema	9734.9 ± 3613.8	4560 - 16551.6	8844.5 ± 3146.8	5258.7 - 14877.7		
	Normal appearing brain	13856.7 ± 1311.9	10654.3 - 15580.4	12452.2 ± 2075.2	8727.9 - 15320.8		
Creatine	Contusion	7531 ± 1484.4	4551.4 - 9245	7324.9 ± 1714	4239.3 - 9518.7	9396.2 ± 1361.4	7860 - 13900
	Pericontusion	8625.1 ± 1421.4	5856.9 - 10343.8	8581.3 ± 1054.4	6474 - 10197.8		
	Cytotoxic oedema	8368.8 ± 1373	6150.5 - 10520.2	8019.1 ± 1129.2	6169.5 - 9190.6		
	Vasogenic oedema	7489.2 ± 2188.1	3027.2 - 11320.9	7298.5 ± 1652.5	4455.6 - 9522.9		
	Normal appearing brain	9419.6 ± 947.5	7539.3 - 10793.6	8927.2 ± 1273.2	6350.6 - 10957.4		
Choline	Contusion	2275.8 ± 601.1	1459.7 - 3280.7	2286.2 ± 785	1100 - 3528.4	2577.9 ± 931.9	1620 - 6700
	Pericontusion	2590.8 ± 660.8	1365.8 - 3901.4	2520.8 ± 479.4	1752.6 - 3269.7		
	Cytotoxic oedema	2708.2 ± 679.9	1758.1 - 3674.2	2440.9 ± 555.5	1227.4 - 3371.1		
	Vasogenic oedema	2238.9 ± 564.9	1078.9 - 2912.5	2286.0 ± 653.8	1131.8 - 3640		
	Normal appearing brain	2470.8 ± 372.8	1836.8 - 3027.4	2226.7 ± 499.3	1005.5 - 2902.1		

Table 9-3 Impact of oxygen therapy on injured brain measured with whole brain proton spectroscopy in patients with severe traumatic brain injury

Data are mean ± standard deviation of the lesion regions of interest and the ranges for N acetyl aspartate (NAA), Creatine and Choline. There were no statistically significant differences between baseline normoxia and hyperoxia.

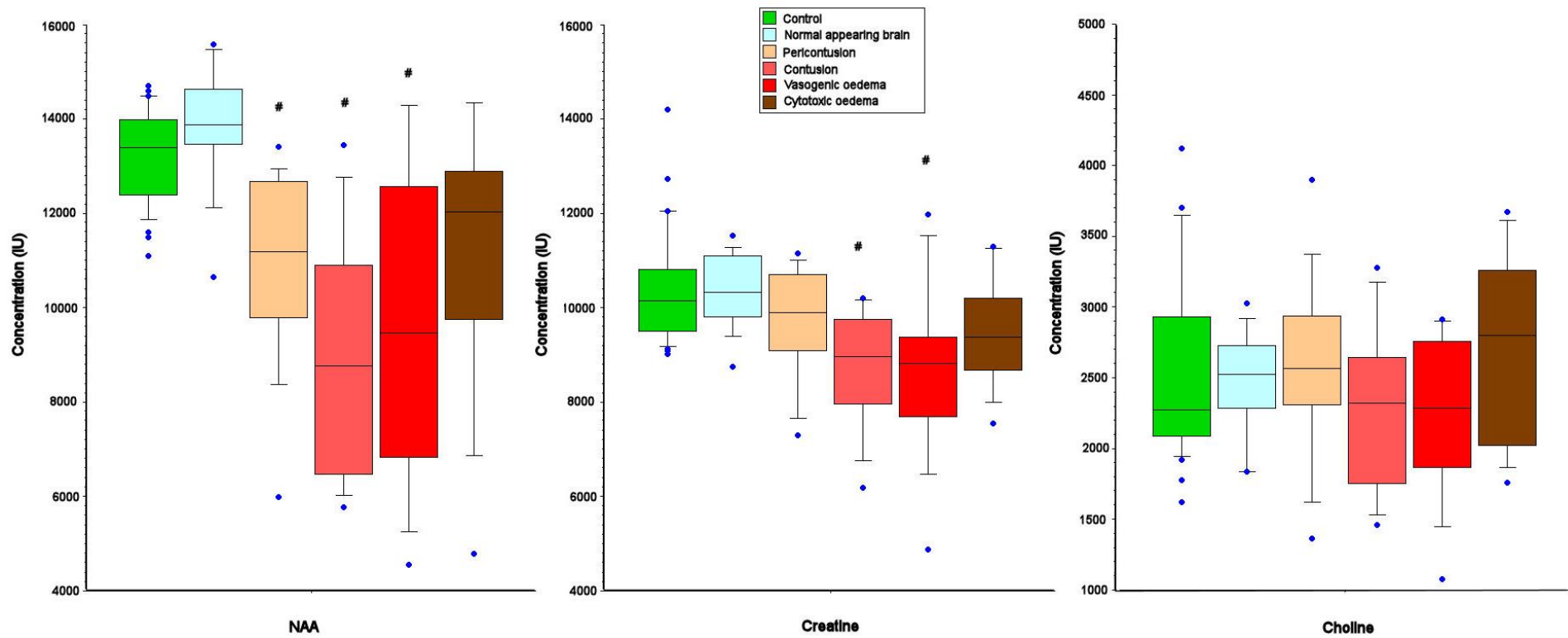


Figure 9-4 Baseline regional physiology

Box and whisker plots within healthy volunteers (control), and normal appearing brain, pericontusion, contusion, cytotoxic oedema and vasogenic oedema from patients for N Acetyl aspartate (NAA), Creatine and Choline. The central lines in each box denote median values, the lower and upper boundaries the 25th and 75th centile, the error bars the 10th and 90th centile, and the closed circles outlying data points. # $p < 0.003$, ANOVA with Dunns test for comparison between normal appearing brain to 'at-risk' regions such as pericontusion, contusion, cytotoxic oedema and vasogenic oedema within patients.

Baseline metabolite concentration in injured brain

Deep grey matter regions of interest: Significant decreases in NAA were found within five out of eight ROIs (63%), while choline was increased in both thalami (25% of ROIs) compared to healthy volunteers (Figure 9-5).

Mixed cortical regions of interest: Significant decreases in NAA were found within seven out of 14 ROIs (50%), decreases in creatine in five ROIs (36%), and decreases in choline in two ROIs (14%) compared to healthy volunteers (Figure 9-6).

White matter regions of interest: Significant decreases in NAA were found within 11 out of 15 ROIs (73%) and decreases in creatine in three ROIs (20%) compared to healthy volunteers (Figure 9-7).

Impact of normobaric hyperoxia on metabolite concentration in patients

The effect of an increase in the fraction of inspired oxygen on WB ¹H MRS parameters within the normal appearing brain from deep grey matter, mixed cortical and white matter regions are shown in Figure 9-5, Figure 9-6 and Figure 9-7. While there were significant differences between baseline patients and healthy volunteers for NAA, creatine and choline within several lesion free brain regions were found, but there were no changes seen following exposure to hyperoxia.

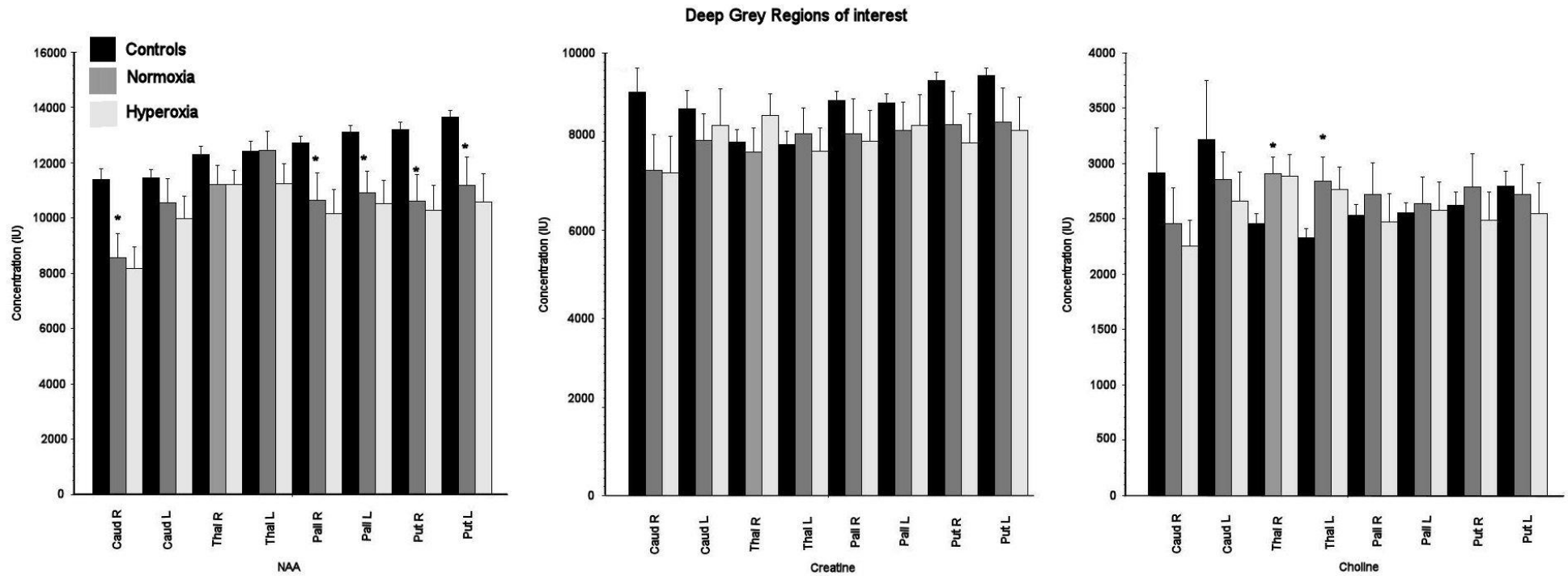


Figure 9-5 Region of interest analysis within deep grey matter regions

N Acetyl aspartate (NAA), Creatine and Choline within atlas regions of interest (ROI) applied in normalised space in 11 healthy volunteers and 12 patients. In patients, these analyses were performed on "lesion free" brain by exclusion of lesion core and contusion tissue. Data displayed are mean \pm standard deviation for deep grey matter ROIs for healthy volunteers (black), patients at baseline (grey) and following hyperoxia (white). (* $p < 0.01$ unpaired t test with Bonferroni correction) for comparison between healthy volunteers and baseline patients. There were significant differences between healthy controls and region of interest at baseline in patients(normoxia) for NAA, and choline. Caud L, caudate left, Caud R, caudate right; Thal L, thalamus left; Thal R, thalamus right, Palli R, pallidum right, Palli L, pallidum Left, Put R, putamen right, Put L, putamen left.

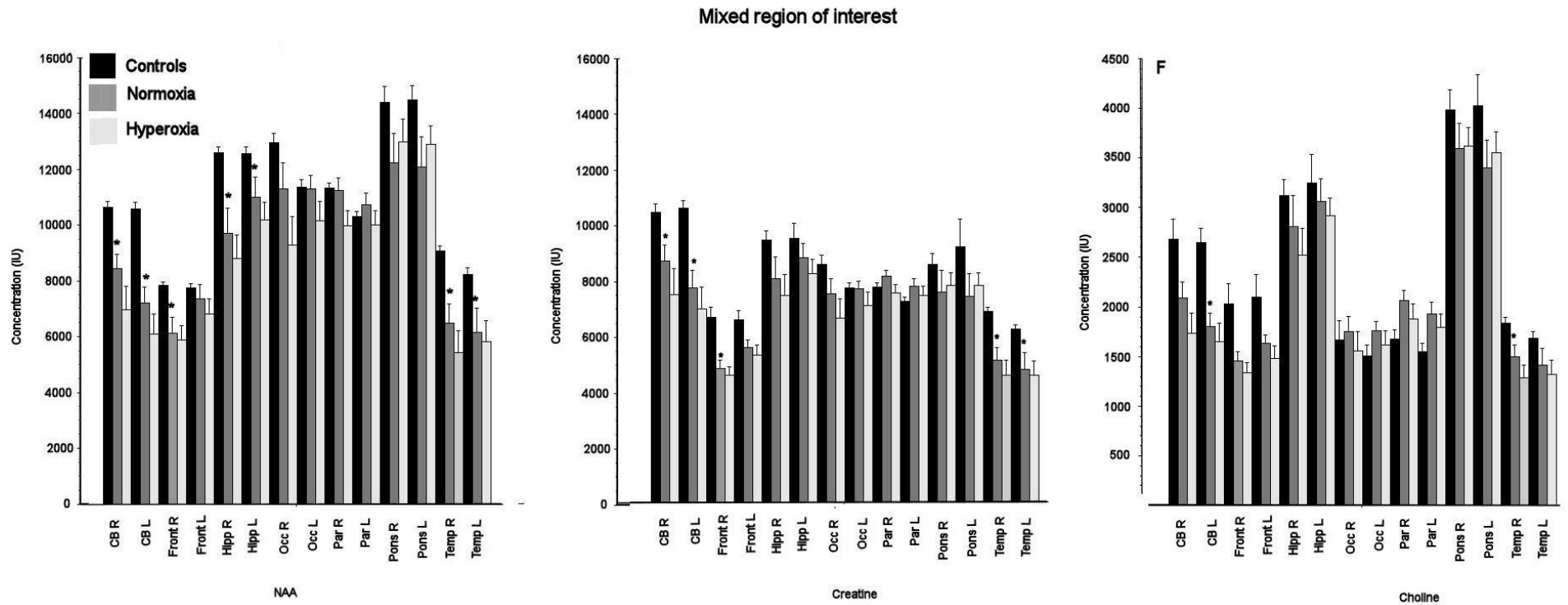


Figure 9-6 Region of interest analysis within mixed cortical regions of interest

N Acetyl aspartate (NAA), Creatine and Choline within atlas regions of interest (ROI) applied in normalised space in 11 healthy volunteers and 12 patients. In patients, these analyses were performed on “lesion free” brain by exclusion of lesion core and contusion tissue. Data displayed are mean \pm standard deviation for mixed ROIs for healthy volunteers (black), patients at baseline (grey) and following hyperoxia (white). (* $p < 0.01$ unpaired t test with Bonferroni correction) for comparison between healthy volunteers and baseline patients. There were significant differences between healthy controls and region of interest at baseline for patients for NAA (seven regions), creatine (five regions) and choline (two regions). CB R cerebellum right, CB L cerebellum left, Front R, frontal lobe right, Front L, Frontal lobe left, Hipp R, hippocampus right, Hipp L, hippocampus left, Occ R, Occipital right, Occ L, Occipital left, Par R, parietal right, Par L parietal left, Pons R, pons right, Pons L, pons left, Temp R, Temporal right, Temp L, temporal left.

White matter regions of interest

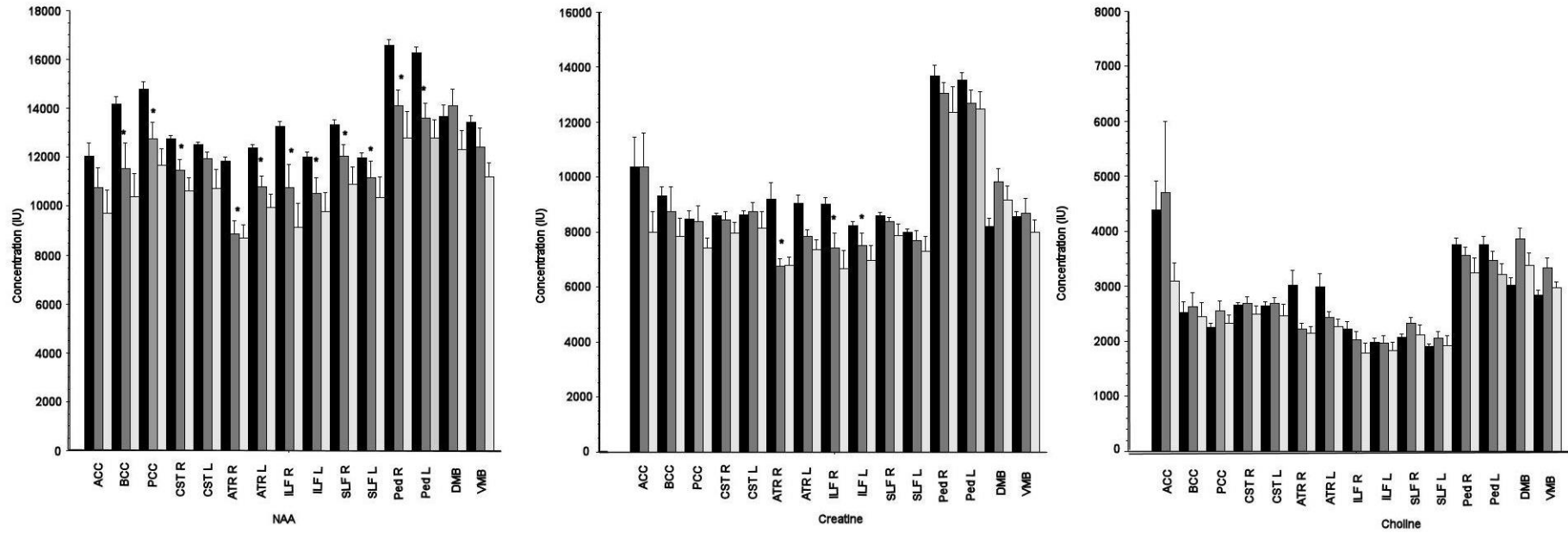


Figure 9-7 Region of interest analysis within white matter regions of interest

N Acetyl aspartate (NAA), Creatine and Choline within atlas regions of interest (ROI) applied in normalised space in 11 healthy volunteers and 12 patients. In patients, these analyses were performed on “lesion free” brain by exclusion of lesion core and contusion tissue. Data displayed are mean \pm standard deviation for white matter ROIs for healthy volunteers (black), patients at baseline (grey) and following hyperoxia (white). (* $p < 0.01$ unpaired t test with Bonferroni correction) for comparison between healthy volunteers and baseline patients. There were significant differences between healthy volunteers and baseline (normoxia) white matter normal appearing regions of interest. ACC, anterior corpus callosum; BCC, body corpus callosum; PCC, posterior corpus callosum; ATR L, anterior thalamic radiation left; ATR R, anterior thalamic radiation right; SLF L, superior longitudinal fasciculus left; SLF R, superior longitudinal fasciculus right; ILF L, inferior longitudinal fasciculus left; ILF R, inferior longitudinal fasciculus right; C L, CST L, corticospinal tract left; CST R, corticospinal tract right, VMB, ventral midbrain, DMB, dorsal midbrain.

Discussion

In this study we used whole brain proton spectroscopy (WB ^1H MRS) to demonstrate derangements in brain metabolism (NAA, creatine and choline) across the injured brain, and whether exposure to normobaric hyperoxia had any beneficial impact. Within the vicinity of brain lesions, we found that contusion, pericontusion and the region of vasogenic oedema showed the most significant reductions in NAA and creatine compared to healthy volunteers and normal appearing brain in patients. In lesion-free brain regions, there were significant reductions in NAA in deep grey matter (63% of ROIs), mixed cortical regions of interest (50% of ROIs) and white matter regions (73% of ROIs) compared to healthy volunteers. There were also reductions in creatine within mixed cortical (50%) and white matter ROIs (20%). These data suggest that following acute severe TBI there is micro-architectural disruption with neuronal and mitochondrial dysfunction, leading to a reduction in NAA,^{168,339,340,342,346,349,358-364} and energy failure resulting in a depletion of creatine.^{239,365} There was also an increase of choline in the thalamus suggestive of neuroinflammation and breakdown of neurons associated with poor neurocognitive outcome.³⁶⁵⁻³⁶⁸

We have previously shown that normobaric hyperoxia (NH) through an increase in brain tissue oxygenation can reduce microdialysis lactate and the lactate-pyruvate ratio and improve brain oxygen metabolism and structural integrity in “at risk” regions.^{19,164,204} We found no evidence of any impact of normobaric hyperoxia on NAA, creatine or choline using whole brain proton spectroscopy in patients or healthy volunteers. There were no identifiable benefits in lesional, perilesional, the regions of cytotoxic and vasogenic oedema and normal appearing brain following trauma. Further studies should address whether a longer period of exposure to normobaric hyperoxia is required to demonstrate evidence of possible benefit. Previous studies have demonstrated that NH results in an increase in brain tissue oxygen levels and an improvement in the cellular redox state.^{309,369} The effects that occur from an improvement in tissue oxygenation are dependent on oxygen delivery and local blood flow. While the measurement of lactate would confirm the existence of tissue ischaemia after NH, at an echo time of 70ms lactate cannot be reliably quantified due to its peculiar chemical shift as a doublet which peaks at long TEs. At short echo times, it is superimposed on the mobile lipids after head injury. While the use of high partial pressures of oxygen may be beneficial in a variety of disease states and following brain injury, there is a relatively narrow margin of safety due to the known toxic effects such as atelectasis and tracheobronchitis while more prolonged exposure (days) can result in diffuse pulmonary damage.^{345,349,363,364,370-372} Central nervous system toxicity is limited to hyperbaric exposures, and symptoms vary in severity and onset depending on the partial pressure and duration of exposure. Symptoms include nausea, headache, dizziness, blurred vision and ultimately seizures.

Concerns regarding oxidative injury have led to the less liberal use of oxygen therapy in conditions such as cardiopulmonary resuscitation, myocardial infarction and stroke — the toxic effects are related to the generation of reactive oxygen species (ROS) and oxidative cellular injury.^{281,364} The generation of ROS is increased following an experimental head injury, and this effect can be potentiated by hyperoxia therapy and result in further tissue injury. However, clinical studies in head injury have used short exposures of normobaric and hyperbaric hyperoxia and failed to demonstrate increased oxidative stress.^{315,318,319} While these clinical studies suggest that the use of high concentrations of inspired oxygen in this context is safe, further studies are required to determine whether such therapy has any beneficial impact on patient outcome. We wished to undertake a Phase II study of hyperoxia following head injury using WB 1H MRS as an intermediate imaging endpoint, to show whether the structural and metabolic changes previously demonstrated resulted in metabolic improvements as defined by WB 1H MRS in at-risk traumatic penumbral tissue. The approach was based on the fact that previous imaging studies have shown increases in oxygen metabolism²⁵ and reversal of cytotoxic oedema within at-risk and perilesional brain tissue following TBI.²⁰⁴ Using WB 1H MRS we were unable to demonstrate any impact of NH across the injured brain. Importantly, we also demonstrate that this is not because exposure to hyperoxia produces a systematic change in WB 1H MRS signal in both healthy volunteers and patients that would limit the utility of such imaging.

The maximum FiO₂ in this interventional study was limited to 0.8 to reduce potential side effects, including alveolar atelectasis and pulmonary injury. Other published studies have used short term exposure with a FiO₂ of 1.0 or repeated short term exposure to hyperbaric oxygen. These have not reported an increased incidence of toxicity. While 9 of 14 subjects underwent intervention within 72 hours of injury, only two subjects were studied within 24 hours of injury. Previous studies have demonstrated that evidence of ischaemia is more evident at this earlier time point following injury. However, derangements in brain metabolism continue for many days post-injury. Therefore, the absence of change in this small pilot cohort does not prove, or disprove, that exposure to NH may result in any significant biological effect. We did not account for hypothermia as a treatment administered to patients (only three patients) as a part of staged management for ICP increases because of small numbers. This may have altered the Cr levels and neuronal energetics in the brain. Another limitation is small number of patients in this phase two study using imaging as a biomarker. It is plausible that that may have contributed to the lack of benefit shown in this study. Rather, it is likely that any effect on brain metabolism that results from exposure to NH may require a longer period of exposure, or that WB 1H MRS is not a sensitive biomarker in this regard. Future studies should explore whether such methodology could be refined to address these issues further.

Chapter 10 Summary and conclusions

In this thesis, I have used diffusion tensor imaging proton (DTI), whole brain spectroscopy (WB ^1H MRS), and ^{15}O in conjunction with ^{18}F Fluoromisonidazole (^{18}F FMISO) positron emission tomography, to improve our understanding of the pathophysiological mechanisms of energy failure and neuronal loss following acute traumatic brain injury. The interpretation of imaging was optimised through assessment of the impact of inter-subject variability and within-session reproducibility on data analyses. The results of my experiments provide an improved understanding of the incidence and burden of cerebral ischaemia, explored mechanisms responsible for the usage of normobaric hyperoxia (NH) as a therapeutic option (using ^{18}F Fluoromisonidazole (^{18}F FMISO)), and assessed the impact of NH as a therapeutic option within injured and normal appearing brain following TBI.

Methodological Aims

Given the potential errors in the acquisition of DTI and WB ^1H MRS data, the following areas were examined before moving to the substantive studies described in this thesis:

Inter-subject variability and reproducibility of Diffusion Tensor Imaging within and between different imaging sessions (Chapter 4)

The quantification of DTI and the construction of parametric maps are heavily reliant on the underlying statistical accuracy of this technique. To optimise the results and applicability of data for patients with TBI, a prospective study was undertaken in a group of healthy volunteers. Twenty-six healthy volunteers without any history of neuropsychiatric disorder or substance abuse underwent imaging using a 3T Siemens Verio MRI scanner (Siemens AG, Erlangen, Germany) within the Wolfson Brain Imaging Centre (WBIC), University of Cambridge. All volunteers were right-handed (ten males and sixteen females) with mean (range) age of 34 (25 – 44) years and employed by Cambridge University Hospitals NHS Trust. In this methodological experiment, I obtained the confidence limits of normative data in grey, white, deep grey and mixed regions of interest, which allowed further studies in patients. Such data processing techniques were aimed to create a pipeline to analyse the DTI data accurately and to use it as an imaging biomarker to study neurotherapeutic options. The results of these studies provide reference data concerning intersubject variability and reproducibility of DTI conducted in a group of healthy volunteers.

Comparison of inter subject variability and reproducibility of whole brain proton spectroscopy (Chapter 5)

This study provides additional reference data concerning intersubject variability and reproducibility of commonly used metabolite ratios (Cho/Cr, NAA/Cho and NAA/Cr) and individual signal-intensity normalised metabolite concentrations (NAA, Cho and Cr) in a group of 32 healthy volunteers. The reproducibility of metabolite ratios was lower than intersubject variability (10 – 15% vs 15 – 20% for NAA/Cr, NAA/Cho and Cho/Cr) but there was substantial variability across the brain for all the calculated parameters. The within and between session reproducibility measurements were similar for Cho/Cr and NAA/Choline, but for NAA/Creatine between session, reproducibility was lower than within session reproducibility. For intensity normalised metabolite concentrations (NAA, Cho and Cr) we found that intersubject variability was high, particularly for Cho. The reproducibility of metabolites was lower than intersubject variability (10 – 15% vs 15 – 30% for NAA, Cho and Cr) but there was substantial variability across the brain for all the calculated parameters. The within and between session reproducibility measurements were similar for Cho and Cr, but for NAA between session reproducibility was lower than within session reproducibility. The estimated overall population 95% prediction intervals for zero change of repeat MIDAS measurements were 3419.4, 1826.4 and 3042.8 iu for NAA, Cho and Cr respectively. Based on these additional results, a reference database concerning intersubject variability and reproducibility of WB ¹H MRS in various regions of interest in volunteers, we conducted experiments with normobaric hyperoxia in patients with TBI. These two studies suggest that we could use absolute metabolite concentration of metabolites as a biomarker for evaluating normobaric hyperoxia as a therapeutic option provided that we apply appropriate corrections for the within session, between session and intersubject variability of the measurement techniques.

Experimental Hypotheses

Hypothesis 1: Tissue hypoxia can occur in the absence of conventional macrovascular ischaemia and is consistent with diffusion hypoxia resulting from microvascular ischaemia (Chapter 6)

The spatial distribution of cerebral ischaemia (IBV) and tissue hypoxia (HBV) did not match, with the HBV found closely related to injured regions and the surrounding border zone. The IBV and HBV had comparable reductions in CBF and CMRO₂, but the HBV had lower CBV and OEF and more CMRO₂ values within the range of irreversible injury. Evidence of cerebral ischaemia and tissue hypoxia were also found within brain regions that appeared structurally normal. These findings suggest that IBV and

HBV identify brain regions at risk of ischaemic injury but that the underlying pathophysiological mechanisms differ. Within the HBV there is little evidence of classical macrovascular ischaemia. Instead, tissue hypoxia occurs in the absence of high OEF and is suggestive of microvascular ischaemia.

Hypothesis II: Diffusion tensor imaging can be utilised to demonstrate the impact of normobaric hyperoxia (NH) within at-risk pericontusional tissue following traumatic brain injury (Chapter 7)

The rim of cytotoxic oedema that we have previously defined as a region of ‘traumatic penumbra’ around brain contusions demonstrated a significant improvement in ADC values towards normal. These results suggest that NH results in benefit within the rim of cytotoxic oedema around brain contusions. This data supports the use of NH as a therapeutic intervention to overcome the microvascular ischaemia demonstrated in hypothesis I.

Hypothesis III: Normobaric hyperoxia will improve derangements in diffusion tensor imaging found distant from visible contusions following traumatic brain injury (Chapter 8)

There were no significant changes in fractional anisotropy (FA), axial diffusivity (AD), radial diffusivity (RD) and mean diffusivity (MD) with an increase in the fraction of inspired oxygen (FiO₂) within normal appearing white matter and mixed cortical and deep grey matter regions of interest (ROIs). This study implies that a short period of NH has no beneficial impact within the brain that appears normal following head injury using conventional structural imaging.

Hypothesis IV: Normobaric hyperoxia will improve metabolic derangements identified by whole-brain proton spectroscopy following traumatic brain injury (Chapter 9)

We found that contusion, pericontusion and the region of vasogenic oedema showed the most significant reductions in NAA and creatine compared to healthy volunteers and normal appearing brain in patients. In lesion-free brain regions, there were significant reductions in NAA within deep grey matter, mixed cortical regions of interest and white matter regions compared to healthy volunteers. There were also reductions in creatine within mixed cortical and white matter ROIs. These data suggest that following acute severe TBI, there is micro-architectural disruption with neuronal and mitochondrial dysfunction, leading to a reduction in NAA, and energy failure resulting in a depletion of creatine. Despite evidence of widespread metabolic derangements, these studies showed no apparent benefit within brain regions defined as lesional, perilesional, cytotoxic and vasogenic oedema with short term exposure to NH. There were also no apparent benefits within brain regions that appeared structurally normal following head injury.

Conclusions

This thesis demonstrates that the pathophysiological derangements following TBI are complex and heterogeneous. They include classical microvascular ischaemia and tissue hypoxia consistent with microvascular ischaemia and mitochondrial dysfunction. Such derangements suggest a target for novel therapeutic interventions and normobaric hypoxia (NH) was chosen as a therapeutic option that can increase tissue oxygenation and could result in benefit. Using DTI, we found an improvement in tissue microstructure within perilesional tissue, but derangements in metabolism identified using whole-brain proton spectroscopy did not improve following a short NH exposure. These discordant findings warrant further exploration of the potential therapeutic benefits of a longer period of exposure to such therapy within a cohort of TBI subjects at risk of metabolic derangements, further neuronal loss and poor outcome.

Chapter 11 The direction of future research

The results of the studies described in this thesis provide answers to some of the questions that were raised in the introduction. However, several issues remain to be answered, and the data raise new questions that will require further experimental studies. The studies detailed in this thesis could be extended or improved upon in several ways.

Extension of present studies

Research hypothesis: Would increasing the number of patients and/or the duration of hyperoxia demonstrate evidence of benefit?

These studies indicate that for the assessment of the impact of normobaric hyperoxia (NH) on cognitive outcomes, the examination of more patients with TBI in a multicentre clinical trial within the first 12-48 hours of head injury is required. To enrich the cohort studied, the inclusion criteria should include the requirement of stage two therapies for high intracranial pressures (ICP) at randomisation, as this subgroup of patients, appear to be at greatest risk of tissue hypoxia and microvascular ischaemia. Also, the selection of this patient group would allow mechanistic evaluation of the incidence, mechanisms and effect on the outcome of regional ischaemia in clinical head injury.

Data analysis techniques

One of the aims of this thesis was to demonstrate that derangements in physiology following head injury are not limited to regions with clearly identifiable structural lesions. Our studies also suggest that normobaric hyperoxia is helpful within regions of the at-risk brain with evidence of cytotoxic oedema on MRI. The next step would be to test the impact of normobaric hyperoxia in regions of microvascular ischaemia identified using novel imaging techniques such as [^{18}F]FMISO PET. The follow-up imaging studies are as follows

Is there evidence that microvascular ischaemia defined by [^{18}F]FMISO PET in TBI would benefit from normobaric hyperoxia therapy?

These studies would utilise ROIs with evidence of microvascular ischaemia generated from [^{18}F]FMISO PET imaging. These patients would then be subjected to normobaric hyperoxia and its impact on microvascular ischaemia assessed. Such data would help define the anatomical and physiological characteristics of brain tissue that represents a realistic target for neuroprotective therapy.

Sequential imaging studies and neurocognitive outcome assessment

To address the importance of early physiological derangements on the outcome would require a series of [¹⁸F]FMISO and ¹⁵O PET data acquisitions and comparison with the late (twelve months) structural (volumetric T1 and T2 MRI) and cognitive outcome (eGOS). Such data would allow the generation of putative thresholds for tissue damage. The significant limitations of such a technique include the high incidence of secondary ischaemic insults and heterogeneity of lesions after head injury. Although there are methodological difficulties, such data would provide evidence concerning the significance of early physiological derangements such as microvascular ischaemia and provide a framework upon which to base clinical care and future neuroprotective therapy. Absence of long term longitudinal follow-up at one year is a significant limitation in traumatic brain injury research, but it is hard to achieve due to the inherent complexity and heterogeneity of this disease. The outcome of large patient cohorts with serial imaging (Track-TBI and Center-TBI) studies may help address this need.

Imaging of neuronal loss

Although several studies of clinical head injury have provided insights into pathophysiology, and many interventions are useful in pre-clinical models, most clinical trials of novel neuroprotective interventions have failed to show a benefit. It is imperative that further studies are required to map the temporal profile of neuronal loss after head injury. These studies would inform when best to apply neurotherapeutic therapies to improve outcome. The data in this thesis provide evidence of regional microvascular ischaemia after head injury. Although these data provide insight into pathophysiological mechanisms of cerebral ischaemia following a head injury, they raise several important questions:

- a) *How does microvascular dysfunction relate to long term neuronal loss?*
- b) *What are the time windows for effective neuroprotection?*
- c) *How does the extent and temporal relationship of neuronal loss relate to behavioural outcome?*

The answers to these questions will go a long way in defining the spatial, temporal and physiological characteristics of tissue that represents a realistic target for neuroprotection following head injury.

To investigate these issues adequately in clinical head injury will require a variety of imaging techniques and assessment of neurocognitive outcome. In addition to sequential ¹⁵O PET imaging, techniques such as MRI (fluid attenuation inversion recovery (FLAIR), DWI and diffusion tensor

imaging (DTI)), WB ^1H MRS and phosphorus spectroscopy should allow improved demonstration of the acute and late impacts of head injury on brain metabolism and tissue outcome.

Clinical implications and the effects of therapy

These studies have shown early physiological derangements such as microvascular ischaemia. The significance of such derangements and how it translates to long term neuronal loss are unknown. To understand this, further studies with serial structural imaging, including diffusion tensor imaging, are required along with longitudinal neurocognitive assessments. Interventions such as NH also need to be longer, at least covering the period where intensive therapy for ICP control is needed in patients with evidence of microvascular ischaemia and mitochondrial dysfunction. The data presented in this thesis provide additional evidence of the potential use of normobaric hyperoxia in head injury. The selection of an optimal partial pressure of oxygen or brain tissue PO_2 based on neuroimaging was not addressed.

These studies should be extended to hyperosmolar therapies to include mannitol and hypertonic saline. Mannitol is a sugar alcohol which exerts its ICP-lowering effects via an immediate non-osmotic and slightly delayed osmotic effects. The early plasma expansion reduces blood viscosity, and this, in turn, improves regional cerebral microvascular flow and oxygenation. Mannitol also establishes an osmotic gradient between plasma and brain cells, drawing water from the cerebral extracellular space into the vasculature, thereby reducing cerebral oedema. Hypertonic saline administration produces an osmotic gradient between the intravascular and intracellular/interstitial compartments, leading to shrinkage of brain tissue (where the blood-brain barrier is intact) and therefore a reduction in ICP. Hypertonic saline also augments volume resuscitation and increases circulating blood volume, mean arterial blood pressure and cerebral perfusion pressure. Future therapeutic studies should target the effects of alternative approaches that are used to improve local perfusion, i.e. those of mannitol and hypertonic saline. The regional effects of such interventions could be addressed by the same methods employed in the studies in this thesis.

References

- 1 Dewan, M. C. *et al.* Estimating the global incidence of traumatic brain injury. *J Neurosurg*, 1-18, doi:10.3171/2017.10.JNS17352 (2018).
- 2 HES. (<https://digital.nhs.uk/data-and-information/data-tools-and-services/data-services/hospital-episode-statistics>, 2018).
- 3 Brazinova, A. *et al.* Epidemiology of Traumatic Brain Injury in Europe: A Living Systematic Review. *J Neurotrauma*, doi:10.1089/neu.2015.4126 (2016).
- 4 Peeters, W. *et al.* Epidemiology of traumatic brain injury in Europe. *Acta Neurochir (Wien)* **157**, 1683-1696, doi:10.1007/s00701-015-2512-7 (2015).
- 5 Selassie, A. W. *et al.* Incidence of long-term disability following traumatic brain injury hospitalization, United States, 2003. *J Head Trauma Rehabil* **23**, 123-131, doi:10.1097/01.HTR.0000314531.30401.39 (2008).
- 6 Wu, X. *et al.* Epidemiology of traumatic brain injury in eastern China, 2004: a prospective large case study. *J Trauma* **64**, 1313-1319, doi:10.1097/TA.0b013e318165c803 (2008).
- 7 Tagliaferri, F., Compagnone, C., Korsic, M., Servadei, F. & Kraus, J. A systematic review of brain injury epidemiology in Europe. *Acta Neurochir (Wien)* **148**, 255-268; discussion 268, doi:10.1007/s00701-005-0651-y (2006).
- 8 Chesnut, R. M. *et al.* The role of secondary brain injury in determining outcome from severe head injury. *The Journal of trauma* **34**, 216-222 (1993).
- 9 collaborators, C.-t. *et al.* Effects of tranexamic acid on death, vascular occlusive events, and blood transfusion in trauma patients with significant haemorrhage (CRASH-2): a randomised, placebo-controlled trial. *Lancet (London, England)* **376**, 23-32 (2010).
- 10 Veenith, T. *Textbook of Neuroanaesthesia and critical care*. (2011).
- 11 Raslan, A. & Bhardwaj, A. Medical management of cerebral edema. *Neurosurgical focus* **22**, E12 (2007).
- 12 Mangat, H. S. Hypertonic saline infusion for treating intracranial hypertension after severe traumatic brain injury. *Crit Care* **22**, 37, doi:10.1186/s13054-018-1963-7 (2018).
- 13 Chesnut, R. M. Hyperventilation in traumatic brain injury: friend or foe? *Critical care medicine* **25**, 1275-1278 (1997).
- 14 Andrews, P. J. *et al.* Hypothermia for Intracranial Hypertension after Traumatic Brain Injury. *N Engl J Med* **373**, 2403-2412, doi:10.1056/NEJMoa1507581 (2015).
- 15 Cooper, D. J. *et al.* Effect of Early Sustained Prophylactic Hypothermia on Neurologic Outcomes Among Patients With Severe Traumatic Brain Injury: The POLAR Randomized Clinical Trial. *JAMA* **320**, 2211-2220, doi:10.1001/jama.2018.17075 (2018).
- 16 Cooper, D. J. *et al.* Decompressive craniectomy in diffuse traumatic brain injury. *The New England journal of medicine* **364**, 1493-1502 (2011).
- 17 Hutchinson, P. J. *et al.* Consensus statement from the International Consensus Meeting on the Role of Decompressive Craniectomy in the Management of Traumatic Brain Injury : Consensus statement. *Acta Neurochir (Wien)*, doi:10.1007/s00701-019-03936-y (2019).
- 18 Needham, E. *et al.* Cerebral Perfusion Pressure Targets Individualized to Pressure-Reactivity Index in Moderate to Severe Traumatic Brain Injury: A Systematic Review. *J Neurotrauma* **34**, 963-970, doi:10.1089/neu.2016.4450 (2017).
- 19 Veenith, T. V. *et al.* Pathophysiologic Mechanisms of Cerebral Ischemia and Diffusion Hypoxia in Traumatic Brain Injury. *JAMA Neurol* **73**, 542-550, doi:10.1001/jamaneurol.2016.0091 (2016).
- 20 Veenith, T., Goon, S. & Burnstein, R. Molecular mechanisms of traumatic brain injury: the missing link in management. *World Journal of Emergency Surgery* **4**, 7 (2009).
- 21 Marmarou, A., Anderson, R. L., Ward, J. D. & J. Impact of ICP instability and hypotension on outcome in patients with severe head trauma. **75 SRC - Google Scholar**, S159-S166 (1991).

- 22 Coles, J. P. Imaging after brain injury. *Br J Anaesth* **99**, 49-60, doi:10.1093/bja/aem141 (2007).
- 23 Carter, E. & Coles, J. P. Imaging in the diagnosis and prognosis of traumatic brain injury. *Expert Opin Med Diagn* **6**, 541-554, doi:10.1517/17530059.2012.707188 (2012).
- 24 Abate, M. G. *et al.* Early derangements in oxygen and glucose metabolism following head injury: the ischemic penumbra and pathophysiological heterogeneity. *Neurocrit Care* **9**, 319-325, doi:10.1007/s12028-008-9119-2 (2008).
- 25 Nortje, J. *et al.* Effect of hyperoxia on regional oxygenation and metabolism after severe traumatic brain injury: preliminary findings. *Crit Care Med* **36**, 273-281, doi:10.1097/01.CCM.0000292014.60835.15 (2008).
- 26 Coles, J. P. Imaging of cerebral blood flow and metabolism. *Curr Opin Anaesthesiol* **19**, 473-480, doi:10.1097/01.aco.0000245270.90377.00 (2006).
- 27 Cunningham, A. S. *et al.* Physiological thresholds for irreversible tissue damage in contusional regions following traumatic brain injury. *Brain* **128**, 1931-1942, doi:10.1093/brain/awh536 (2005).
- 28 Wu, H. M., Huang, S. C., Vespa, P., Hovda, D. A. & Bergsneider, M. Redefining the pericontusional penumbra following traumatic brain injury: evidence of deteriorating metabolic derangements based on positron emission tomography. *J Neurotrauma* **30**, 352-360, doi:10.1089/neu.2012.2610 (2013).
- 29 Coles, J. P. *et al.* Early metabolic characteristics of lesion and nonlesion tissue after head injury. *Journal of cerebral blood flow and metabolism : official journal of the International Society of Cerebral Blood Flow and Metabolism* **29**, 965-975 (2009).
- 30 Werner, C. & Engelhard, K. Pathophysiology of traumatic brain injury. *Br J Anaesth* **99**, 4-9, doi:10.1093/bja/aem131 (2007).
- 31 Amorini, A. M. *et al.* Severity of experimental traumatic brain injury modulates changes in concentrations of cerebral free amino acids. *J Cell Mol Med* **21**, 530-542, doi:10.1111/jcmm.12998 (2017).
- 32 Sulhan, S., Lyon, K. A., Shapiro, L. A. & Huang, J. H. Neuroinflammation and blood-brain barrier disruption following traumatic brain injury: Pathophysiology and potential therapeutic targets. *J Neurosci Res*, doi:10.1002/jnr.24331 (2018).
- 33 Roth, C. *et al.* Early Physiotherapy by Passive Range of Motion Does Not Affect Partial Brain Tissue Oxygenation in Neurocritical Care Patients. *J Neurol Surg A Cent Eur Neurosurg* **78**, 42-45, doi:10.1055/s-0036-1592160 (2017).
- 34 Munakomi, S. & Cherian, I. Newer insights to pathogenesis of traumatic brain injury. *Asian J Neurosurg* **12**, 362-364, doi:10.4103/1793-5482.180882 (2017).
- 35 Yan, E. B. *et al.* Activation of the kynurenine pathway and increased production of the excitotoxin quinolinic acid following traumatic brain injury in humans. *J Neuroinflammation* **12**, 110, doi:10.1186/s12974-015-0328-2 (2015).
- 36 Morganti-Kossmann, M. C., Satgunaseelan, L., Bye, N. & Kossmann, T. Modulation of immune response by head injury. *Injury* **38**, 1392-1400 (2007).
- 37 Thelin, E. P. *et al.* Elucidating Pro-Inflammatory Cytokine Responses after Traumatic Brain Injury in a Human Stem Cell Model. *J Neurotrauma* **35**, 341-352, doi:10.1089/neu.2017.5155 (2018).
- 38 Guilfoyle, M. R. *et al.* Matrix Metalloproteinase Expression in Contusional Traumatic Brain Injury: A Paired Microdialysis Study. *J Neurotrauma* **32**, 1553-1559, doi:10.1089/neu.2014.3764 (2015).
- 39 Helmy, A. *et al.* Recombinant human interleukin-1 receptor antagonist in severe traumatic brain injury: a phase II randomized control trial. *Journal of cerebral blood flow and metabolism : official journal of the International Society of Cerebral Blood Flow and Metabolism* **34**, 845-851 (2014).

- 40 Helmy, A., Carpenter, K. L., Menon, D. K., Pickard, J. D. & Hutchinson, P. J. The cytokine response to human traumatic brain injury: temporal profiles and evidence for cerebral parenchymal production. *J Cereb Blood Flow Metab* **31**, 658-670, doi:10.1038/jcbfm.2010.142 (2011).
- 41 Ma, J., Huang, S., Qin, S., You, C. & Zeng, Y. Progesterone for acute traumatic brain injury. *Cochrane Database Syst Rev* **12**, CD008409, doi:10.1002/14651858.CD008409.pub4 (2016).
- 42 The, C. t. m. g. & The, C. t. c. The CRASH trial protocol (Corticosteroid randomisation after significant head injury) [ISRCTN74459797]. *BMC Emerg Med* **1**, 1 (2001).
- 43 Edwards, P. *et al.* Final results of MRC CRASH, a randomised placebo-controlled trial of intravenous corticosteroid in adults with head injury-outcomes at 6 months. *Lancet* **365**, 1957-1959, doi:10.1016/S0140-6736(05)66552-X (2005).
- 44 Adams, H. *et al.* Temporal profile of intracranial pressure and cerebrovascular reactivity in severe traumatic brain injury and association with fatal outcome: An observational study. *PLoS Med* **14**, e1002353, doi:10.1371/journal.pmed.1002353 (2017).
- 45 Raghupathi, R., Graham, D. I. & McIntosh, T. K. Apoptosis after traumatic brain injury. *Journal of neurotrauma* **17**, 927-938 (2000).
- 46 Raghupathi, R. Cell death mechanisms following traumatic brain injury. *Brain pathology (Zurich, Switzerland)* **14**, 215-222 (2004).
- 47 Kraus, M. F. *et al.* White matter integrity and cognition in chronic traumatic brain injury: a diffusion tensor imaging study. *Brain : a journal of neurology* **130**, 2508-2519 (2007).
- 48 van Eijck, M. M., Schoonman, G. G., van der Naalt, J., de Vries, J. & Roks, G. Diffuse axonal injury after traumatic brain injury is a prognostic factor for functional outcome: a systematic review and meta-analysis. *Brain Inj* **32**, 395-402, doi:10.1080/02699052.2018.1429018 (2018).
- 49 Aldossary, N. M., Kotb, M. A. & Kamal, A. M. Predictive value of early MRI findings on neurocognitive and psychiatric outcomes in patients with severe traumatic brain injury. *J Affect Disord* **243**, 1-7, doi:10.1016/j.jad.2018.09.001 (2019).
- 50 Blumbergs, P. C., Jones, N. R. & North, J. B. Diffuse axonal injury in head trauma. *J Neurol Neurosurg Psychiatry* **52**, 838-841, doi:10.1136/jnnp.52.7.838 (1989).
- 51 Vieira, R. C. *et al.* Diffuse Axonal Injury: Epidemiology, Outcome and Associated Risk Factors. *Front Neurol* **7**, 178, doi:10.3389/fneur.2016.00178 (2016).
- 52 Carron, S. F., Alwis, D. S. & Rajan, R. Traumatic Brain Injury and Neuronal Functionality Changes in Sensory Cortex. *Front Syst Neurosci* **10**, 47, doi:10.3389/fnsys.2016.00047 (2016).
- 53 Atkins, C. M. Decoding hippocampal signaling deficits after traumatic brain injury. *Transl Stroke Res* **2**, 546-555, doi:10.1007/s12975-011-0123-z (2011).
- 54 Gale, S. D., Johnson, S. C., Bigler, E. D. & Blatter, D. D. Nonspecific white matter degeneration following traumatic brain injury. *J Int Neuropsychol Soc* **1**, 17-28 (1995).
- 55 Levin, H. S. *et al.* Diffusion tensor imaging of mild to moderate blast-related traumatic brain injury and its sequelae. *Journal of neurotrauma* **27**, 683-694 (2010).
- 56 Wu, L. *et al.* Thalamic atrophy and dysfunction in patients with mild-to-moderate traumatic diffuse axonal injury: a short-term and mid-term MRI study. *Neuroreport* **29**, 1282-1287, doi:10.1097/WNR.0000000000001106 (2018).
- 57 McDonald, S., Dalton, K. I., Rushby, J. A. & Landin-Romero, R. Loss of white matter connections after severe traumatic brain injury (TBI) and its relationship to social cognition. *Brain Imaging Behav*, doi:10.1007/s11682-018-9906-0 (2018).
- 58 Molteni, E. *et al.* Fronto-temporal vulnerability to disconnection in paediatric moderate and severe traumatic brain injury. *Eur J Neurol*, doi:10.1111/ene.13963 (2019).
- 59 Newcombe, V. *et al.* Mapping traumatic axonal injury using diffusion tensor imaging: correlations with functional outcome. *PLoS one* **6**, e19214 (2011).

- 60 Ware, J. B. *et al.* Inter-Subject Variability of Axonal Injury in Diffuse Traumatic Brain Injury. *J Neurotrauma* **34**, 2243-2253, doi:10.1089/neu.2016.4817 (2017).
- 61 Ljungqvist, J. *et al.* Longitudinal changes in diffusion tensor imaging parameters of the corpus callosum between 6 and 12 months after diffuse axonal injury. *Brain Inj* **31**, 344-350, doi:10.1080/02699052.2016.1256500 (2017).
- 62 Kirov, I. *et al.* Proton MR spectroscopy correlates diffuse axonal abnormalities with post-concussive symptoms in mild traumatic brain injury. *J Neurotrauma* **30**, 1200-1204, doi:10.1089/neu.2012.2696 (2013).
- 63 Kirov, I. *et al.* Diffuse axonal injury in mild traumatic brain injury: a 3D multivoxel proton MR spectroscopy study. *J Neurol* **260**, 242-252, doi:10.1007/s00415-012-6626-z (2013).
- 64 Kirov, I. I. *et al.* Diffuse axonal injury in mild traumatic brain injury: a 3D multivoxel proton MR spectroscopy study. *Journal of neurology* (2012).
- 65 Hiebert, J. B., Shen, Q., Thimmesch, A. R. & Pierce, J. D. Traumatic brain injury and mitochondrial dysfunction. *Am J Med Sci* **350**, 132-138, doi:10.1097/MAJ.0000000000000506 (2015).
- 66 Fischer, T. D. *et al.* Altered Mitochondrial Dynamics and TBI Pathophysiology. *Front Syst Neurosci* **10**, 29, doi:10.3389/fnsys.2016.00029 (2016).
- 67 Brown, G. C. Nitric oxide inhibition of cytochrome oxidase and mitochondrial respiration: implications for inflammatory, neurodegenerative and ischaemic pathologies. *Molecular and cellular biochemistry* **174**, 189-192 (1997).
- 68 Petkus, V. *et al.* Optimal cerebral perfusion pressure-targeted treatment for severe traumatic brain injury. *J Neurotrauma*, doi:10.1089/neu.2019.6551 (2019).
- 69 Rangel-Castilla, L., Gasco, J., Nauta, H. J., Okonkwo, D. O. & Robertson, C. S. Cerebral pressure autoregulation in traumatic brain injury. *Neurosurg Focus* **25**, E7, doi:10.3171/FOC.2008.25.10.E7 (2008).
- 70 Beqiri, E. *et al.* Feasibility of individualised severe traumatic brain injury management using an automated assessment of optimal cerebral perfusion pressure: the COGITATE phase II study protocol. *BMJ Open* **9**, e030727, doi:10.1136/bmjopen-2019-030727 (2019).
- 71 Newcombe, V. F. J., Das, T. & Cross, J. J. Diffusion imaging in neurological disease. *Journal of neurology* **260**, 335-342 (2013).
- 72 Newcombe, V. F. J. *et al.* Microstructural basis of contusion expansion in traumatic brain injury: insights from diffusion tensor imaging. *Journal of cerebral blood flow and metabolism : official journal of the International Society of Cerebral Blood Flow and Metabolism* **33**, 855-862 (2013).
- 73 Newcombe, V. F. J. *et al.* Aetiological differences in neuroanatomy of the vegetative state: insights from diffusion tensor imaging and functional implications. *Journal of neurology, neurosurgery, and psychiatry* **81**, 552-561 (2010).
- 74 Budde, M. D., Janes, L., Gold, E., Turtzo, L. C. & Frank, J. A. The contribution of gliosis to diffusion tensor anisotropy and tractography following traumatic brain injury: validation in the rat using Fourier analysis of stained tissue sections. *Brain : a journal of neurology* **134**, 2248-2260 (2011).
- 75 Mori, S. & Barker, P. B. Diffusion magnetic resonance imaging: its principle and applications. *The Anatomical record* **257**, 102-109 (1999).
- 76 Le, T. H. & Gean, A. D. Neuroimaging of traumatic brain injury. *The Mount Sinai journal of medicine, New York* **76**, 145-162 (2009).
- 77 Mukherjee, P., Berman, J. I., Chung, S. W., Hess, C. P. & Henry, R. G. Diffusion tensor MR imaging and fiber tractography: theoretic underpinnings. *AJNR. American journal of neuroradiology* **29**, 632-641 (2008).
- 78 Roberts, T. P. L. & Schwartz, E. S. Principles and implementation of diffusion-weighted and diffusion tensor imaging. *Pediatric radiology* **37**, 739-748 (2007).

- 79 Le Bihan, D. *et al.* Diffusion tensor imaging: concepts and applications. *Journal of magnetic resonance imaging : JMRI* **13**, 534-546 (2001).
- 80 Basser, P. J. & Jones, D. K. Diffusion-tensor MRI: theory, experimental design and data analysis - a technical review. *NMR in biomedicine* **15**, 456-467 (2002).
- 81 Jones, D. K. & Leemans, A. Diffusion tensor imaging. *Methods in molecular biology (Clifton, N.J.)* **711**, 127-144 (2011).
- 82 Jellison, B. J. *et al.* Diffusion tensor imaging of cerebral white matter: a pictorial review of physics, fiber tract anatomy, and tumor imaging patterns. *AJNR. American journal of neuroradiology* **25**, 356-369 (2004).
- 83 Alexander, A. L., Lee, J. E., Lazar, M. & Field, A. S. Diffusion tensor imaging of the brain. *Neurotherapeutics* **4**, 316-329, doi:10.1016/j.nurt.2007.05.011 (2007).
- 84 Pierpaoli, C. & Basser, P. J. Toward a quantitative assessment of diffusion anisotropy. *Magn Reson Med* **36**, 893-906 (1996).
- 85 Salmond, C. H. *et al.* Diffusion tensor imaging in chronic head injury survivors: correlations with learning and memory indices. *Neuroimage* **29**, 117-124, doi:10.1016/j.neuroimage.2005.07.012 (2006).
- 86 Xu, J., Rasmussen, I.-A., Lagopoulos, J. & Håberg, A. Diffuse axonal injury in severe traumatic brain injury visualized using high-resolution diffusion tensor imaging. *Journal of neurotrauma* **24**, 753-765 (2007).
- 87 Wu, T. C. *et al.* Evaluating the relationship between memory functioning and cingulum bundles in acute mild traumatic brain injury using diffusion tensor imaging. *Journal of neurotrauma* **27**, 303-307 (2010).
- 88 Castano-Leon, A. M. *et al.* Longitudinal Analysis of Corpus Callosum Diffusion Tensor Imaging Metrics and its Association with Neurological Outcome. *J Neurotrauma*, doi:10.1089/neu.2018.5978 (2019).
- 89 Wedeen, V. J. *et al.* Diffusion spectrum magnetic resonance imaging (DSI) tractography of crossing fibers. *NeuroImage* **41**, 1267-1277 (2008).
- 90 Pfefferbaum, A., Adalsteinsson, E., Spielman, D., Sullivan, E. V. & Lim, K. O. In vivo spectroscopic quantification of the N-acetyl moiety, creatine, and choline from large volumes of brain gray and white matter: effects of normal aging. *Magnetic resonance in medicine : official journal of the Society of Magnetic Resonance in Medicine / Society of Magnetic Resonance in Medicine* **41**, 276-284 (1999).
- 91 Brateman, L. Chemical shift imaging: a review. *AJR. American journal of roentgenology* **146**, 971-980 (1986).
- 92 Alger, J. R. Quantitative proton magnetic resonance spectroscopy and spectroscopic imaging of the brain: a didactic review. *Topics in magnetic resonance imaging : TMRI* **21**, 115-128 (2010).
- 93 Zhu, H. & Barker, P. B. MR spectroscopy and spectroscopic imaging of the brain. *Methods Mol Biol* **711**, 203-226, doi:10.1007/978-1-61737-992-5_9 (2011).
- 94 Brown, T. R., Kincaid, B. M. & Ugurbil, K. NMR chemical shift imaging in three dimensions. *Proceedings of the National Academy of Sciences of the United States of America* **79**, 3523-3526 (1982).
- 95 Barker, P. B., Bizzi, A. & Stefano, N. D. *Clinical MR Spectroscopy*. (Cambridge Univ Pr, 2009).
- 96 Maudsley, A. A. *et al.* Comprehensive processing, display and analysis for in vivo MR spectroscopic imaging. *NMR in biomedicine* **19**, 492-503 (2006).
- 97 Gasparovic, C. *et al.* Neurometabolite concentrations in gray and white matter in mild traumatic brain injury: an 1H-magnetic resonance spectroscopy study. *Journal of neurotrauma* **26**, 1635-1643 (2009).
- 98 Bertholdo, D., Watcharakorn, A. & Castillo, M. Brain Proton Magnetic Resonance Spectroscopy. *AJNR. American journal of neuroradiology* (2003).

- 99 Govindaraju, V., Young, K. & Maudsley, A. A. Proton NMR chemical shifts and coupling constants for brain metabolites. *NMR in biomedicine* **13**, 129-153 (2000).
- 100 Peter B. Barker, D. D. M. L. In vivo proton MR spectroscopy of the human brain. *Progress in Nuclear Magnetic Resonance Spectroscopy* **49**, 99-128 (2006).
- 101 Gillard, J. H., Waldman, A. D. & Barker, P. B. *Clinical MR neuroimaging*. (Cambridge Univ Pr, 2005).
- 102 McLean, M. A., Woermann, F. G., Simister, R. J., Barker, G. J. & Duncan, J. S. In vivo short echo time 1H-magnetic resonance spectroscopic imaging (MRSI) of the temporal lobes. *Neuroimage* **14**, 501-509, doi:10.1006/nimg.2001.0827 (2001).
- 103 McLean, M. A., Woermann, F. G., Barker, G. J. & Duncan, J. S. Quantitative analysis of short echo time (1)H-MRSI of cerebral gray and white matter. *Magnetic resonance in medicine : official journal of the Society of Magnetic Resonance in Medicine / Society of Magnetic Resonance in Medicine* **44**, 401-411 (2000).
- 104 Verma, G. *et al.* Whole-brain analysis of amyotrophic lateral sclerosis by using echo-planar spectroscopic imaging. *Radiology* **267**, 851-857 (2013).
- 105 Stagg, C. J. *et al.* Whole-brain magnetic resonance spectroscopic imaging measures are related to disability in ALS. *Neurology* **80**, 610-615 (2013).
- 106 Maudsley, A. A., Govind, V. & Arheart, K. L. Associations of age, gender and body mass with 1H MR-observed brain metabolites and tissue distributions. *NMR in biomedicine* **25**, 580-593 (2012).
- 107 Maudsley, A. A., Govind, V. & Arheart, K. L. Associations of age, gender and body mass with (1) H MR-observed brain metabolites and tissue distributions. *NMR in biomedicine* (2011).
- 108 Govind, V. *et al.* Whole-Brain Proton MR Spectroscopic Imaging of Mild-to-Moderate Traumatic Brain Injury and Correlation with Neuropsychological Deficits. *Journal of neurotrauma* **27**, 483-496 (2010).
- 109 Maudsley, A. A., Domenig, C. & Sheriff, S. Reproducibility of serial whole-brain MR spectroscopic imaging. *NMR in biomedicine* **23**, 251-256 (2010).
- 110 Govindaraju, V. *et al.* Volumetric proton spectroscopic imaging of mild traumatic brain injury. *AJNR. American journal of neuroradiology* **25**, 730-737 (2004).
- 111 Li, B. S. Y., Babb, J. S., Soher, B. J., Maudsley, A. A. & Gonen, O. Reproducibility of 3D proton spectroscopy in the human brain. *Magnetic resonance in medicine : official journal of the Society of Magnetic Resonance in Medicine / Society of Magnetic Resonance in Medicine* **47**, 439-446 (2002).
- 112 Young, K., Khetselius, D., Soher, B. J. & Maudsley, A. A. Confidence images for MR spectroscopic imaging. *Magnetic resonance in medicine : official journal of the Society of Magnetic Resonance in Medicine / Society of Magnetic Resonance in Medicine* **44**, 537-545 (2000).
- 113 Veenith, T. V. *et al.* Comparison of inter subject variability and reproducibility of whole brain proton spectroscopy. *PLoS One* **9**, e115304, doi:10.1371/journal.pone.0115304 (2014).
- 114 Robin, A. D. G. *In vivo NMR spectroscopy*. (Wiley-Interscience, 2007).
- 115 Veenith, T. & Coles, J. P. Anaesthesia for magnetic resonance imaging and positron emission tomography. *Current opinion in anaesthesiology* **24**, 451-458 (2011).
- 116 Coles, J. P. *et al.* Intersubject variability and reproducibility of 15O PET studies. *Journal of cerebral blood flow and metabolism : official journal of the International Society of Cerebral Blood Flow and Metabolism* **26**, 48-57 (2006).
- 117 Pickard, J. D. *et al.* Imaging of cerebral blood flow and metabolism in brain injury in the ICU. *Acta neurochirurgica. Supplement* **95**, 459-464 (2005).
- 118 Coles, J. P. *et al.* Hyperventilation following head injury: effect on ischemic burden and cerebral oxidative metabolism. *Critical care medicine* **35**, 568-578 (2007).

- 119 Steiner, L. A. *et al.* Predicting the response of intracranial pressure to moderate hyperventilation. *Acta Neurochir (Wien)* **147**, 477-483; discussion 483, doi:10.1007/s00701-005-0510-x (2005).
- 120 Coles, J. P. *et al.* Incidence and mechanisms of cerebral ischemia in early clinical head injury. *J Cereb Blood Flow Metab* **24**, 202-211, doi:10.1097/01.WCB.0000103022.98348.24 (2004).
- 121 Coles, J. P. *et al.* Defining ischemic burden after traumatic brain injury using 15O PET imaging of cerebral physiology. *Journal of cerebral blood flow and metabolism : official journal of the International Society of Cerebral Blood Flow and Metabolism* **24**, 191-201 (2004).
- 122 Coles, J. P. Regional ischemia after head injury. *Curr Opin Crit Care* **10**, 120-125 (2004).
- 123 Menon, D. K. *et al.* Diffusion limited oxygen delivery following head injury. *Critical care medicine* **32**, 1384-1390 (2004).
- 124 Kinahan, P. E., Rogers, J. G. & Ieee. Analytic 3D image reconstruction using all detected events. *Nucl Sci* **36 SRC - Google Scholar**, 964-968 (1989).
- 125 Lammertsma, A. A. & Jones, T. Low oxygen extraction fraction in tumours measured with the oxygen-15 steady state technique: effect of tissue heterogeneity. *The British journal of radiology* **65**, 697-700 (1992).
- 126 Lammertsma, A. A., Martin, A. J., Friston, K. J. & Jones, T. In vivo measurement of the volume of distribution of water in cerebral grey matter: effects on the calculation of regional cerebral blood flow. *Journal of cerebral blood flow and metabolism : official journal of the International Society of Cerebral Blood Flow and Metabolism* **12**, 291-295 (1992).
- 127 Levin, C. S. & Hoffman, E. J. Calculation of positron range and its effect on the fundamental limit of positron emission tomography system spatial resolution. *Physics in medicine and biology* **44**, 781-799 (1999).
- 128 Smielewski, P. *et al.* Integrated image analysis solutions for PET datasets in damaged brain. *Monit Comput In Press* (2003).
- 129 Ibaraki, M. *et al.* PET measurements of CBF, OEF, and CMRO2 without arterial sampling in hyperacute ischemic stroke: method and error analysis. *Annals of nuclear medicine* **18**, 35-44 (2004).
- 130 Coles, J. P. *et al.* Incidence and mechanisms of cerebral ischemia in early clinical head injury. *Journal of cerebral blood flow and metabolism : official journal of the International Society of Cerebral Blood Flow and Metabolism* **24**, 202-211 (2004).
- 131 Smielewski, P. *et al.* Integrated image analysis solutions for PET datasets in damaged brain. *Journal of clinical monitoring and computing* **17**, 427-440 (2002).
- 132 Blomqvist, G., Lammertsma, A. A., Mazoyer, B. & Wienhard, K. Effect of tissue heterogeneity on quantification in positron emission tomography. *European journal of nuclear medicine* **22**, 652-663 (1995).
- 133 Lammertsma, A. A. *et al.* Combination of dynamic and integral methods for generating reproducible functional CBF images. *Journal of cerebral blood flow and metabolism : official journal of the International Society of Cerebral Blood Flow and Metabolism* **10**, 675-686 (1990).
- 134 Lammertsma, A. A. *et al.* The C15O2 build-up technique to measure regional cerebral blood flow and volume of distribution of water. *Journal of cerebral blood flow and metabolism : official journal of the International Society of Cerebral Blood Flow and Metabolism* **9**, 461-470 (1989).
- 135 Lammertsma, A. A., Correia, J. A. & Jones, T. Stability of arterial concentrations during continuous inhalation of C15O2 and 15O2 and the effects on computed values of CBF and CMRO2. *Journal of cerebral blood flow and metabolism : official journal of the International Society of Cerebral Blood Flow and Metabolism* **8**, 411-417 (1988).
- 136 Lammertsma, A. A., Baron, J. C. & Jones, T. Correction for intravascular activity in the oxygen-15 steady-state technique is independent of the regional hematocrit. *Journal of*

- cerebral blood flow and metabolism : official journal of the International Society of Cerebral Blood Flow and Metabolism* **7**, 372-374 (1987).
- 137 Kanno, I. *et al.* Measurement of cerebral blood flow using bolus inhalation of C15O2 and positron emission tomography: description of the method and its comparison with the C15O2 continuous inhalation method. *Journal of cerebral blood flow and metabolism : official journal of the International Society of Cerebral Blood Flow and Metabolism* **4**, 224-234 (1984).
- 138 Lammertsma, A. A. *et al.* In vivo measurement of regional cerebral haematocrit using positron emission tomography. *Journal of cerebral blood flow and metabolism : official journal of the International Society of Cerebral Blood Flow and Metabolism* **4**, 317-322 (1984).
- 139 Lammertsma, A. A. & Jones, T. Correction for the presence of intravascular oxygen-15 in the steady-state technique for measuring regional oxygen extraction ratio in the brain: 1. Description of the method. *Journal of cerebral blood flow and metabolism : official journal of the International Society of Cerebral Blood Flow and Metabolism* **3**, 416-424 (1983).
- 140 Lammertsma, A. A., Heather, J. D., Jones, T., Frackowiak, R. S. & Lenzi, G. L. A statistical study of the steady state technique for measuring regional cerebral blood flow and oxygen utilisation using 15O. *Journal of computer assisted tomography* **6**, 566-573 (1982).
- 141 Lammertsma, A. A., Jones, T., Frackowiak, R. S. & Lenzi, G. L. A theoretical study of the steady-state model for measuring regional cerebral blood flow and oxygen utilisation using oxygen-15. *Journal of computer assisted tomography* **5**, 544-550 (1981).
- 142 Read, S. J. *et al.* The fate of hypoxic tissue on 18F-fluoromisonidazole positron emission tomography after ischemic stroke. *Ann Neurol* **48**, 228-235 (2000).
- 143 Markus, R. *et al.* Topography and temporal evolution of hypoxic viable tissue identified by 18F-fluoromisonidazole positron emission tomography in humans after ischemic stroke. *Stroke* **34**, 2646-2652, doi:10.1161/01.STR.0000094422.74023.FF (2003).
- 144 Markus, R. *et al.* Hypoxic tissue in ischaemic stroke: persistence and clinical consequences of spontaneous survival. *Brain* **127**, 1427-1436, doi:10.1093/brain/awh162 (2004).
- 145 Saita, K. *et al.* Imaging the ischemic penumbra with 18F-fluoromisonidazole in a rat model of ischemic stroke. *Stroke* **35**, 975-980, doi:10.1161/01.STR.0000121647.01941.ba (2004).
- 146 Spratt, N. J., Ackerman, U., Tochon-Danguy, H. J., Donnan, G. A. & Howells, D. W. Characterization of fluoromisonidazole binding in stroke. *Stroke* **37**, 1862-1867, doi:10.1161/01.STR.0000226908.93295.9d (2006).
- 147 Heckl, S. Future contrast agents for molecular imaging in stroke. *Curr Med Chem* **14**, 1713-1728 (2007).
- 148 Spratt, N. J., Donnan, G. A. & Howells, D. W. Characterisation of the timing of binding of the hypoxia tracer FMISO after stroke. *Brain Res* **1288**, 135-142, doi:10.1016/j.brainres.2009.06.102 (2009).
- 149 Heiss, W. D. The concept of the penumbra: can it be translated to stroke management? *Int J Stroke* **5**, 290-295, doi:10.1111/j.1747-4949.2010.00444.x (2010).
- 150 Cheng, J. *et al.* 18F-fluoromisonidazole PET/CT: a potential tool for predicting primary endocrine therapy resistance in breast cancer. *J Nucl Med* **54**, 333-340, doi:10.2967/jnumed.112.111963 (2013).
- 151 Kobayashi, H. *et al.* Usefulness of FMISO-PET for glioma analysis. *Neurol Med Chir (Tokyo)* **53**, 773-778 (2013).
- 152 Mariotti, E. *et al.* Assessing radiotracer kinetics in the Langendorff perfused heart. *EJNMMI Res* **3**, 74, doi:10.1186/2191-219X-3-74 (2013).
- 153 Hirano, T. Searching for salvageable brain: the detection of ischemic penumbra using various imaging modalities? *J Stroke Cerebrovasc Dis* **23**, 795-798, doi:10.1016/j.jstrokecerebrovasdis.2013.10.003 (2014).

- 154 Baskin, A., Buchegger, F., Seimbille, Y., Ratib, O. & Garibotto, V. PET Molecular Imaging of Hypoxia in Ischemic Stroke: An Update. *Curr Vasc Pharmacol* **13**, 209-217 (2015).
- 155 Hong, Y. T., Beech, J. S., Smith, R., Baron, J. C. & Fryer, T. D. Parametric mapping of [18F]fluoromisonidazole positron emission tomography using basis functions. *J Cereb Blood Flow Metab* **31**, 648-657, doi:10.1038/jcbfm.2010.141 (2011).
- 156 Takasawa, M. *et al.* Imaging of brain hypoxia in permanent and temporary middle cerebral artery occlusion in the rat using 18F-fluoromisonidazole and positron emission tomography: a pilot study. *J Cereb Blood Flow Metab* **27**, 679-689, doi:10.1038/sj.jcbfm.9600405 (2007).
- 157 Fryer, T. D. *et al.* Effects of hyperoxia on 18F-fluoro-misonidazole brain uptake and tissue oxygen tension following middle cerebral artery occlusion in rodents: Pilot studies. *PLoS One* **12**, e0187087, doi:10.1371/journal.pone.0187087 (2017).
- 158 Hlatky, R., Valadka, A. B. & Robertson, C. S. Intracranial hypertension and cerebral ischemia after severe traumatic brain injury. *Neurosurgical focus* **14**, e2 (2003).
- 159 Vespa, P. M. *et al.* Pericontusional brain tissue exhibits persistent elevation of lactate/pyruvate ratio independent of cerebral perfusion pressure. *Critical care medicine* **35**, 1153-1160 (2007).
- 160 Xu, Y. *et al.* Early nonischemic oxidative metabolic dysfunction leads to chronic brain atrophy in traumatic brain injury. *Journal of cerebral blood flow and metabolism : official journal of the International Society of Cerebral Blood Flow and Metabolism* **30**, 883-894 (2010).
- 161 Price, D. J. & Murray, A. The influence of hypoxia and hypotension on recovery from head injury. *Injury* **3**, 218-224 (1972).
- 162 Okonkwo, D. O. *et al.* Brain Oxygen Optimization in Severe Traumatic Brain Injury Phase-II: A Phase II Randomized Trial. *Crit Care Med* **45**, 1907-1914, doi:10.1097/CCM.0000000000002619 (2017).
- 163 March, K. Retrograde jugular catheter: monitoring SjO₂. *The Journal of neuroscience nursing : journal of the American Association of Neuroscience Nurses* **26**, 48-51 (1994).
- 164 Nortje, J. *et al.* Effect of hyperoxia on regional oxygenation and metabolism after severe traumatic brain injury: preliminary findings. *Critical care medicine* **36**, 273-281 (2008).
- 165 Tolia, C. M. *et al.* Normobaric hyperoxia--induced improvement in cerebral metabolism and reduction in intracranial pressure in patients with severe head injury: a prospective historical cohort-matched study. *Journal of neurosurgery* **101**, 435-444 (2004).
- 166 Cheng, G., Kong, R. H., Zhang, L. M. & Zhang, J. N. Mitochondria in traumatic brain injury and mitochondrial-targeted multipotential therapeutic strategies. *Br J Pharmacol* **167**, 699-719, doi:10.1111/j.1476-5381.2012.02025.x (2012).
- 167 Gupta, D. *et al.* Detection of metabolic pattern following decompressive craniectomy in severe traumatic brain injury: A microdialysis study. *Brain Inj* **31**, 1660-1666, doi:10.1080/02699052.2017.1370553 (2017).
- 168 Moffett, J. R., Ross, B., Arun, P., Madhavarao, C. N. & Namboodiri, A. M. A. N-Acetylaspartate in the CNS: from neurodiagnostics to neurobiology. *Progress in neurobiology* **81**, 89-131 (2007).
- 169 Mazzeo, A. T. *et al.* Brain metabolic and hemodynamic effects of cyclosporin A after human severe traumatic brain injury: a microdialysis study. *Acta Neurochir (Wien)* **150**, 1019-1031; discussion 1031, doi:10.1007/s00701-008-0021-7 (2008).
- 170 Robertson, C. L. Mitochondrial dysfunction contributes to cell death following traumatic brain injury in adult and immature animals. *J Bioenerg Biomembr* **36**, 363-368, doi:10.1023/B:JOB.0000041769.06954.e4 (2004).
- 171 Signoretti, S. *et al.* N-Acetylaspartate reduction as a measure of injury severity and mitochondrial dysfunction following diffuse traumatic brain injury. *Journal of neurotrauma* **18**, 977-991 (2001).

- 172 Vagnozzi, R. *et al.* Changes of cerebral energy metabolism and lipid peroxidation in rats leading to mitochondrial dysfunction after diffuse brain injury. *Journal of neurotrauma* **16**, 903-913 (1999).
- 173 Hutchinson, P. J. *et al.* A combined microdialysis and FDG-PET study of glucose metabolism in head injury. *Acta neurochirurgica* **151**, 51-61; discussion 61 (2009).
- 174 Fernandez-Maza, L. *et al.* Rapid and simplified synthesis of [¹⁸F]Fluoromisonidazole and its use in PET imaging in an experimental model of subarachnoid hemorrhage. (2018).
- 175 Sato, J. *et al.* Hypoxic volume evaluated by ¹⁸F-fluoromisonidazole positron emission tomography (FMISO-PET) may be a prognostic factor in patients with oral squamous cell carcinoma: preliminary analyses. (2018).
- 176 Kawamura, M. *et al.* EP-1068: Hypoxic imaging obtained at 2-h postinjection in FMISO-PET. (2017).
- 177 Lee, G. h. *et al.* ¹⁸F-fluoromisonidazole (FMISO) Positron Emission Tomography (PET) Predicts Early Infarct Growth in Patients with Acute Ischemic Stroke. (2014).
- 178 Veenith, T. V. *et al.* Normobaric hyperoxia does not improve derangements in diffusion tensor imaging found distant from visible contusions following acute traumatic brain injury. *Sci Rep* **7**, 12419, doi:10.1038/s41598-017-12590-2 (2017).
- 179 Veenith, T. V. *et al.* Use of diffusion tensor imaging to assess the impact of normobaric hyperoxia within at-risk pericontusional tissue after traumatic brain injury. *Journal of cerebral blood flow and metabolism : official journal of the International Society of Cerebral Blood Flow and Metabolism* **34**, 1622-1627 (2014).
- 180 Newcombe, V. F. J. *et al.* Analysis of acute traumatic axonal injury using diffusion tensor imaging. *British journal of neurosurgery* **21**, 340-348 (2007).
- 181 Hannoun, S. *et al.* Diffusion Tensor-MRI Evidence for Extra-Axonal Neuronal Degeneration in Caudate and Thalamic Nuclei of Patients with Multiple Sclerosis. *AJNR. American journal of neuroradiology* (2012).
- 182 Senda, J. *et al.* MRI mean diffusivity detects widespread brain degeneration in multiple sclerosis. *Journal of the neurological sciences* **319**, 105-110 (2012).
- 183 Cassol, E. *et al.* Diffusion tensor imaging in multiple sclerosis: a tool for monitoring changes in normal-appearing white matter. *Multiple sclerosis (Houndmills, Basingstoke, England)* **10**, 188-196 (2004).
- 184 Bozzali, M. *et al.* White matter damage in Alzheimer's disease assessed in vivo using diffusion tensor magnetic resonance imaging. *Journal of neurology, neurosurgery, and psychiatry* **72**, 742-746 (2002).
- 185 Friston, K. J. & Frith, C. D. Schizophrenia: a disconnection syndrome? *Clinical neuroscience (New York, N.Y.)* **3**, 89-97 (1995).
- 186 Assaf, Y. & Pasternak, O. Diffusion tensor imaging (DTI)-based white matter mapping in brain research: a review. *Journal of molecular neuroscience : MN* **34**, 51-61 (2008).
- 187 Hakulinen, U. *et al.* Repeatability and variation of region-of-interest methods using quantitative diffusion tensor MR imaging of the brain. *BMC medical imaging* **12**, 30 (2012).
- 188 Brander, A. *et al.* Diffusion tensor imaging of the brain in a healthy adult population: Normative values and measurement reproducibility at 3 T and 1.5 T. *Acta radiologica (Stockholm, Sweden : 1987)* **51**, 800-807 (2010).
- 189 Cercignani, M., Bammer, R., Sormani, M. P., Fazekas, F. & Filippi, M. Inter-sequence and inter-imaging unit variability of diffusion tensor MR imaging histogram-derived metrics of the brain in healthy volunteers. *AJNR. American journal of neuroradiology* **24**, 638-643 (2003).
- 190 Takao, H., Hayashi, N., Kabasawa, H. & Ohtomo, K. Effect of scanner in longitudinal diffusion tensor imaging studies. *Human brain mapping* **33**, 466-477 (2012).

- 191 Takao, H., Hayashi, N. & Ohtomo, K. Effect of scanner in asymmetry studies using diffusion tensor imaging. *NeuroImage* **54**, 1053-1062 (2011).
- 192 Takao, H. *et al.* Gray and white matter asymmetries in healthy individuals aged 21-29 years: a voxel-based morphometry and diffusion tensor imaging study. *Human brain mapping* **32**, 1762-1773 (2011).
- 193 Jansen, J. F. A., Kooi, M. E., Kessels, A. G. H., Nicolay, K. & Backes, W. H. Reproducibility of quantitative cerebral T2 relaxometry, diffusion tensor imaging, and 1H magnetic resonance spectroscopy at 3.0 Tesla. *Investigative radiology* **42**, 327-337 (2007).
- 194 Farrell, J. A. D. *et al.* Effects of signal-to-noise ratio on the accuracy and reproducibility of diffusion tensor imaging-derived fractional anisotropy, mean diffusivity, and principal eigenvector measurements at 1.5 T. *Journal of magnetic resonance imaging : JMRI* **26**, 756-767 (2007).
- 195 Landman, B. A. *et al.* Effects of diffusion weighting schemes on the reproducibility of DTI-derived fractional anisotropy, mean diffusivity, and principal eigenvector measurements at 1.5T. *NeuroImage* **36**, 1123-1138 (2007).
- 196 Pfefferbaum, A., Adalsteinsson, E. & Sullivan, E. V. Replicability of diffusion tensor imaging measurements of fractional anisotropy and trace in brain. *Journal of magnetic resonance imaging : JMRI* **18**, 427-433 (2003).
- 197 Huppertz, H.-J., Kröll-Seger, J., Klöppel, S., Ganz, R. E. & Kassubek, J. Intra- and interscanner variability of automated voxel-based volumetry based on a 3D probabilistic atlas of human cerebral structures. *NeuroImage* **49**, 2216-2224 (2010).
- 198 Ciccarelli, O. *et al.* From diffusion tractography to quantitative white matter tract measures: a reproducibility study. *NeuroImage* **18**, 348-359 (2003).
- 199 Danielian, L. E., Iwata, N. K., Thomasson, D. M. & Floeter, M. K. Reliability of fiber tracking measurements in diffusion tensor imaging for longitudinal study. *NeuroImage* **49**, 1572-1580 (2010).
- 200 Hermoye, L. *et al.* Pediatric diffusion tensor imaging: normal database and observation of the white matter maturation in early childhood. *NeuroImage* **29**, 493-504 (2006).
- 201 Wakana, S. *et al.* Reproducibility of quantitative tractography methods applied to cerebral white matter. *NeuroImage* **36**, 630-644 (2007).
- 202 Heiervang, E., Behrens, T. E. J., Mackay, C. E., Robson, M. D. & Johansen-Berg, H. Between session reproducibility and between subject variability of diffusion MR and tractography measures. *NeuroImage* **33**, 867-877 (2006).
- 203 Huisman, T. A. G. M. *et al.* Quantitative diffusion tensor MR imaging of the brain: field strength related variance of apparent diffusion coefficient (ADC) and fractional anisotropy (FA) scalars. *European radiology* **16**, 1651-1658 (2006).
- 204 Veenith, T. V. *et al.* Use of diffusion tensor imaging to assess the impact of normobaric hyperoxia within at-risk pericontusional tissue after traumatic brain injury. *J Cereb Blood Flow Metab* **34**, 1622-1627, doi:10.1038/jcbfm.2014.123 (2014).
- 205 Newcombe, V. F. J. *et al.* Parcellating the neuroanatomical basis of impaired decision-making in traumatic brain injury. *Brain : a journal of neurology* **134**, 759-768 (2011).
- 206 Smith, S. M. *et al.* Advances in functional and structural MR image analysis and implementation as FSL. *NeuroImage* **23 Suppl 1**, S208-219 (2004).
- 207 Woolrich, M. W. *et al.* Bayesian analysis of neuroimaging data in FSL. *NeuroImage* **45**, S173-186 (2009).
- 208 Collins, D. L., Holmes, C. J., Peters, T. M. & Evans, A. C. Automatic 3-D model-based neuroanatomical segmentation. *Human Brain Mapping* **3**, 190-208 (1995).
- 209 Studholme, C., Hill, D. L. & Hawkes, D. J. Automated 3-D registration of MR and CT images of the head. *Medical image analysis* **1**, 163-175 (1996).

- 210 Lancaster, J. L. *et al.* Automated Talairach atlas labels for functional brain mapping. *Human brain mapping* **10**, 120-131 (2000).
- 211 Bisdas, S., Bohning, D. E., Besenski, N., Nicholas, J. S. & Rumboldt, Z. Reproducibility, interrater agreement, and age-related changes of fractional anisotropy measures at 3T in healthy subjects: effect of the applied b-value. *AJNR. American journal of neuroradiology* **29**, 1128-1133 (2008).
- 212 Alves, G. S. *et al.* Different patterns of white matter degeneration using multiple diffusion indices and volumetric data in mild cognitive impairment and Alzheimer patients. *PloS one* **7**, e52859 (2012).
- 213 Stampfli, P. *et al.* Subtle white matter alterations in schizophrenia identified with a new measure of fiber density. *Sci Rep* **9**, 4636, doi:10.1038/s41598-019-40070-2 (2019).
- 214 McGuire, S. A. *et al.* Reproducibility of quantitative structural and physiological MRI measurements. *Brain Behav* **7**, e00759, doi:10.1002/brb3.759 (2017).
- 215 Stamatakis, E. A., Shafto, M. A., Williams, G., Tam, P. & Tyler, L. K. White matter changes and word finding failures with increasing age. *PloS one* **6**, e14496 (2011).
- 216 Lebel, C. *et al.* Diffusion tensor imaging of white matter tract evolution over the lifespan. *NeuroImage* **60**, 340-352 (2012).
- 217 Price, S. J. & Gillard, J. H. Imaging biomarkers of brain tumour margin and tumour invasion. *The British journal of radiology* **84 Spec No 2**, S159-167 (2011).
- 218 Holshouser, B. A., Tong, K. A. & Ashwal, S. Proton MR spectroscopic imaging depicts diffuse axonal injury in children with traumatic brain injury. *AJNR. American journal of neuroradiology* **26**, 1276-1285 (2005).
- 219 Gonen, O. *et al.* Total brain N-acetylaspartate: a new measure of disease load in MS. *Neurology* **54**, 15-19 (2000).
- 220 Ruiz-Peña, J. L. *et al.* Magnetic resonance spectroscopy of normal appearing white matter in early relapsing-remitting multiple sclerosis: correlations between disability and spectroscopy. *BMC neurology* **4**, 8 (2004).
- 221 Govind, V. *et al.* Comprehensive evaluation of corticospinal tract metabolites in amyotrophic lateral sclerosis using whole-brain 1H MR spectroscopy. *PloS one* **7**, e35607 (2012).
- 222 Watanabe, T., Shiino, A. & Akiguchi, I. Hippocampal metabolites and memory performances in patients with amnesic mild cognitive impairment and Alzheimer's disease. *Neurobiology of learning and memory* **97**, 289-293 (2012).
- 223 Kraguljac, N. V. *et al.* Neurometabolites in schizophrenia and bipolar disorder - a systematic review and meta-analysis. *Psychiatry research* **203**, 111-125 (2012).
- 224 Szulc, A., Waszkiewicz, N., Bibulowicz, D., Konarzewska, B. & Tarasow, E. Proton magnetic resonance spectroscopy changes after antipsychotic treatment. *Current medicinal chemistry* (2012).
- 225 Klein, J. Membrane breakdown in acute and chronic neurodegeneration: focus on choline-containing phospholipids. *Journal of neural transmission (Vienna, Austria : 1996)* **107**, 1027-1063 (2000).
- 226 Wylezinska, M. *et al.* Thalamic neurodegeneration in relapsing-remitting multiple sclerosis. *Neurology* **60**, 1949-1954 (2003).
- 227 Signoretti, S. *et al.* Assessment of mitochondrial impairment in traumatic brain injury using high-resolution proton magnetic resonance spectroscopy. *Journal of neurosurgery* **108**, 42-52 (2008).
- 228 Ebel, A., Soher, B. J. & Maudsley, A. A. Assessment of 3D proton MR echo-planar spectroscopic imaging using automated spectral analysis. *Magnetic resonance in medicine : official journal of the Society of Magnetic Resonance in Medicine / Society of Magnetic Resonance in Medicine* **46**, 1072-1078 (2001).

- 229 Maudsley, A. A., Wu, Z., Meyerhoff, D. J. & Weiner, M. W. Automated processing for proton spectroscopic imaging using water reference deconvolution. *Magnetic resonance in medicine : official journal of the Society of Magnetic Resonance in Medicine / Society of Magnetic Resonance in Medicine* **31**, 589-595 (1994).
- 230 Langer, D. L., Rakaric, P., Kirilova, A., Jaffray, D. A. & Damyanovich, A. Z. Assessment of metabolite quantitation reproducibility in serial 3D-(1)H-MR spectroscopic imaging of human brain using stereotactic repositioning. *Magnetic resonance in medicine : official journal of the Society of Magnetic Resonance in Medicine / Society of Magnetic Resonance in Medicine* **58**, 666-673 (2007).
- 231 Maudsley, A. A. *et al.* Mapping of brain metabolite distributions by volumetric proton MR spectroscopic imaging (MRSI). *Magnetic resonance in medicine : official journal of the Society of Magnetic Resonance in Medicine / Society of Magnetic Resonance in Medicine* **61**, 548-559 (2009).
- 232 Veenith, T. V. *et al.* Inter subject variability and reproducibility of diffusion tensor imaging within and between different imaging sessions. *PLoS One* **8**, e65941, doi:10.1371/journal.pone.0065941 (2013).
- 233 Ebel, A. & Maudsley, A. A. Comparison of methods for reduction of lipid contamination for in vivo proton MR spectroscopic imaging of the brain. *Magnetic resonance in medicine : official journal of the Society of Magnetic Resonance in Medicine / Society of Magnetic Resonance in Medicine* **46**, 706-712 (2001).
- 234 Klein, A. *et al.* Evaluation of 14 nonlinear deformation algorithms applied to human brain MRI registration. *NeuroImage* **46**, 786-802 (2009).
- 235 Vagnozzi, R. *et al.* Assessment of metabolic brain damage and recovery following mild traumatic brain injury: a multicentre, proton magnetic resonance spectroscopic study in concussed patients. *Brain : a journal of neurology* **133**, 3232-3242 (2010).
- 236 Tavazzi, B. *et al.* Cerebral oxidative stress and depression of energy metabolism correlate with severity of diffuse brain injury in rats. *Neurosurgery* **56**, 582-589; discussion 582-589 (2005).
- 237 Fatouros, P. P. *et al.* Comparison of NAA measures by MRS and HPLC. *Acta neurochirurgica. Supplement* **76**, 35-37 (2000).
- 238 Vagnozzi, R. *et al.* Temporal window of metabolic brain vulnerability to concussion: a pilot 1H-magnetic resonance spectroscopic study in concussed athletes--part III. *Neurosurgery* **62**, 1286-1295; discussion 1295 (2008).
- 239 Signoretti, S. *et al.* Transient alterations of creatine, creatine phosphate, N-acetylaspartate and high-energy phosphates after mild traumatic brain injury in the rat. *Mol Cell Biochem* **333**, 269-277, doi:10.1007/s11010-009-0228-9 (2010).
- 240 Faul, F., Erdfelder, E., Lang, A.-G. & Buchner, A. G*Power 3: a flexible statistical power analysis program for the social, behavioral, and biomedical sciences. *Behavior research methods* **39**, 175-191 (2007).
- 241 Saunders, D. E., Howe, F. A., van den Boogaart, A., Griffiths, J. R. & Brown, M. M. Aging of the adult human brain: in vivo quantitation of metabolite content with proton magnetic resonance spectroscopy. *Journal of magnetic resonance imaging : JMRI* **9**, 711-716 (1999).
- 242 Christiansen, P., Toft, P., Larsson, H. B., Stubgaard, M. & Henriksen, O. The concentration of N-acetyl aspartate, creatine + phosphocreatine, and choline in different parts of the brain in adulthood and senium. *Magnetic resonance imaging* **11**, 799-806 (1993).
- 243 Veenith, T., Goon, S. & Burnstein, R. M. Molecular mechanisms of traumatic brain injury: the missing link in management. *World J Emerg Surg* **4**, 7, doi:10.1186/1749-7922-4-7 (2009).
- 244 Vespa, P. *et al.* Metabolic crisis without brain ischemia is common after traumatic brain injury: a combined microdialysis and positron emission tomography study. *J Cereb Blood Flow Metab* **25**, 763-774, doi:10.1038/sj.jcbfm.9600073 (2005).

- 245 Timofeev, I. *et al.* Interaction between brain chemistry and physiology after traumatic brain injury: impact of autoregulation and microdialysis catheter location. *Journal of neurotrauma* **28**, 849-860 (2011).
- 246 Hutchinson, P. J. *et al.* Consensus statement from the 2014 International Microdialysis Forum. *Intensive Care Med* **41**, 1517-1528, doi:10.1007/s00134-015-3930-y (2015).
- 247 Dellazizzo, L. *et al.* Minimal PaO₂ threshold after traumatic brain injury and clinical utility of a novel brain oxygenation ratio. *J Neurosurg*, 1-9, doi:10.3171/2018.5.JNS18651 (2018).
- 248 Beynon, C., Kiening, K. L., Orakcioglu, B., Unterberg, A. W. & Sakowitz, O. W. Brain tissue oxygen monitoring and hyperoxic treatment in patients with traumatic brain injury. *Journal of neurotrauma* **29**, 2109-2123 (2012).
- 249 Hirschi, R. *et al.* Analysis of high-frequency PbtO₂ measures in traumatic brain injury: insights into the treatment threshold. *J Neurosurg*, 1-11, doi:10.3171/2018.4.JNS172604 (2018).
- 250 Bullock, R., Maxwell, W. L., Graham, D. I., Teasdale, G. M. & Adams, J. H. Glial swelling following human cerebral contusion: an ultrastructural study. *Journal of neurology, neurosurgery, and psychiatry* **54**, 427-434 (1991).
- 251 Stein, S. C., Graham, D. I., Chen, X.-H. & Smith, D. H. Association between intravascular microthrombosis and cerebral ischemia in traumatic brain injury. *Neurosurgery* **54**, 687-691; discussion 691 (2004).
- 252 Schwarzmaier, S. M., Kim, S. W., Trabold, R. & Plesnila, N. Temporal profile of thrombogenesis in the cerebral microcirculation after traumatic brain injury in mice. *J Neurotrauma* **27**, 121-130, doi:10.1089/neu.2009.1114 (2010).
- 253 Friedrich, B., Muller, F., Feiler, S., Scholler, K. & Plesnila, N. Experimental subarachnoid hemorrhage causes early and long-lasting microarterial constriction and microthrombosis: an in-vivo microscopy study. *J Cereb Blood Flow Metab* **32**, 447-455, doi:10.1038/jcbfm.2011.154 (2012).
- 254 Takasawa, M., Moustafa, R. R. & Baron, J. C. Applications of nitroimidazole in vivo hypoxia imaging in ischemic stroke. *Stroke* **39**, 1629-1637, doi:10.1161/STROKEAHA.107.485938 (2008).
- 255 Alawneh, J. A. *et al.* Diffusion and perfusion correlates of the 18F-MISO PET lesion in acute stroke: pilot study. *Eur J Nucl Med Mol Imaging* **41**, 736-744, doi:10.1007/s00259-013-2581-x (2014).
- 256 Markus, R. *et al.* Statistical parametric mapping of hypoxic tissue identified by [(18)F]fluoromisonidazole and positron emission tomography following acute ischemic stroke. *Neuroimage* **16**, 425-433, doi:10.1006/nimg.2002.1056 (2002).
- 257 Hong, Y. T. & Fryer, T. D. Kinetic modelling using basis functions derived from two-tissue compartmental models with a plasma input function: general principle and application to [18F]fluorodeoxyglucose positron emission tomography. *Neuroimage* **51**, 164-172, doi:10.1016/j.neuroimage.2010.02.013 (2010).
- 258 Smielewski, P. *et al.* Integrated image analysis solutions for pet datasets in damaged brain. *J Clin Monit Comput* **17**, 427-440 (2002).
- 259 Smith, S. M. Fast robust automated brain extraction. *Human brain mapping* **17**, 143-155 (2002).
- 260 Fletcher, P. C. *et al.* Is multivariate analysis of PET data more revealing than the univariate approach? Evidence from a study of episodic memory retrieval. *Neuroimage* **3**, 209-215, doi:10.1006/nimg.1996.0023 (1996).
- 261 Coles, J. P. *et al.* Defining ischemic burden after traumatic brain injury using 15O PET imaging of cerebral physiology. *J Cereb Blood Flow Metab* **24**, 191-201 (2004).
- 262 Coles, J. P. *et al.* Hyperventilation following head injury: effect on ischemic burden and cerebral oxidative metabolism. *Crit Care Med* **35**, 568-578 (2007).

- 263 Moustafa, R. R. & Baron, J. C. Clinical review: Imaging in ischaemic stroke--implications for
acute management. *Crit Care* **11**, 227, doi:10.1186/cc5973 (2007).
- 264 Marshall, L. F. *et al.* The diagnosis of head injury requires a classification based on computed
axial tomography. *J Neurotrauma* **9 Suppl 1**, S287-292 (1992).
- 265 Patlak, C. S., Blasberg, R. G. & Fenstermacher, J. D. Graphical evaluation of blood-to-brain
transfer constants from multiple-time uptake data. *J Cereb Blood Flow Metab* **3**, 1-7,
doi:10.1038/jcbfm.1983.1 (1983).
- 266 Coles, J. P. *et al.* Does induced hypertension reduce cerebral ischaemia within the
traumatized human brain? *Brain* **127**, 2479-2490, doi:10.1093/brain/awh268 (2004).
- 267 Bartlett, R. M. *et al.* Image-guided PO₂ probe measurements correlated with parametric
images derived from 18F-fluoromisonidazole small-animal PET data in rats. *J Nucl Med* **53**,
1608-1615, doi:10.2967/jnumed.112.103523 (2012).
- 268 Coles, J. P. *et al.* Early metabolic characteristics of lesion and nonlesion tissue after head
injury. *J Cereb Blood Flow Metab* **29**, 965-975, doi:10.1038/jcbfm.2009.22 (2009).
- 269 Read, S. J. *et al.* Identifying hypoxic tissue after acute ischemic stroke using PET and 18F-
fluoromisonidazole. *Neurology* **51**, 1617-1621, doi:10.1212/wnl.51.6.1617 (1998).
- 270 Moen, K. G. *et al.* A longitudinal MRI study of traumatic axonal injury in patients with
moderate and severe traumatic brain injury. *J Neurol Neurosurg Psychiatry* **83**, 1193-1200,
doi:10.1136/jnnp-2012-302644 (2012).
- 271 Gross, M. W., Karbach, U., Groebe, K., Franko, A. J. & Mueller-Klieser, W. Calibration of
misonidazole labeling by simultaneous measurement of oxygen tension and labeling density
in multicellular spheroids. *Int J Cancer* **61**, 567-573 (1995).
- 272 Pennings, F. A., Schuurman, P. R., van den Munckhof, P. & Bouma, G. J. Brain tissue oxygen
pressure monitoring in awake patients during functional neurosurgery: the assessment of
normal values. *J Neurotrauma* **25**, 1173-1177, doi:10.1089/neu.2007.0402 (2008).
- 273 Meixensberger, J., Dings, J., Kuhnigk, H. & Roosen, K. Studies of tissue PO₂ in normal and
pathological human brain cortex. *Acta Neurochir Suppl (Wien)* **59**, 58-63 (1993).
- 274 Cleveland WS, D. S. Locally weighted regression: an approach to regression analysis by local
fitting. *J Am Stat Assoc* **83**, 596-610 (1988).
- 275 Alian, A. A. & Rafferty, T. The best fit function for the tee short axis left ventricular ejection
fraction and radionuclear "gold standard" relationship is curvilinear. *J Clin Monit Comput* **22**,
169-173, doi:10.1007/s10877-008-9118-z (2008).
- 276 Valadka, A. B., Gopinath, S. P., Contant, C. F., Uzura, M. & Robertson, C. S. Relationship of
brain tissue PO₂ to outcome after severe head injury. *Crit Care Med* **26**, 1576-1581 (1998).
- 277 Bouma, G. J., Muizelaar, J. P., Choi, S. C., Newlon, P. G. & Young, H. F. Cerebral circulation
and metabolism after severe traumatic brain injury: the elusive role of ischemia. *J Neurosurg*
75, 685-693. (1991).
- 278 Bullock, R., Maxwell, W. L., Graham, D. I., Teasdale, G. M. & Adams, J. H. Glial swelling
following human cerebral contusion: an ultrastructural study. *J Neurol Neurosurg Psychiatry*
54, 427-434. (1991).
- 279 Vilalta, A. *et al.* Normobaric hyperoxia in traumatic brain injury. Does brain metabolic state
influence the response to hyperoxic challenge? *Journal of neurotrauma* (2011).
- 280 O'Connell, M. T. *et al.* Glucose metabolism in traumatic brain injury: a combined
microdialysis and [18F]-2-fluoro-2-deoxy-D-glucose-positron emission tomography (FDG-
PET) study. *Acta neurochirurgica. Supplement* **95**, 165-168 (2005).
- 281 Rodgers, J. L., Iyer, D., Rodgers, L. E., Vanthenapalli, S. & Panguluri, S. K. Impact of hyperoxia
on cardiac pathophysiology. *J Cell Physiol* **234**, 12595-12603, doi:10.1002/jcp.28136 (2019).
- 282 Ejaz, S. *et al.* Normobaric hyperoxia markedly reduces brain damage and sensorimotor
deficits following brief focal ischaemia. *Brain* **139**, 751-764, doi:10.1093/brain/awv391
(2016).

- 283 Hafner, S., Beloncle, F., Koch, A., Radermacher, P. & Asfar, P. Hyperoxia in intensive care, emergency, and peri-operative medicine: Dr. Jekyll or Mr. Hyde? A 2015 update. *Ann Intensive Care* **5**, 42, doi:10.1186/s13613-015-0084-6 (2015).
- 284 Pilcher, J. *et al.* The effect of hyperoxia following cardiac arrest - A systematic review and meta-analysis of animal trials. *Resuscitation* **83**, 417-422, doi:10.1016/j.resuscitation.2011.12.021 (2012).
- 285 Stub, D. *et al.* A randomized controlled trial of oxygen therapy in acute myocardial infarction Air Verses Oxygen In myocardial infarction study (AVOID Study). *Am Heart J* **163**, 339-345 e331, doi:10.1016/j.ahj.2011.11.011 (2012).
- 286 Iscoe, S., Beasley, R. & Fisher, J. A. Supplementary oxygen for nonhypoxemic patients: O2 much of a good thing? *Critical care (London, England)* **15**, 305 (2011).
- 287 Bellomo, R. *et al.* Arterial hyperoxia and in-hospital mortality after resuscitation from cardiac arrest. *Critical care (London, England)* **15**, R90 (2011).
- 288 Calzia, E. *et al.* Hyperoxia may be beneficial. *Critical Care Medicine* **38** (2010).
- 289 Davis, D. P. *et al.* Both hypoxemia and extreme hyperoxemia may be detrimental in patients with severe traumatic brain injury. *Journal of neurotrauma* **26**, 2217-2223 (2009).
- 290 Bitterman, H. Bench-to-bedside review: oxygen as a drug. *Crit Care* **13**, 205, doi:10.1186/cc7151 (2009).
- 291 Moccia, M., de Stefano, N. & Barkhof, F. Imaging outcome measures for progressive multiple sclerosis trials. *Mult Scler* **23**, 1614-1626, doi:10.1177/1352458517729456 (2017).
- 292 Yuh, E. L. *et al.* Diffusion tensor imaging for outcome prediction in mild traumatic brain injury: a TRACK-TBI study. *Journal of neurotrauma* **31**, 1457-1477 (2014).
- 293 Casson, I. R., Viano, D. C., Haacke, E. M., Kou, Z. & LeStrange, D. G. Is There Chronic Brain Damage in Retired NFL Players? Neuroradiology, Neuropsychology, and Neurology Examinations of 45 Retired Players. *Sports Health* **6**, 384-395, doi:10.1177/1941738114540270 (2014).
- 294 Betz, J., Zhuo, J., Roy, A., Shanmuganathan, K. & Gullapalli, R. P. Prognostic value of diffusion tensor imaging parameters in severe traumatic brain injury. *J Neurotrauma* **29**, 1292-1305, doi:10.1089/neu.2011.2215 (2012).
- 295 Nakamura, K. *et al.* Reduced white matter fractional anisotropy and clinical symptoms in schizophrenia: A voxel-based diffusion tensor imaging study. *Psychiatry research* (2012).
- 296 McGinn, M. J. & Povlishock, J. T. Pathophysiology of Traumatic Brain Injury. *Neurosurg Clin N Am* **27**, 397-407, doi:10.1016/j.nec.2016.06.002 (2016).
- 297 Fernández-Espejo, D. *et al.* Diffusion weighted imaging distinguishes the vegetative state from the minimally conscious state. *NeuroImage* **54**, 103-112 (2011).
- 298 Mannion, R. J. *et al.* Mechanism-based MRI classification of traumatic brainstem injury and its relationship to outcome. *Journal of neurotrauma* **24**, 128-135 (2007).
- 299 Arfanakis, K. *et al.* Diffusion tensor MR imaging in diffuse axonal injury. *AJNR. American journal of neuroradiology* **23**, 794-802 (2002).
- 300 Ling, J. M. *et al.* Biomarkers of increased diffusion anisotropy in semi-acute mild traumatic brain injury: a longitudinal perspective. *Brain : a journal of neurology* **135**, 1281-1292 (2012).
- 301 Bullock, R. *et al.* The time course of vasogenic oedema after focal human head injury--evidence from SPECT mapping of blood brain barrier defects. *Acta Neurochir Suppl (Wien)* **51**, 286-288 (1990).
- 302 Menzel, M. *et al.* Increased inspired oxygen concentration as a factor in improved brain tissue oxygenation and tissue lactate levels after severe human head injury. *J Neurosurg* **91**, 1-10, doi:10.3171/jns.1999.91.1.0001 (1999).
- 303 Taher, A., Pilehvari, Z., Poorolajal, J. & Aghajani, M. Effects of Normobaric Hyperoxia in Traumatic Brain Injury: A Randomized Controlled Clinical Trial. *Trauma Mon* **21**, e26772, doi:10.5812/traumamon.26772 (2016).

- 304 Stiefel, M. F. *et al.* Reduced mortality rate in patients with severe traumatic brain injury treated with brain tissue oxygen monitoring. *Journal of neurosurgery* **103**, 805-811 (2005).
- 305 Wilensky, E. M. *et al.* Brain tissue oxygen practice guidelines using the LICOX CMP monitoring system. *J Neurosci Nurs* **37**, 278-288 (2005).
- 306 Nangunoori, R. *et al.* Brain tissue oxygen-based therapy and outcome after severe traumatic brain injury: a systematic literature review. *Neurocrit Care* **17**, 131-138, doi:10.1007/s12028-011-9621-9 (2012).
- 307 Hlatky, R., Valadka, A. B., Gopinath, S. P. & Robertson, C. S. Brain tissue oxygen tension response to induced hyperoxia reduced in hypoperfused brain. *Journal of neurosurgery* **108**, 53-58 (2008).
- 308 Diringer, M. N., Aiyagari, V., Zazulia, A. R., Videen, T. O. & Powers, W. J. Effect of hyperoxia on cerebral metabolic rate for oxygen measured using positron emission tomography in patients with acute severe head injury. *Journal of neurosurgery* **106**, 526-529 (2007).
- 309 Tisdall, M. M., Tachtsidis, I., Leung, T. S., Elwell, C. E. & Smith, M. Increase in cerebral aerobic metabolism by normobaric hyperoxia after traumatic brain injury. *J Neurosurg* **109**, 424-432, doi:10.3171/JNS/2008/109/9/0424 (2008).
- 310 Micarelli, A., Jacobsson, H., Larsson, S. A., Jonsson, C. & Pagani, M. Neurobiological insight into hyperbaric hyperoxia. *Acta Physiol (Oxf)* **209**, 69-76, doi:10.1111/apha.12116 (2013).
- 311 Verweij, B. H. *et al.* Impaired cerebral mitochondrial function after traumatic brain injury in humans. *Journal of neurosurgery* **93**, 815-820 (2000).
- 312 Zhou, Z. *et al.* Protection of mitochondrial function and improvement in cognitive recovery in rats treated with hyperbaric oxygen following lateral fluid-percussion injury. *Journal of neurosurgery* **106**, 687-694 (2007).
- 313 Palzur, E., Zaaroor, M., Vlodaysky, E., Milman, F. & Soustiel, J. F. Neuroprotective effect of hyperbaric oxygen therapy in brain injury is mediated by preservation of mitochondrial membrane properties. *Brain Res* **1221**, 126-133, doi:10.1016/j.brainres.2008.04.078 (2008).
- 314 Puccio, A. M. *et al.* Effect of short periods of normobaric hyperoxia on local brain tissue oxygenation and cerebrospinal fluid oxidative stress markers in severe traumatic brain injury. *J Neurotrauma* **26**, 1241-1249, doi:10.1089/neu.2008-0624
10.1089/neu.2008.0624 (2009).
- 315 Rockswold, S. B., Rockswold, G. L., Zaun, D. A. & Liu, J. A prospective, randomized Phase II clinical trial to evaluate the effect of combined hyperbaric and normobaric hyperoxia on cerebral metabolism, intracranial pressure, oxygen toxicity, and clinical outcome in severe traumatic brain injury. *J Neurosurg* **118**, 1317-1328, doi:10.3171/2013.2.JNS121468 (2013).
- 316 Narotam, P. K., Morrison, J. F. & Nathoo, N. Brain tissue oxygen monitoring in traumatic brain injury and major trauma: outcome analysis of a brain tissue oxygen-directed therapy. *Journal of neurosurgery* **111**, 672-682 (2009).
- 317 Pinggera, D., Petr, O., Putzer, G. & Thome, C. Adjustable and Rigid Fixation of Brain Tissue Oxygenation Probe (Licox) in Neurosurgery: From Bench to Bedside. *World Neurosurg* **117**, 62-64, doi:10.1016/j.wneu.2018.05.154 (2018).
- 318 Rockswold, S. B. *et al.* A prospective, randomized clinical trial to compare the effect of hyperbaric to normobaric hyperoxia on cerebral metabolism, intracranial pressure, and oxygen toxicity in severe traumatic brain injury. *J Neurosurg* **112**, 1080-1094, doi:10.3171/2009.7.JNS09363 (2010).
- 319 Rockswold, G. L., Ford, S. E., Anderson, D. C., Bergman, T. A. & Sherman, R. E. Results of a prospective randomized trial for treatment of severely brain-injured patients with hyperbaric oxygen. *J Neurosurg* **76**, 929-934, doi:10.3171/jns.1992.76.6.0929 (1992).
- 320 Marenco, S. *et al.* Regional distribution of measurement error in diffusion tensor imaging. *Psychiatry research* **147**, 69-78 (2006).

- 321 Lazaridis, C., Rusin, C. G. & Robertson, C. S. Secondary brain injury: Predicting and preventing
insults. *Neuropharmacology* **145**, 145-152, doi:10.1016/j.neuropharm.2018.06.005 (2019).
- 322 Daly, S. *et al.* Hyperbaric Oxygen Therapy in the Treatment of Acute Severe Traumatic Brain
Injury: A Systematic Review. *J Neurotrauma* **35**, 623-629, doi:10.1089/neu.2017.5225 (2018).
- 323 Spiotta, A. M. *et al.* Brain tissue oxygen-directed management and outcome in patients with
severe traumatic brain injury. *Journal of neurosurgery* **113**, 571-580 (2010).
- 324 Quintard, H., Patet, C., Suys, T., Marques-Vidal, P. & Oddo, M. Normobaric hyperoxia is
associated with increased cerebral excitotoxicity after severe traumatic brain injury.
Neurocrit Care **22**, 243-250, doi:10.1007/s12028-014-0062-0 (2015).
- 325 Lang, M. *et al.* A pilot study of hyperoxemia on neurological injury, inflammation and
oxidative stress. *Acta Anaesthesiol Scand* **62**, 801-810, doi:10.1111/aas.13093 (2018).
- 326 Ahn, E. S., Robertson, C. L., Vereczki, V., Hoffman, G. E. & Fiskum, G. Normoxic ventilatory
resuscitation following controlled cortical impact reduces peroxynitrite-mediated protein
nitration in the hippocampus. *J Neurosurg* **108**, 124-131,
doi:10.3171/JNS/2008/108/01/0124 (2008).
- 327 Reinert, M., Schaller, B., Widmer, H. R., Seiler, R. & Bullock, R. Influence of oxygen therapy
on glucose-lactate metabolism after diffuse brain injury. *J Neurosurg* **101**, 323-329,
doi:10.3171/jns.2004.101.2.0323 (2004).
- 328 Huang, L. & Obenaus, A. Hyperbaric oxygen therapy for traumatic brain injury. *Med Gas Res*
1, 21, doi:10.1186/2045-9912-1-21 (2011).
- 329 Newcombe, V. F. *et al.* Dynamic Changes in White Matter Abnormalities Correlate With Late
Improvement and Deterioration Following TBI: A Diffusion Tensor Imaging Study.
Neurorehabil Neural Repair **30**, 49-62, doi:10.1177/1545968315584004 (2016).
- 330 Hattori, N. *et al.* Acute changes in regional cerebral (18)F-FDG kinetics in patients with
traumatic brain injury. *J Nucl Med* **45**, 775-783 (2004).
- 331 Liu, Y. *et al.* Serial diffusion tensor MRI after transient and permanent cerebral ischemia in
nonhuman primates. *Stroke* **38**, 138-145, doi:10.1161/01.STR.0000252127.07428.9c (2007).
- 332 Puig, J. *et al.* Increased corticospinal tract fractional anisotropy can discriminate stroke onset
within the first 4.5 hours. *Stroke* **44**, 1162-1165, doi:10.1161/STROKEAHA.111.678110
(2013).
- 333 Bhagat, Y. A. *et al.* Elevations of diffusion anisotropy are associated with hyper-acute stroke:
a serial imaging study. *Magnetic resonance imaging* **26**, 683-693 (2008).
- 334 Anzai, Y. *et al.* Paramagnetic effect of supplemental oxygen on CSF hyperintensity on fluid-
attenuated inversion recovery MR images. *AJNR Am J Neuroradiol* **25**, 274-279 (2004).
- 335 Waldau, T., Larsen, V. H. & Bonde, J. Evaluation of five oxygen delivery devices in
spontaneously breathing subjects by oxygraphy. *Anaesthesia* **53**, 256-263 (1998).
- 336 Mayer, A. R., Hanlon, F. M. & Ling, J. M. Gray matter abnormalities in pediatric mild
traumatic brain injury. *J Neurotrauma* **32**, 723-730, doi:10.1089/neu.2014.3534 (2015).
- 337 Ling, J. M., Klimaj, S., Toulouse, T. & Mayer, A. R. A prospective study of gray matter
abnormalities in mild traumatic brain injury. *Neurology* **81**, 2121-2127,
doi:10.1212/01.wnl.0000437302.36064.b1 (2013).
- 338 Sidaros, A. *et al.* Diffusion tensor imaging during recovery from severe traumatic brain injury
and relation to clinical outcome: a longitudinal study. *Brain : a journal of neurology* **131**, 559-
572 (2008).
- 339 D'Angio, C. T. *et al.* Changes in surfactant protein gene expression in a neonatal rabbit model
of hyperoxia-induced fibrosis. *Am J Physiol* **272**, L720-730 (1997).
- 340 Thiagarajan, A., Goverdhan, P. D., Chari, P. & Somasunderam, K. The effect of
hyperventilation and hyperoxia on cerebral venous oxygen saturation in patients with
traumatic brain injury. *Anesthesia and analgesia* **87**, 850-853 (1998).

- 341 Charbel, F. T., Hoffman, W. E., Misra, M. & Ausman, J. I. Increased brain tissue oxygenation during arteriovenous malformation resection. *Neurol Med Chir (Tokyo)* **38 Suppl**, 171-176 (1998).
- 342 Zhang, Y., Porat, R. M., Alon, T., Keshet, E. & Stone, J. Tissue oxygen levels control astrocyte movement and differentiation in developing retina. *Brain Res Dev Brain Res* **118**, 135-145 (1999).
- 343 Manley, G. T. *et al.* Brain tissue oxygenation during hemorrhagic shock, resuscitation, and alterations in ventilation. *J Trauma* **46**, 261-267 (1999).
- 344 Rossi, S. *et al.* Brain oxygen tension during hyperoxia in a swine model of cerebral ischaemia. *Acta neurochirurgica. Supplement* **76**, 243-245 (2000).
- 345 Singhal, A. B. *et al.* A pilot study of normobaric oxygen therapy in acute ischemic stroke. *Stroke; a journal of cerebral circulation* **36**, 797-802 (2005).
- 346 Singhal, A. B. Oxygen therapy in stroke: past, present, and future. *International journal of stroke : official journal of the International Stroke Society* **1**, 191-200 (2006).
- 347 Fehlings, M. G. & Baker, A. Is there a role for hyperoxia in the management of severe traumatic brain injury? *Journal of neurosurgery* **106**, 525; discussion 525 (2007).
- 348 Liu, Z.-J. & Velazquez, O. C. Hyperoxia, endothelial progenitor cell mobilization, and diabetic wound healing. *Antioxidants & redox signaling* **10**, 1869-1882 (2008).
- 349 Fisher, A. B. & Beers, M. F. Hyperoxia and acute lung injury. *American journal of physiology. Lung cellular and molecular physiology* **295**, L1066; author reply L1067 (2008).
- 350 Hong, Y. T. *et al.* Amyloid imaging with carbon 11-labeled Pittsburgh compound B for traumatic brain injury. *JAMA Neurol* **71**, 23-31, doi:10.1001/jamaneurol.2013.4847 (2014).
- 351 Frahm, J. *et al.* Localized high-resolution proton NMR spectroscopy using stimulated echoes: initial applications to human brain in vivo. *Magnetic resonance in medicine : official journal of the Society of Magnetic Resonance in Medicine / Society of Magnetic Resonance in Medicine* **9**, 79-93 (1989).
- 352 Charles, H. C. *et al.* Proton spectroscopy of human brain: effects of age and sex. *Prog Neuropsychopharmacol Biol Psychiatry* **18**, 995-1004 (1994).
- 353 Miller, B. L. *et al.* In vivo ¹H MRS choline: correlation with in vitro chemistry/histology. *Life sciences* **58**, 1929-1935 (1996).
- 354 Brooks, W. M., Friedman, S. D. & Stidley, C. A. Reproducibility of ¹H-MRS in vivo. *Magnetic resonance in medicine : official journal of the Society of Magnetic Resonance in Medicine / Society of Magnetic Resonance in Medicine* **41**, 193-197 (1999).
- 355 Maudsley, A. A. & Hilal, S. K. Field inhomogeneity correction and data processing for spectroscopic imaging. *Magnetic resonance in medicine : official journal of the Society of Magnetic Resonance in Medicine / Society of Magnetic Resonance in Medicine* **2**, 218-233 (1985).
- 356 Wilson, M. *et al.* Methodological consensus on clinical proton MRS of the brain: Review and recommendations. *Magn Reson Med* **82**, 527-550, doi:10.1002/mrm.27742 (2019).
- 357 Donadieu, M. *et al.* Metabolic counterparts of sodium accumulation in multiple sclerosis: A whole brain ²³Na-MRI and fast ¹H-MRSI study. *Mult Scler* **25**, 39-47, doi:10.1177/1352458517736146 (2019).
- 358 Gasparovic, C. *et al.* Neurometabolite concentrations in gray and white matter in mild traumatic brain injury: an ¹H-magnetic resonance spectroscopy study. *J Neurotrauma* **26**, 1635-1643, doi:10.1089/neu.2009-0896
10.1089/neu.2009.0896 (2009).
- 359 Bates, T. E. *et al.* Inhibition of N-acetylaspartate production: implications for ¹H MRS studies in vivo. *Neuroreport* **7**, 1397-1400 (1996).

- 360 Shannon, R. J. *et al.* Extracellular N-Acetylaspartate in Human Traumatic Brain Injury. *J Neurotrauma* **33**, 319-329, doi:10.1089/neu.2015.3950 (2016).
- 361 Ratai, B., Sorensen, Vangel, Koroshetz, Schaefer, Lo, Gonzalez, Singhal.
- 362 Singhal, A. B., Dijkhuizen, R. M., Rosen, B. R. & Lo, E. H. Normobaric hyperoxia reduces MRI diffusion abnormalities and infarct size in experimental stroke. *Neurology* **58**, 945-952 (2002).
- 363 Longhi, L. & Stocchetti, N. Hyperoxia in head injury: therapeutic tool? *Current opinion in critical care* **10**, 105-109 (2004).
- 364 Singhal, A. B. Oxygen therapy in stroke: past, present, and future. *Int J Stroke* **1**, 191-200, doi:10.1111/j.1747-4949.2006.00058.x (2006).
- 365 Stovell, M. G. *et al.* Corrigendum: Assessing Metabolism and Injury in Acute Human Traumatic Brain Injury with Magnetic Resonance Spectroscopy: Current and Future Applications. *Front Neurol* **8**, 642, doi:10.3389/fneur.2017.00642 (2017).
- 366 Gooijers, J. *et al.* Subcortical Volume Loss in the Thalamus, Putamen, and Pallidum, Induced by Traumatic Brain Injury, Is Associated With Motor Performance Deficits. *Neurorehabil Neural Repair* **30**, 603-614, doi:10.1177/1545968315613448 (2016).
- 367 Ruet, A. *et al.* Severe Traumatic Brain Injury Patients without Focal Lesion but with Behavioral Disorders: Shrinkage of Gray Matter Nuclei and Thalamus Revealed in a Pilot Voxel-Based MRI Study. *J Neurotrauma* **35**, 1552-1556, doi:10.1089/neu.2017.5242 (2018).
- 368 Leunissen, I. *et al.* Subcortical volume analysis in traumatic brain injury: the importance of the fronto-striato-thalamic circuit in task switching. *Cortex* **51**, 67-81, doi:10.1016/j.cortex.2013.10.009 (2014).
- 369 Ghosh, A. *et al.* Hyperoxia results in increased aerobic metabolism following acute brain injury. *J Cereb Blood Flow Metab* **37**, 2910-2920, doi:10.1177/0271678X16679171 (2017).
- 370 Alves, O. L., Daugherty, W. P. & Rios, M. Arterial hyperoxia in severe head injury: a useful or harmful option? *Curr Pharm Des* **10**, 2163-2176 (2004).
- 371 Palzur, E. *et al.* Hyperbaric oxygen therapy for reduction of secondary brain damage in head injury: an animal model of brain contusion. *J Neurotrauma* **21**, 41-48, doi:10.1089/089771504772695931 (2004).
- 372 Vespa, P. M. A breath of fresh air: the potential use for hyperoxia in traumatic brain injury. *Crit Care Med* **36**, 363-365, doi:10.1097/01.CCM.0000297946.34037.31 (2008).